UNIVERSITY OF SOUTHAMTON

FACULTY OF SCIENCE

DEPARTMENT OF OCEANOGRAPHY

EXPERIMENTS WITH A HIGH FREQUENCY LASER SLOPE METER

by

Valerie Jean Ballard

A thesis submitted for the degree of Doctor of Philosophy

January 2001

UNIVERSITY OF SOUTHAMPTON

ABSTRACT

FACULTY OF SCIENCE
OCEANOGRAPHY

Doctor of Philosophy

EXPERIMENTS WITH A HIGH FREQUENCY LASER SLOPE METER

By Valerie Jean Ballard

In this thesis research is presented which aims to explore and exploit the capability of a single point Laser Slope meter for measuring the two-dimensional surface slope of water waves. The instrument is capable of being deployed in the field as well as wind wave tanks and these two environments are used to explore the full capability of the instrument for determining the applicability of wave tank data to the ocean environment. Two areas of research are concentrated on; these are the ambient surface wave field and interactions between surface waves and a horizontally varying surface current. Measurements of the ambient wave field in both the field and a wave tank are presented. The results have led to a questioning of the Gram-Charlier behaviour of the two-dimensional surface slope probability distribution reported by Cox and Munk. Techniques are used in both the wave tank and the field to estimate the ambient wavenumber spectrum. In the field the results support a k^{-4} spectrum whilst in the wave tank, the spectral form is more complicated but does have regions that vary as k^{-4}. The results also show that using suitable techniques for calculating the wind friction velocity allows a direct comparison of data collected in different ocean environments. An experiment has been designed in which the Laser Slope meter has been used successfully to measure modulations in the surface wave field caused by a horizontally varying surface current. A numerical model is developed to solve the action balance equation describing surface wave-surface current interactions, which is capable of accepting experimentally measured background spectra and surface currents. This model is used to provide a theoretical comparison for the experimentally measured interaction data. The research concentrates on investigating the most effective way of performing the experiment, analysing the experimental data and manipulating the theoretical results, rather than on the results from this experiment specifically. However, the model data are found to predict well some of the experimentally measured variations.

List of contents

Symbols and abbreviations

A	height wavenumber density
A_q	Normalising constant in angular part of spectrum
a	Charnock constant, or wave amplitude
$a_{\underline{k}}$	amplitude of wavevector $\underline{k}$
ak	slope
B	degree of saturation
$b_{n,m}$	coefficients in expansion of f(x,y) in terms of Hermite polynomials in Appendix A
c_g	group speed
c_p	phase speed
c_z	drag coefficient
c_{10}	drag coefficient at 10m above sea level
C_{ij}	Gram-Charlier coefficients
c_{ff}	autocorrelation function
d_1	constant in Amorocho and DeVries work
d_2	constant in Amorocho and DeVries work
d_c	distance between cameras in stereo photography
d_l	distance to image location in left camera in stereo photography
d_r	distance to image location in right camera in stereo photography
dB	decibels
E(k)	spectral energy density
F(ϕ)	angular part of wavenumber spectrum
F(z)	vertical function in solution to linear surface waves
FT(f)	value of Fourier Transform at frequency, f
f	frequency
f_{max}	Nyquist frequency
f()	general function
g	acceleration due to gravity
H	Hermite polynomials
H(ω)	Wave height frequency spectrum

h	height from datum, e.g. depth of water
i	angle of incidence relative to normal, or general index
J_n	Bessel function
j	general index
k	wavenumber
k_x	wavenumber component in x-direction
k_y	wavenumber component in y-direction
k_1	wavenumber component in 1-direction
k_2	wavenumber component in 2-direction
L	length scale
l	laser slope angle relative to vertical
M	inversion matrix
$m_{n,m}$	moment about the mean
$m'_{n,m}$	moment about the origin
N	general total number of points
$N(k)$	action spectral density per unit wavenumber space
N_B	background action spectrum
N_D	action due to wave dissipation
N_G	action due to wave growth
N_{NL}	action due to non-linear wave-wave interactions
n	ratio of refractive index of air to water, general point index
O	orthogonal matrix
O_{ij}	orthogonal matrix elements
p	pressure, or power of decay term in action balance equation
$p(x)$	probability
$p(x,y)$	probability of x,y
$p_g(x,y)$	Gaussian probability density function
Q	Runge kutta terms
q	angular index in wavenumber spectrum
Re	real part of
r	angle of refraction relative to normal
r_s	ratio in Nyquist explanation
$S(\underline{k})$	total slope full wavenumber spectrum

$S(k,\phi)$	total slope full wavenumber spectrum
$S_x(\underline{k})$	x-slope component full wavenumber spectrum
$S_x(k,\phi)$	x-slope component full wavenumber spectrum
$S_y(\underline{k})$	y-slope component full wavenumber spectrum
$S_y(k,\phi)$	y-slope component full wavenumber spectrum
$S_x(k)$	wavenumber part of x-slope wavenumber spectrum
$S_y(k)$	wavenumber part of y-slope wavenumber spectrum
$S(\omega)$	surface slope frequency spectrum
$S_{ml}(\omega')$	Frequency spectrum measured by TLS
s	slope time series
s_c	cross wind slope component
s_u	along wind slope component
T	surface tension of water
T_w	Time length of window function
T_s	Time length of data series
T_p	period of gravity waves supporting capillary waves
t	time, or laser tilt angle in water
$\underline{U}$	vector surface current velocity
U_x	x-component of surface current
$\underline{u}$	velocity vector
u_z	vertical velocity of surface wave motion
u*	wind friction velocity
v	velocity of sub-surface carriage, velocity of TLS
$\underline{v}_n$	voltage of diode number n multiplied by unit vector in n^{th} dimension
$\underline{v}_c$	normalised calibration data voltage vector
$\underline{v}_d$	difference voltage vector
$\underline{v}_r$	normalised run data voltage vector
W	window function
w	water slope angle relative to horizontal, or wind speed
w_{fx}	horizontal component of instantaneous wind velocity
w_{fz}	vertical component of instantaneous wind velocity
w_{10}	wind speed at 10m above sea level

X	dominant symmetric axis used in diagonalisation
x	horizontal co-ordinate
x_{nd}	non-dimensionalised fetch
Y	dominant asymmetric axis used in diagonalisation
y	horizontal co-ordinate
z	vertical co-ordinate, usually measured from sea level
α	Phillips wave growth parameter
β	Miles wave growth parameter
β_d	constant in decay term
$\chi(k)$	wavenumber height spectrum integrated over all angles
Δ	small change in, del operator
δ	delta function, or constant in front of Phillips decay term
ε	small fraction of
Φ	velocity potential
Φ_0	linear component of velocity potential
ϕ	angle between wind and wavenumber k in angular distribution of wave field
ϕ_w	wind direction
Γ	Gamma function
γ	constant term in wave decay parameter, or power of term in Banner's spectral form
η	wave height amplitude
ϑ	arbitrary phase constant
φ	angle between current and wind direction
κ	Von Karman constant
Λ	sum of wave growth, dissipation and wave-wave interactions terms
λ	wavelength
μ	relaxation rate
ν	kinematic viscosity
Π	quasi wavenumber, frequency term
π	3.141592654
Θ	wavenumber height spectrum angular distribution
θ	angle between current and wavenumber k

ρ	density of water
ρ_a	density of air
Σ	sum over
σ	standard deviation, or radar cross section
σ_B	background radar cross section
σ_c	rms cross wind
σ_u	rms along wind
σ^2	variance
τ	stress, or dummy variable of integration
ς	standardised y-slope component
Ω	angular frequency of surface waves measured by observer on sub-surface carriage
ω	intrinsic angular frequency of surface waves (measured by observer moving with mean flow)
ω'	frequency of encounter
Ξ	general function in Runge-Kutta routine
ξ	standardised x-slope component
$\Psi(\underline{k})$	full wave height wavenumber spectrum
$\Psi(k,\theta)$	full wave height wavenumber spectrum
$\Psi(k_1,k_2)$	full wave height wavenumber spectrum
$\psi(k)$	wave height wavenumber spectrum at an angle of θ
ζ	mean
CTD	Conductivity-Temperature-Depth
DERA	Defence Evaluation and Research Agency
DFT	Digital Fourier Transform
DGPS	Differential Global Positioning System
DML	Dunstaffnage Marine Laboratory
FFT	Fast Fourier Transform
GPS	Global Positioning System
IDL	Interactive Data Language
IMU	Inertial Motion Unit
LL97	Loch Linnhe Experiment 1997

mss	mean square slope
MTF	Modulation Transfer Function
OEL	Ocean Engineering Laboratory
OIP	Ocean Imaging Programme
pdf	probability density function
PSD	Power Spectral Density
rms	root mean square
SAR	Synthetic Aperture Radar
SARSEX	SAR Internal Wave Signature Experiment
TLS	Towed Laser Slope meter
UCSB	University of California, Santa Barbara

Preface

During the Laser Slope meter project, the Author has been the lead scientist responsible for the design of the Laser Slope meter experiments, writing the experimental plans and leading a team of scientists to gather the experimental data. This has involved defining the type of experiment needed, ensuring appropriate subsidiary data was collected, as well as day to day planning and scientific management of the team. She has also been responsible for the data analysis, writing appropriate software where necessary, as well as considering theoretical comparisons with the data. She has been involved with the progress of the instrument, playing a supportive role in defining improvements as part of a larger team.

Chapters 5 to 9 of this thesis contain a description of, and the results from, the original research which has been conducted. During the course of the research, the Author has married. Therefore, her work is contained in references to Taylor, VJ as well as Ballard, VJ.

Acknowledgements

During the course of this research I have received a great deal of guidance and assistance from many people. I would like to take this opportunity to express my thanks to everyone who has contributed in any way, however small. In the list below I have mentioned just a few of those people who have been particularly supportive throughout.

First of all I must say thank you to the Defence Evaluation and Research Agency who have allowed me to use my research for them as the basis of this thesis. They have also provided funding for all of the research work and for my PhD fees. Many of my colleagues have contributed considerable advice and support and many useful ideas have been born through discussions with them. In particular I would like to mention Dr Jon Perry and Dr Tom Cooper who have been a constant source of help and encouragement in everything I have done. Other colleagues who have contributed help and support, particularly during trials work are Mr Brian Barber, Dr Ian Lee-Bapty, Mr Richard Love, Mr Tim Knight, Mr Giles Gibson, Mr Chris Nott, Mrs Jane Penny, Miss Angelina Dawson, Mr Dominic Walker and Mr Tim Lamont-Smith.

Staff at the Dunstaffnage Marine Laboratory, Oban, and the crew on the Seol Mara (the fishing vessel from which the TLS was deployed) have provided support on the field trial in Loch Linnhe. Thanks go to them for their co-operation and support. Also, Dr Bill Peirson of the Water Research Laboratory, University of New South Wales, Australia has given help and guidance at various times and Dr Jamie Barter and his colleagues at TRW, USA have willingly lent equipment and provided results and reports which have been used.

Particular thanks go to Professor Marshall Tulin at the Ocean Engineering Laboratory, Santa Barbara who has allowed the use of the facility for our experiments. He has encouraged his staff, Mr Tobias O'Cruise and Mr Dominic Regas to help us in any way possible. This has undoubtedly enabled an increased amount of research to be completed.

My supervisor, Professor Ian Robinson, has provided help and encouragement throughout the life of the PhD. He has made suggestions as to the progression of the work and more recently has read through endless draft copies making useful comments.

Finally, I would like to thank my personal friends and relations for all their support and encouragement. Of my friends, many are already mentioned above, remaining are Rachel Bird and Kathryn Clayton. All my friends have been wonderful at putting up with me and all my moods! My Mum, Dad, brother, Peter and sister Jenni have also given much encouragement over the years. Last of all, I would like to thank my husband Andy for all his love and support, often at difficult times, when there's no dinner ready or the washing's not done because I'm too busy working.

Chapter 1

Introduction

The research described in this thesis encompasses a wide range of ocean phenomena which can all be associated with a particular focused field of study. The research concentrates on experiments using a Laser Slope meter in both field and laboratory situations, with the particular aim of assessing and exploiting the capability of the instrument. In doing so, studies are centred around measurements of the ambient surface wind wave field and modulations of the ambient conditions by surface currents. In support of the measurements, various theories are considered and extended to provide verification of, and comparison with, the measurements.

The driving force behind the research has been the need to improve understanding of the ocean surface roughness, particularly at high frequencies, and the way it is affected by other ocean phenomena. This understanding is necessary so that remote sensing tools, such as radar, which detect the roughness patterns on the ocean surface, can lead to knowledge of the underlying ocean phenomena simply by imaging the surface (De Loor, 1981, Alpers and Hennings, 1984). This research is intended to contribute toward fulfilling the potential of radar as an imaging tool for upper ocean processes.

Over the last 20 years, since the advent of satellite remote sensing, interest in the short-scale (few centimetres to 1m) characteristics of the ocean has increased. This particularly came about as a result of the advent of Synthetic Aperture Radar (SAR). The first extensive collection of SAR images of the ocean, from the Seasat satellite in 1978, showed that a large number of unexpected ocean features were visible in radar images of the ocean. These features included fronts, plumes, ship wakes, upwelling, ice, internal waves, bathymetry, ocean swell and slicks due to surfactants. There has been considerable research into many of these phenomena in an attempt to understand the mechanisms by which they are imaged (Alpers and Hennings, 1984, Alpers, 1985, Phillips, 1984, Perry, 1988, Hwang and Shemdin, 1990, Miller and Shemdin, 1991) so that improved images may be obtained and

that more information may be extracted from existing images. A lot of progress has been achieved; however, there is still not a complete understanding of these ocean phenomena and the way in which they are imaged.

This thesis concentrates on improving knowledge of the short-scale, high frequency, features on the ocean surface; an area in which there is still much research to do. In the past, researchers have tended to study longer scale characteristics (i.e. waves of order a metre to several kilometres) due to the limitations of their instrumentation and because such phenomena are responsible for events which can have a large impact on the lives of local communities. For example, large ocean waves and storms are responsible for the immense forces that produce coastline erosion, and extreme waves may cause sudden and unexpected flooding resulting in significant damage and loss of lives. Recently, advances in the exploration of space have led to the use of space for monitoring the earth. For this purpose remote sensing equipment has been developed, such as altimeters and imaging radars (Allan, 1983), for deployment on satellite and airborne systems. To be able to make full use of the information now available from such sensors, scientists have needed more information about the high frequency end of the spectrum of ocean waves, as it is these waves which are imaged by radar. In addition to discovering further details about the ambient wave spectrum, research has shown that modulation of these short waves can occur owing to interactions with surface currents associated with other ocean phenomena. This can lead to visibility in radar images of *sub*-surface features such as sand banks and internal waves, as well as other surface features including swell (Alpers and Hennings, 1984, Alpers *et al,* 1981). These features have previously been undetected by other imaging instruments.

The potential uses for an improved understanding of these processes are numerous. Already in trial use from current satellite systems are real time information relay systems on weather fronts and ice movements. These have the ability to provide potentially life saving information for shipping as well as being an important source of information for the military. Upwelling is produced where wind driven currents cause bulk movement of water away from coastlines which is then replaced by cooler denser water from below at depths of 100m to 300m, setting up a circulation process which is usually seen as a divergence of surface currents. This deeper water is often richer in nutrients than the surface layer and tends to attract a high fish population. Therefore, knowledge of the location of upwelling

regions can be important for the fishing industry. Similar forms of upwelling may also occur at frontal regions with corresponding implications for fishing. Where plumes of a lower density water enter the main ocean, a front and regions of upwelling often exist; thus, the plumes can be visible in satellite imagery. This can be useful for monitoring the progress of pollutants which often enter the ocean from estuarine regions from which the plumes emanate.

The Dutch currently use airborne systems for monitoring movements of sand banks around their coastlines (Barber, 1999). They are attempting to improve their knowledge of precisely how the radar imagery relates to the local position of the sand bank in terms of the roughness patterns which are generated at the water surface (Gommenginger *et al*, 1999). This is being achieved by obtaining radar imagery of the sea surface coincident with direct surface roughness versus water depth measurements.

The mechanisms by which a sand bank can be imaged are similar to those which enable an internal wave to be visible in a radar image (Alpers, 1985). Internal waves can be generated naturally in stratified water when the static equilibrium of the water column is subjected to a disturbance such as the tide pushing the body of water over a ridge or ocean shelf. This disturbance to the equilibrium of the water column sets up an oscillation from which internal waves radiate. Natural internal waves generated in this way are many kilometres in wavelength and can be seen easily in a radar image of the ocean as a series of bright and dark stripes that get gradually longer in wavelength as they travel further from the source. The detection of natural internal waves provides information to oceanographers that may be of use in a variety of ways as their presence announces the existence of a density stratification in the water column. This may affect the propagation of sonar rays which are used both actively and passively for other types of oceanographic measurements (HMS Dryad).

As well as being generated naturally, internal waves may also be created by vessels travelling through stratified waters, though these waves are of much shorter wavelength than their natural counterparts. This can lead to the "dead water effect" (LeBlond and Mysak, 1978, Lamb, 1975) in which ships and submarines lose power if they travel at a particular speed. This is caused by energy being pumped into the water to create the internal

waves rather than being used to power the vessel. Under the right oceanographic and meteorological conditions, it is possible to detect the internal wave generated by a ship in a radar image, known as the internal wave wake. The detection of ships by their wakes rather than directly has powerful military applications and is a subject of much research. However, so far it has been difficult to gain sufficient signal to noise ratio for the imaging to be very successful and so a more complete knowledge of the effects of the internal wave on the water surface is essential to develop better detection techniques.

Many of the above ocean phenomena have a common feature. They create weak varying currents at the surface of the ocean that modulate the short-scale ocean roughness, causing variations which are easily detected by radar instruments. Unfortunately, the exact way in which the currents modulate the surface is not fully understood, which causes difficulties in the interpretation of the resulting radar images. This is the main topic that has driven the research in this thesis: to improve understanding of the way in which surface currents modulate the ambient surface wave field. However, part of this problem is that the behaviour of the high frequency, short scale, end of the ambient ocean wave field is not known in detail when these waves exist as part of a wave field consisting of both gravity and capillary waves. Therefore, to be able to progress with this research it is necessary to have a good understanding of the ambient surface wave field and the practicalities of measuring short scale ocean surface waves. For this reason, initially, this topic is studied extensively. A second mechanism by which it is thought that phenomena such as internal waves may become visible is by damping due to surface films of organic material when they are periodically compacted and expanded in the internal wave field. This thesis does not consider this mechanism but instead concentrates only on modulations of the surface waves by surface currents.

In order for this research project to proceed, a non-intrusive, high-frequency, high accuracy research instrument was needed. A Laser Slope meter device was designed and developed by a team from the departments of Physics and Oceanography at the University of Southampton (Ghataure and Ramsden, 1992, Ghataure *et al.*, 1993, Lee, 1995) and later by Aquatec Electronics (Good, 1997a), both under contract to the Defence Evaluation and Research Agency (DERA). This device is capable of making a single point measurement of the two-dimensional surface slope of the water surface. It uses a non-intrusive optical

technique at a high sampling rate, and is thus capable of making measurements of the highest frequency components present on the ocean surface. The prototype device developed by the University of Southampton was assessed by Willoughby (1998) in his PhD thesis and was found to be a useful tool for short scale ocean surface measurements. The measurement capabilities of the instrument have provided the opportunity for new detailed observations of surface slope at high spatial and temporal frequency. Such observations, their analysis and the interpretation of the slope data form the substantial part of the work in this thesis. Here, these capabilities are explored in a greater variety of conditions than used by Willoughby, and with an enhanced instrument. The emphasis has changed from determining whether the instrument provides data products consistent with visual observations and general ocean phenomena to a concentrated effort to explore its full potential for supplying new information about a variety of ocean phenomena. It should be noted that in terms of the instrument itself, apart from suggestions for various improvements that were implemented during the period of this research, the Author played only a small part in the design of the instrument. She had no participation in its development or construction, or in the writing of the logging and processing software.

In order to pursue a better understanding of those ocean processes that modulate the short-scale surface roughness using small surface currents, it is first necessary to understand the characteristics of the ambient surface wave field. Therefore, this thesis concentrates on a fairly broad range of experiments all of which aim to exploit the new instrument under a wide range of circumstances. It does not aim specifically to provide new results on ocean phenomena, although these are the ultimate driving force behind the research, but instead is aimed at realising the full potential of this new instrument for measuring very high frequency components of the surface wave slope. This involves experimentation in a wave tank and the field as well as using and extending existing theories to produce meaningful and useful results from the raw data. Once this potential is established, a whole new set of research questions can be investigated which were not possible previously. Therefore, this thesis is aimed primarily at proving the capability of the Laser Slope meter to detect, and measure, surface roughness modulation, in doing so, complementing and extending the work of Willoughby (1998). The research concentrates on characterising the surface temporally, statistically and spectrally and on the way in which the surface currents modulate these

measurements with particular reference to the advantages and disadvantages of this instrument.

Using this instrument, experiments have been conducted in the field and the ocean simulation environment of a wind wave tank, studying both the background water surface characteristics and then the modulation of these results by surface currents. Throughout, the novel and unique features of the instrument are discussed, together with the way in which they improve the possible measurements compared with more traditional measuring techniques. Where some aspect of the instrument causes analysis difficulties in its attempt to better previous measurements, these are investigated. The Author has been the primary research lead for all of the experiments described, designing, implementing and leading each experiment as well as carrying out the majority of the data processing and performing the analysis.

The main oceanographic and instrument research objectives that have been targeted in this thesis are:

- to establish the advantages of the Laser Slope meter over other instruments with similar objectives, but also to identify its disadvantages;
- to compare a variety of data from this instrument with previous data and theory, so as to verify it as a correctly working scientific tool;
- to extend knowledge of background wind wave fields both in the field and the wave tank, particularly concentrating on the high frequency end of the spectrum, which is important for radar imaging of the ocean;
- to compare ambient wave field data from the wave tank and the field and assess the usefulness of tank experiments in understanding real ocean phenomena;
- to use the Laser Slope meter to study the high frequency behaviour of ocean phenomena which modulate the ambient surface wave field through the production of weak varying surface currents, and to compare the results with previous research.

Each chapter of this thesis concentrates on a different area. In Chapter 2 a critical review of other ocean characterising instruments is performed and a discussion is presented of the way in which the design of the Towed Laser Slope meter originated. Its particular benefits are

highlighted and results from tests of its performance are examined. The design of the basic detector and the individual elements, which are used in the ocean and tank experiments, are emphasised. In its prototype configuration it was initially deployed in Loch Linnhe and the North Sea, the results of which are presented in Willoughby (1998) and Gommenginger *et al.* (1999). After some minor improvements it was used again in a field experiment in Loch Linnhe, Scotland. Following this experiment major improvements were made to the initial design. These are described along with justification for the modifications. The improved instrument was used for the remaining experiments presented here. Aspects, where the Author has participated in the design work, are highlighted.

In chapter 3 a scientific description is given of the ambient surface wave field and of how the theory to account for it has developed over the last century. Established and well known results are noted and areas where further research is needed are identified. Here, the entire subject is outlined which is then built upon in later chapters of the thesis.

The work presented in chapter 4 considers situations in which the ambient surface wave field may be modulated by a horizontal varying surface current. The fundamental kinematic and dynamic equations are given and these are combined to produce the action balance equation. This equation models energy exchanges in these types of interaction. A literature review of previous solutions to the action balance equation is presented and their limitations are discussed.

In chapters 5 and 6 the emphasis of the thesis changes from the initial introductory material to the presentation of actual data collected with the Laser Slope meter. These two chapters focus on analysis of data collected in Loch Linnhe, Scotland. The data from this experiment was used to make a thorough study of the ambient surface wave field. At this stage the instrument was in relative infancy; therefore, initially the experiment was used to provide verification that the basic results were consistent with visual observations and photographs of the surface as well as with results obtained by previous researchers, such as Cox and Munk (1954a, 1954b). These tests are mentioned only briefly in this thesis in chapter 2, with the detailed work presented in Taylor (1997). In this experiment, the instrument was towed across the wave field in an attempt to provide spatial, as well as temporal, information. However, due to the fairly random motion of the surface waves within the wave field, the

collected data contain many ambiguities that can only be reduced by careful preparation and analysis. A technique presented previously by Hughes (1978) is developed in order to make an estimation of the surface wavenumber spectrum. Chapter 5 considers the statistics of the measured ambient wave field whilst chapter 6 concentrates on spectral variations.

The data presented in chapters 7 and 9 were collected during tank experiments at the Ocean Engineering Laboratory (OEL), University of California, Santa Barbara (UCSB). Here, just the detector system was used without the catamaran. Therefore, the instrument was deployed so that it was stationary within the wave tank, providing only temporal information. Although such data are not identical to those obtained in the field, many comparisons can be made, particularly because exactly the same detector system was used. It is unusual to have a system capable of being deployed in both the tank and ocean environments. This puts the Laser Slope meter at an advantage over many other types of measuring systems.

Chapter 7 concentrates on the ambient surface wave field in the wave tank. Initially, statistical variations of the wind wave field with wind speed are studied, including histograms of the along and cross tank slope components and the mean square slope. The latter is presented as a function of the wind friction velocity and is compared to the results collected in Loch Linnhe. Very high frequency spectral measurements have been made in two positions within the tank. These two results are compared with each other and with theory, noting in particular where there are agreements and discrepancies between these results and the theory and with real ocean measurements. A practical study of the effect of the laser spot size on the resulting spectra has been performed, as have theoretical considerations of the same effect. Also discussed is the information that may be obtained about the angular distribution of the wave field by considering the cross and along tank components of the surface slope. This type of analysis can lead to an estimate of the wavenumber spectrum. This is used and the results are compared with theory and previous experimental data. Detailed wave profiles have been obtained over a wide range of wind speeds, showing examples of capillary waves. These are believed to be the most detailed of this kind of measurement of capillary wave slopes. In addition, data and photographs have been obtained of mechanically generated wave groups. Some of these are presented to show the enormous potential of the instrument for such measurements.

In chapter 8 the work focuses on surface current modulations to the ambient wind wave field. Initially, the theory is studied in more depth and a numerical program is written and tested which is capable of solving the action balance equation to determine the variations caused by a surface current to the wavenumber spectrum. The program is written in such a way that it is possible to insert any surface current and ambient spectral form, rather than needing a functional form. Additionally, any form of growth, decay and interactions terms can be used. In this chapter, functional forms of surface current and background spectrum are used as examples so that the variation of the action modulation with other parameters within the equation can be examined. The program has been written specifically so that theory can be compared with experimental results in chapter 9.

Chapter 9 presents Laser Slope meter data of surface current / surface wind wave field interactions in the wave tank. A new and innovative method of producing a varying surface current is used, and the effect of this on the background wave field is studied both spatially and spectrally over a range of wind speeds and surface currents. These results are compared with other similar experiments such as those conducted by Miller and Shemdin (1991) and Miller *et al.* (1991) and with theoretical predictions of the interaction. The theoretical results are calculated using the program developed in chapter 8 and ambient wavenumber spectra estimated using the methods described in chapter 7. Discrepancies between the experimental results and the theory are discussed and reasons for the differences are suggested.

Finally, the thesis is concluded with a discussion of the main results and techniques presented. The future possibilities of the Laser Slope meter are discussed, highlighting where the advantages of the instrument have led to an improved knowledge of ocean processes and also where there is potential for further experimentation. The disadvantages of the instrument are also discussed and suggestions are made for potential improvements. Areas of research where the Laser Slope meter has already made a significant contribution to current research are discussed in detail with a summary of the main results.

Chapter 2

A critical review of surface wave field measuring instruments and the Towed Laser Slope meter

2.1 Introduction and scope of chapter

In this chapter a critical review is given of previous attempts to devise instruments and deployment methods capable of making useful scientific measurements of the ocean surface characteristics. The advantages and disadvantages of each set-up are discussed, particularly considering how appropriate each particular technique is to producing specific kinds of data products. The application of this knowledge for the construction of an improved instrument is discussed briefly and then the design of the Towed Laser Slope meter is outlined. The development of the instrument during the lifetime of this research project is described. Finally, the performance of the instrument is assessed through the analysis of some simple laboratory and wave tank tests.

2.2 Methods of characterising the ambient ocean surface

Many types of instruments have been used to make measurements of the ocean surface characteristics; these include accelerometers, pressure gauges, wire gauges and optical methods. The optical methods consist of three main types: reflective, refractive and stereoscopic. Each of these techniques has advantages and disadvantages that are described below, along with details of the equipment and the way in which it is deployed.

For measurements of metre scale ocean waves, accelerometers were used to measure the wave height (Cartwright, 1963), also reviewed in Willoughby (1998). An accelerometer is deployed from a platform that floats on the waves being measured. In order to measure roll, pitch and yaw, three accelerometers are needed for the three rotation axes. Information

from an accelerometer can be integrated twice in time to produce the wave displacement. Another traditional form of wave height sensor that is capable of measuring slightly shorter waves than the accelerometer is the pressure gauge (Vilensky *et al.,* 1961), again reviewed in Willoughby (1998). As a wave moves up and down it creates a pressure fluctuation in the water column directly beneath the wave. The pressure variations can be detected down to approximately half the wavelength of the wave and so the sensor needs to be closer to the surface, the shorter the wave being measured. In order for the sensor to remain under the water, there is a limitation on the length scale of the wave that can be measured.

Wire gauge instruments measure the water surface height at a single point. A wire is suspended vertically through the surface of the water so the water level never rises above or falls below the extent of the wire. The wire is designed so that either the electrical impedance or the capacitance of the wire varies as the amount of wire immersed in the water changes. The varying impedance or capacitance is recorded and is converted into wave height by using measured calibration coefficients for the wire (Kinsman, 1984, Vilensky *et al.,* 1961, Lobemeier, 1981, McGoldrick, 1971).

The above techniques were designed when the majority of interest was in long surface waves and for this they were very successful. By using an array of sensors, such as a line of wire gauges, simultaneous measurements could be used together to provide spatial information on the surface wave field. This could even be extended to provide a two-dimensional picture of the ocean surface. More recently, the information that is required is of the characteristics of the high frequency end of the ocean wave spectrum. For providing data on shorter, higher frequency waves, the above techniques are less useful. The physical size of an accelerometer restricts the range of wavelengths to which it is capable of responding. A pressure gauge cannot be placed close enough to the water surface to measure the shortest waves without breaking the water surface as longer waves pass the instrument. Even a wire gauge, which can accurately measure fairly short waves (down to wavelengths of several centimetres), is not capable of making measurements of the shortest waves error free. The intersection of the wire with the water surface creates a meniscus around the wire that distorts the true measurements of the surface height. This error is negligible for low frequency waves, but becomes of great significance when high frequency waves, such as capillary waves, are considered. It has been found experimentally (Lange *et*

al., 1982) that a particular wire of 0.075mm diameter had a meniscus of 2.15mm, allowing accurate measurements of waves of only greater than 4.3mm in wavelength. This means that only waves with wavelengths of approximately 60 times the diameter of the wire or greater can be measured accurately. Sturm and Sorrell (1973), however, found that a wire with a diameter of 0.5mm produced a meniscus causing an effective diameter of approximately 6.5mm (dependant upon the surface tension).

Another disadvantage of the above techniques is that they measure directly, or the output is used to calculate, the height of ocean waves. This means that they are usually limited to one order of magnitude of waves in order to gain the required resolution. Most optical methods record the surface slope. Therefore, they are capable of measuring waves over a large range of wavelengths as the wave slopes all vary over the same range of values. On occasions, the slope measurement is the required output and from a surface height gauge it can only be determined by coarse differentiation which leads to noisy data.

All optical methods have an advantage over the techniques presented above because they are non-invasive. This means that the instrument does not directly affect the surface it is trying to measure and so allows an undisturbed measurement of the surface wave field. The first optical method considered is stereo-photography (Lee, 1995) which still measures surface height and not the slope of the waves. A diagram of a typical set-up is given in figure 2-1. Two cameras are set up a known distance apart, d_c, and a known height, h, above a particular datum, for example the average height of the water surface. The cameras take simultaneous pictures of the water surface. By identifying the location of the image of a particular point on the water surface in both pictures and measuring the relative positions of those locations (i.e. d_l in the left camera and dr in the right camera), the distance, h, of the water facet from the stereo baseline can be determined as,

$$h = \frac{d_c f}{d_l - d_r} \qquad 2\text{-}1$$

This can be converted to the wave height using information about the height of the cameras from the known datum. A full 2-dimensional image of the sea-surface height can be built up by repeating this process for each point on the water surface. The resolution of this

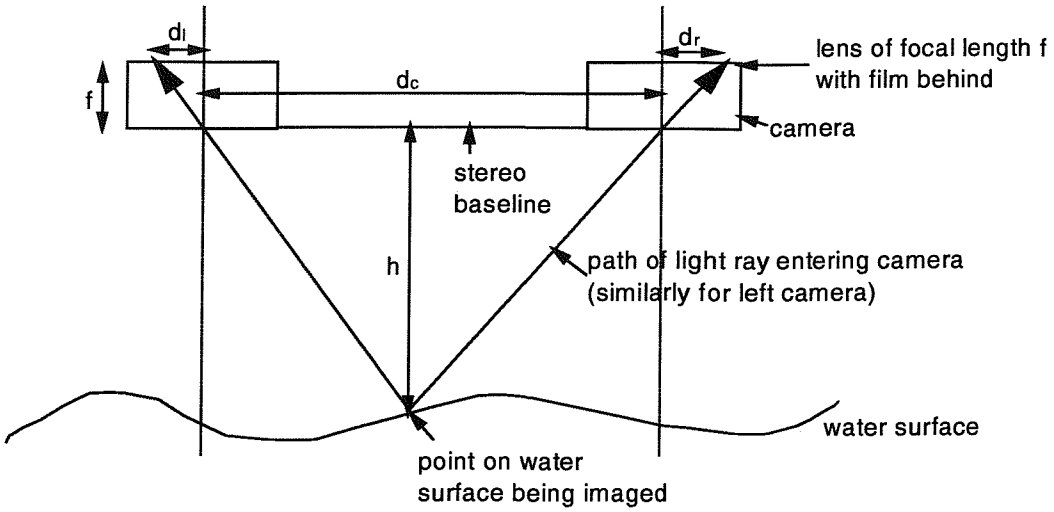

Figure 2-1: Illustration of stereo-photography

technique is severely limited by the ability to resolve two points in the photographic images and therefore only allows data of longer waves, e.g. gravity waves, rather than capillary waves, to be obtained. It is also a very time consuming and computationally greedy process to identify each water surface point in each image.

Specular reflection from the ocean has been used to study the distribution of two-dimensional surface slopes. The reflectivity of vertical and horizontal polarisation is dependent on the angle between the incoming ray and the reflecting surface. Horizontal polarisation displays a curve in which the reflectivity is proportional to the angle for small angles. If the ocean is lit by an extended source, then the intensity of the image of horizontally polarised light reflected from the ocean will vary depending only the slope of the wave from which the light was reflected. Uniform sky radiance has been used as an extended source for this purpose (Stilwell, 1969, Stilwell and Pilon, 1974) and the technique is known as Stilwell photography. Photographs of the sea surface were taken using a filter which only transmitted horizontal polarisation. A transparency of the photograph was illuminated with collimated light to reproduce the image intensity at the camera. The far field (or Fraunhofer) diffraction pattern from the light through the transparency was studied. Since this diffraction pattern is equivalent to the Fourier transform of the transparency, the square of the resultant pattern was proportional to the slope energy spectrum. The limitations of the method are in obtaining an entirely uniform

sky illuminance, and in the assumption that the wave slopes are small. This latter problem means that the technique is only really valid for fairly smooth seas and is not valid for capillary waves which tend to be steep.

Reflection of the sun's glitter pattern has been used (Cox and Munk, 1954a, 1954b) to determine the two-dimensional probability density function of surface slopes on the sea surface. Photographs of the glitter pattern produce an image which can be related to the distribution provided the inclination of the sun is known. If the water surface was completely flat then the image of the sun would appear as a single point at the region of specular reflection from the surface. As the surface becomes rippley, each water facet will create its own image of the sun at the specular reflection point for that facet. As the range of water surface slopes increases, the number of images of the sun will also increase and the spread of the images will extend further from the location of the original sun reflection. Therefore, the image intensity as a function of position in the image plane will be related to the number of water surface slopes at a particular angle. In the image plane, the further the distance of the image from the flat water specular reflection point, the greater the water surface slope angle. Each pattern is unique to the slope distribution from which the light is reflected.

The sun glitter method produces a result that is the cumulative effect of reflections from a large area of water. Statistics taken from the images will be relevant to the average roughness on the water over the area imaged but will not be capable of providing detailed statistics of roughness variations over short scales. Therefore, it can not be used to yield information on the roughness changes over relatively short spaces such as in ship wakes. Stillwell photography can be used to provide such information but only within the limitations mentioned.

If a highly directional light source is shone at an air-water interface, from either above or below the water surface, then the refraction experienced by the light beam can be related to the slope of the water surface at the intersection. A number of devices have been built incorporating this design. If a laser beam and detector system is used, firing the laser beam from above the water surface allows a much larger range of slopes to be measured as there is no limitation due to total internal reflection. It also enables the detector system, which

senses the position of the light beam after refraction, to be smaller (Jahne and Shultz, 1992). However, having a large detector system underwater is likely to create a significant disturbance of the water surface being measured. This disadvantage far outweighs the benefits of having the laser above the water, but the alternative does require a method for delivering the laser light below the water. This can be achieved by firing it from beneath a glass plate or by using a fibre optic cable to deliver the light source into the water. This overcomes the need for putting the laser itself into the body of water.

An alternative refractive method, illustrated in figure 2-2, which can also be used to provide spatial information (Jahne and Shultz, 1992), is to use an extended light source beneath a glass plate which emits light isotropically but in such a way that the brightness varies spatially and is uniquely related to a particular position on the emitting plate. If a lens is placed beneath the water at a distance from the emitting plate equal to the focal length, f, of the lens, it will direct all rays arriving from one position on the plate towards the surface at one angle. These rays will be refracted at the water surface and those rays leaving the water surface vertically will be recorded by a camera situated above the water as an image on photographic film. The spatial co-ordinates on the film will match those of the water surface. The slope at each location on the water surface will be given by the intensity of the light reaching the film at each position. Each water facet of a particular angle will only be able to refract light originating from one location on the glass plate into the camera. Therefore, the variation in image intensity of the film will actually relate directly to the angle of the water at each location. Unfortunately, due to the difficulties of producing the sophisticated light intensity pattern, this method is not practical in the field.

Optical refraction devices, like the ones presented above, are capable of taking very high data rate measurements of the water surface to provide detailed information on the two-dimensional surface slope. Some of these instruments collect data at a single point on the water surface. If this type of instrument is stationary, it is only capable of providing information on the frequency of the waves. If it is moving, it will record the frequency at which it encounters the waves so the data is actually a mixture of frequency and wavenumber information, which can be difficult to interpret due to the complexities of the ambient surface wave field motion. More modern versions of this type instrument perform a high speed scan of the water which records almost a "snap-shot" of the water surface.

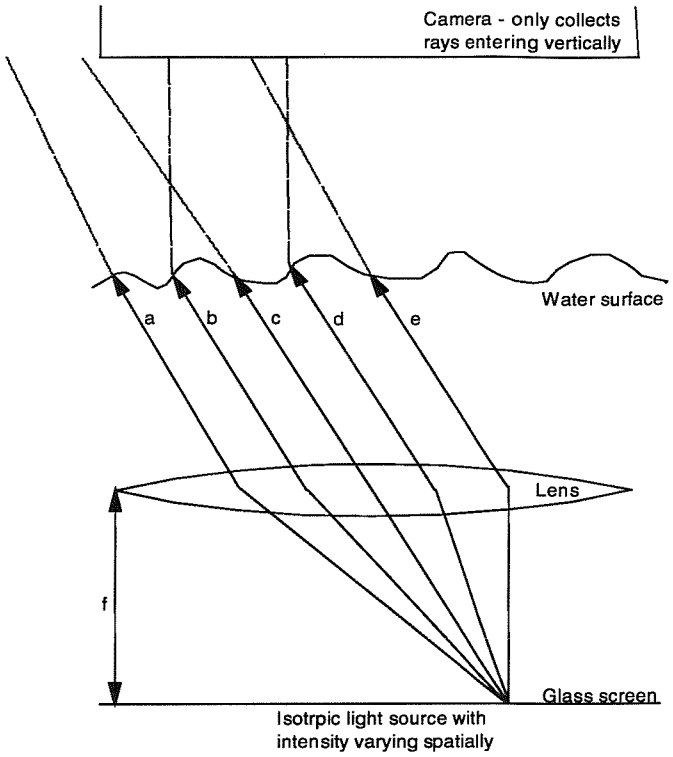

Figure 2-2: Diagram of the set-up to image the two-dimensional slope of the water surface using a light box, underwater lens and camera. Only the light from rays b and d will enter the camera.

However, even for these instruments, the water motion can cause distortions in the resulting data unless the scan rate is very high indeed (Hara *et al.*, 1997).

Another disadvantage of many of the earlier refractive slope measuring instruments was that they used only a single detection of the light beam after refraction to determine the surface slope. This meant a wave height measurement was still required which, again, limited the resolution of the system. In principle, however, with perfect detection equipment, the spatial resolution of such systems is limited only by the size of the light spot that is used. Lasers are normally used for this purpose in order to obtain a highly directional source with a very small spot size.

The techniques reviewed above cover the majority of methods that have been used to measure the surface structure of the ocean. Knowledge gained from other people's experience of using these techniques was used to improve the design of the Laser Slope

meter used for this research project over previous similar instruments. Although the Author was not involved in the original design of this instrument, the way in which the instrument evolved, which is critical to the discussion in the rest of this thesis, is described in the next section. Details of the initial instrument design and subsequent modifications made to it are then summarised.

2.3 The prototype Towed Laser Slope meter

2.3.1 Introduction

The first prototype of the Towed Laser Slope-meter (TLS) was designed and developed under contract to the Defence Evaluation and Research Agency (DERA) by a small team from the departments of physics and oceanography at the University of Southampton (Ghataure and Ramsden, 1992, Ghataure *et al.*, 1993, Lee, 1995). The overall objective of the instrument was that it would provide high quality information about the high frequency components of the undisturbed two-dimensional slope distribution of the ocean surface. The particular interest of the Ocean Imaging Programme (OIP) at DERA were the surface modulations caused by the interactions between surface currents, generated by sub-surface features such as internal waves, and the ambient surface wave field, with the intention of improving understanding of how these features are imaged by radar.

One of the most important factors in the pursuit of understanding radar imaging of the ocean is to make high frequency spatial measurements of the surface wave field. It is thought that short waves, which are comparable in scale to the component of the radar wavelength on the ocean surface, are most important in causing radar backscatter. Therefore, modulations to these short scale waves may be the mechanism by which the radar detects the underlying features responsible for the surface currents that interact with the ambient wave field. Most traditional techniques of measuring the ocean surface concentrate on either low frequency temporal or long wavelength spatial measurements, as was described in section 2.2. These methods are, therefore, not appropriate for examining the surface waves in the spectral region of interest. Recently, there have also been suggestions that the exact shape of the waves is also of great importance (Fuchs *et al.*, 1997). It is therefore important that such an instrument be capable of providing information on the detailed shapes with high accuracy.

In order to gain the accuracy required for the new instrument, an optical refractive technique was selected. This enabled fine resolution measurements of the water surface without the need to interact with the surface and thus disturb it. The detector system was chosen to ride above the water surface so that it did not create disturbances to the wave field being measured. To improve on previous systems and so better the resolution over these systems, two detector screens were used to measure the position of the laser spot after refraction at the water surface. This enabled a calculation of the surface slope without reference to a wave height measurement. One of the novel design features incorporated into the TLS was that it could be towed across a wave field, partially bridging the gap between temporal and fully spatial measurements of the surface wave field.

These factors influenced the design of the TLS, which is described in detail in the rest of this section. The prototype version of this instrument was used to collect the data presented in chapters 5 and 6. Following experience with the instrument, a number of improvements were made in preparation for the next series of experiments. The results from these experiments are presented in chapters 7 and 9.

2.3.2 The main detector system

A diagram of the main detector system is shown in figure 2-3. The laser light is injected into a fibre optic cable that is fed beneath the water surface to the base of the instrument. At the end of the fibre optic, a collimator focuses the laser light into a low divergence beam which waists in water approximately 0.5m from the end of the collimator. The collimator is held in position approximately 0.5m below the water surface. The laser beam leaves the fibre optic and travels towards the water-air interface where it undergoes refraction at the density interface. After refraction, the beam continues on its new course until it reaches the first of two wavelength shifting, plane circular screens situated concentrically above the collimator. At the first screen, approximately 50% of the light is passed and this continues in a straight line towards the second screen. At each screen the wavelength of some of the light is shifted from the blue region of the electromagnetic spectrum into the green region. Some of the green light becomes trapped internally to each screen and propagates radially towards the edges of the screens by total internal reflection at the screen boundaries as is shown in figure 2-4. Around the edges of each screen are 6 photodiodes, spaced equidistantly, which have a potential difference across them depending on the amount of laser light received. A

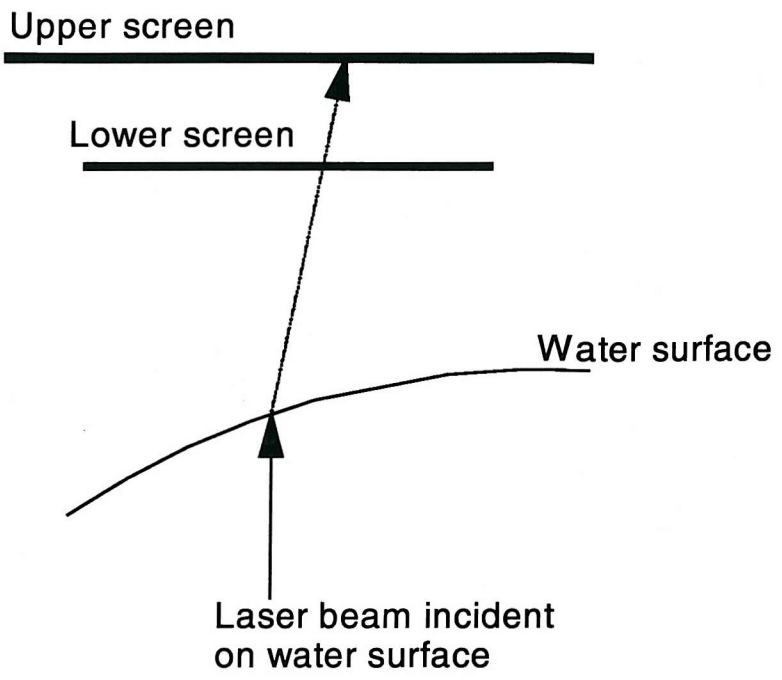

Figure 2-3: The detector system

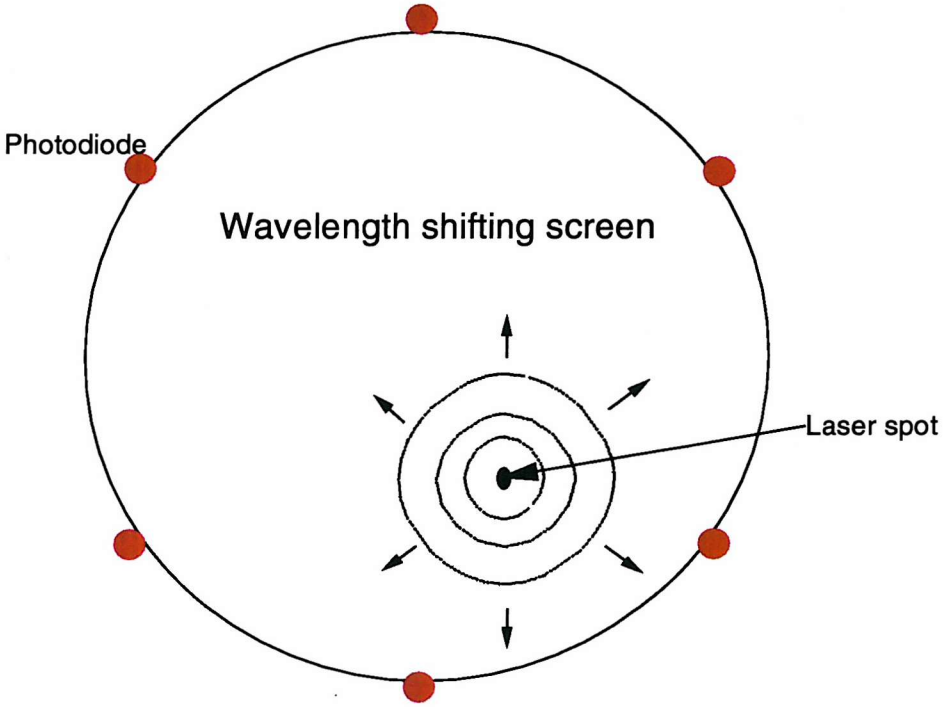

Figure 2-4: The propagation of the laser light through the screens

lookup table of the relationship between the position of the laser spot and the light level at each photodiode can be used to determine the spot position on each screen. These two positions are used to compute the laser angle relative to the instrument. With additional information about the orientation of the instrument with respect to an earth co-ordinate system, the water surface slope can be calculated.

The laser light selected for this process was a single mode helium-cadmium laser (HeCd) with a wavelength of 442nm and a power of 90mW. This light is particularly suitable because wavelength shifting material is readily available for this wavelength. Also, light in the blue region of the spectrum suffers little attenuation whilst travelling in water. In order to reduce ambient light entering the instrument, a blue filter was located beneath the first wavelength shifting screen. To reduce back reflections from the upper screen, a second blue filter was located above the lower wavelength shifting screen. In addition to this, the laser beam was modulated at 9.6kHZ and split so that the refracted beam could be selected uniquely from the photodiode return by using matched filtering with the unrefracted beam. Variations in the amplitude of the light from the laser were removed by calculating the ratio of diode voltages, using the diodes in pairs according to those situated directly opposite on the screens. Due to a need to reduce the size of the telemetry packets, which transferred the raw data from the instrument to a data logger, in this prototype design the raw data were recorded as ratios of difference divided by sum of opposite diode voltages.

The maximum water surface slope angle that can be recorded by this method is limited by total internal refraction of the laser beam at water angles of 48°. The size of the screens further limits this value as the laser beam must be able to produce a spot on both screens, see figure 2-5. From figure 2-5 it can be shown that the relationship between the water slope, w, and the laser slope, l, is given by equation 2-2, where n is the ratio of the refractive index of water to the refractive index of air, taken to be 1.339 (Kaye and Laby, 1978).

$$\tan w = \frac{\sin l}{n - \cos l} \qquad 2\text{-}2$$

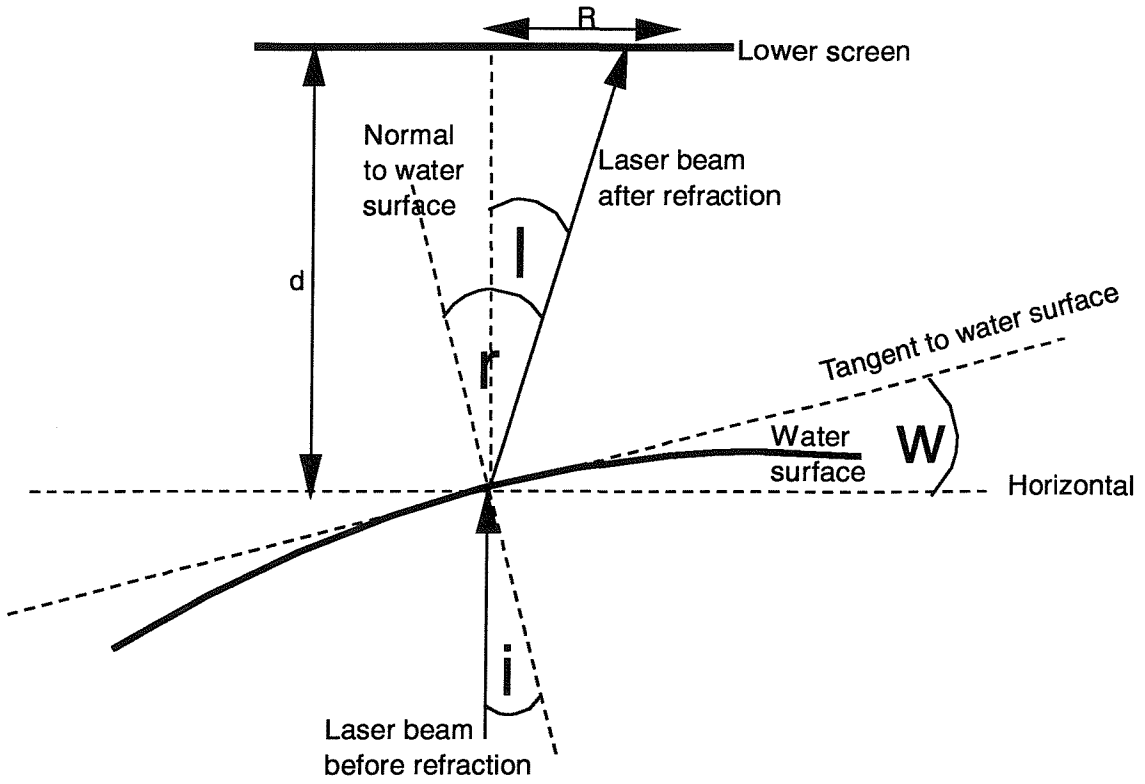

Figure 2-5: Relationship between the water slope, laser slope and angles of incidence and refraction

The lower screen was selected to have a diameter, R, of 0.5m and was located approximately 0.5m above mean water level, d. The upper screen was 0.3m above this with a diameter of 1m. Using the full screen area this allows laser angles of up to 27° to be measured and hence water angles of up to 46°. In practice, the particular processing method used for this early version of the instrument only allowed approximately half of each screen area to be useful, limiting the measurable water angles further to 34°. Previous work, such as that by Cox and Munk (1954b) has shown that the majority of water slopes fall below 30° and so this restriction was not thought to limit the instrument too severely.

2.3.3 Towing the Laser Slope meter

In order to gain some form of spatial information about the water surface, the Laser Slope meter was designed so that it could be placed onto a catamaran and towed across the wave field. When the instrument is used in this way it will be referred to as the Towed Laser Slope meter or TLS. When it is deployed as just the detector system, or this is referred to, it will be called simply the Laser Slope meter. A diagram of the system on the catamaran is

shown in figure 2-6a and a photograph of the deployed TLS beside the towing vessel is shown in figure 2-6b.

A standard racing catamaran was obtained and modified to accept the Laser Slope meter, positioned on a platform at the front of the catamaran, between the main hulls, and forward of the wake created by the fins as they cut through the water. The laser collimator was held below the water on a special supporting tripod which can be seen below the yellow detector system in figure 2-6b. The laser beam cut the surface between the two forward struts which are visible. The third strut is hidden from view. In addition to providing spatial information, a moving catamaran was used to reduce artefacts in the data created by reflections of the surface waves off the catamaran structure. An Inertial Motion Unit (IMU) was stationed beside the detector system to record the attitude motions of roll, pitch and yaw of the catamaran. The computer system was located aft of the catamaran along with batteries to power the system. A data cable and the fibre optic cable linked the catamaran to a powered small vessel that was used to tow the catamaran. Tow ropes were attached carefully to the catamaran so that control over the towing direction could be obtained from the towing vessel. A remote controlled rudder system was also connected to the aft of the catamaran for further control. A GPS and a meteorological station were located on the towing vessel to provide additional information on the actual location and direction of heading of the vessels and the local meteorological conditions affecting the water surface.

2.3.4 Calibration and processing

To calibrate the Laser Slope meter the laser beam was swept beneath the screens in a particular geometry whilst the diode readings were recorded. A purpose built inverted tripod was used for this process which contained a pair of servos at the base. The servos were used to manoeuvre the laser beam around the screens to predefined locations. The objective was to provide a grid of points at which the response of each photodiode was accurately known. The specific grid layout was not important provided sufficient points were sampled so that interpolation between the grid points could provide the required accuracy in recreating the position of the laser beam on each screen. For convenience a square grid was chosen. In order that the calibration procedure was not too lengthy the grid spacing was chosen to be 5mm on the lower screen and hence 7.96mm on the upper screen. With this spacing, one calibration took about 2 hours. The resulting data were recorded as

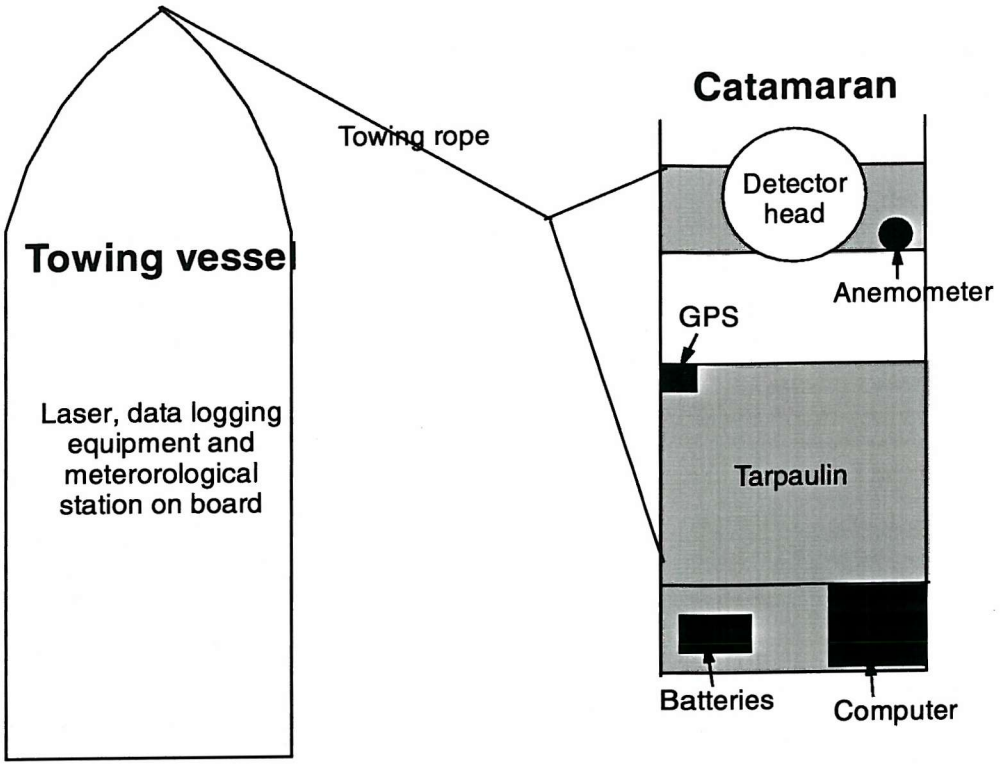

Figure 2-6a: Layout of equipment on the catamaran and towing vessel

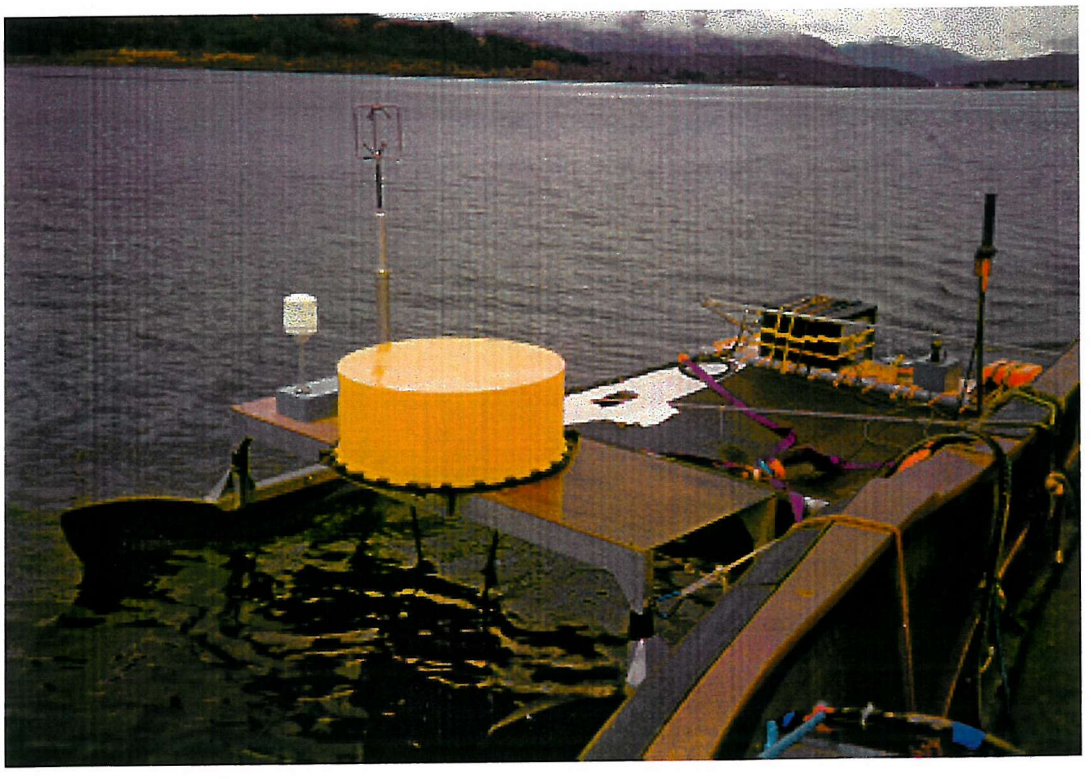

Figure 2-6b: Photograph of TLS beside towing vessel

x,y co-ordinates of the laser beam on each screen and the response of all six photodiodes (as difference over sum ratios of opposite pairs) at each laser position.

Data processing of actual water slope data was carried out in a number of steps to progress from the raw photodiode ratio values to an accurate water surface slope measurement. Prior to each experiment, and where possible at intervals during and after it, calibration files were collected of the photodiode ratios produced with the laser beam fired at the screens in the grid pattern. The calibration grid was used as a look up table to form loci of the possible positions of the laser beam given the photodiode ratios. On each screen, the three ratios each provided a locus of possible positions and the intersection of these loci gave the actual position of the laser beam on the screen. Having three ratios allowed redundancy in the calculation. Via this method, the position of the intersection of the laser beam with each screen was found. As the grids on each of the screens were located about the same axial central point, this information was sufficient to determine the slope of the laser beam relative to the instrument. When data was collected with the instrument being towed it was necessary to convert this laser slope relative to the instrument to a water slope relative to the instrument. This could then be converted into water slope relative to an earth co-ordinate system, by making use of the data from the IMU. A flow diagram of the processing method is given in figure 2-7.

2.3.5 Testing and accuracy

A test of the processing software and instrument variations between calibrations was performed by Good (1997b) by processing the data contained in one calibration file with a second calibration file. It was found that, in general, the accuracy of the data points was well predicted by the error calculations performed automatically by the processing software and that the majority of the data had low errors. However, there were a few anomalous points where the actual error was large but the calculated error was small. These points corresponded to lines of reflection between photodiodes where the anomalous brightness observed along these lines in the calibration files was effectively averaged out by the processing method. It was found to be impossible to remove these data points from a data series of slope measurements. As the number of points affected was very small it seemed unlikely that they would have a significant effect on the data.

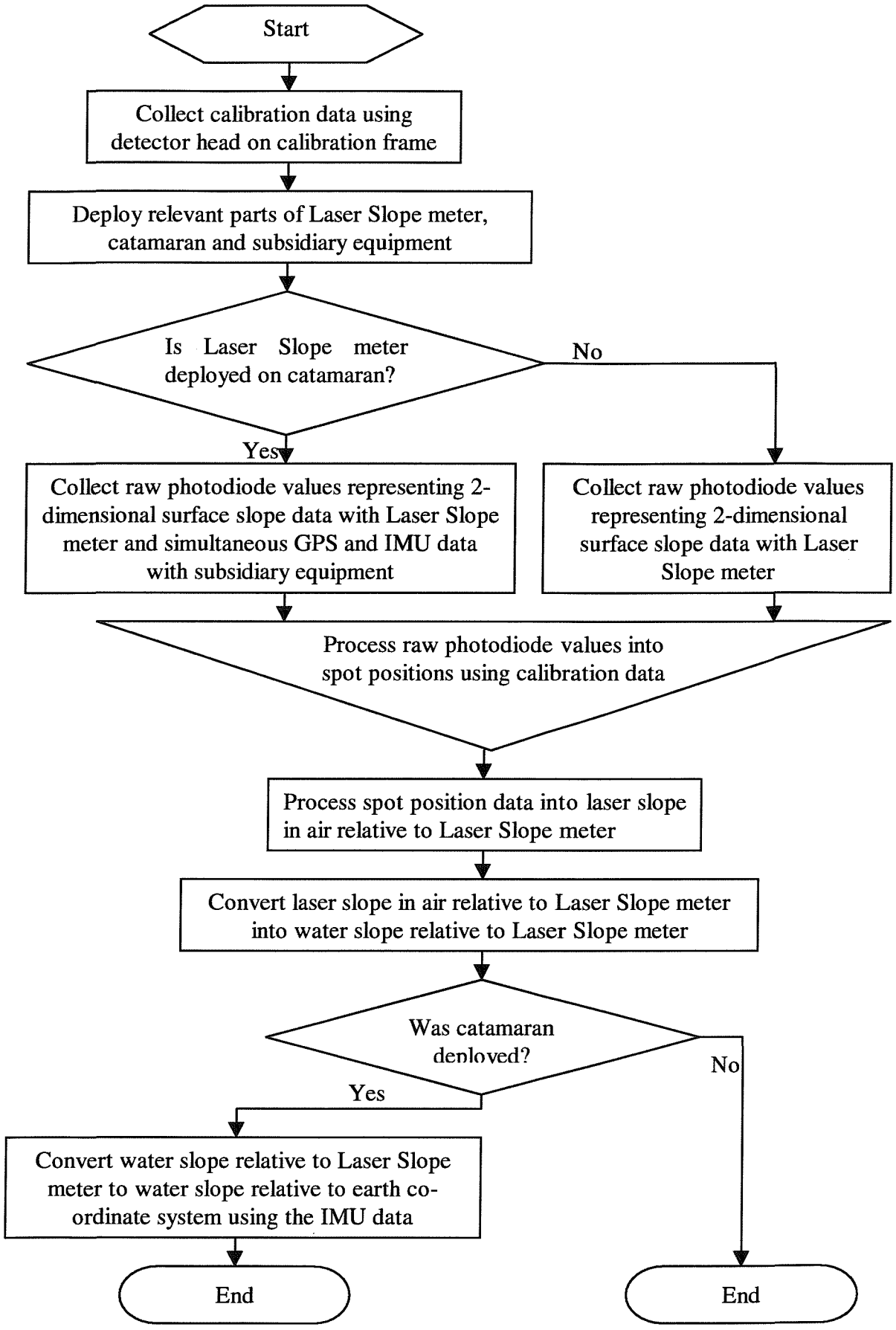

Figure 2-7: Flow chart of the deployment and processing method

Two different methods were investigated to process the data from a spot position on each screen to the laser slope angle. If no errors were present then this would be a simple calculation. However, as with any real instrument, data errors are present; these errors are investigated here. The first method investigated used the additional information that the axis of the laser beam was known, as well as the two calculated laser beam / screen intersections. The incidence angle was calculated assuming the lower and upper screen positions lay on a line from the axis. It assumed the horizontal separation of the points was given by the magnitude of the vector from the central axis to the laser spot on the upper screen minus the magnitude of the vector from the central axis to the laser spot on the lower screen. The vertical distance was the screen separation. The azimuth angle was taken as the average azimuth of the lower and upper screens, where each azimuth was measured from the axis to the spot position. By including this additional information it was thought that the resulting slope calculated would be less prone to errors in the spot position calculation as a third accurate point would be used. This method also had the advantage that it was possible to calculate the water height by extrapolating the laser beam angle back to the laser beam axis. The second method investigated simply used the calculated laser beam / screen intersection positions without any reference to the original laser beam axis. This method was thought to be more prone to spot position errors but less prone to errors in the screen centres relative to which the spot positions were measured. The two methods were simulated by a routine written in Matlab in which the effect of screen centre errors was investigated. It was found that the first method introduced artefacts into the probability density function of surface slope, whereas the second method simply translated the probability density function, producing an error on a slope component that was constant and was dependent on the difference between the centre errors on each screen (Taylor, 1999).

An assessment of the errors in the laser slope was performed using laboratory tests carried out by Good (1997b) and analysed by the author (Taylor, 1997b). Two types of test were performed. The first comprised a series of concentric circles, centred on the optic axis of the instrument, with radii between 0.1° and 16° in laser slope. The radial spacing was 0.1° up to 2° and then 0.5° thereafter and the azimuth spacing was 15°. The second test comprised radial spokes from 0° to 16° with an azimuth spacing of 15°. A schematic of the laser patterns drawn out on the screens is given in figures 2-8a and 2-8b. Figures 2-9a and 2-9b

display the results in the form of the input versus the output slope angle averaged for each circle or radial spoke, respectively. The error bars represent the standard deviation of the data. It can be seen that between 1° and 12° the accuracy is approximately 0.5°. Outside these limits the errors are much greater. The water slopes which correspond to these refracted laser angles are 2.95° and 30°. This is the range of water slope angles that can be accurately measured by the Laser Slope meter. The spatial frequency range over which it is possible to make measurements is limited by the laser spot size which was approximately 2mm for the prototype instrument. Therefore, very high frequency information would not be recorded because the spot would act as a low pass filter on the water surface. The conclusion from the above tests and the Matlab analysis was that more consistent results were obtained if the second processing method was used, as it preserved the real statistical relationships between the slope measurements, introducing a constant systematic error within the data. This method was used throughout the rest of this thesis.

During the Loch Linnhe experiment the state of the water surface was recorded by photographs taken from the hillside above the Loch and by visual observations, which were recorded in a log. The visual observations were carefully time located with the rest of the data and were then subjectively digitised for comparison with the data based on the Author's interpretation of the water roughness. '0' was used to represent essentially smooth water (slick-like conditions) whilst '1' was used to represent the roughest conditions experienced during the experiment. The digitisations were determined at intervals of 0.1.

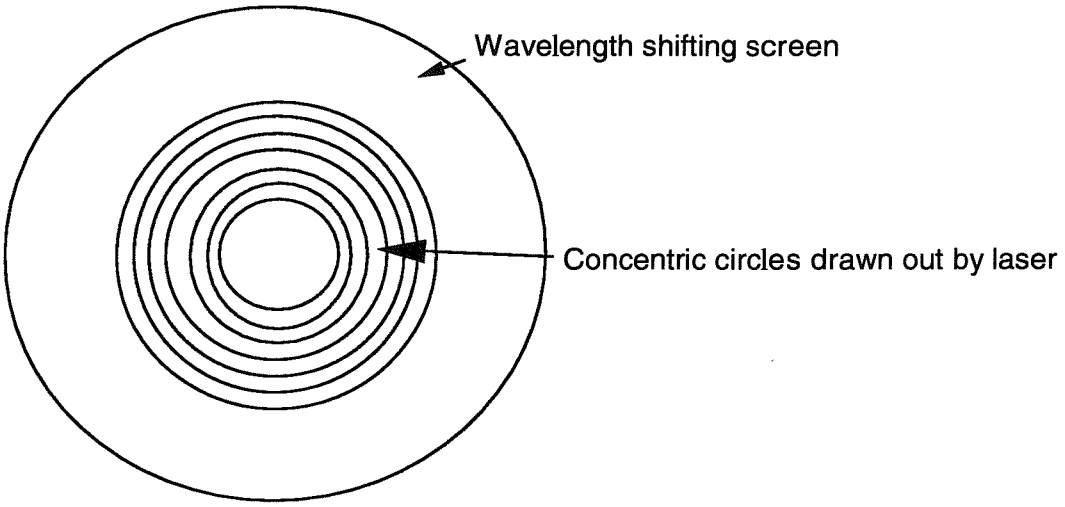

Figure 2-8a: Schematic of the laser pattern drawn out on the wavelength shifting screens during the circles test

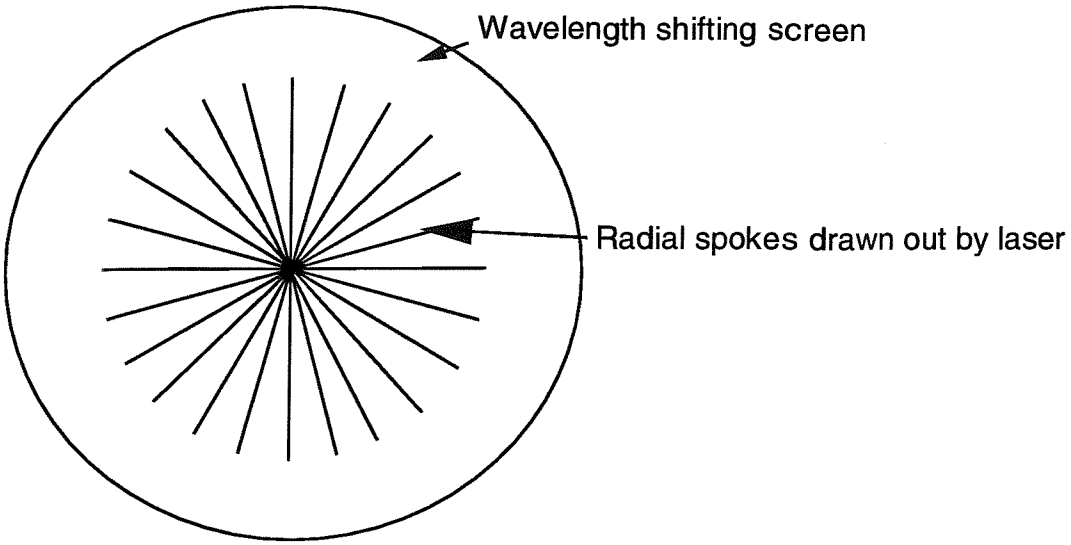

Figure 2-8b: Schematic of the laser pattern drawn out on the wavelength shifting screen during the radial test

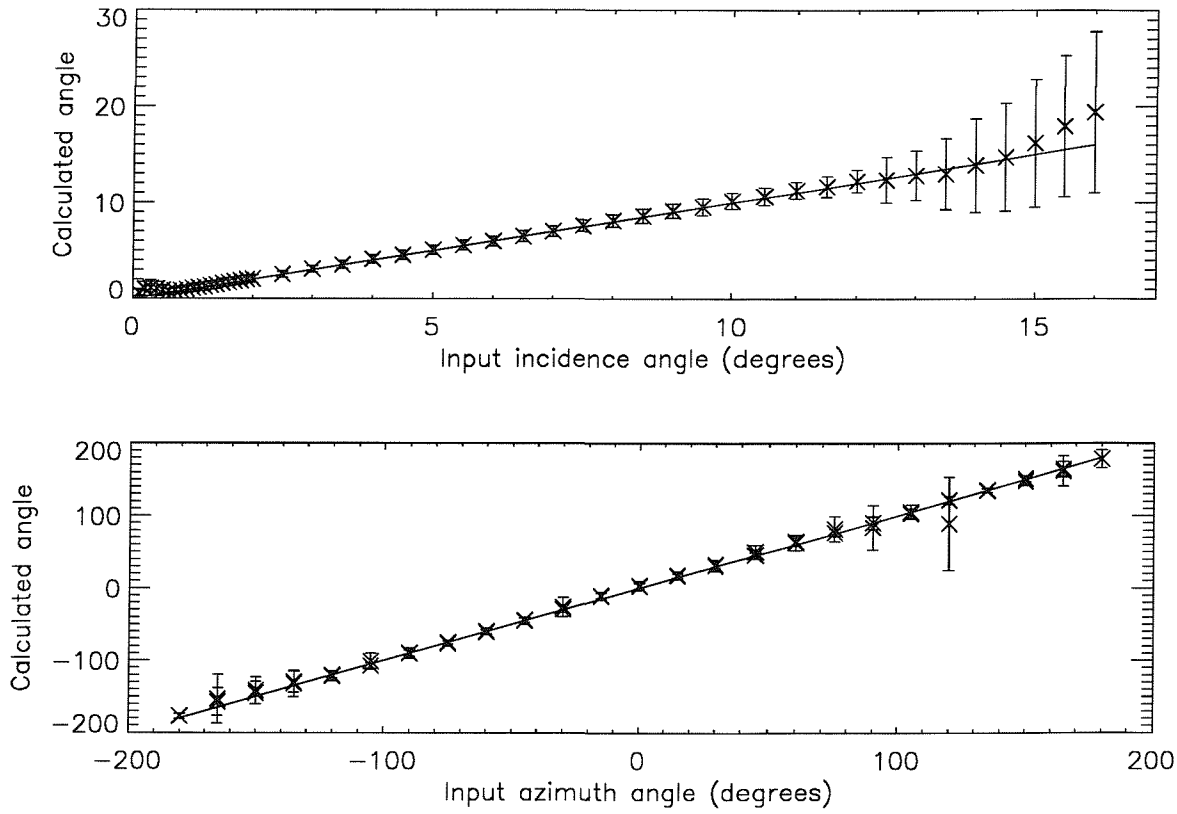

Figures 2-9 a and b: Laboratory test results

These observations were compared with the photographic evidence and with the data. Comparisons between the observations and all of the data sets were completed and are reported in (Taylor, 1997b). It was only possible to compare the measured surface roughness, visual observations and photographs of the surface subjectively and qualitatively. However, within these boundaries, the agreement was found to be good.

The characteristics of the data were observed to vary considerably as the wind speed increased. In particular, at very low wind speeds, the data files were similar in behaviour to pure noise. As the wind speed increased, the maximum measured slope value increased and also the period of the dominant oscillations increased for a constant towing speed. At higher wind speeds the surface became much rougher and lots of high frequency behaviour was observed. This simple analysis of the variation with wind speed is presented in Taylor and Cooper (1999). In addition to this, the process of using the IMU data to provide data relative to an earth co-ordinate system was investigated. This procedure was not found to introduce any significant errors.

These simple tests, both in the laboratory and the field, gave confidence that the instrument was accurately reproducing the angle of entry of the laser into the instrument. This, in turn, suggested that the calculated water slope angle was accurate provided the initial tilt of the laser beam was known relative to the catamaran, and that the inertial motions of the catamaran were removed from the data. The field tests showed that the instrument was responding well to visually observed changes in the surface roughness.

2.4 TLS improvements

2.4.1 Introduction

Following the experiments performed in Loch Linnhe in January 1997, it was thought that the information that could be obtained by the Laser Slope meter would be greatly improved by a number of developments. The intention was not to redesign the basic concept but merely to enhance it through replacement of some of the worn parts and a refinement of the general idea. This section describes the reasoning behind, and implementation of, the improvements as well as initial testing of the new instrument (both in the laboratory and in a

wind wave facility). To test the performance of the instrument, monochromatic waves were measured simultaneously by the Laser Slope meter and by a wire wave gauge.

2.4.2 The modifications and improvements

During the trials prior to, and including, the experiment in Loch Linnhe, the Laser Slope meter was often subjected to relatively harsh conditions for a prototype instrument. This included its being deployed in rough sea conditions which resulted in some water ingress into the detector system and damage to the wavelength shifting screens. In an earlier incident, the screens were also contaminated with sewage whilst the system was under construction at the University of Southampton. Replacement of these damaged parts was the first step in the scheme to improve the Laser Slope meter.

Analysis of the data from the experiments described above indicated that there was room for improvement in the accuracy and precision of locating the laser beam intersection with each screen, which is the fundamental part of processing the raw photodiode values into useful slope information. The processing method used also did not allow for spot solutions to be found over the entire screen area. A third fault with the original design was that reflections between diodes situated in exactly opposite locations, or in an exact equilateral triangle, around the edge of the screens caused significantly increased errors along these lines.

Finally, it was considered that an increased sampling rate would allow much finer resolution of the wave components leading to an enhanced ability to measure small ocean features such as capillary waves. With an increased sampling rate it was necessary to ensure the laser beam spot size was small enough to take advantage of this; otherwise the small wave components would cause a distortion of the beam due to the high curvatures within a small spatial area.

In order to satisfy these requirements the following modifications and improvements were made to the Laser Slope meter:

- new wavelength shifting screens;
- increased number of photodiodes to eight per screen;
- new arrangement of photodiodes which was not symmetric;

- ability to record photodiode values rather than difference over sum ratios;
- new processing software;
- smaller spot size;
- increased sampling rate.

New wavelength shifting screens were ordered from a specialist company in the USA. The screens were of similar sizes to the original screens and again the doping level was reduced in the lower screen to allow approximately 50% of the laser beam to continue through onto the upper screen. The lower screen was sandwiched between two blue filters to reduce input of ambient light into the detector head and leakage of wavelength-shifted light between the screens.

The number of photodiodes around each screen was increased in number from six to eight. It was hoped this would allow redundancy in the event of a photodiode failing as well as improving the resolution across the screens. In an attempt to reduce reflections, the photodiodes were arranged to lie in 17th's around the edge of the screens alternating the diodes between lower and upper screens. The 17th position did not have a photodiode fixed. A photograph of the inside of the new instrument is given in figure 2-10.

New processing software was designed to find the position of intersection of the laser beam with each screen. This software used a novel mathematical technique to determine the spot position from the raw photodiode values (rather than ratios) (Cooper, 2000a). To process the Laser Slope meter data, a calibration file was used analogously to a look up table. The calibration file consisted of a series of positions on each screen, each of which has a unique set of 8 diode voltages associated with it. The raw data for each measurement and for each screen is a set of 8 diode voltages which needs to be translated into a position on the screen via the calibration file. Using this method, each screen is treated independently. Initially, the diode voltages are normalised to remove laser fluctuations. This involves making the magnitude of the vector (in 8-d space) of the diode voltages for one position equal to one, i.e. a unit vector.

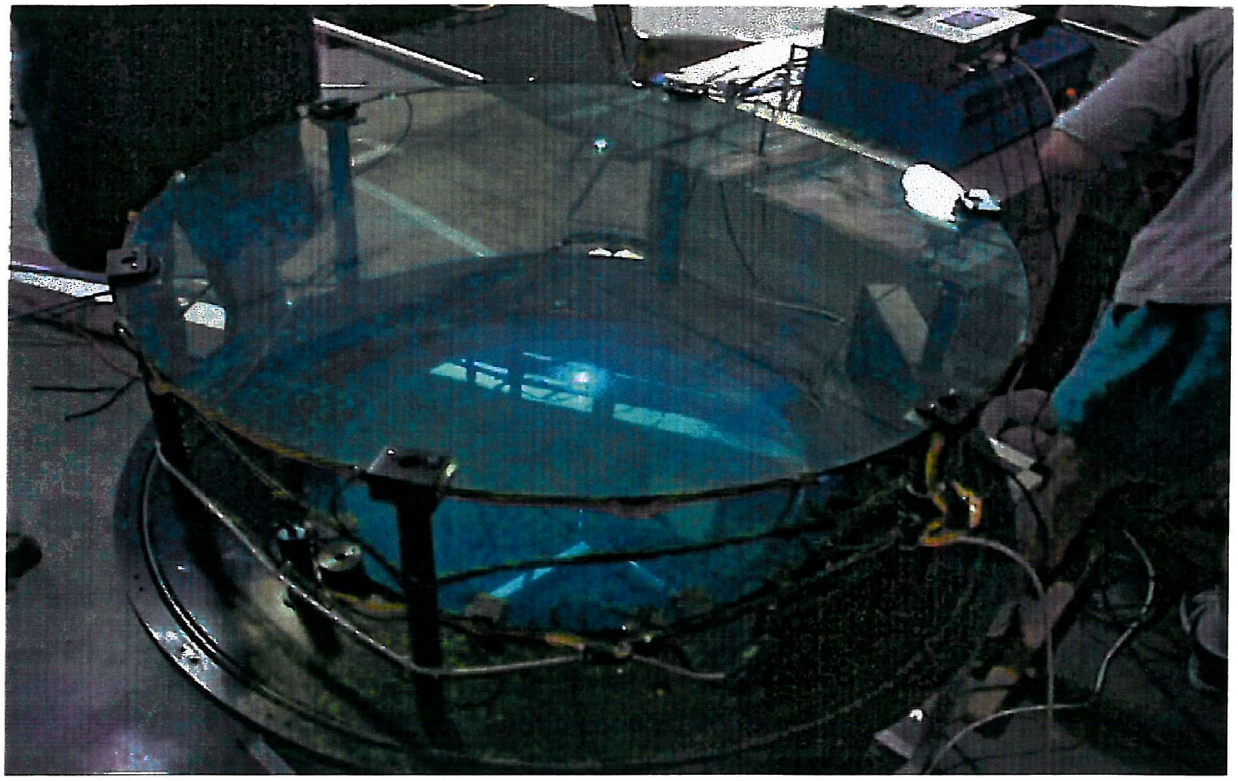

Figure 2-10: Photograph of inside of improved Laser Slope meter

$$\text{Normalised voltage vector}=\frac{(\underline{v}_1,\underline{v}_2,\underline{v}_3,\underline{v}_4,\underline{v}_5,\underline{v}_6,\underline{v}_7,\underline{v}_8)}{\sqrt{v_1^2+v_2^2+v_3^2+v_4^2+v_5^2+v_6^2+v_7^2+v_8^2}} \qquad 2\text{-}3$$

This is completed for both the calibration and run data. From now on "voltage" should be read as "normalised voltage". The voltage vector will be called $\underline{v}_r$ for the run data and $\underline{v}_c$ for the calibration. A difference vector can also be defined between any calibration point and any run point.

$$\text{Difference voltage vector}=\underline{v}_r-\underline{v}_d \qquad 2\text{-}4$$

The calibration point that is nearest to any particular run point will have the smallest magnitude of difference vector. For each run point, all the calibration points could be tested one by one to find the nearest calibration points; however, this is very time consuming. In order to reduce the time taken, the calibration grid is mapped onto the surface of a unit sphere in 8-d space by the vectors created from the voltages. Using a geometrical method, the equation for the smallest sphere encompassing all of the points is calculated for the 8-d

space and is stored along with a pointer to one sample calibration point within each sphere. The set of calibration points is then divided in half to provide two sets of points in the 8-d space. The process of sphere calculation and storage of a pointer to a sample point in each sphere is repeated for each set of points. This process of sub-division continues until there is only one point in each sphere. A tree structure is created within the computer to hold this data. This process is illustrated in 2-d space in figures 2-11a and figure 2-11b.

For each run point, R, in turn, the following process is carried out. The magnitude of the difference vector, $\underline{v}_d$, from R to the sample calibration point, C1, for the largest sphere is calculated. This value is compared with the magnitude of the distance from R to the nearest edge of sphere 1 (magnitude written as $|\underline{v}_{s1}|$, and with the magnitude negative if the point is found to be inside the sphere, as it will be for the 1st sphere). If $|\underline{v}_d|$ is smaller than $|\underline{v}_{s1}|$, then any spheres for which this is true (and all the smaller spheres contained within) are discarded. Of course for this first sphere, no spheres will be discarded. Next, the magnitude of the difference vector from R to the sample calibration points, C2 and C3, are calculated and the smallest one selected as $\underline{v}_d$. This is compared with the distance from R to the nearest edge of spheres 2 and 3 (i.e. comparison of $|\underline{v}_d|$ with $|\underline{v}_{s2}|$ and $|\underline{v}_{s3}|$, again with the magnitudes negative if the run point is found to be inside the sphere). If $|\underline{v}_d|$ is smaller than either $|\underline{v}_{s2}|$ and $|\underline{v}_{s3}|$ as is demonstrated in figure 2-10a, then any spheres for which this is true (and all the smaller spheres contained within) are discarded, i.e. circle 3 in this case.

This process can then be applied to the two spheres within sphere 2 (i.e. spheres 4 and 5, first selecting the nearest calibration point out of C_2, C_4 and C_5 for the comparison. If no sphere can be discarded, as shown in figure 2-11b, then the process continues with all four of the smaller spheres inside spheres 2 and 3 (i.e. 4,5,6 and 7) etc... Eventually, the lowest level of spheres will be reached which contain only one calibration point each. Each of these spheres remaining can be checked to find the nearest calibration point.

In practice, the nearest 12 calibration points are stored throughout the calculation and so the distance comparisons are made with the 12th nearest calibration point. Interpolation is used at the end between these points to calculate the actual spot position more accurately in between the calibration points.

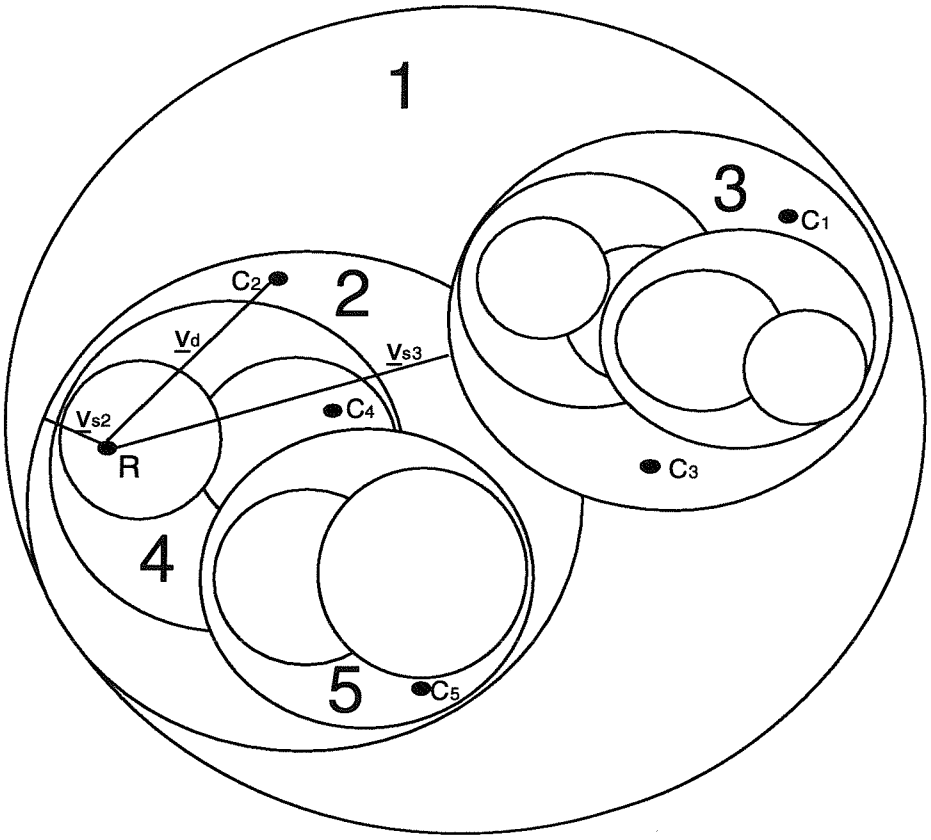

Figure 2-11a: Illustration in 2-dimensions of the processing software

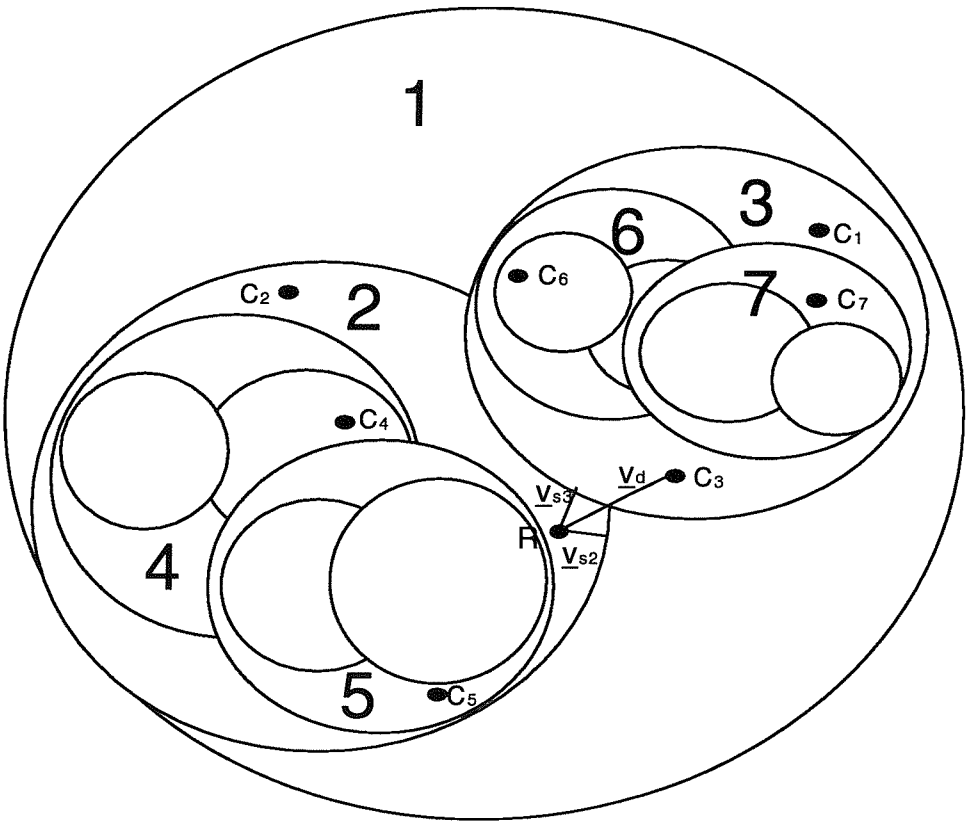

Figure 2-11b: Illustration in 2-dimensions of the processing software

The sampling rate was increased to a maximum possible value of 10.667kHz. A value of approximately 10kHz was chosen to enable accurate measurement of small capillary waves travelling at the speed of gravity waves (i.e. assuming the capillary waves were bound). The chosen figure allowed at least two samples of a 1mm wave travelling at the speed of a 1m gravity wave. With this sampling rate, the above processing method takes approximately 20 times as long to process a data section on a 400MHz PC, as the collection time. This is completed off-line by running batch files to make most efficient use of any available time.

For the first experiment with the improved instrument, time restrictions meant that the spot size was not reduced and remained approximately 2mm. For the second experiment, a special tube was developed into which lenses could be inserted which were capable of focusing the laser beam after it exited the collimator at the end of the optical fibre. This tube was fully adjustable to allow focusing of the laser beam at the average water surface height for any depth required for the collimator. A spot diameter of approximately 0.5mm at the average water surface was chosen for the second set of experiments.

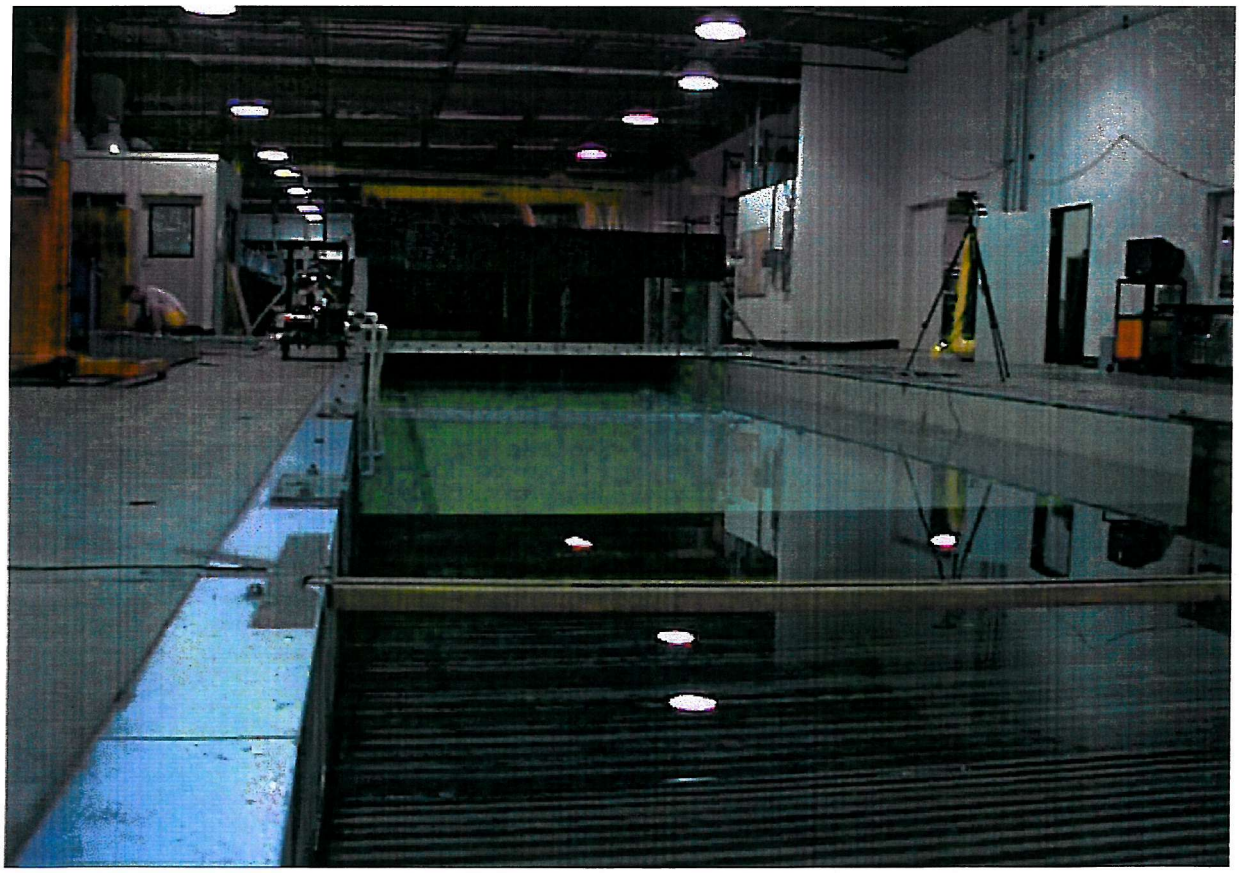

Figure 2-12: Video still of the UCSB wind wave facility

Although the Author did not actually administer the improvements to the instrument, she was part of a team that decided which improvements should be made and how these should be implemented. In particular, she performed calculations that led to the decision of the optimum laser spot size and the sampling rate.

2.4.3 Testing the new instrument

The refurbished Laser Slope meter was taken to a world class wind wave tank situated at the University of California, Santa Barbara, pictured in figure 2-12. This facility is capable of producing computer controlled mechanical wave fields and wind wave fields for wind speeds in the range 1.6 to 12m/s. As well as a large number of "dry" tests which were used to assess the instrument's performance, it was subjected to rigorous "wet" testing using simple mechanically generated waves and more complicated wind generated wave fields. Dry tests of the input laser angle versus the output computed by the processing software (similar to those carried out for the prototype instrument, described in section 2.3.5) were performed and the results are presented in figures 2-13a to 2-13c.

Figure 2-13a shows the results of the average computed Laser Slope meter incidence angle versus the input angle, averaged around each circle for a series of circles between 10mm and 200mm radius, with a spacing of 10mm, as measured on the lower screen (see figure 2-8a for a schematic of the laser pattern drawn out on the wavelength shifting screens). Data were collected every 10° in azimuth angle. The error bars are the standard deviation. Figure 2-13b shows the results for a similar test, but describing the accuracy in the centre of the screen only. The circles had radii between 1mm and 50mm with a spacing of 1mm, as measured on the lower screen. Again, the spacing in azimuth angle was 10°. Figure 2-13c shows the results for a test that determined the accuracy of the computed azimuth angle. Radial spokes were scanned by the laser beam over the screen area. The spokes were separated by 15° and data was collected every 13.9mm on the lower screen (see figure 2-8b for a schematic of the laser pattern drawn out on the wavelength shifting screens). The average value of the computed azimuth angle is plotted against the input angle for each spoke.

In the wave tank, it was found to be impossible to set up the collimator so that it was precisely vertical. Therefore, the input laser angle (known as the laser tilt angle) was estimated from data collected with the laser beam pointing at still water with a horizontal surface (Taylor, 1999).

A study of the contribution from each type of error and its overall effect on the magnitude of the water surface slope was undertaken using analysis completed by Cooper but presented in an appendix in Taylor (1999). From Taylor (1999) the error on the calculated water surface angle, w, due to an error in the refractive index, n, is $|\Delta w| \leq \frac{\Delta n}{n-1}$. It is unlikely that the error on this value is greater than 0.005 radians. Therefore, $|\Delta w| \leq 0.9°$.

The error on the calculated water surface angle due to an error in the estimate of the tilt of the laser beam in water is $|\Delta w| \leq \frac{n\Delta t}{n-1}$ where Δt is the angular error in the estimate of the tilt. By averaging the data from the 'flat' water files it was found that $\Delta t<0.3°$. Therefore, $|\Delta w| < 1.2°$. The contribution to this error from instrument noise was obtained by using the standard deviation on any one noise file (a file collected with the laser beam pointing directly upwards). This value was 0.14° giving $|\Delta w| < 0.55°$. The remainder of this error will mainly be due to any water oscillations, As these are likely to be approximately evenly spread around flat water, they are unlikely to alter the mean value of the tilt measured and thus should not affect the accuracy of the measurement significantly.

The error on the calculated water surface angle due to an error in the tilt of the laser beam in air is $|\Delta w| \leq \frac{\Delta r}{n-1}$ where Δr is the angular error in the tilt. The results of the analysis of the dry tests show that $\Delta r \sim \pm 0.3°$ for the errors calculated on the laser slope incidence angle. Therefore, $|\Delta w| \leq 0.9°$.

The error on the laser slope azimuth angle has been estimated from the flat water files and will not be modified by the refraction process. In order to allow the azimuth angle to be well

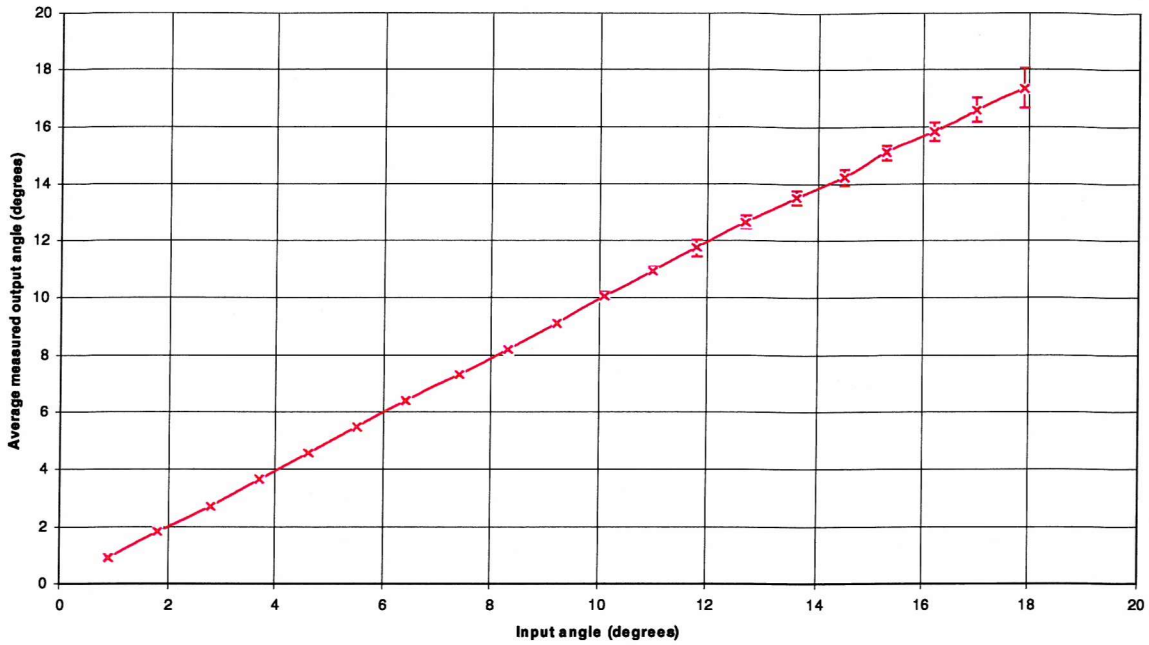

Figure 2-13a: Averaged circle radii with error bars for low resolution circle test

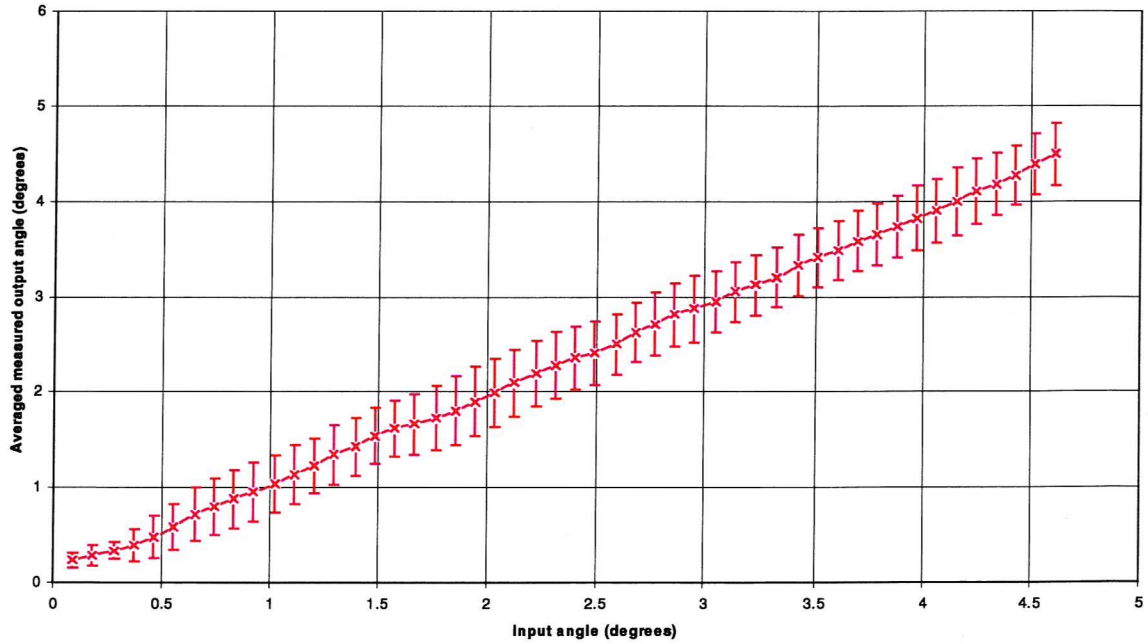

Figure 2-13b: Averaged circle radii with error bars for high resolution circle test

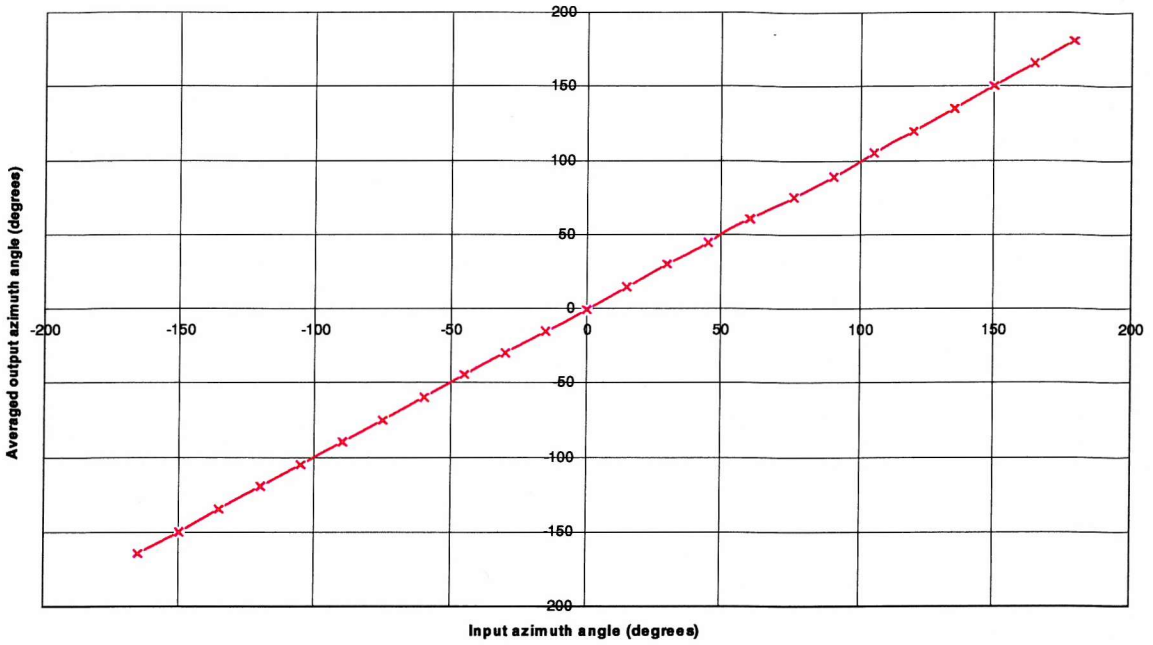

Figure 2-13c: Averaged azimuth angles with error bars for radial test

resolved, the incidence tilt angle was increased to a few degrees. The azimuth angle error was measured as approximately 1°.

Combining these errors statistically provides an overall error on the water slope incidence angle of <1.7° and on the water slope azimuth angle of <1°. Of these laser slope incidence angle errors, approximately 0.5° is random error and approximately 1° is systematic error.

Additionally, a comparison was made between the results of the Laser Slope meter and a wire gauge. Simultaneous measurements were made of mechanically generated monochromatic waves. Spectral calculations on the wave height measurements from the wave wire and on the wave slope measurements by the Laser Slope meter are presented in figure 2-14 (the logarithms are base 10). The top three graphs show clearly that the Laser Slope meter is much more sensitive to the higher harmonics contained in the monochromatic waves. This is likely to be due to wave slope, ak, being more sensitive to harmonics than wave height.

These tests clearly show the instrument to be functioning very well, providing accurate water slope output and enhanced information above that which can be provided by a wire wave gauge.

2.5 Future improvements

It had always been the intention that the improved Laser Slope meter would be deployed out in the open ocean on the existing catamaran. However, attempts to do this have failed for a variety of reasons:

- the large swell encountered in the open ocean was too great for the catamaran to cope with. The vehicle motion was increased compared with the prototype instrument due to increased weight of the detector head, which had to be counterbalanced by additional weight at the rear of the catamaran. This tended to cause a "see-saw" motion which was increased by resonance with certain frequency swell waves;
- difficulty was experienced in finding a suitable towing vessel. The towing vessel needed to be small enough to respond quickly to instructions given when towing the catamaran, yet, it still needed to be able to travel at a slow speed (approximately 1m/s) in a near straight line through relatively rough sea conditions. It was also necessary for the catamaran to be taken to the location at which data collection was to commence. This required either the towing vessel to be large enough to lift the catamaran on board, or both the towing vessel and the catamaran to be taken there by a further vessel. Towing the catamaran more than short distances is not practical;
- additionally, DERA had a requirement to measure natural internal waves at a particular site using the Laser Slope meter. It was found that it was only possible to predict the time at which the natural internal waves would arrive at this location to within approximately an eight hour period. Deploying the Laser Slope meter on the catamaran in its current form is simply not practical for eight hours given the stamina demands on the crew and scientific staff and the physical battering of the catamaran and Laser Slope meter system by the sea.

For these reasons a new approach to deployment in the open ocean is being undertaken. A much larger more stable platform has been designed and has recently undergone model development (Love, 2000). The intended structure will be largely autonomous and will have

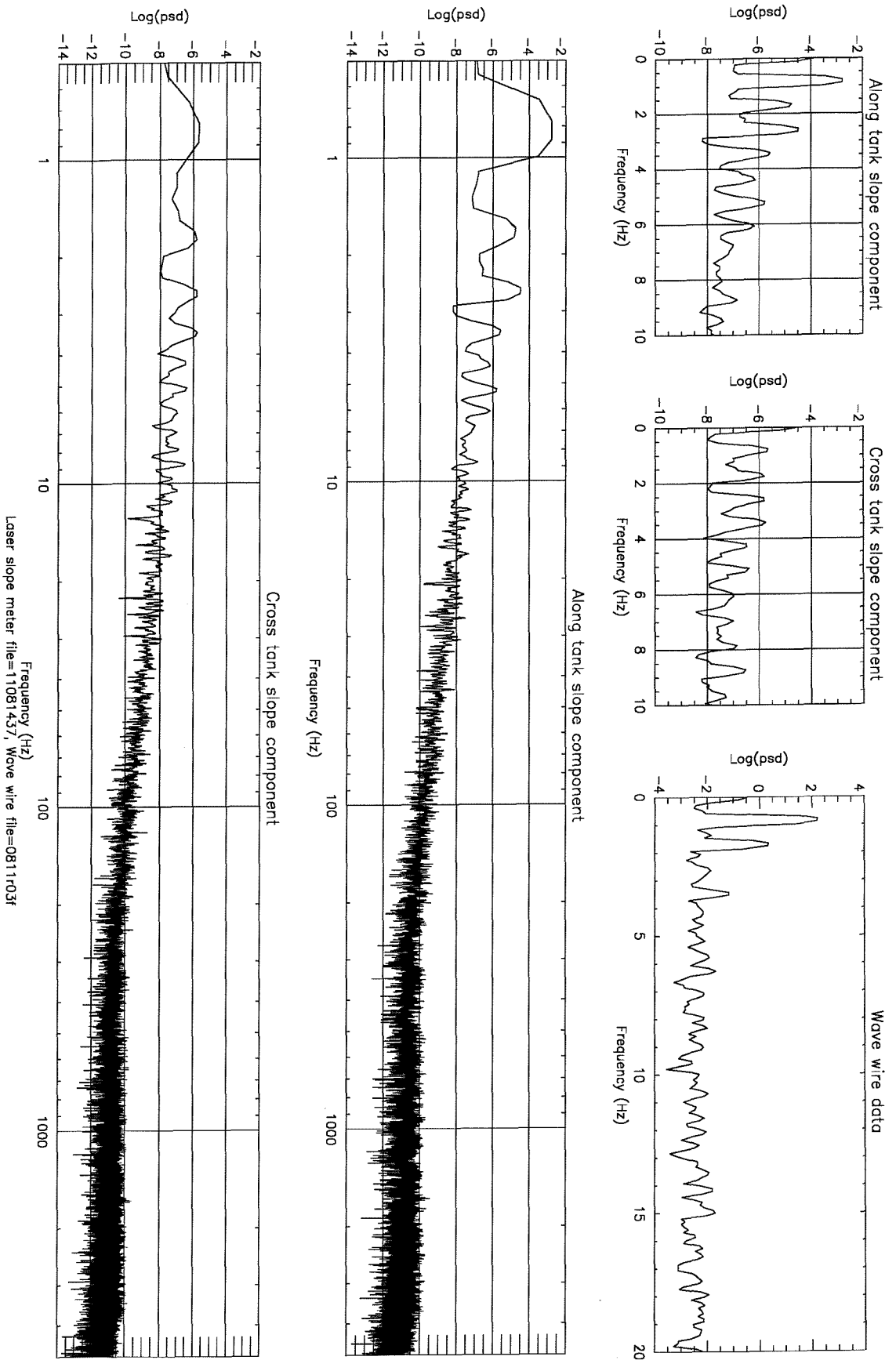

Figure 2-14: Spectral behaviour of Laser slope meter and wire gauge data for wave of 2.0m wavelength and 0.28 steepness

a remotely controlled rudder and power system which can be operated from another vessel. No part of the new system will be physically attached to another vessel. It will be self orientating into the dominant wind direction and will be capable of being deployed to collect data whilst moving slowly or stationary. By orientating into the wind direction, it automatically collects data suitable for spectral analysis as described in chapter 6. This also reduces any interference from waves created by struts that must inevitably break the water surface. The entire unit will be capable of being brought to an experiment location on another vessel where it will be assembled. It will also be capable of being deployed over long time periods.

The capabilities of this system are being designed so that it will be compatible with the current Laser Slope meter, but also with a scanning laser slope meter, which is in its design phase (Love and Cooper, 1999). A scanning laser slope meter would produce a very fast scan of the water surface rather than making a single point measurement. If the scan is fast enough, the surface can be considered to be stationary during the scan period. However, it is also possible to take this scan rate into account during the analysis (Cooper, 2000b). As a scanning laser slope meter automatically provides spatial information, it is no longer necessary for the instrument to travel through the water. Indeed, motion of this kind will merely introduce further errors. Therefore, the new platform must be capable of stationary deployment. However, some form of motion will always be necessary for moving into the required position for data collection.

It is hoped that these additional improvements to the system as a whole will allow for highly accurate and detailed measurements to be made in the future, of both the temporal high frequency and spatial short scale components of the ocean surface. These measurements should improve current knowledge and eventually lead to a significantly improved understanding of radar imaging of ocean phenomena.

Chapter 3

A scientific description of the ambient sea surface

3.1 Introduction and scope of chapter

The objective of this chapter is to present a scientific description of the ambient sea surface according to current understanding. Initially, wave generation by the wind is discussed including how stresses that arise in the atmosphere lead to the development of surface waves. Using the fundamental equations for a fluid, linear solutions for surface waves are derived coupled with the corresponding dispersion relation. Although non-linear solutions to the equations are not given explicitly, the changes from the linear sinusoidal wave shape are discussed. Using a mathematical technique, the statistics of a linear wave field are investigated. These are compared with previous experimental measurements of surface wave field statistics. The relationships between various types of surface wave spectra are examined, as is the way in which the particular type of measuring instrument, and its deployment, can alter the information provided about the sea surface. The effects of aliasing and errors introduced in a spectral calculation by the Digital Fourier Transform (DFT) are considered. Finally, the possible spectral forms that can result from a theoretical approach to the dynamics of surface wave growth, decay and interaction are reviewed. These are compared with previous experimental measurements of surface wave spectra. The chapter is concluded with a discussion of the way in which instruments like the Laser Slope meter may be able to enhance knowledge of the ambient surface wave field.

3.2 Wave generation by the wind

Waves are generated on the sea surface by energy exchange with the wind. When the wind speed is small, tiny ripples are created which are called capillary waves. These ripples are resisted by surface tension, which acts as a restoring force, and they die out due to damping by viscosity if the wind ceases to blow. At larger wind speeds, waves of greater wavelength

are formed; these waves are different from the capillary waves in that gravity, rather than surface tension, forms the restoring force. Such waves will continue to propagate, with very little dissipation, until the limit of fetch is reached, regardless of whether or not the wind is still acting on them. These waves are known as gravity waves. There are two sorts of gravity waves which may exist (Kinsman, 1984):

- sea waves, when the waves are still being worked on by the wind that produced them;
- swell waves, when the waves have escaped the influence of the generating wind.

The principal mechanism for the generation of waves on the surface of the ocean is momentum transfer from winds in the atmosphere to the water surface (Gill, 1982). If there was no frictional contact of the atmosphere with the surface of the earth then the wind speed would extend uniformly down to ground level. However, there is frictional contact so the vertical velocity at ground level must be zero. Therefore, a velocity gradient, or shear, exists near to the ground. The shear flow is not stable: small disturbances grow and make the flow turbulent, so the stress exerted on the surface is not a constant over time. If a long time period, or large area is considered (but not so long or large that temporal or spatial variations become important), a mean velocity can be determined at each height above the ocean surface. Because layers of air at different heights above the earth's surface are moving at different speeds, momentum is transferred downwards by 'parcels' of air which cause a vertical stress on the water surface resulting in waves. The growth of the surface waves is thought to depend on the stress exerted rather than on the wind velocity.

If the horizontal component of the instantaneous wind velocity is represented by w_{fx}, the vertical component of the instantaneous wind velocity by w_{fz}, and the air density by ρ_a, then, apart from viscous stresses, the vertical flux of horizontal momentum is given by $\rho_a w_{fx} w_{fz}$. The mean value of this quantity over a long time or a large area is equal to the mean stress, τ.

$$\tau = \rho_a \overline{w_{fx} w_{fz}} \qquad 3\text{-}1$$

Researchers have found it convenient to describe the stress in terms of a 'friction' velocity, u_* defined by,

$$\tau = \rho_a u_*^2 \qquad 3\text{-}2$$

The stress exerted can also be related to the horizontal wind velocity at some reference height, usually taken to be 10m above sea level, by introducing a 'drag coefficient', c_{10}.

$$\tau = \rho_a c_{10} w_{10}^2 \qquad 3\text{-}3$$

This allows a direct relation of the friction velocity to the wind velocity through the drag coefficient,

$$u_*^2 = c_{10} w_{10}^2 \qquad 3\text{-}4$$

In this way, the stress that actually causes the surface waves can be related to an easily measurable quantity, the wind speed. However, the relationship involves knowledge of the way in which the drag coefficient varies with wind speed, fetch, stability and other parameters, for example the amount of sheltering of the patch of water. The drag coefficient may also change between different experimental environments, such as the ocean and wind wave tanks. For example, the stress tends to be higher for a given wind speed where the fetch is short. Nevertheless, with knowledge of how the drag coefficient varies, it is possible to predict wave states in all environments just by measuring the wind speed. For this reason, a considerable amount of research has been completed in an attempt to determine the behaviour of the drag coefficient at various heights above sea level, (written as c_z for height z) under many different environmental, and experimental, conditions. This work will be reviewed now, as it is relevant in later chapters (where Laser Slope meter data is compared with other data presented in the literature).

Charnock (1955) used the results from an experiment and some dimensional analysis to obtain a relationship between the wind speed at a height z and the friction velocity in conditions of neutral stability (where the air and water temperatures are equal),

$$\frac{w_z}{u_*} = \frac{1}{\kappa} \ln\left(\frac{gz}{u_*^2}\right) + \text{constant} \qquad 3\text{-}5$$

If the constant is represented by $(1/\kappa)\ln(1/a)$, then using the relationships given above, this can be rearranged to give,

$$c_z = \left(\frac{\kappa}{\ln\left(\frac{gz\rho_a}{a\tau}\right)}\right)^2 \qquad 3\text{-}6$$

where κ is the von Karman constant and a is the Charnock constant.

In studies of experimental data it has been found that the coefficient c_z takes a different form for different regions of wave growth and air turbulence. The first comprehensive compilation of experimental data was performed by Wu, throughout the late sixties and seventies. Wu (1968a) showed that Charnock's relationship was true when the surface roughness was governed by gravity waves. However, at lower wind velocities where the roughness, as opposed to the wave height, was governed by capillary ripples, this relationship was found not to apply. In the same year Wu (1968b) also considered how to scale data between the laboratory (and limited fetch conditions) and the ocean, by use of a Froude number. He applied these theories (Wu, 1969a) to the available ocean data and found that there were three distinct regions relating wind stress to wind velocity. These corresponded to:

- an initial region, when the air flow was aerodynamically smooth;
- a central transition region for wind velocities < 15m/s where the surface roughness was established;
- a final region for wind velocities > 15m/s where, once the roughness was established, the surface became saturated and the wind stress became constant.

$$c_{10} = \frac{1.25\times10^{-3}}{w_{10}^{\frac{1}{5}}} \qquad w_{10} < 1\text{m/s} \qquad 3\text{-}7$$

$$c_{10} = 0.5 w_{10}^{\frac{1}{2}} \times 10^{-3} \qquad 1\text{m/s} < w_{10} < 15\text{m/s}$$

$$c_{10} = 2.6\times10^{-3} \qquad w_{10} > 15\text{m/s}$$

Later, Wu (1971) showed that there were other stages in the behaviour of the wind stress with wind speed. Measuring the wind speed at the water surface, below 1.9m/s the flow was laminar. Between 1.9m/s and 2.4m/s there was a transition to turbulent flow and a change in character of the relationship. Once the boundary layer was turbulent there was a transition from smooth to rough flow between 2.4m/s and 3.5m/s. For rough flow, two regions were observed; one was for a surface roughness governed by capillary waves and in the other the surface roughness was governed by gravity waves. Other measurements such as those by Smith and Banke (1975) agree with this theory.

Garratt (1977) re-evaluated a large amount of experimental data collected prior to 1977 where he determined that a considerable quantity of the variation found in the data by previous authors was due to experimental error and differing experimental techniques. He concluded that observations of wind stress and wind profiles over the ocean reported in the experimental studies were consistent with Charnock's relation with a=0.0144 and κ=0.41. A further study by Wu (1980) produced near equivalent values of a=0.0185 with κ=0.4.

A more recent investigation by Amorocho and DeVries (1980) showed a similar behaviour to the above, relating a change in regimes to the onset and saturation of breaking waves. Due to differences in laboratory flumes and differing environmental conditions of field experiments such as the fetch and depth, the wind speed at which breaking waves are first observed varied greatly between experiments. This led to the definition of three regions for c_z, as the wind speed increased:

- a lower region where the wind friction velocity varies linearly with w_{10}. In this region there are no breaking waves;
- an intermediate region where there is the transition between the onset of breaking and full breaker saturation;

- an upper limiting region where the wind friction velocity is again a linear function of w_{10} and the wave field is fully saturated with breakers.

c_{10}=0.00104	No breakers	3-8
c_{10} varies non-linearly with w_{10}	Transition region	
c_{10}=0.00254	Breaker saturation	

Amorocho and DeVries developed a theory based on rapid breaker growth initially following breaker onset, followed by a gradual reduction in the growth towards zero at breaker saturation. This theory led to the following equations for u_* and c_{10},

$$u_* = \left\{0.0015\left[1+\exp\left(-\frac{w_{10}-d_1}{d_2}\right)\right]^{-1}+0.00104\right\}^{\frac{1}{2}} w_{10} \qquad 3\text{-}9$$

$$c_{10} = 0.0015\left[1+\exp\left(-\frac{w_{10}-d_1}{d_2}\right)\right]^{-1}+0.00104 \qquad 3\text{-}10$$

where d_1 and d_2 were determined to be 12.5m/s and 1.56m/s respectively by fitting the expression to the data by least squares. These values for d_1 and d_2 were based on breaker onset at w_{10}=7m/s and saturation at w_{10}=20m/s.

Smith (1988) developed an iterative method to calculate the wind stress in terms of the wind velocity measured at a known height and the sea and air temperatures. However, the resulting relation was only valid for open sea conditions, and higher friction velocities needed to be used for regions of limited fetch. Smith also reviewed many of the studies performed on the data presented in the literature, and concluded that for the majority of cases a logarithmic profile could be assumed. For coastal waters, he suggested that the results of the studies conducted by Garratt (1977) and Wu (1980) should be applied as the majority of experiments used in these studies were in coastal areas or regions of limited depth. The value of the Charnock constant, a, found from these studies was greater than that found for open oceans. Larger values of the Charnock constant in regions of limited fetch is consistent with data collected in wind wave tanks where the fetch is very short.

Smith (1980) has also made measurements of wind stress versus wind speed in the deep water wave regime for higher wind speeds in the range w_{10}=6m/s to 22m/s. The results showed that the sea surface drag coefficient increased gradually with increasing wind speed.

Recently, there has been considerable interest in whether the drag coefficient really is dependant upon the wave age = c_p/u_*, i.e., whether the wind stress is modified by the stage of development of the wind sea. Yelland and Taylor (1996) collected a considerable amount of data and summarised in Yelland and Taylor (1999) that from the measurements, it did not look as though the wind stress was wave age dependant in the open ocean. Instead, they found that the results which have suggested this were likely to be contaminated by experimental noise. A large amount of the noise was likely to be due to air flow disturbance by the ship and anemometer, with the wind direction over the hull having a large effect on the disturbance and thus the results. Since a change in wind direction is often associated with a change in sea state, it was difficult to distinguish between the effects. Janssen (1997) performed a statistical analysis of the HEXMAX data and also found that the results indicated there was no wave age dependency of the wind stress. However, measurements in coastal waters have found a higher wind stress for a given wind speed. At present there are no clues of the mechanism, but it is thought that it could be related to an increase in the wave steepness or slope, caused by the longer waves shoaling in shallow water.

The above literature review clearly demonstrates the uncertainty that exists in relating the stress exerted on the water surface to the wind speed. This leads to a fundamental difficulty in determining the likely sea state in a particular environment purely from a measurement of the wind speed. However, in certain conditions a great deal of experimental evidence has provided a reasonable way of estimating the wind stress. These results will be used in later chapters to compare experimentally measured sea states in different environmental conditions.

The above has established that waves are generated by the stress exerted on the water surface by the atmosphere and how the amount of stress, and hence the final sea state, might be related to the wind speed for an unstratified atmosphere. Now, the way in which the stress causes the wave growth will be examined.

Various mechanisms have been proposed to model the growth of waves due to the wind. Two of these form the basis of the present day theories. Phillips (1957) assumed there was a resonant forcing of free surface waves by turbulent pressure fluctuations. The resonance would occur where the scale of the fluctuations was comparable to the wavelength of the surface wave and when the velocity was comparable with the wave phase speed. This type of mechanism led to linear wave growth. Miles (1957) considered a resonant interaction between the wave induced pressure fluctuations and the free surface waves. In other words, an existing surface waviness would cause a disturbance in the air flow. The pressure fluctuations from the disturbance would then act to increase the energy of the surface wave field. This effect was proportional to the wave spectrum and led to exponential growth.

Neither of these theories included all the observed effects. Currently, linear growth is taken to be the main growth when no wave field exists prior to the wind starting to blow. Once small waves are generated, exponential growth takes over. Plant (1982) has considered a large amount of experimental data from which he developed a relationship that describes the observed exponential wave growth. This relationship is widely used and so is presented below.

Plant compiled a large range of experimental results which aimed to measure the growth of waves shorter than 10cm. He found that there was a maximum in the growth rate for waves at about 20Hz where the wave speed is small. This growth rate reduced rapidly for longer waves at the point where the wave speed approached the wind speed. In the frequency range between the maximum growth rate (at ~20Hz) and the minimum value ($c_p \rightarrow w_{10}$), there existed a single well defined equation for the growth rate, given by 3-1. ω is the angular frequency of the waves, ϕ is the angle between the wind and the waves, c_p is the phase speed of the waves, w_{10} is the wind speed at a height of 10m above sea level and β is the growth rate of the waves of frequency ω.

$$\beta = \frac{(0.04 \pm 0.02) u_*^2 \omega \cos\phi}{c_p^2} \quad \text{for} \quad \frac{g}{w_{10}} < \omega < 2\pi.20 \text{ rad/s} \qquad 3\text{-}11$$

If there was no energy loss from the waves they would continue to grow indefinitely; however, in a real process this does not occur. Energy is dissipated mainly due to breaking but also by the viscosity of the water. There is also a transfer of energy between the waves of different wavenumbers which can be described as non-linear wave-wave interactions. An energy balance that limits the wave growth can be formulated and can be used to predict theoretical wave spectra.

3.3 Fundamental equations

Assuming the flow to be irrotational and incompressible, from the equation for vorticity and the equation of continuity, Laplace's equation for the velocity potential, Φ can be derived, 3-12. This equation says that fluid mass is conserved.

$$\nabla^2\Phi = 0 \qquad 3\text{-}12$$

By considering the momentum equations for the fluid in terms of the forces due to pressure and gravity and using the material derivative, Bernoulli's equation, 3-13, can be derived, which conserves energy and relates the pressure and velocity, $\underline{u}$, at depth z.

$$\frac{p}{\rho} + \frac{\partial\Phi}{\partial t} + \frac{1}{2}\underline{u}^2 + gz = 0 \qquad 3\text{-}13$$

In order to solve Laplace's equation, the boundary conditions must be considered at the free surface and at the sea bed. At the free surface, the vertical velocity has a component from the time derivative of the sea surface height and a component from the horizontal velocity due to the slope of the wave,

$$u_z = \frac{\partial\eta}{\partial t} + u\frac{\partial\eta}{\partial x} \qquad 3\text{-}14$$

In general there is also a non-zero pressure difference across the surface caused by surface tension. Thus, the pressure at the water surface is equal to atmospheric pressure plus an extra term due to the surface tension. Substituting this into Bernoulli's equation and

combining it with the vertical velocity term using linear approximations leads to the linear surface boundary condition (where Φ_0 represents the linear component of Φ),

$$\frac{\partial^2\Phi_0}{\partial t^2}+\left(g+\frac{k^2T}{\rho}\right)\frac{\partial\Phi_0}{\partial z}=0 \text{ at } z=0 \qquad 3\text{-}15$$

At the sea bed, the vertical velocity component must be equal to zero.

$$\frac{\partial\Phi}{\partial z}=0 \text{ at } z=-h \qquad 3\text{-}16$$

Laplace's equation must be solved subject to these boundary conditions. A two-dimensional plane wave solution to Laplace's equation can be chosen of the form,

$$\Phi_0=\mathrm{Re}[F(z)\exp(kx-\omega t)] \qquad 3\text{-}17$$

Substituting this into Laplace's equation and using the boundary conditions leads to,

$$\Phi_0=C\cosh k(z+h)\cos(kx-\omega t) \qquad 3\text{-}18$$

where C is a constant. From this, the form for the dispersion relation, 3-19, is also found, which relates the wavenumber, k, and frequency, ω, of the waves. This relationship can be used to calculate the speed at which the component frequencies propagate along the surface. In the case of deep water, as $h\to\infty$ the familiar forms for the velocity potential and dispersion relation appear.

$$\omega^2=\left(gk+\frac{k^3T}{\rho}\right)\tanh kh \qquad 3\text{-}19$$

If the surface boundary conditions are combined without taking linear approximations then Stokes waves are obtained (Stokes, 1847, 1880). These higher order terms alter the shape of the surface waves from being sinusoidal, tending to sharpen the wave crests and flatten

the troughs. The dispersion relation is also modified to include terms involving the amplitude of the waves.

3.4 A simple linear theory of surface waves

The linear theory of surface waves is only valid if the wave steepness can be considered to be small, i.e. if $ak \ll 1$, where a is the wave amplitude and k is the wavenumber of the waves in question. This is a good assumption for many of the waves present in the ocean, provided the external conditions affecting the waves are not sufficient for linear waves to produce non-linear characteristics and become unstable.

The mathematical analysis of a sum of linear waves was first considered by Raleigh (1894) in connection with his theory of sound. It was later examined by Rice (1944) in the analysis of random noise and by Longuet-Higgins (1957) in connection with sea waves. In the linear approximation, the solution to Laplace's equation for surface waves has sinusoidal solutions and the overall surface wave field behaves as a linear combination of independent sinusoids of varying amplitude, frequency and phase.

If the height of a surface wave field is considered to be the sum of the contributions from a large number of independent sinusoidal wavenumber components then the Central Limit Theorem can be applied. This shows that, under certain conditions, the probability distribution of the sum of the components is a Gaussian distribution. The key point in this theorem is that the waves must be independent. This is true in the ocean because each component is generated by many independent events.

This theory can be generalised to an infinite number of dimensions. Therefore, still in the linear approximation, each component of the surface slope is also a combination of contributions from the wavenumber components and, therefore, also tends towards a Gaussian distribution. A generalisation of the central limit theorem to higher dimensions shows that the vector slope has a two-dimensional Gaussian probability distribution function. A full proof of the central limit theorem and the conditions can be found in Uspensky (1937).

When the magnitude of the wind is small, the above approximation is good. However, as the wind speed increases, non-linear effects start to occur as the wave steepness becomes large. The distribution of wave slopes becomes more peaked and skewed in the direction of the wind. In these situations the probability distribution can be better represented by other functions.

3.5 Deviations from the linear theory

The linear theory presented above suggests that the probabllity distribution for either sea surface height or for the components of sea surface slope might be a Gaussian distribution. Experimental measurements of the distributions of height and slope (for example, Schooley, 1954, Cox and Munk, 1954a, 1954b) have shown that the distributions are approximately Gaussian, but with some deviations causing the along wind slope distribution to become skewed away from the wind direction, with increasing skew as the wind speed increased. The peakedness of the along and cross wind distributions was also slightly modified from that of a Gaussian distribution, causing very small and very large slopes to be more probable than in the linear case. The peakedness was found to be independent of wind speed.

Cox and Munk fitted a Gram-Charlier distribution, 3-25, to their data to quantify the variations. This distribution is based upon a Gaussian shape, but models small deviations from the Gaussian distribution, once the distribution has been rotated to the principal axes, in terms of Hermite polynomials, H. In the approximation considered, this was accurate for slopes up to $\xi=\varsigma=2.5$; where $\xi=s_c/\sigma_c$, $\varsigma=s_u/\sigma_u$, s_c, s_u are the cross wind and along wind slope components respectively and σ_c, σ_u are the root mean square (rms) slopes of each component.

$$\text{pdf} = \frac{1}{2\pi\sigma_c\sigma_u}\exp\left[-\frac{1}{2}\left(\xi^2+\varsigma^2\right)\right]\times\left[1+\sum_{i,j=1}^{\infty}C_{i,j}H_i(\xi)H_j(\varsigma)\right] \qquad 3\text{-}25$$

The coefficients of the Gram-Charlier distribution are determined by the moments of a distribution. The first moment about the origin is the mean or expectation value. In general, the second and all further moments are usually taken about the mean and represent variations of the distribution from the mean value.

In 1-dimension, about the origin,

$$1^{st} \text{ moment about origin} = \sum_x p(x)x = \bar{x} = \text{mean of } x \qquad 3\text{-}26$$

About the mean value, $\bar{x}$,

$$1^{st} \text{ moment about mean} = \sum_x p(x)\left(x - \bar{x}\right) = 0 \qquad 3\text{-}27$$

$$2^{nd} \text{ moment about mean} = \sum_x p(x)\left(x - \bar{x}\right)^2 = \overline{x^2} - \bar{x}^2 = \text{variance}$$

$$3^{rd} \text{ moment about mean} = \sum_x p(x)\left(x - \bar{x}\right)^3 = \text{skewness}$$

$$4^{th} \text{ moment about mean} = \sum_x p(x)\left(x - \bar{x}\right)^4 = \text{kurtosis}$$

The second moment about the mean is the variance. This provides information about the spread of the distribution. The third moment indicates how skewed the distribution is (a positive skew has a long tail of high values whilst a negative skew has a long tail of low values). The fourth moment indicates the peakedness of a distribution and the amount of energy contained within the tails.

In two dimensions the number of moments increases as there are the moments as defined above for each dimension and then additional moments which represent the cross terms between the two dimensions.

About the origin, the 1^{st} moments are,

$$\sum_x p(x,y)x = \bar{x} = \text{mean of } x \qquad 3\text{-}28$$

$$\sum_y p(x,y)y = \bar{y} = \text{mean of } y$$

About the mean the second moments are,

$$\sum_x p(x,y)(x-\bar{x})^2 = \overline{x^2} - \bar{x}^2 = \text{variance of x} \qquad 3\text{-}29$$

$$\sum_y p(x,y)(y-\bar{y})^2 = \overline{y^2} - \bar{y}^2 = \text{variance of y}$$

$$\sum_{x,y} p(x,y)(x-\bar{x})(y-\bar{y}) = \overline{xy} - \bar{x}\,\bar{y} = \text{covariance of x,y}$$

The two-dimensional Gram-Charlier distribution can be developed in terms of the moments about the mean (Kendall and Stewart, 1963) so that the Hermite polynomials in the standard definition of a Gram-Chalier distribution can be expanded, 3-30, where the coefficients C_{nm} can be written in terms of the moments as given by 3-31. The full development is given in Appendix A.

$$p(x,y) = \frac{1}{2\pi\sigma_x\sigma_y} e^{-\frac{1}{2}(\xi^2+\varsigma^2)} \left[\begin{array}{l} C_{00} - \frac{C_{21}}{2}(\xi^2-1)\varsigma - \frac{C_{03}}{6}(\varsigma^3-3\varsigma) + \\ \frac{C_{40}}{24}(\xi^4-6\xi^2+3) + \frac{C_{22}}{4}(\xi^2-1)(\varsigma^2-1) + \\ \frac{C_{04}}{24}(\varsigma^4-6\varsigma^2+3) \end{array} \right] \qquad 3\text{-}30$$

$$\begin{aligned} C_{00} &= 1 \\ C_{21} &= -m_{21} \\ C_{03} &= -m_{03} \\ C_{40} &= m_{40} - 3 \\ C_{22} &= m_{22} - 1 \\ C_{04} &= m_{04} - 3 \end{aligned} \qquad 3\text{-}31$$

This model of the sea surface is used as a representation of the deviations of the statistics of the sea surface from linearity.

3.6 Variations of the second moment with wind speed

If the mean slope is zero the variance is equal to the mean square slope of the water surface. A number of measurements have been made of the variation of mean square slope with wind speed. In the ocean, measurements of the mean square slope variation with wind speed such as those by Cox and Munk (1954a), Hughes *et al.* (1977), Haimbach and Wu (1985),

Khristoforov *et al* (1992), Shaw and Churnside (1996) and Shaw *et al.* (1997) have revealed a linear relationship provided no slicks were present on the water surface.

In the presence of natural slicks (which were found in the wind speed range of 1.7 to 3.0m/s) , Kristoforov *et al.* discovered that the relationship was not linear. Instead, below ~1.8m/s the mean square slope was independent of wind speed with a value of ~0.004. It then increased sharply reaching 0.025 at 3m/s. This is in contrast to Cox and Munk's results in the presence of artificial slicks where the slicks were found to persist up to wind speeds of 12m/s and the relationship remained linear.

The result obtained by Khristoforov *et al.* in the presence of natural slicks is very similar to measurements of the variation of mean square slope with wind speed measured in wind wave tanks. Measurements in wave tanks have been made by Cox (1958), Wu (1971, 1976), and Koyuncu (1995). All of these showed an initial period where no waves were generated until the wind reached a minimum critical velocity. After this, in general the data did not vary linearly through all the wind speeds, although there was a linear region. It should be noted, however, that some of the differences at higher wind speeds, particularly in the case of Cox may well be due to experimental error caused by the limitations of the instrument.

The main candidate for the discrepancies in the measurements between the ocean and the wave tank at low wind speeds is swell. At sea, low wind speed measurements are often contaminated by residual swell which has not been created by the local wind. The presence of even a small swell is likely to increase the number of small waves that are generated on the surface at a particular wind speed. This has been observed experimentally by Miller *et al.* (1991) and was thought to be due to the break up of surface films by the long waves.

It is difficult to make a proper comparison between the data sets reported above because the generation of waves by the wind should be related to the stress exerted on the water surface by the wind rather than directly to the wind speed, as was discussed previously. It is therefore necessary either to measure the stress directly or to convert the wind speed into stress using the most suitable relationship from those reviewed in section 3.2. This latter method is used in chapters 5 and 7 of this thesis.

3.7 Spectral variations

3.7.1 Introduction

So far, the variation of the total slope variance with wind speed has been discussed. No consideration has been given to how the energy in the wave field may be distributed among the spectral components of the wind wave field. As was described in section 3.3, the ocean surface can be considered as being made up of an infinite number of independent wavelength, or frequency, components. If the surface height or slope is measured at a single point over a period of time, the resulting time profile can be Fourier transformed to reveal the energy, or slope variance, contained in each frequency component of the surface. Similarly, if a spatial picture of the ocean is taken at a single instant in time, the spatial profile can be Fourier transformed to reveal the energy, or slope variance, contained in each wavenumber component of the surface. The presentation of the energy as a function of the frequency or wavenumber is known as a frequency or wavenumber spectrum.

A frequency spectrum can not provide directional information but instead supplies the energy in each frequency integrated over waves travelling in all directions. A one-dimensional wavenumber spectrum also does not provide directional information. There are several different types of one-dimensional wavenumber spectra. These types of spectra can be visualised using figure 3-1. Two-dimensional k-space has been drawn and the relationship to the frequency domain can be considered by assuming that there is a third axis (pointing out of the page) which represents frequency. If ω is a function of k then the energy within the anulus of width dk can be related to the energy in a frequency ω within a range $d\omega$ by,

$$H(\omega)d\omega = \chi(k)dk \qquad 3\text{-}32$$

were $H(\omega)$ is the wave height frequency spectrum and $\chi(k)$ is the one-dimensional wave height wavenumber spectrum.

A one-dimensional spectrum may refer to knowledge about just one spatial dimension of the surface, for instance information about the k_x components of the wave field but with no information about the k_y direction. An example of this is the spectrum of wave heights

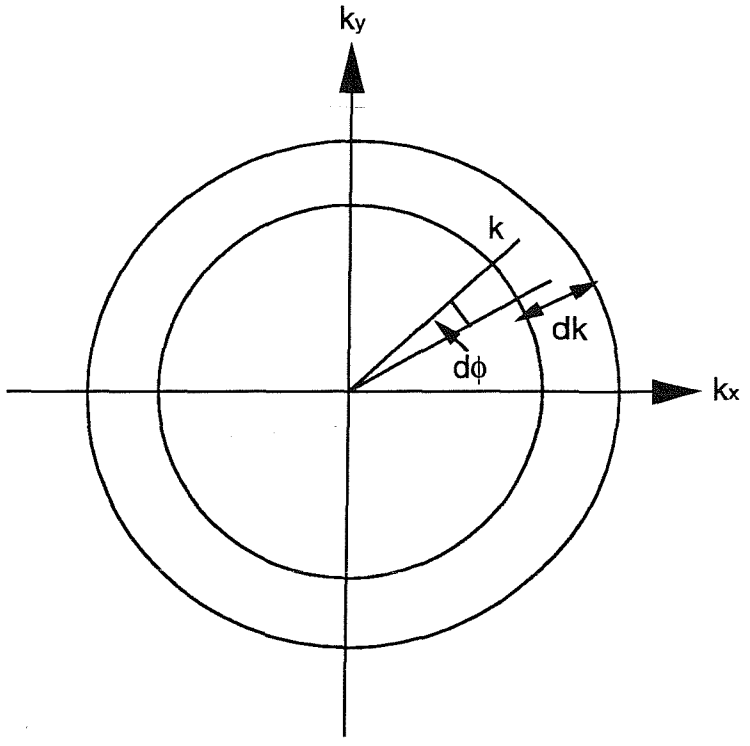

Figure 3-1: Relationship between 2-dimensional and 1-dimensional wavenumber spectra

measured along a section in the x-direction, or the spectrum of the y-slope component measured along a section in the x-direction. Alternatively, it may provide the energy in each particular total wavenumber, k, regardless of direction. The relationship between this latter type of one-dimensional spectrum, $\chi(k)$, and a full two dimensional spectrum, $\Psi(k,\phi)$, can also be visualised using figure 3-1. The one-dimensional spectrum can be considered to be the integral over all angles of the two-dimensional spectrum. Hence, the total energy in the annulus is equal to the sum (or integral, as the distribution is continuous) of contributions from individual elements in the two-dimensional wavenumber spectrum,

$$\chi(k)dk = \int_0^{2\pi} \Psi(k,\phi)kdkd\phi = C\psi(k)kdk \qquad 3\text{-}33$$

For a full description of the sea surface, a two-dimensional spectrum is needed which gives details about both the magnitude and direction of the waves contained within the surface. This can be obtained for each component of the vector property being measured. For example, in the ocean it is possible to measure the two-dimensional wave height spectrum.

It is also possible to measure the two-dimensional spectrum for each of the two components of wave slope. The two components of the wavenumber wave slope spectra, $S_x(k,\phi)$ and $S_y(k,\phi)$, can be related simply to the wavenumber total slope spectrum, $S(k, \phi)$, and the wavenumber height spectrum, $\Psi(k, \phi)$, by,

$$S(k,\phi) = S_x(k,\phi) + S_y(k,\phi) = \left(k_x^{\,2} + k_y^{\,2}\right)\Psi(k,\phi) = k^2\Psi(k,\phi) \qquad 3\text{-}34$$

The full two dimensional wave height wavenumber spectrum is formally defined to be the Fourier transform of the covariance of the surface displacement, η, at points separated by a distance $\underline{r}$,

$$\Psi(\underline{k}) = \frac{1}{(2\pi)^2}\int \langle \eta(\underline{x})\eta(\underline{x}+\underline{r})\rangle e^{-i\underline{k}\cdot\underline{r}}\,d\underline{r} \qquad 3\text{-}35$$

A spectrum is only meaningful if it can provide information about the real properties of the subject being measured. In the case of the ocean, the wave field has two useful properties, the frequency of the waves and their wavelength. For an instrument that collects data at a single point, a stationary instrument would be able to measure the frequency properties but would not provide information on the wavelength of the waves without prior knowledge of the speeds and directions at which the waves were travelling. Conversely, an instrument which provides a 'snapshot' picture of the ocean would be able to provide wavelength information but could not provide information about the period of the waves. In terms of information that may be able to improve understanding of radar imaging of the ocean, it is important to be able to provide wavenumber information. Unfortunately, traditional methods of recording the wavelength of ocean waves do not provide the necessary resolution to 'see' the small-scale features on the ocean surface, which are important in radar scattering.

The spectrum can be estimated from a finite section of a discrete data series by a process called the Digital Fourier Transform. It is assumed that the section of data is representative of the entire data set. The resulting spectrum consists of a series of points that represent the energy contained in a finite frequency band. There will also be spurious energy effects in

each frequency band due to aliasing of energy from very high frequency components in the original data that were sampled insufficiently to be recorded at their correct frequencies. The highest frequency that can be measured at a particular sample rate is given by the Nyquist criterion and is equal to half the sampling frequency. Errors are also introduced by recording data over a finite period. This effectively causes the frequency behaviour of the data to be convolved with the Fourier transform of the window function, which is a square window for the case of a short sample of data. These effects can be reduced by multiplying the data section by a different window function which has a Fourier transform that causes smaller errors in the frequency domain.

3.7.2 Aliasing

When a signal is sampled at finite intervals, the Nyquist criterion states that for any wave to be measured accurately there must be at least two measurements per cycle. Thus, the maximum frequency that can be measured is given by,

$$f_{max} = \frac{f}{2} \qquad 3\text{-}36$$

where f is the sampling frequency. If a wave is undersampled then the measurements will be identical to those of a wave of lower frequency and so all the energy in the high frequency wave appears to be spuriously moved into the lower frequency wave. This effect is known as aliasing. Because of the way in which lower frequency waves fit the sampled points of the waves with frequencies greater than f_{max}, the energy in these higher frequencies is reflected back about the Nyquist frequency. Therefore, the energy contained in the under sampled wave will be added to the energy of the recorded frequency, giving a false impression of the energy spectrum. Figure 3-2 and the following mathematics show why this is.

Two different sinusoidal waves can represented by,

$$\eta_1(t) = a_1 \cos \omega_1 t + b_1 \sin \omega_1 t \qquad 3\text{-}37$$
$$\eta_2(t) = a_2 \cos \omega_2 t + b_2 \sin \omega_2 t$$

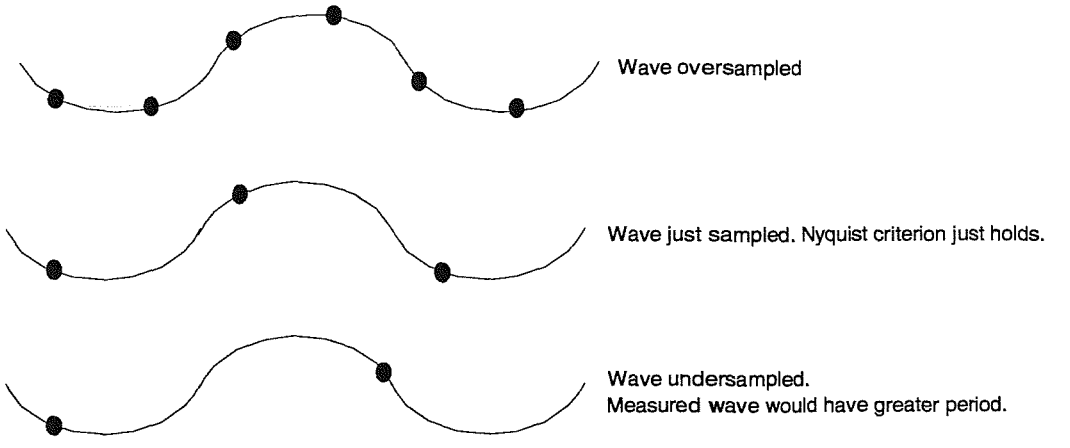

Figure 3-2: Effect of aliasing on sampling rate

Assume that these waves are sampled every Δt in time and that at these points, $\eta_1=\eta_2$. There is at least one sample where η is not zero and this is taken as the origin of t. Therefore, setting t=0 in 3-37 gives, $a_1=a_2$. Therefore, at $t=\Delta t$ and at $t=-\Delta t$, equations 3-38 and 3-39 are true.

$$a\cos\omega_1\Delta t + b_1\sin\omega_1\Delta t = a\cos\omega_2\Delta t + b_2\sin\omega_2\Delta t \qquad 3\text{-}38$$

$$a\cos\omega_1\Delta t - b_1\sin\omega_1\Delta t = a\cos\omega_2\Delta t - b_2\sin\omega_2\Delta t \qquad 3\text{-}39$$

Taking 3-39 from 3-38, and assuming a is non-zero gives,

$$\cos\omega_1\Delta t = \cos\omega_2\Delta t \qquad 3\text{-}40$$

Therefore,

$$\omega_1 = \frac{2\pi n}{\Delta t} \pm \omega_2 = 2n\omega_N \pm \omega_2 \qquad 3\text{-}41$$

where ω_N is the angular Nyquist frequency. This says that due to the finite sampling, the two waves, ω_1 and ω_2, are indistinguishable. Therefore, all the energy in the undersampled

frequency, ω_2, will appear in the spectrum at frequency, ω_1, where the two frequencies are related by 3-41. It can be seen that 3-41 leads to the energy being reflected about the Nyquist frequency.

3.7.3 Theoretical and experimental spectra

Understanding how the energy varies between the different spectral components is one of the mysteries of the ocean which scientists are endeavouring to unravel. Many authors have attempted to calculate theoretically the form the spectrum might take, whilst others have made many measurements of the actual spectrum present in different environmental conditions.

As energy is input into a wave field as described earlier, each component will grow until eventually a stage is reached where the increase in energy is exactly balanced by dissipation due to viscosity and breaking and any non-linear wave-wave interactions. By assuming breaking is dominant over all other forms of energy loss or interactions, Phillips (1958) postulated that the spectrum would be determined by the physical parameters that govern the discontinuity of the surface at the breaking point and would therefore depend only on g,ω or g,k for the frequency or wavenumber spectra, respectively. He showed by dimensional analysis that a limiting form for the frequency and wavenumber spectra under these conditions of equilibrium would be 3-42 or 3-43, respectively. No assumption was made about the form of the angular dependence.

$$H(\omega) \propto g^2 \omega^{-5} \qquad 3\text{-}42$$

$$\Psi(\underline{k}) \propto F(\phi) k^{-4} \qquad 3\text{-}43$$

This form of spectrum is only valid beyond the spectral peak as these are the wave components that will be in equilibrium. At lower frequencies, there would be insufficient energy being input by the wind at these frequencies for saturation to be reached. As the wind speed increases, since the high frequencies are already saturated, no more energy can be input into these frequencies and so the only growth will be amongst the lower frequencies until they too become saturated. Therefore, the functional behaviour of the

spectrum will extend to lower frequencies causing the spectral peak to do the same. The principle of similarity appears to apply well to the spectra as the basic shape is the same for each wind speed.

Other authors such as Toba (1972, 1973) have considered how to calculate the spectrum of the sea. Their results are in agreement with Phillips' for a fully developed sea. However, they show a dependence on friction velocity where the sea has been limited in fetch or duration and so is not fully developed.

This functional form has been found in certain regions of the spectrum by a number of experiments. Banner *et al* (1989) used a stereophotogrammetric method in the field to determine the two-dimensional wavenumber spectra. They concluded that the spectra were predominantly k^{-4} with a very weak dependence on wind magnitude and direction. Stilwell and Pilon (1974) also measured a k^{-4} spectrum when their sea had reached equilibrium. Lubard *et al.* (1980) measured frequency and wavenumber spectra with a laser slope meter and an optical technique, respectively. Both spectra agreed with k^{-4} in the gravity region (converting the laser slope meter data using the gravity dispersion relation).

Other forms of the wavenumber spectrum have also been suggested. Kitaigorodskii (1983) proposed the existence of a 'Kolmogoroff-type' energy cascade. He considered that the rate of energy transfer from the large scale motion (at which energy was input into the ocean) to the small scale motion (where energy is dissipated) and the kinematic viscosity, ν, were the only parameters which determined the spectral energy density E(k). Then, provided the regions of generation (at low wavenumbers) and dissipation (at high wavenumbers) were separated by a broad region in wavenumber space, Kitaigorodskii proposed there would exist a sub-range where the spectral energy flux was determined entirely by non-linear wave-wave interactions and was inherently constant. The energy would be passed down from wavenumber to wavenumber with the action spectral density being independent of gravity. This led to forms for the wavenumber and frequency spectra given in 3-44 and 3-45, respectively.

$$\psi(k) \propto g^{-\frac{1}{2}} k^{-\frac{7}{2}} \qquad 3\text{-}45$$

$$H(\omega) \propto g\omega^{-4} \qquad 3\text{-}45$$

At high wavenumbers, where gravitational instability is important, Kitaigorodskii suggested Phillips' 1958 theory would apply. He discussed the possibility that both a Kolmogoroff subrange and a Phillips subrange could exist with an unknown transition between the two regions.

Phillips (1985) later considered an energy balance approach where he postulated that the rate of action flux divergence in non-linear wave-wave interactions was exactly balanced by the rate of growth of the action spectral density due to wind and its rate of dissipation due to wave breaking, viscous dissipation and turbulent diffusion. Action is a quantity defined as energy divided by intrinsic angular frequency. The action spectral density, $N(\underline{k})$, is the amount of action per unit wavenumber space and unit area. For a fully developed sea in equilibrium, Phillips postulated that the terms would exactly balance at each local wavenumber, 3-46, so that the energy at each wavenumber is independent of time. If N_w is the growth due to the wind, N_D is due to dissipation and N_{NL} is due to wave-wave interactions.

$$N_W + N_D + N_{NL} = 0 \qquad 3\text{-}46$$

The form of the spectrum that Phillips found to be consistent with this balance was exactly that found by Toba for a sea which was not fully developed and therefore had a dependence on friction velocity. These spectra were also consistent with Kitaigorodskii's spectra in the Kolmogoroff sub-range.

Banner *et al.* (1989) considered other spectra which were also consistent with Phillips' action balance approach (3-46) by assuming that the dissipation term could be written as a power law of Phillips' equilibrium constant, $k^4\Psi(\underline{k})$. They used dimensional reasoning assuming each term to be comparable in magnitude in pairwise combinations. This gave three alternative forms for the spectrum depending on the terms being compared. Comparing N_{NL} and N_W gives 3-44 and comparing N_{NL} and N_D gives 3-43. However, comparing N_W and N_D gives a spectrum of the form,

$$\psi(k) \sim \left(\frac{u_*^2 k}{g}\right)^{\gamma} k^{-4} \qquad 3\text{-}46$$

with γ yet to be determined. Banner *et al.* argued that the form of the non-linear term used by Phillips, which was based on Hasselsmann's wave-wave interactions, is for strongly non-linear behaviour only. However, Hasselmann thought that the dissipation process may be quasi-linear in certain regions of the spectrum. Therefore, Banner *et al.* assumed 3-47 to be the most reliable form of the spectrum, where the non-linear term was not used in the comparison.

Recently, Belcher and Vassilicos (1997) have developed a theory for the equilibrium range on the basis that wave breaking is the controlling process and that breaking waves have a near discontinuity in slope at their crests. The wavenumber spectrum is determined by the discontinuity leading to a k^{-4} spectrum. The frequency spectrum is also determined by the breaking waves, assuming that in the equilibrium range the waves are scale invariant. Instead of assuming weak non-linear behaviour linking frequency to wavenumber via the dispersion relation, it is assumed that each breaking crest has a range of Fourier components which all propagate at the same speed. Because the longer waves move faster, the time differential of the wave height will be greater for the longer waves than for the shorter ones and the discontinuity will appear greater. This means that the frequency spectrum will be dominated by the largest breaking waves with the energy from smaller breakers being too insignificant to affect the shape of the spectrum. Using these ideas, Belcher and Vassilicos found that the frequency and wavenumber spectra varied as,

$$\psi(k) \propto k^{-4} \qquad 3\text{-}47$$

$$H(\omega) \propto \omega^{-4} \qquad 3\text{-}48$$

In addition to the spectra presented above, there have been many other measurements which have provided other options for the wavenumber height spectrum. These include the work of Lee *et al.* (1992) which found the spectrum varied as k^{-6}.

Recently, a number of scanning laser slope meters have been developed which are capable of measuring the full two-dimensional wavenumber spectrum and the frequency spectrum. At present they all assume that the wave field is stationary for a very short period of time over which a scan of the surface is made. This introduces some errors into the data but they do show the relationship between the wavenumber and frequency spectra. This information is very important because, in general, most high frequency instruments, such as the Laser Slope meter, record frequency spectra with wavenumber spectral measurements lagging behind in resolution. In order to obtain spatial information from such data it is necessary to know accurately how to convert between the two types of spectra. Scanning devices, such as the one deployed by Hara *et al.* (1997), have shown that the along wind slope component is affected by the surface drift velocity and, for shorter waves, by advection by the orbital velocities of the long waves. This causes the relationship between ω and k to deviate from that given by the gravity-capillary dispersion relation. The cross wind component follows the gravity-capillary dispersion relationship closely.

3.8 Discussion

This chapter has provided a detailed look at the theoretical and experimental knowledge of the background wind wave field as it is known today. It has been seen that there are many areas in which further research is needed before a full description of the ocean is available. In this thesis, some of these areas will be explored further. Chapters 5, 6 and 7 concentrate on measurements of the ambient wind wave field with the Laser Slope meter, both in the field and in the UCSB wind wave facility, comparing and contrasting these new results with those presented above. In particular, attempts are made to verify results and extend the available data to a higher range of wave frequencies than has been done previously. However, the emphasis of this research is not purely the extension of these results, but is intended to explore the kind of results which are available with this Laser Slope meter. Therefore, particular care will be given to the determination of results *from this instrument*, comparing and contrasting the practicalities of deployment and analysis with other instrumentation and highlighting its advantages and disadvantages. An attempt will also be made to compare data collected both in the field and in a wind wave tank with *the same* instrument. This is not possible with most kinds of instrument as they can only be deployed

in one type of environment. This puts the Laser Slope meter at an advantage over many other types of measuring techniques.

Chapter 4

The kinematics and dynamics of surface wave – surface current interactions

4.1 Introduction and scope of chapter

In this chapter the interaction between a horizontally varying surface current and a surface wind wave field is examined. This type of interaction is of interest because regions of surface straining have been found to produce areas of convergence and divergence within a wave field that can be imaged by air- and space-borne SAR. Consideration is given only to those cases in which the current varies slowly over the length and time scales of surface wind waves with which it is interacting. This means that, apart from wave growth, dissipation and wave-wave interactions, the total action of the system may be assumed to be conserved.

Initially, a review is presented of the ocean processes which may lead to a horizontally varying surface current. These include:

- tidal flow over bathymetry;
- fronts / upwelling;
- internal waves;
- swell.

The governing equations of the kinematics and dynamics of the surface wave – surface current interactions are presented followed by a discussion of the derivation of the wave action equation. This equation describes fully the interaction processes as they are currently understood, allowing for different forms of the growth, dissipation and non-linear wave-wave interaction terms. A review of possible forms of the wind growth, dissipation and wave-wave interaction terms is given including a discussion of the results found by

previous researchers using a variety of terms and solution methods. Finally, areas in which further research is still needed are highlighted.

4.2 Possible generation mechanisms of surface currents

Currents may be generated in the ocean by a number of mechanisms. Perhaps the most familiar of these are tidal currents. These are very large scale currents generated by the gravitational forces associated with the sun and the moon. In general, the spatial and temporal variation of these currents is so slow and over such long length scales that the only effect they have on the surface is to uniformly increase or decrease the speed of travel of the surface waves. The currents which are of interest here are those which vary slowly, but noticeably, in space or time so that the straining of the surface waves caused by the current can be seen as a change in the energy and wavelength of the surface wind waves. Under certain circumstances, however, even tidal currents may be able to generate a significant surface strain if the magnitude of the current is caused to vary by a secondary parameter.

One mechanism by which the tidal current may vary is if the sea bed contains large variations in depth. Such changes in the bathymetry will cause the speed of the flow over the bottom to vary in such a way as to keep the fluid flux a constant. This essentially means that the number of fluid particles travelling over the topography through a sequence of plane parallel vertical cross sections must be conserved. In general, the change in the mean water level at the surface is negligible and so if the water depth is less in some region, the fluid must flow faster in order to conserve the amount of fluid flowing over the bed. If the depth changes significantly, then so too will the surface current, and a strain will be created at the surface which is capable of causing large changes in the surface wind wave field. Such variations can be seen clearly in SAR satellite imagery as regions of enhanced and reduced backscatter. A schematic diagram of the surface roughness created and approximately how this may be imaged is given in figure 4-1.

Research is in progress currently to determine the relationship between the sandbank, the tide and the current variations over the sandbank, and the relationship between the current pattern and the radar image intensity. One of the regions used by DERA for their research

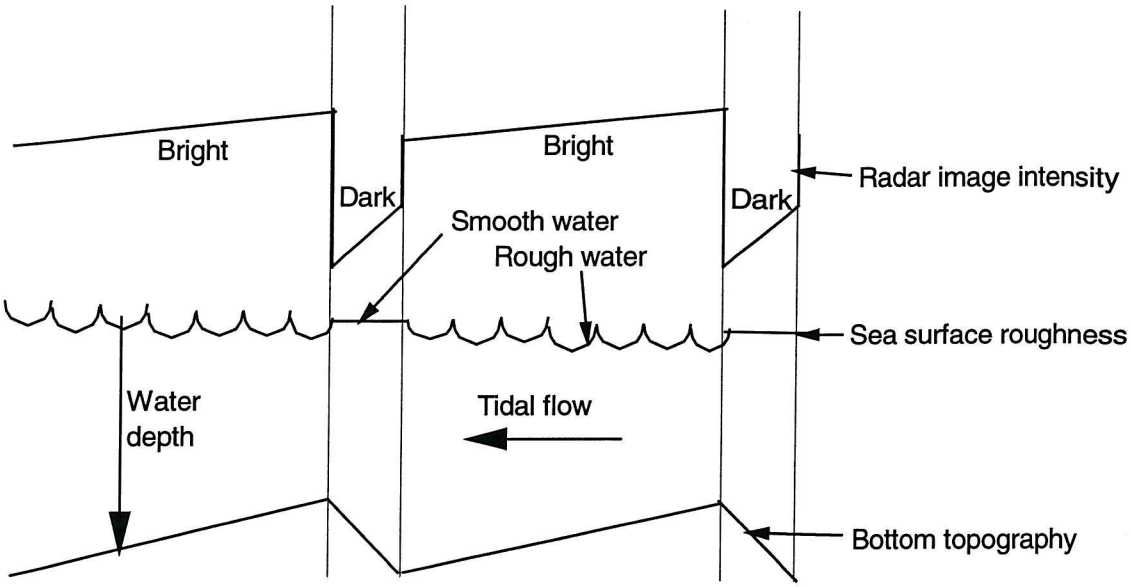

Figure 4-1: Schematic diagram of how a sand bank may be imaged

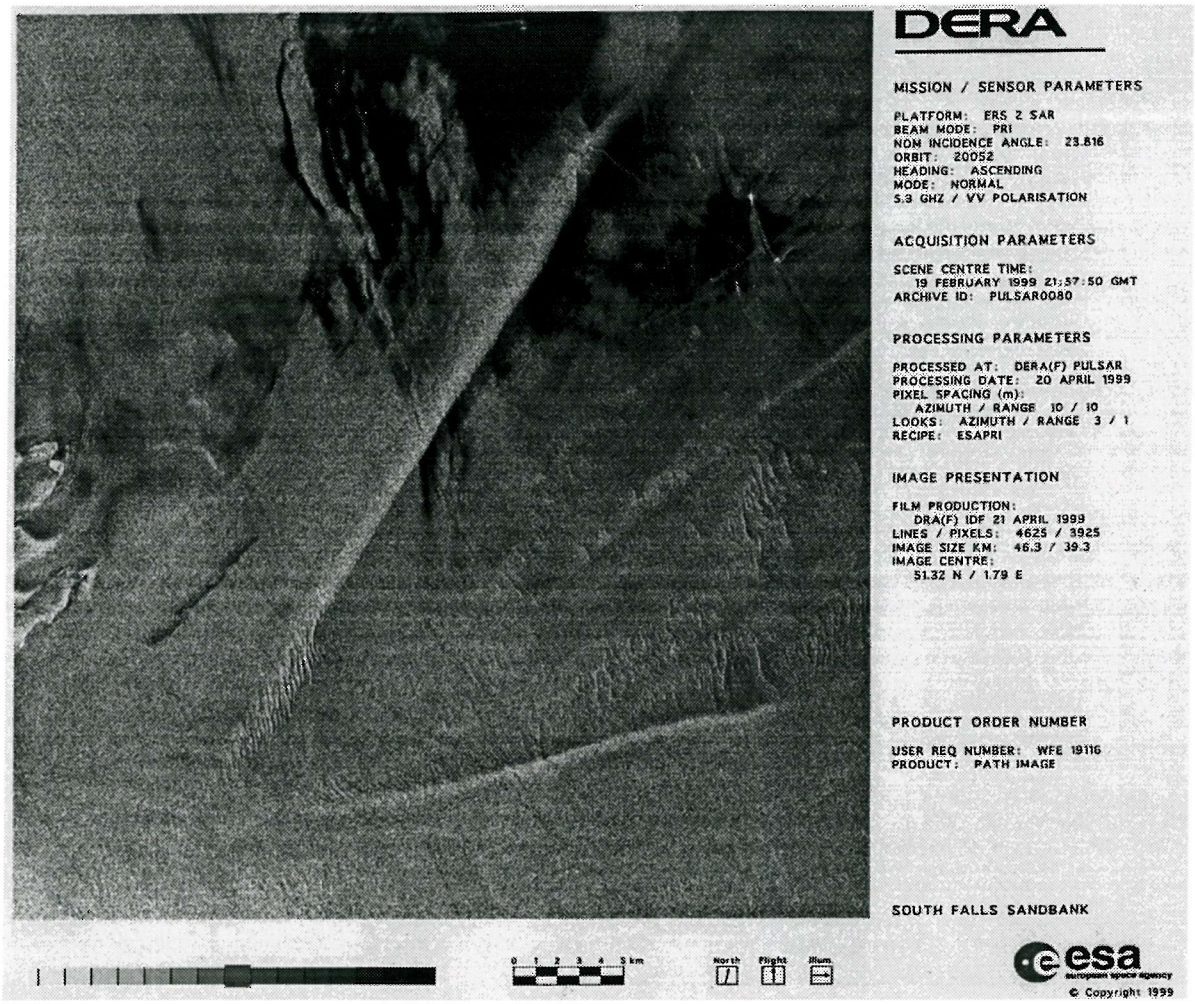

Figure 4-2: Section of SAR image of the South Falls sand bank. Also seen in the image are other sand ridges, sand waves and regions of very calm water.

is the South Falls sand bank, pictured in figure 4-2. DERA use specialist measuring equipment to determine the currents over the bank at a range of depths during satellite passes which collect imagery of the scene. Knowledge gained of the interaction processes and relationships will eventually be of use in monitoring movement of soft substances in the ocean bed, as well as being applicable to imaging other ocean phenomena which create similar surface features.

A front occurs when two different types of water bodies meet. On a small scale these can be where a river may flow into an estuary or where a channel of water enters the coastal region of the open sea. On a larger scale, over the continental shelf, stratified coastal water created by relatively fresh water from rivers and estuaries lying on top of the denser coastal water, may meet vertically mixed oceanic water. In the deep ocean, fronts will occur between water masses with different properties. Where the water masses meet, the denser water tends to travel beneath the less dense water as shown in figure 4-3. This can create circulation of the water in the frontal region which may lead to regions of upwelling (not shown in diagram). One of the ways in which a front can be observed is because of the strain at the surface associated with horizontally varying currents due to the different velocities of the water masses. Additionally, there may be a colour difference due to the nutrients brought to the surface and a temperature difference, both caused by the upwelling, as well as floating debris or foam, the latter of which is produced at the convergence (Bowden, 1983). A SAR image showing a front is displayed in figure 4-4.

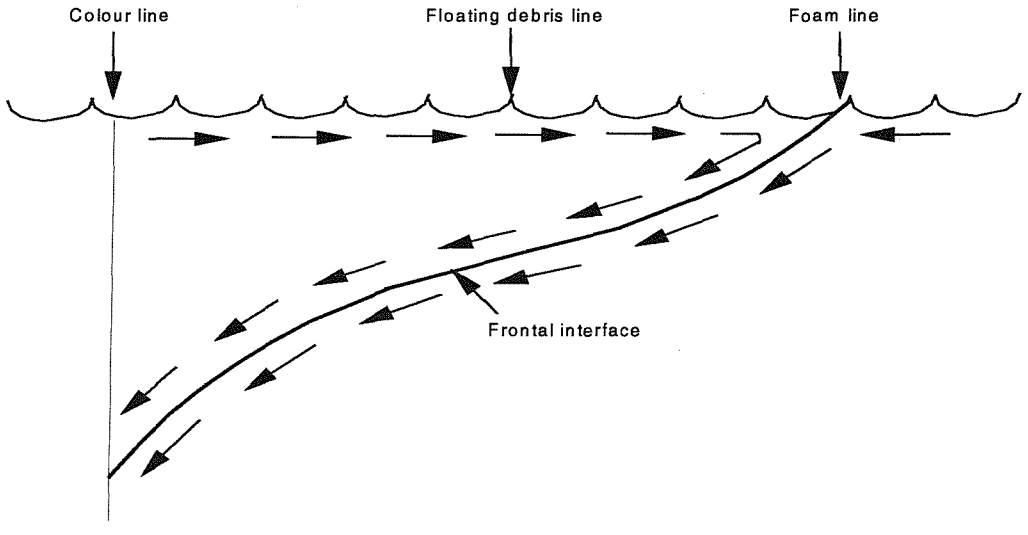

Figure 4-3: Schematic of the surface currents generated at an ocean front and other features of interest in imagery of frontal behaviour

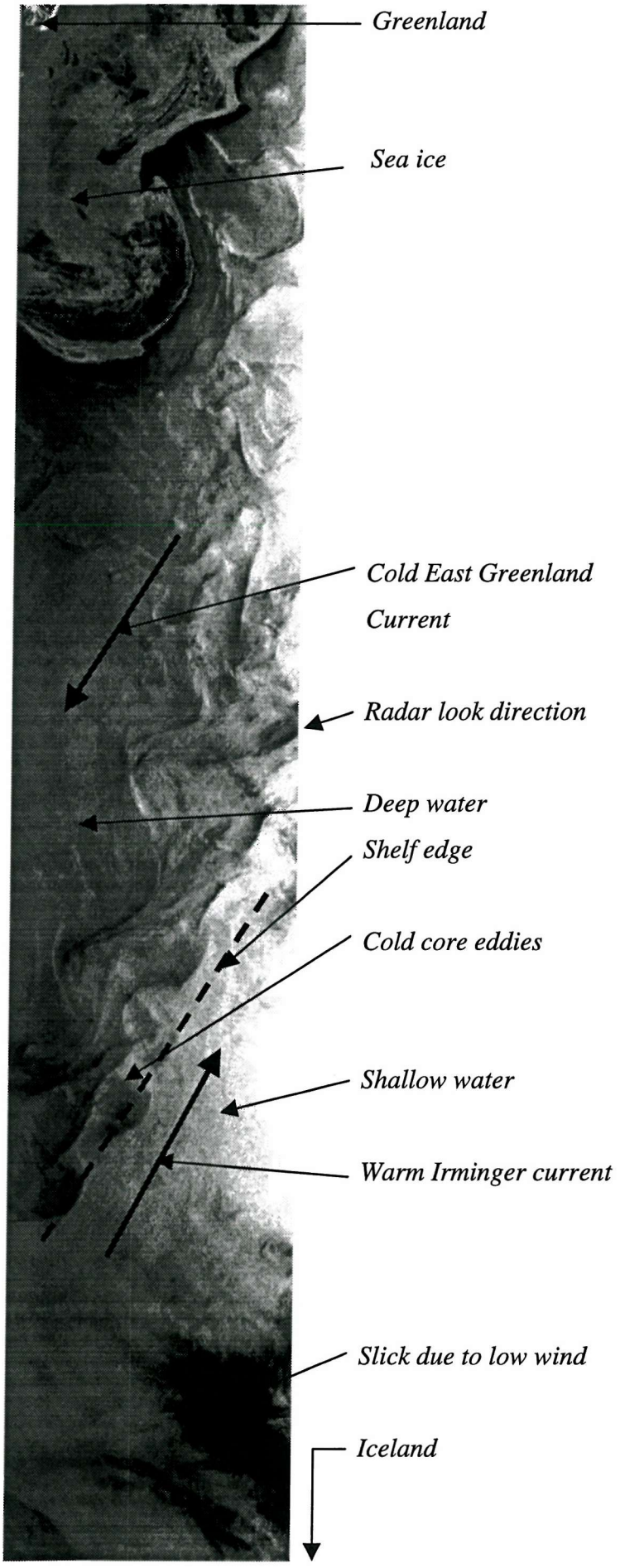

Figure 4-4: SAR image of an ocean front in the Denmark Strait. Image data from ERS-1 satellite, descending pass, orbit no. 6195, 21/09/92, processed by DERA, Information obtained from Brownsword (2000)

Within many regions of the ocean, there is a tendency for the surface layer of the water to become warm due to thermal heating from the sun, as only a small amount of the absorbed energy is lost through conduction and radiation. Wind stress and wave action cause mixing within the upper ocean region extending down to several tens of metres. Beyond this depth, the wind and waves have little effect. At the bottom of this mixed layer a sharp density gradient exists between the mixed layer and the colder ocean water below. As the thermocline starts to grow it becomes more stable than the surrounding water which tends to reduce the mixing between the upper and lower layers, increasing the gradient further (Bowden, 1983).

Similar effects can also be generated in coastal regions where relatively fresh estuarine water sits on top of the dense ocean water. Here, the density gradient is generated due to the change in salinity. This is also observed in regions where large amounts of ice melt, diluting the surface layer of the ocean, and in Scottish sea lochs where fresh (less dense) rain water runs off the hills into the Lochs where it lies on top of the salty (more dense) sea water. Many areas of the ocean have a complicated stratification due to a combination of these effects.

In regions of the ocean containing strong density gradients, any instability in the water column may lead to the production of a lesser known phenomenon called internal waves. In the same way that surface waves are formed on the air-water interface where there is a sharp density change, internal waves may be formed within a body of water where a density variation exists. The amplitude of the internal wave varies with depth, depending on the strength of the density stratification at each point. In order to create an internal wave, a body of water must be vertically disturbed from its equilibrium position. In returning to equilibrium, the body overshoots and sets up an oscillation which radiates away from the source of generation. Where there is a region with a sharp thermocline, the internal waves can become trapped within this layer and propagate horizontally. The fluctuations of the wave cause an oscillatory motion within the water column which leads to a variable surface current creating areas of convergence and divergence at the water surface, as is illustrated in figure 4-5. The convergence and divergence causes a very small change in surface height but is mostly apparent as a varying surface current.

An internal wave can be generated in a number of ways. The hull of a ship moving through a shallow stratification causes a displacement of water that may generate a spectrum of internal waves as the ship passes. The internal waves from a ship are known as the internal wave wake. This wake is often much larger and propagates for much longer than the commonly known surface, or Kelvin, wake of the vessel. The third type of wake generated is the turbulent wake. All three types of wake can be observed in radar images of the ocean.

Where stratified water exists, tidal flow may cause a disturbance to the equilibrium by forcing the water over an ocean ridge. In figure 4-6 a SAR image of an internal wave is displayed. At the boundary between the Meditteranean Sea and the Atlantic Ocean a front exists with the warmer (although more saline due to evaporation) sea water lying on top of the colder and more dense ocean water (hence there is a strong stratification). This front is moved back and forth by the tidal current over the top of a sea bed ridge situated right at the entrance to the Meditteranean Sea. This ridge causes a disturbance in the pycnocline which in turn leads to the creation of a train of internal waves propagating out into the Meditteranean Sea.

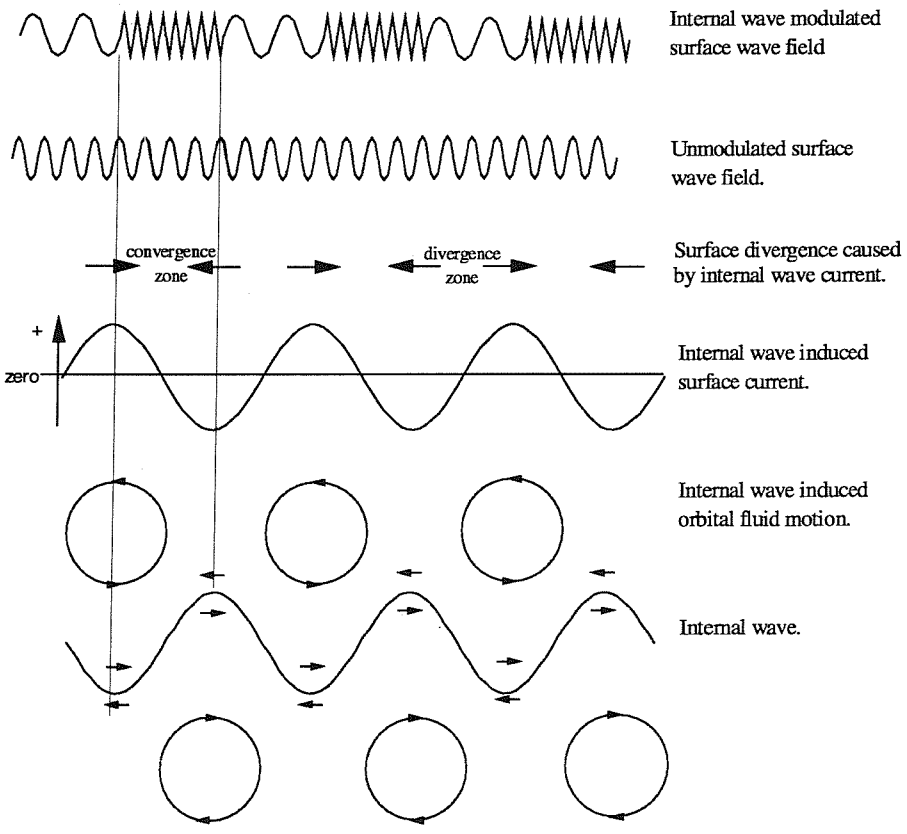

Figure 4-5: The mechanisms by which an internal wave affects a surface wind wave field

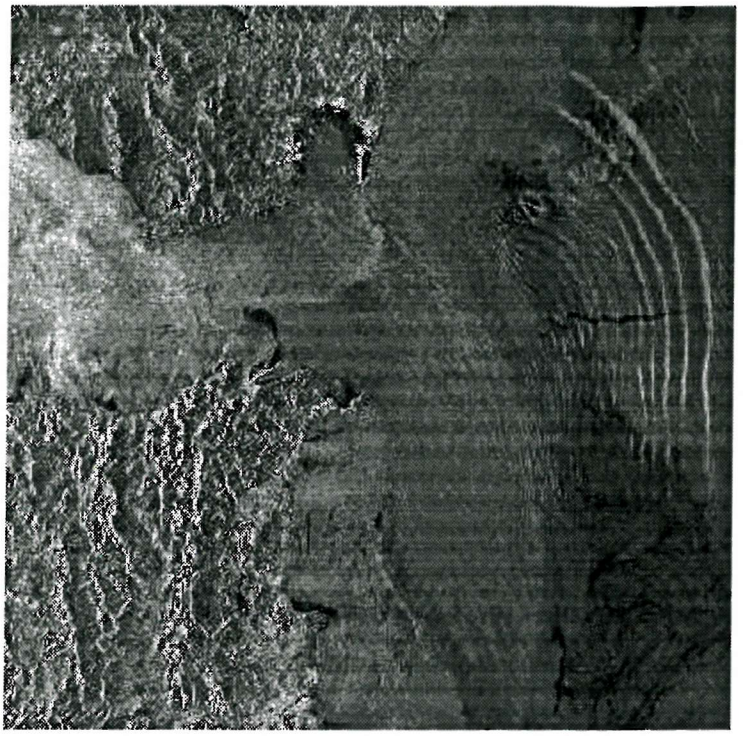

Figure 4-6: This is an ERS-1 SAR image (approx. 90km x 90km) of the Strait of Gibraltar, acquired on January 1, 1993, 22:39 UT. It shows pronounced signatures of an eastward travelling internal wave train. Another interesting feature is the dark streak across the internal wave field, which looks like a typical signature of an oil spill.

A fourth interaction method which can be treated as a surface current interacting with a surface wind wave field, is the interaction between surface waves of very different length scales. If a surface wave has a period and wavelength very much larger than the surrounding waves in the wind wave field, such as is the case with very long swell waves, then the horizontal component of the orbital velocity of the long wave can be considered as a surface current interacting with the shorter waves. Such interactions can be studied in exactly the same way as above examples, except that as the vertical component of the orbital velocity is also appreciable, the effective gravity felt by the shorter waves must be modified to take account of the accelerations of the long wave. In addition to this, the finite amplitude also causes other imaging effects such as "velocity bunching" and "azimuth smear".

Figure 4-7: Image of swell waves in the Straits of Gibraltar. The swell is the grainy lines seen throughout the image but particularly near the bottom of the image oriented NNE. This image was collected for and processed by DERA. It is a Radarsat SAR image collected on 18/12/97 at 18:11:09 GMT, beam mode W1, nominal incidence angle 20-31, ascending, 5.3GHz, HH polarization, pixel spacing 15mx15m, scale of 1cm=3.15km.

In this chapter no further consideration will be given as to the particular method by which the current is generated. Instead, it will be assumed simply that there is a varying horizontal current, which is interacting with a surface wind wave field. Apart from a brief discussion in the next section, no account will be taken of any component of vertical velocity or acceleration. The derivation of the action balance equation is discussed, which allows a calculation of the effect of the current on each wavenumber component of the surface wind wave field, taking into account growth and dissipation. Previous solutions to this equation are presented highlighting their limitations and aspects that require further research. This research is continued in chapters 8 and 9 after the presentation of measurements of the ambient surface wind wave field.

4.3 Fundamental equations of surface wave - surface current interactions

4.3.1 Introduction

The effect of a varying surface current on a surface wave field was first correctly calculated by Longuet-Higgins and Stewart (1960). They showed that the results of Unna (1947) were flawed as he had neglected the work done by the longer waves against the radiation stress of the short waves. He also assumed that the sum of the potential and kinetic energies was conserved in an accelerated frame of reference. For the case of currents due to deep water waves, these two mistakes exactly cancelled whereas, in general they do not cancel.

If second order terms for wave motion are considered, it is found that the waves have a horizontal momentum which is not discovered if only first order solutions are considered (LeBlond and Mysak, 1978). These momentum terms indicate that there is a horizontal stress created at the water surface, known as the radiation stress. If a varying horizontal current is also present at the surface, it has the effect of stretching and compressing the surface waves as the surface is accelerated and decelerated in the horizontal plane. Because of the radiation stress, work must be done by the surface current against this stress and this work appears as additional energy in the surface waves. If the varying current is caused by a long wavelength surface wave or by another form of varying surface displacement the short surface waves will also experience vertical accelerations. As there is no component

of radiation stress in the vertical plane, there will be no additional work performed against the radiation stress due to the vertical motion.

However, in the accelerating frame of reference the vertical accelerations do cause a change in the effective value of gravity felt by the surface waves. The overall energy of the surface waves, as seen in the accelerating frame, is increased over the value for a stationary system in a stationary frame because the effective gravity is increased. Also, for a given amount of energy, the maximum amplitude of the surface waves will be greater or smaller due to the decreased or increased effective gravity, respectively.

It is clear that the total energy of the surface wave system is not conserved due to its interaction with the surface current which causes energy exchanges. Bretherton and Garrett (1969) have shown that the equations, which describe the changes in the energy of the surface wave system in the accelerated reference frame, can be written in a more simple form by using a quantity called "action". Action is equivalent to the energy in a particular intrinsic frequency divided by that angular frequency. The changes in energy of the system as measured in the accelerated reference frame vary in the same way as the angular frequency as measured in the accelerated reference frame. Therefore, action, rather than energy, is conserved in systems such as this, provided wave growth, dissipation and wave-wave interactions are ignored. The wave action equation takes into account all the above phenomena and can be used to calculate the variation of action spectral density of the surface waves due to the surface current.

The wave action equation uses the knowledge that action is conserved to follow a wave packet around a surface wave field. The action of the packet in the accelerated reference frame is a constant at all times. As the packet experiences changes in the surface current, its wavelength is changed. In the accelerated frame, the packet continues to move with the group velocity determined by the normal dispersion relation and the new wavelength. Looking at the accelerated system from a stationary reference frame, the packet moves with the sum of the group velocity, as calculated in the accelerated frame with the new wavelength, and the current velocity. Therefore, as viewed from the stationary reference frame, the dispersion relation has been altered.

Action conservation is not true where there are other effects such as wave growth and dissipation. Other authors, for example Hughes (1978), Alpers and Hennings (1984), Alpers (1985) Phillips (1984), Perry (1988) and Miller and Shemdin (1991) have considered some of these effects and primitively modelled how they will affect the surface roughness.

4.3.2 Kinematic equations

The equations which describe the kinematics of the surface wave trains in the presence of a slowly varying surface current were originally developed by Ursell (1960). They describe the refraction of the surface waves caused by the surface current. For waves with a wave vector, $\underline{k}$, and intrinsic angular frequency, $\omega = \sqrt{gk + \frac{Tk^3}{\rho}}$, where $k = |\underline{k}|$,

$$\underline{\nabla} \wedge \underline{k} = 0 \qquad 4\text{-}1$$

$$\frac{\partial \underline{k}}{\partial t} + \underline{\nabla}(\omega + \underline{k}.\underline{U}) = 0 \qquad 4\text{-}2$$

where $\underline{U}$ is the vector surface current. Equation 4-2 states that the rate of change of the wave vector is balanced by the flux of wave crests past a point. Therefore, wave crests are conserved.

4.3.3 The wave action equation

Bretherton and Garrett (1969) have shown that for a wave train of energy density E moving in a region with a current U, the dynamics of the system can be represented by,

$$\frac{\partial}{\partial t}\left(\frac{E}{\omega}\right) + \nabla.\left\{(U + c_g)\frac{E}{\omega}\right\} = 0 \qquad 4\text{-}3$$

This equation was shown by Whitham (1974) to be equivalent to the equation developed by Longuet-Higgins and Stewart (1960) which showed that the change in energy was due to the work done against the radiation stress.

Generalising to a whole spectrum of wind waves, where $\Psi(\underline{k})$ represents the wave height spectrum, the energy contained in a spatial unit area and wavenumber area $\delta k_1 \delta k_2$ is given by 4-4 where E is the spatial energy density, or energy per unit area. The energy can also be related to the action spectral density, $N(\underline{k})$, that is, the action per unit spatial area per unit wavenumber area.

$$E = \rho g \Psi(\underline{k}) \delta k_1 \delta k_2 = \omega N(\underline{k}) \delta k_1 \delta k_2 \qquad 4\text{-}4$$

Therefore, the action spectral density is related to the wave height wavenumber spectrum by,

$$N(\underline{k}) = \frac{\rho g}{\omega} \Psi(\underline{k}) \qquad 4\text{-}5$$

Substituting $N=E/\omega$ into 4-3, Phillips (1977) and Hughes (1978) have shown in different ways that,

$$\frac{dN}{dt} = \frac{\partial N}{\partial t} + \frac{\partial N}{\partial x}\frac{dx}{dt} + \frac{\partial N}{\partial k}\frac{dk}{dt} = 0 \qquad 4\text{-}6$$

This means that in the absence of growth, dissipation and wave-wave interactions, the total time differential of the action is zero. Therefore, action is conserved.

4.3.4 The action balance equation

4.3.4.1 Specification of equation

Equation 4-6 takes no account of any effects on the action of growth, dissipation or non-linear interaction. To take account of these effects, the full action balance equation is assumed to read as,

$$\frac{dN}{dt} = N_G + N_D + N_{NL} = \Lambda \qquad 4\text{-}7$$

where, N_G represents wave growth, N_D represents viscous dissipation and wave breaking and N_{NL} represents non-linear wave-wave interactions.

4.3.4.2 Discussion of terms

There are two main types of wave growth; initial growth and exponential growth. These types were described in chapter 3 and are summarised here. Initial growth is a linear process that occurs where there are no waves present. In this model, those surface waves which travel at the same speed as the turbulent forcing function will be acted on for longer than other surface wave components and so will grow more rapidly This is called the resonance model which was first developed by Phillips (1957). To complement the resonance model, there is the feedback mechanism developed by Miles (1957). If the sea surface is already wavy, it can cause a waviness in the airflow above it. In return, the forcing from these pressure fluctuations acts on the wave creating them causing exponential growth. In reality there will be a combination of the two models acting to cause wave growth. The exact balance is not known and will depend upon the particular conditions.

Surface waves may also lose energy by a number of mechanisms. One of these is by internal dissipation due to viscous effects. In the linear theory, for a particular wavenumber, k, there is a proportional dissipation of wave energy per unit time of,

$$4\nu k^2 \qquad 4\text{-}8$$

where ν is the kinematic viscosity of water (Lighthill, 1979).

Breaking will occur at the point where the particle velocity at the wave crest exceeds the wave velocity. When this happens, the wave crest will become unstable and will break. This leads to the assumption that there will be some critical wave amplitude beyond which no further growth may occur. This simple idea led to Stokes' limiting waveform (Stokes, 1880) having a maximum crest angle of 120°. Previous authors have assumed more than one type of form for the breaking term and these are described below.

Wave-wave interactions rearrange the energy within a wave spectrum between different wavenumbers. Interactions may occur between three or more wave components at one time (Phillips, 1977). Hasselman (1962) has shown that wave-wave interactions may be represented by a collision integral. Longuet-Higgins later showed that the rate of energy

transfer was proportional to N^3k^6. According to Perry (1988), these transfer rates are greatest at the spectral peak and the transfer occurs both towards lower and higher wavenumbers. This decreases the action at the spectral peak, but increases the action elsewhere in the spectrum.

4.4 Discussion of previous attempts to solve action balance equation

The various studies are presented below in chronological order to provide some indication of how the research has progressed over the years and where there is a need for further research.

To represent Λ in 4-7, Hughes (1978) considers an expansion of Λ in powers of N, as given in 4-9. Each term was related to one of the real physical phenomena occurring within the wave field, described above.

$$\Lambda = \alpha + \beta N - \gamma N^2 .... \qquad 4\text{-}9$$

α represents Phillips resonant growth which Hughes ignored as the effects are only important if the entire wave field is effectively extinguished by the internal wave which is not a common occurrence. The second term represents Miles-Benjamin exponential growth. The remaining terms in the power series represent dissipation. Here Hughes used the leading term only to represent a non-linear limitation to the growth. This term does not account for the overshoot effect but will provide an upper limit to the spectral value.

$$\frac{dN}{dt} = \beta N - \gamma N^2 \qquad 4\text{-}10$$

Considering that Λ=0 at equilibrium, Hughes' formulation means 4-10 can be re-written as,

$$\frac{dN}{dt} = \beta N\left(1 - \frac{N}{N_B}\right) \qquad 4\text{-}11$$

Where N_B is the ambient value of the action density at each wavenumber, k.

Hughes solved this equation for a small current approximation in the case of internal waves causing the surface current variations. The current pattern was assumed to be stationary with respect to the internal wave phase speed. He defined a sensitivity and a phase by correlating perturbations of slope variance with phase-shifted current values. The phase was defined as the phase shift that maximised the correlation and the sensitivity as the corresponding regression slope. Theoretical results from these linearised solutions to 4-11 were compared with experimental measurements in the Georgia Straits using a laser slope meter. Good agreement was found between the sensitivities but poor agreement between the phases, although the correct quadrant was predicted.

Alpers and Hennings (1984) considered solutions to the action balance equation of the form given in 4-12.

$$\frac{dN}{dt} = \left(\frac{\partial}{\partial t} + \frac{d\underline{x}}{dt}\frac{\partial}{\partial \underline{x}} + \frac{d\underline{k}}{dt}\frac{\partial}{\partial \underline{k}} \right) N = -\mu \delta N(\underline{x}, \underline{k}, t) \qquad 4\text{-}12$$

Therefore, the action would decay back to its original value exponentially where the rate was determined by the amount of dis-equilibrium caused in the system by the current and the relaxation time, $1/\mu$ (μ is the relaxation rate). i.e. the amount of time taken for the waves to regenerate. By assuming that $N(\underline{x}, \underline{k}, t) = N_B(\underline{k}) + \delta N(\underline{x}, \underline{k}, t)$ and $U(\underline{x}, t) = U_0 + \delta U(\underline{x}, t)$, and ignoring very small terms, Alpers and Hennings derived an equation for the changes to the action wave field,

$$\left(\frac{\partial}{\partial t} + (\underline{c}_g + \underline{U}_0)\frac{\partial}{\partial \underline{x}} + \mu \right) \delta N = \underline{k}.\frac{\partial \underline{U}}{\partial \underline{x}}.\frac{\partial N_B}{\partial \underline{k}} \qquad 4\text{-}13$$

They produced a solution to compare with the observed surface roughness due to surface currents by considering the relative balances of the three relaxation times in the left hand side of equation 4-13, depending on the phenomenon causing the surface current. They argued that for a sand bank, the first two terms on the left hand side of 4-13 would be much smaller than the third and therefore retained this term only. Then, assuming a Phillips

spectrum of $k^{-7/2}$, which is equivalent to an action spectrum of k^{-4}, for gravity waves, and writing $\delta\sigma = \sigma - \sigma_B$ as the deviation from the background radar cross section, σ_B, they derived an equation that directly related the variation in radar cross section to the strain rate at the surface,

$$\frac{\delta\sigma}{\sigma_B} = \frac{\delta N}{N_B} = \frac{\delta E}{E_B} = -\left(4 + \frac{c_g}{c_p}\right)\frac{1}{\mu}\frac{\partial U_x}{\partial x} \qquad 4\text{-}14$$

This equation has been widely used in relating radar backscatter to current generated surface patterns. The modulation transfer function (MTF) is defined such that,

$$\frac{\delta\sigma}{\sigma_B} = \mathrm{MTF}\frac{\partial U}{\partial x} \qquad 4\text{-}15$$

Phillips (1984) considered a solution to equation 4-7 to improve understanding of imaging of internal waves. Since Bragg scattering of radar waves produces images by "seeing" changes only in a particular wavenumber in the surface wave field, Phillips rewrote equation 4-7 to provide results describing the changes in the surface wave energy at a fixed wavenumber. In deriving the equation he defined a parameter, $b=B(k)/B_0(k)$ where $B(k)=k^4\psi(k)$ which has become known as the degree of saturation and also assumed that variations in B(k) with respect to k and ϕ (the angle between the wind and k) could be ignored. He used a form of Λ that was similar to the one used by Hughes (1978), 4-10, except that the limiting term was written as a cubic to represent a wave breaking term, determined theoretically on dimensional grounds in Phillips (1985). Terms for wave-wave interactions and viscous effects were assumed to be insignificant when compared to wave growth and breaking effects.

$$\Lambda = \beta N - \delta N^3 \qquad 4\text{-}16$$

Considering that Λ=0 at equilibrium, Phillips formulation means 4-7 can be re-written as,

$$\frac{dN}{dt} = \beta N\left(1 - \frac{N^2}{N_B{}^2}\right) \qquad 4\text{-}17$$

The form for the current was assumed to be,

$$U = \frac{U_0}{2}\left(1 + \tanh\left(\frac{x}{L}\right)\right) \qquad 4\text{-}18$$

where L was taken to be the length scale of the internal wave, so that the theory is non-dimensionalised. Some example cases were computed with the approximations given above.

Alpers (1985) performed a small study which extended the work of Alpers and Hennings (1984). The relative strengths of the relaxation, advection and local time terms were discussed with reference to internal waves and surface swell waves. He showed that internal waves can be approximated in the same way as sand banks, provided they are of a long period, whereas, for swell waves, the local time is more important leading to,

$$\frac{\delta\sigma}{\sigma_B} = \frac{\delta N}{N_B} = \frac{\delta E}{E_B} = -\left(4 + \frac{c_g}{c_p}\right)\frac{1}{\omega}\frac{\partial U_x}{\partial x} \qquad 4\text{-}19$$

where ω is the radian frequency of the swell waves.

Thompson and Gasparovic (1986) studied internal wave signatures during the SARSEX experiment. The results for L (24cm) and X (3.2cm) band radar were compared with action balance theory written as 4-11. The theory was found to predict the L band return well but under predicted the return at X-band wavelengths. They showed that returns from metre-scale waves were of the magnitude measured at X-band and hence suggested that the shorter scale waves were generated by wave-wave interactions directly from the metre-scale waves.

Perry (1988) used the action balance equation derived by Phillips (1984), also solving it for a constant surface wavenumber. Here he used a current of the form,

$$U = U_0 \sec h^2\left(\frac{x}{L}\right) \qquad 4\text{-}20$$

which is the limiting form for an internal soliton. The action balance equation was solved numerically so that the variation in the action spectral density relative to its ambient value could be studied for variations in the different parameters. He uses an action spectrum of k^{-4}, which is equivalent to an energy spectrum of $k^{-\frac{7}{2}}$.

Hwang and Shemdin (1990) considered solutions to the action balance equation with,

$$\Lambda = \beta N - \beta_d N^{p+1} \qquad 4\text{-}21$$

where β represents the Miles exponential growth discussed earlier and β_d is a constant for the decay term and p determines the rate at which the decay occurs (assumed to be either 1 or 2 by the above authors). They considered the effect of different parameters on the resultant variations in action spectral density using a background energy spectrum of $k^{-\frac{7}{2}}$. In particular, their results demonstrated that the particular specification of p is very important in the correct determination of the variations. Different relaxation terms were also considered, as well as how the effects of short scale current interactions may differ from the effect of longer scale current interactions, such as the current produced by natural internal waves.

Miller compared theoretical predictions and experimental results of the modulation of short surface waves by longer surface waves. She considered the variation of the surface slope variance (Miller *et al.*, 1991) and spectral components (Miller and Shemdin, 1991) caused by the interaction. The experimental results were obtained in a wind wave tank using a laser slope meter to record the variations in surface wave slope. The results were compared with theoretical predictions based on the work of Longuet-Higgins and Stewart (1960), assuming that the variation in the amplitude and wavenumber was caused by the surface current in the absence of any wind growth or dissipation. Theoretically calculated surface slope variance variations fitted the data less well as the wind speed increased. As the data were collected using a stationary laser slope meter, the two components of surface slope were used to generate a form of the wavenumber spectrum. In doing this, the gravity-

capillary dispersion relation was assumed to apply, modified by the surface drift current. More recent experiments, (Hara *et al.,* 1997) have shown that this is not the case for short wavelengths as they are advected by the orbital velocities of the longer waves. Miller used 4-9 as the form of action balance equation for comparison with the data. She found the MTF to be approximately 2-3 times that predicted by the model and to increase with wind speed. Phase agreement was also found to be unsatisfactory.

Recently, a model has been developed (SWAN – Simulating Waves Nearshore (Booij *et al.*, 1999)) which uses numerical techniques to solve the action balance equation to describe the evolution of the wave spectrum. This model is based around an extension to the ideas used in the WAM model (WAMDI Group, 1988) which considered waves in deep and intermediate-depth water, to gain understanding of the effects in shallow depth with ambient currents, as is often found in coastal areas. The model considers the propagation of wave energy, while taking into account the processes of generation and dissipation such as wind generation, whitecapping, triad and quadruplet wave-wave interactions, bottom friction and depth-induced wave breaking. The model has been compared with data and is generally found to represent the results well, although the tests have not been entirely conclusive. It represents fairly well the state of the art in coastal wave modelling.

4.5 Summary and discussion

In this chapter a review has been given of the research conducted over the last 20 years with the objective of explaining how features such as swell, bathymetry, fronts and internal waves can be imaged by SAR. What all these ocean phenomena have in common is that they generate horizontal currents at the water surface which modulate the background wind wave field. The radar backscatter is related to the amount of energy contained in a wavenumber component; as this varies, the image intensity varies and so a characteristic pattern is formed in the image. For swell waves, there are many other factors that also influence the way they are imaged.

The action balance model has been developed to describe changes in a system where the dispersion relation is changing slowly. For a slowly varying current, this model is appropriate. The main assumption is that, in the absence of growth, decay and wave-wave

interactions, and in a weakly varying current, the action of a wave packet is conserved. The variation of the action of a wave packet caused by growth, decay and wave-wave interactions can be modelled by including other terms in the action balance equation.

Various authors have attempted to solve the action balance equation using essentially the same form of equation but with different forms of Λ, the term representing the growth, decay and wave-wave interactions. Currently, there is still considerable debate about which form should be used. Alpers and Hennings (1984) model is widely used in terms of relating the radar backscatter to the surface strain rate via a modulation term. It assumes that the modulations only cause small variations from the equilibrium value of the surface wave spectrum. The forms used by Hughes (1978), Phillips (1984) and Perry (1988) are similar, having only a different power for the breaking term. They make assumptions which imply a simple relationship between the relaxation rate and the growth rate. The power of the breaking term is still in debate, and as Hwang and Shemdin (1990) have shown, the power of this term has a large effect upon the resulting action spectral density variations. The recent work by Miller *et al.* (1991) and Miller and Shemdin (1991) has attempted to perform experiments in controlled conditions so that a better understanding can be gained of the mechanisms causing the surface variations. However, as this work used swell waves to produce the surface currents, there are additional factors causing surface roughness variations which make the results less applicable to the larger scale ocean phenomena.

The main experimental element which has been missing from the research performed so far is a series of experiments which aim to measure the surface roughness changes associated with surface current – surface wave modulations, where the experiments are performed in controlled conditions with a full wind wave spectrum and the surface current is not generated by swell waves. In doing this type of experiment and in the data analysis, particular attention needs to be paid to:

- producing a surface current which is has temporal and spatial scale similar to (or at least approximately similar to) those features of interest in the ocean so that the physical mechanisms in the interaction are similar;
- measurements of high frequency and short scale parts of the wave spectra;
- using the true ambient spectra in the theoretical simulations so that the modulations can be modelled correctly;

- using terms to represent the growth, decay and wave-wave interactions of all terms in the spectrum in the action balance equation.

In addition to such laboratory experiments, further field measurements are necessary with the significantly improved equipment that is now available. In later chapters of this thesis, the research is aimed towards fulfilling some of these objectives. In chapter 8 a simple model is developed to solve the action balance equation which is used in chapter 9 to compare with the experimental data presented there. It would be advantageous for this research for the results from the experiment described in chapter 9 to be compared with the output to the SWAN model described above. This model would be able to describe the processes involved more accurately than the model developed in chapter 8, particularly as it would be able to account for wave-wave interactions, and would add further insight into the processes involved in the surface wave – surface current interactions.

Chapter 5

Loch Linnhe Experiment 1997: Statistical analysis

5.1 Introduction and scope of chapter

This is the first of two chapters which present analysis of the two-dimensional surface slope data collected during a field experiment in Loch Linnhe, Scotland, in which the TLS was deployed as part of a much larger experiment. Its intended role in the experiment was to measure the background wave field in the Loch and attempt to measure the effect of internal waves on the surface wave field. Due to the failure of an echo sounder for locating the internal waves beneath the TLS, no progress has been made towards this second objective. However, the data have been extensively analysed to provide information on the ambient wave field. In doing so, an assessment has been made as to how effective this type of instrument is in providing reliable statistical and spectral information about the ambient wave field. An attempt has been made to enhance current knowledge of the background wave field, and relationships between the open ocean, coastal waters and wind wave tanks have been studied. This analysis is presented in this chapter and chapter 6.

It was established in chapter 2 that laboratory tests of the TLS showed the instrument to be functioning correctly within certain error limits. The output from the TLS was also found to be consistent with visual observations of the water surface, and thus it appeared to be responding as expected to the surface wind waves. Therefore, the first objective for this experimental data set was to extract all possible statistical information about the background surface wave field in the Loch. In doing this there were a number of objectives:

- to assess the capability of the TLS in providing reliable surface slope statistical information;
- to compare these results with those of previous experiments to determine how statistical information varied between the open ocean, coastal waters and wind wave tanks;

- to compare these results with theory and to discuss current usage of theoretical methods.

In pursuit of these objectives, in this chapter a study of the following is presented:

- the two-dimensional probability distribution of the slopes in the surface wave field. Variations from the linear theory are examined and are compared with previous measurements in different ocean conditions;
- the variation of the mean square slope with wind speed;
- application of a suitable wind stress model to the wind speed measured in Loch Linnhe to allow for the variation of mean square slope with wind friction velocity to be plotted.

In the next chapter the analysis of this data set is continued. There, the research concentrates on assessing the potential use of the TLS for providing reliable surface wavenumber spectra.

5.2 Overview of experiment

5.2.1 General

The Loch Linnhe Experiment 1997 (LL97) (Gibson, 1997) was organised and run by DERA as part of their Ocean Imaging research programme. The overall aim of the programme is to further understanding of radar imaging of the ocean, and particularly of internal wave wakes. This experiment was one in a series of experiments over the last 12 years collecting data under differing conditions. The primary aim of this experiment was to obtain surface and in-water data coincident with low grazing angle and very low grazing angle radar images of the internal wave wake of a ship.

Various in-water instruments were deployed to support the analysis of the radar images (Hill and Lamont-Smith, 1997) of the internal wave wakes. These included a chain of Conductivity-Temperature-Depth (CTD) sensors (Knight, 1997a), a yo-yo-ing CTD sensor (Knight, 1997b), an Acoustic Doppler Current Profiler (ADCP) (Flatman, 1998), S4 current meters (Griffiths and MacDougall, 1997) and the TLS, which also included a meteorological station as part of its suite of instruments (Taylor, 1998). Additionally, photographs of the trials scene were taken from the hills beside the Loch and all the vessels

were tracked using DGPS (Meldrum and Peppe, 1997). The main experimental results are summarised in Gibson *et al* (1998).

5.2.2 Data collection by Towed Laser Slope meter

During the experiment the TLS collected 79 files of surface slope data under differing environmental conditions. Two different types of data run were used in order to meet the objectives described in the introduction: one involved the TLS being towed perpendicularly across the path of the wake generator, whilst in the other type of run the TLS was towed into the dominant wave direction. The first run type was to be used for comparison of the measured surface roughness patterns due to the internal waves with radar measurements of the same phenomenon. The second run type was included specifically for spectral analysis of the TLS data. Towing into the wind has been shown to reduce data ambiguities in spectral calculations (Taylor, 1997a) and is discussed in detail in chapter 6.

5.3 Assessment of the TLS for providing reliable statistical data

The TLS collects single point measurements of the two-dimensional slope of the water surface along a trajectory defined by the towing direction of the instrument. The prototype instrument used in Loch Linnhe sampled the water surface at 250Hz, thus making a measurement every 4mm, at a towing speed of 1m/s. Provided that sampling is continued for a significant length of time, and that no special towing direction is selected (e.g. along the crest of a swell wave), it is reasonable to assume that the surface slope will be sampled randomly for the purpose of calculating the slope probability distribution functions.

For accurate water slope data, inertial motions of the TLS need to be removed from the data so that the resulting water slope measurement is meaningful. Additionally, the heading of the catamaran must be known so that the data can be resolved along sensible axes. In the Loch environment, where the wind can vary spatially due to channelling by the surrounding mountains, care must be taken to ensure that the wind direction remains constant for the data section of interest.

5.4 Two-dimensional slope statistics of the surface wave field

5.4.1 Introduction

The two dimensional slope distribution of the surface wave field was studied to determine variations from the linear case, as described in chapter 3, and so that these variations could be compared with previous experimental measurements in different ocean conditions. The most famous measurements of the two-dimensional slope distribution of the open ocean were made by Cox and Munk (1954a, 1954b) and the results of this experiment are widely used (Nickolaev and Yordanov, 1992) as a basis for theoretical modelling of scattering from non-Gaussian surfaces. Other similar experiments have been performed by Duntley (1950) and Schooley (1954).

Additionally, within the DERA programme there was a need for in-situ measurements of the actual wave statistics in the Loch to enable understanding of the radar images collected during this experiment. By using appropriate parameters in the radar scattering theories it becomes possible to compare these data with other results collected elsewhere, allowing similarities and differences to be identified between the various experimental regions. As Loch Linnhe is a coastal region, it is reasonable to assume that the slope statistics may differ from those in the open ocean. The traditionally used results of Cox and Munk were collected in an open ocean environment, which may be different from coastal waters. Therefore, it was decided that local measurements should be made to test whether or not the results of Cox and Munk are valid in these different conditions.

5.4.2 Calculation of principal axes

At low wind speeds, the surface of the ocean is a combination of approximately sinusoidal waves of varying wavelength and direction, which superpose to form the complicated wave patterns that are observed. Linear theory suggests that the resulting two-dimensional surface slope distribution should be a two-dimensional Gaussian distribution. This theory provides a basis from which to study the non-linearity of the surface wave field by calculating deviations of the measured data from the basic Gaussian shape. These deviations can be expanded in terms of the moments of the distribution, see Appendix A and also Kendall and Stewart (1963). Other authors, such as Hughes *et al.* (1977) have also considered this method. In this analysis, a Gram-Charlier distribution, defined in equation

3-25, has been used in such as way that it assumes that the data are aligned along two orthogonal and independent axes which are symmetrical in one direction and may be asymmetric in the other direction. Cox and Munk found that these axes were approximately perpendicular and parallel to the wind direction, respectively.

In this analysis a mathematical technique has been used to determine the two independent axes (known as the principal axes), and then these axes are compared with the measured wind direction. Moments can be used to determine the angle between the Northings and Eastings coordinate system the data is measured relative to, and the coordinate system defined by the principal axes. The data can then be defined relative to the principal axes. A matrix method called diagonalisation (Barnett, 1979) has been used to do this for the Loch Linnhe data set. The mathematics is presented in Appendix B. By using this mathematical technique, two uncorrelated directions are used automatically.

This process does not provide a single valued rotation angle as the principal axes, X and Y, are not uniquely defined. This means the method is unable to distinguish between X, Y, -X and –Y, and that this must be done by some other method. In this case each distribution has been studied and multiples of 90° added in an attempt to determine the symmetric and asymmetric axes. It has been assumed (based on the findings of Cox and Munk) that the mean square slope of the slope component along the asymmetric axis will be greater then the mean square slope of the slope component along the symmetric axis. Where the mean square slope values were very similar, the asymmetric axis was taken to be the axis closest to the wind direction. An attempt has been made to select the asymmetric axis so that a histogram of the data is positively skewed.

5.4.3 Results

Initially, relatively long sections of data were studied (approximately 20 minutes of data corresponding to approximately 300000 data points). For each data set, the dominant axes were calculated and the symmetric and asymmetric axes were determined as described above. Some examples of the slope distribution along the principal axes are presented in figure 5-1, with the x-slope meant to be symmetric and the y-slope meant to be positively skewed. The five files were randomly selected to demonstrate the characteristics of the data (wind speed increases down the page). It can be seen that this method has not always

selected the most appropriate axes as the x-slope distribution is not always symmetric and the y-slope distribution is not always positively skewed. In the cases where the x-slope distribution appears more skewed than the y-slope distribution, the methods used may have incorrectly assigned the rotation angle. Other departures from the expected distributions may be due to a number of factors including:

- instrument error;
- wind variability over short time scales and spatially within the loch.

To investigate whether this problem has arisen due to wind variability, the distributions have been plotted for much shorter data sections. Figure 5-2 contains histograms from short sections (1.2 minutes or approximately 18000 samples) of data files where the wind variability is not so likely to affect the data. Again wind speed increases down the page. It can be seen that for the last four samples the rotation angle has led to the data being approximately symmetrical in the x-slope distribution and positively skewed in the y-slope distribution. This is evidence that the behaviour of figure 5-1 is likely to be due to lack of homogeneity in the wave field over large space / time scales, possibly due to wind variability.

In both figures 5-1 and 5-2, a clear increase in the width of the two-dimensional distribution can be seen as the wind speed increases. This variation of the mean square slope with wind speed is investigated further in section 5.5. Due to the apparent wind variability in the data presented in figure 5-1, the shorter data sections in figure 5-2 are used for the following analysis.

Having rotated the data so that the slope components are aligned along the principal axes of the distribution, the Gram-Charlier analysis can proceed. The Gram-Charlier routine developed for this research uses the moments of the distribution to calculate the coefficients. To test the routine, time series' of data were generated using a Gaussian random number generator in IDL. The Gram-Charlier coefficients were calculated for these data samples using the moments of the data samples and the curves were found to fit the data well. After the routine had been tested, it was used to calculate the Gram-Charlier coefficients in terms of the moments of the distributions for two of the short sections of data displayed in figure 5-2. The calculated coefficients are displayed in table 5-1.

Gram-Charlier coefficient	File: 29115603	File: 26140928
C_{00}	1	1
C_{21}	-0.254305	-0.368133
C_{22}	0.820211	1.44090
C_{03}	-0.662611	-0.877205
C_{04}	2.18961	3.67142
C_{40}	2.15565	3.20456

Table 5-1: Gram-Charlier coefficients for selected file sections

Using these coefficients, a two-dimensional Gram-Charlier distribution was fitted to each of these data sets using the coefficients in table 5-1. This enables the accuracy of the fits to be investigated at a number of values of x- and y- slopes. The corresponding fits in the x-slope distribution at different values of y-slope are given in figures 5-3 and 5-5 whilst the fits to the y-slope distribution at different values of x-slope are given in figures 5-4 and 5-6 for the two files (for traceability purposes the original filenames are recorded in the figure labels). The Gram-Charlier fit is over-plotted in green and the fit from a Gaussian distribution having the same mean square slopes is over-plotted in red. If s represents a slope component and $\sqrt{\overline{s^2}}$, the rms slope for that slope component, then according to Cox and Munk the Gram-Charlier fit should be accurate for slopes for which,

$$\frac{s-\bar{s}}{\sqrt{\overline{s^2}}} \leq 2.5 \qquad 5\text{-}1$$

For the first data set, the Gram-Charlier fit should be accurate for x-slopes up to 0.18 and y-slopes up to 0.25, whilst for the second data set, the fit should be accurate for x-slopes up to 0.27 and y-slopes up to 0.34. Due to the small data sample, when the distribution is divided up in this way, there will only be a few data points within each bin, which may lead to significant random errors. However, taking a longer sample may lead to wind variability within the sample as discussed previously.

It can be seen that, as expected, there is quite a lot of randomness in the data. It does seem likely that this is due to the size of the data sample, as this variability was not obvious in the presentations of the full three-dimensional distribution displayed in figure 5-2. It can be seen that neither the Gaussian fit nor the Gram-Charlier fit is a good representation of the data. The Gram-Charlier fit, in general, more accurately represents the peak value of the distribution, but is not accurate consistently throughout the distribution. The Gaussian distribution appears to provide an improved fit to the tails of the distribution. It can be seen that the Gram-Charlier fit is quite good for the negative slopes along the asymmetric axis (slopes on the back faces of the waves). This is confirmed by studying the x-slope fits at cuts through the distribution at negative y-slope values. However, for the positive y-slopes, the Gram-Charlier fit is very poor. Again, this can be seen clearly in the fits of the x-slope distribution at cuts through the distribution at positive y-slope.

Further investigation of these fits has shown that the large slope values significantly affect the value of the rms slope. This means that the Gaussian distribution does not fit the distribution at smaller slope values so well. If large slope values are ignored, then the Gaussian fit to the data is better and the Gram-Charlier coefficients are correspondingly smaller. However, the Gram-Charlier fit obtained is qualitatively no better than with the large coefficients. This suggests that a Gaussian distribution is a reasonable fit to the data provided only small slope components are considered in the calculation. In this case, the fit can be improved slightly by using a Gram-Charlier distribution. However, if all slope components are considered then the Gaussian fit is poor and the Gram-Charlier coefficients must be large to improve the fit.

Comparing these results with those of Cox and Munk, it is immediately clear that the Gram-Charlier coefficients for the TLS data are much larger than the corresponding coefficients calculated by Cox and Munk. There are a number of possible reasons for this. The first point to note is that the Gaussian distribution calculated by Cox and Munk from their rms slopes was a much better fit to their data than the Gaussian distributions calculated for the TLS data. From this research it has been found that this is strongly related to the large slope components in the distribution. Cox and Munk noted that, using their method, the computation of large slope components was limited by the disappearance of the sun glitter from specular reflection into background light. Therefore, it may be that

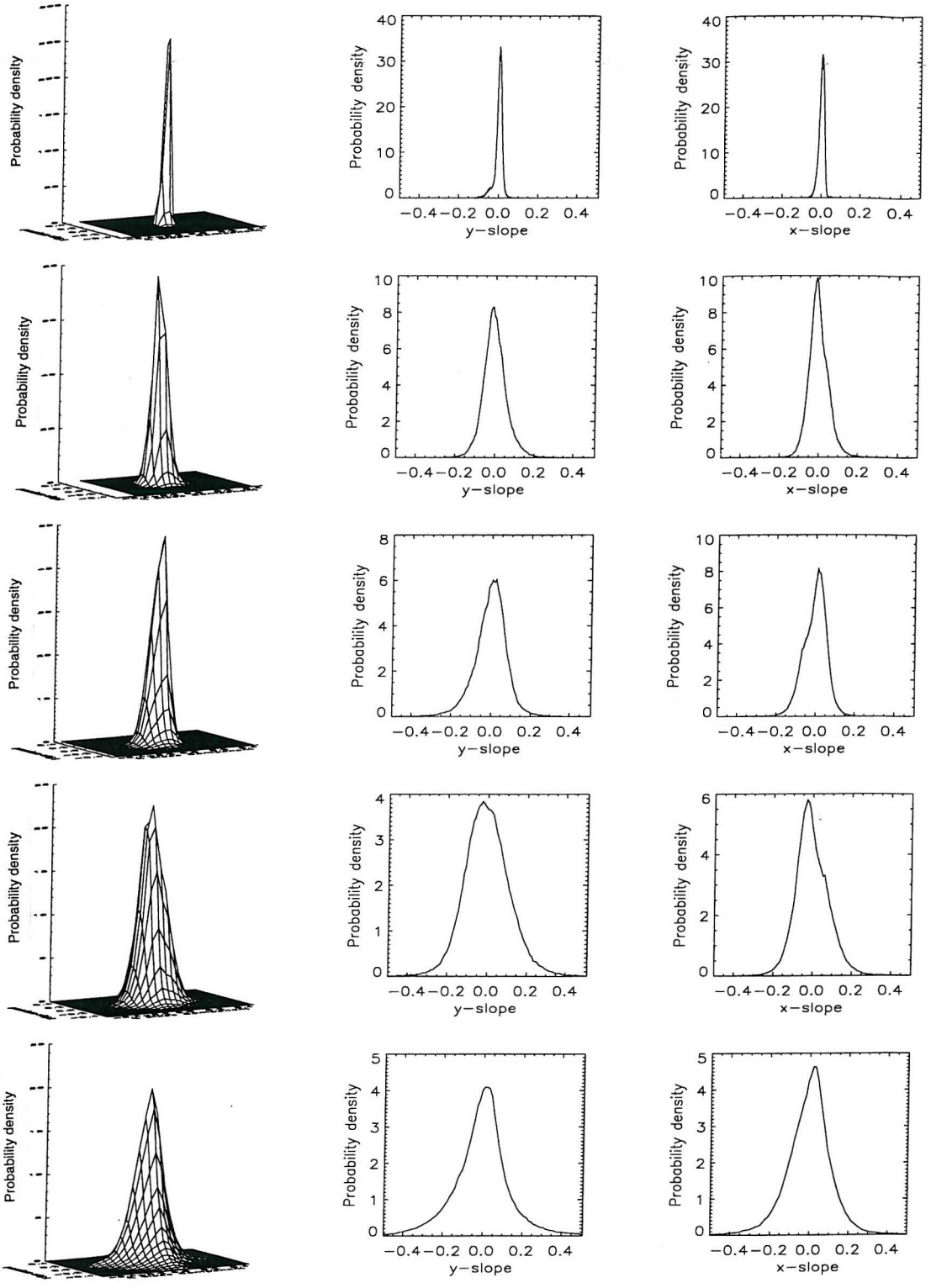

Figure 5-1: 2-dimensional histograms and 1-dimensional histograms along (y-slope) and across (x-slope) wind for five randomly selected data files (from top to bottom, files are, 25145921 (w=0.60m/s), 27152319 (w=2.06m/s), 28134029 (w=3.27m/s), 31112606 (w=4.53m/s), 26135456 (w=7.59m/s))

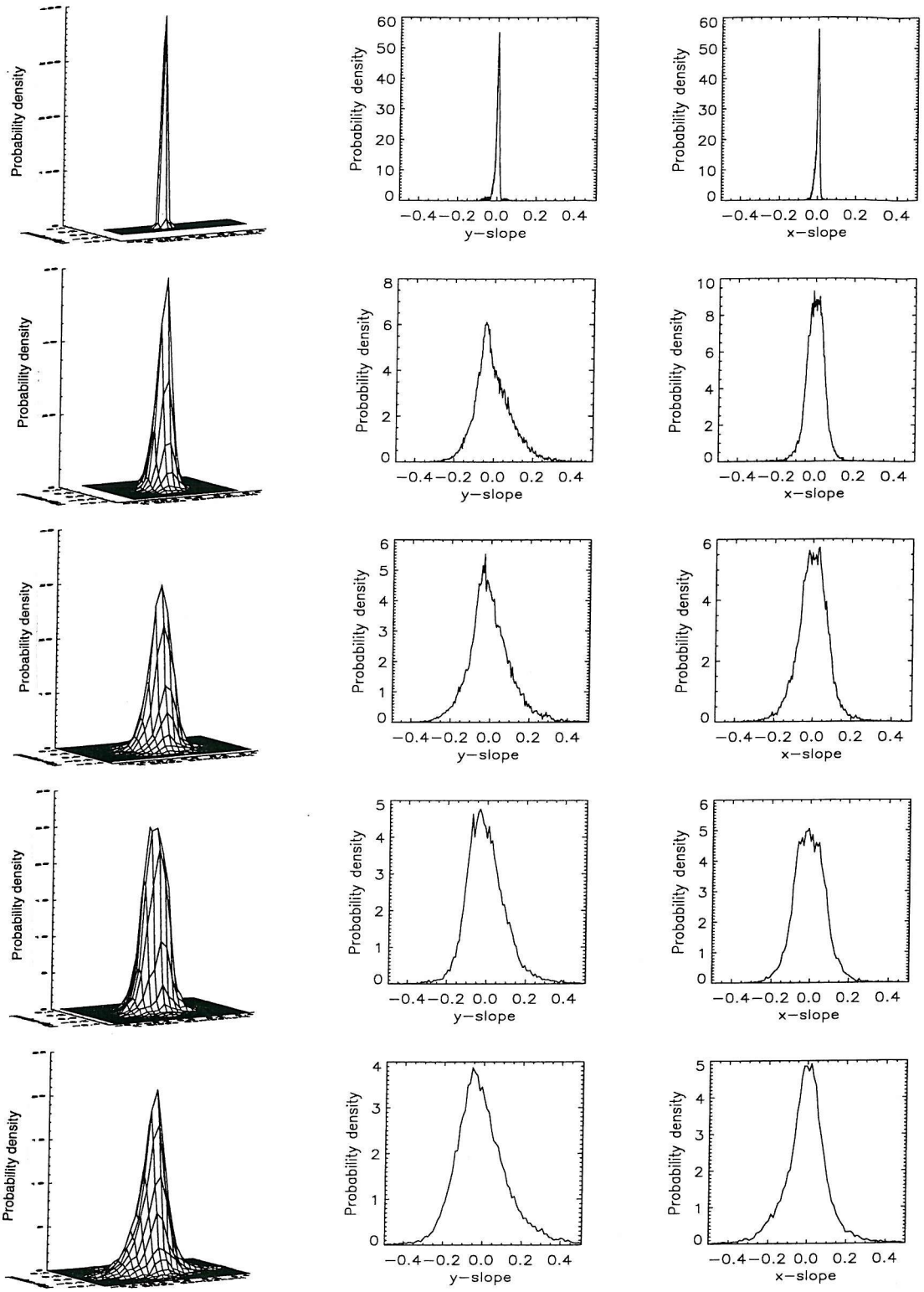

Figure 5-2: 2-dimensional histograms and 1-dimensional histograms along (y-slope) and across (x-slope) wind for five data sections (from top to bottom, files are, 28120103, 12.09-12.11 (w=1.07m/s), 28120103, 12.19-12.21 (w=2.55m/s), 29115603, 11.99-12.01 (w=3.41m/s), 25131618, 13.34-13.36 (w=3.78m/s), 26140928, 14.29-14.31 (w=7.94m/s)).

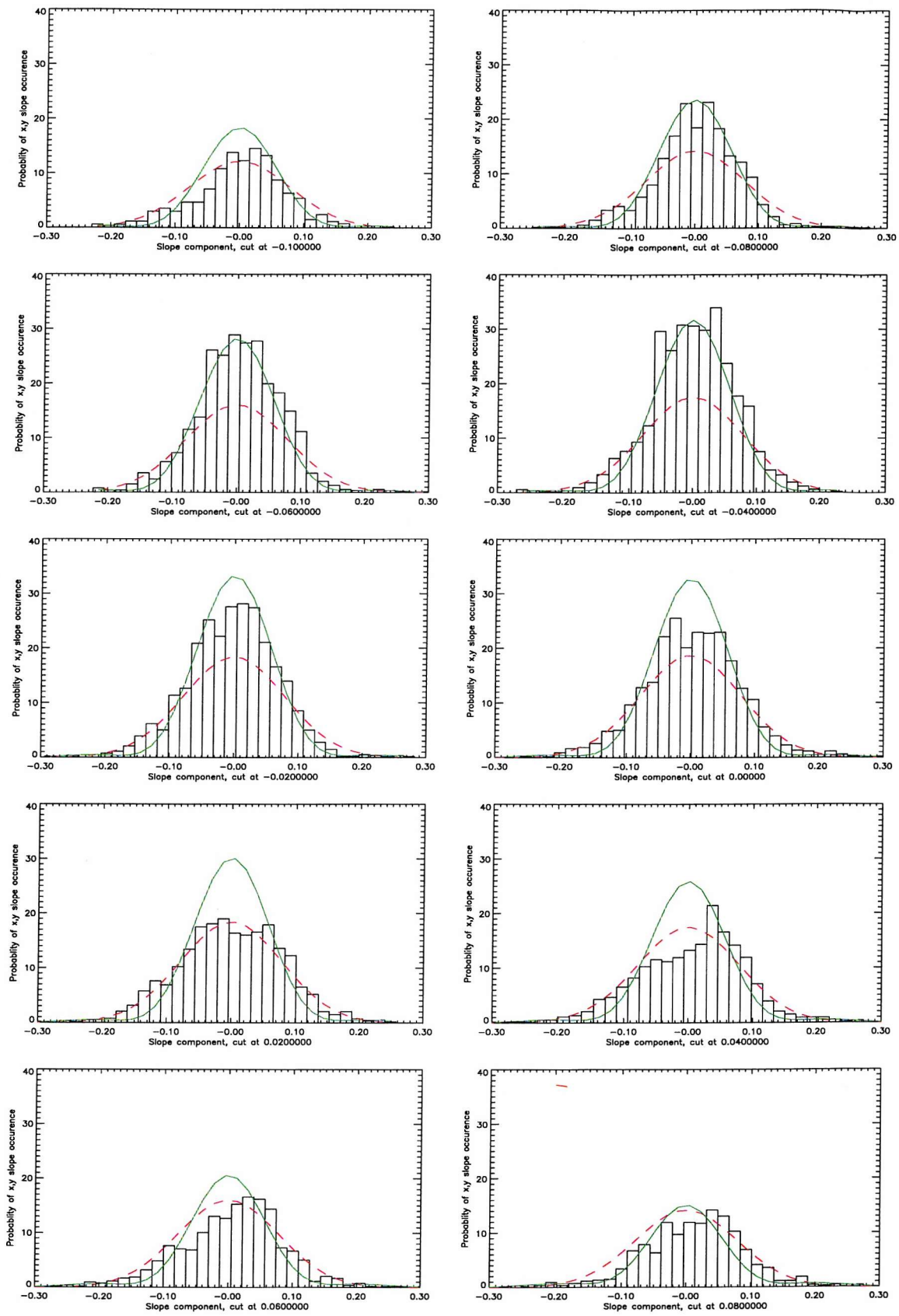

Figure 5-3: Gram-Charlier (green) and Gaussian (red) fits, sections parallel to cross wind direction for file section 29115603, 11.99-12.01, w=3.41m/s

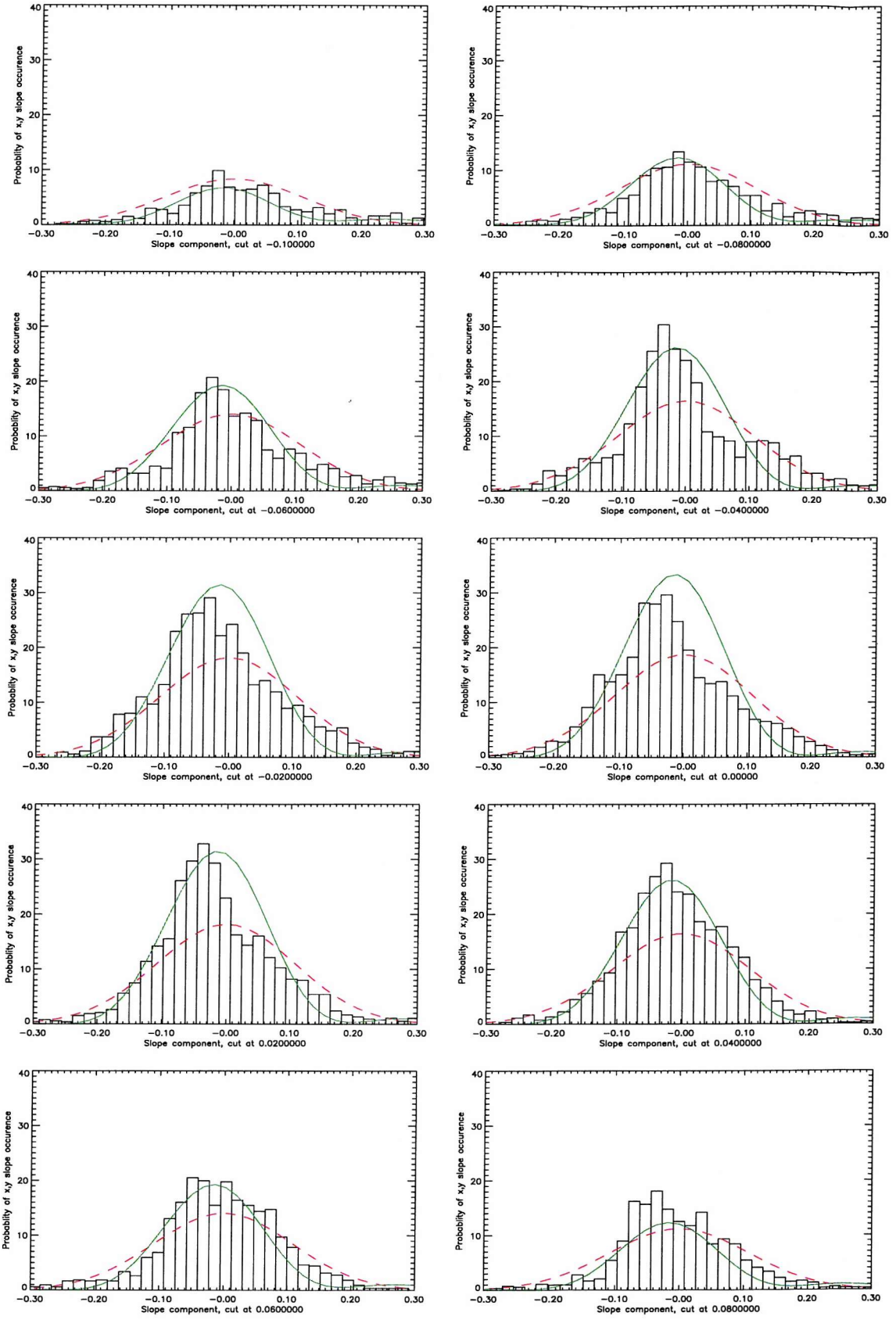

Figure 5-4: Gram-Charlier (green) and Gaussian (red) fits, sections parallel to along wind direction for the same data used in figure 5-3

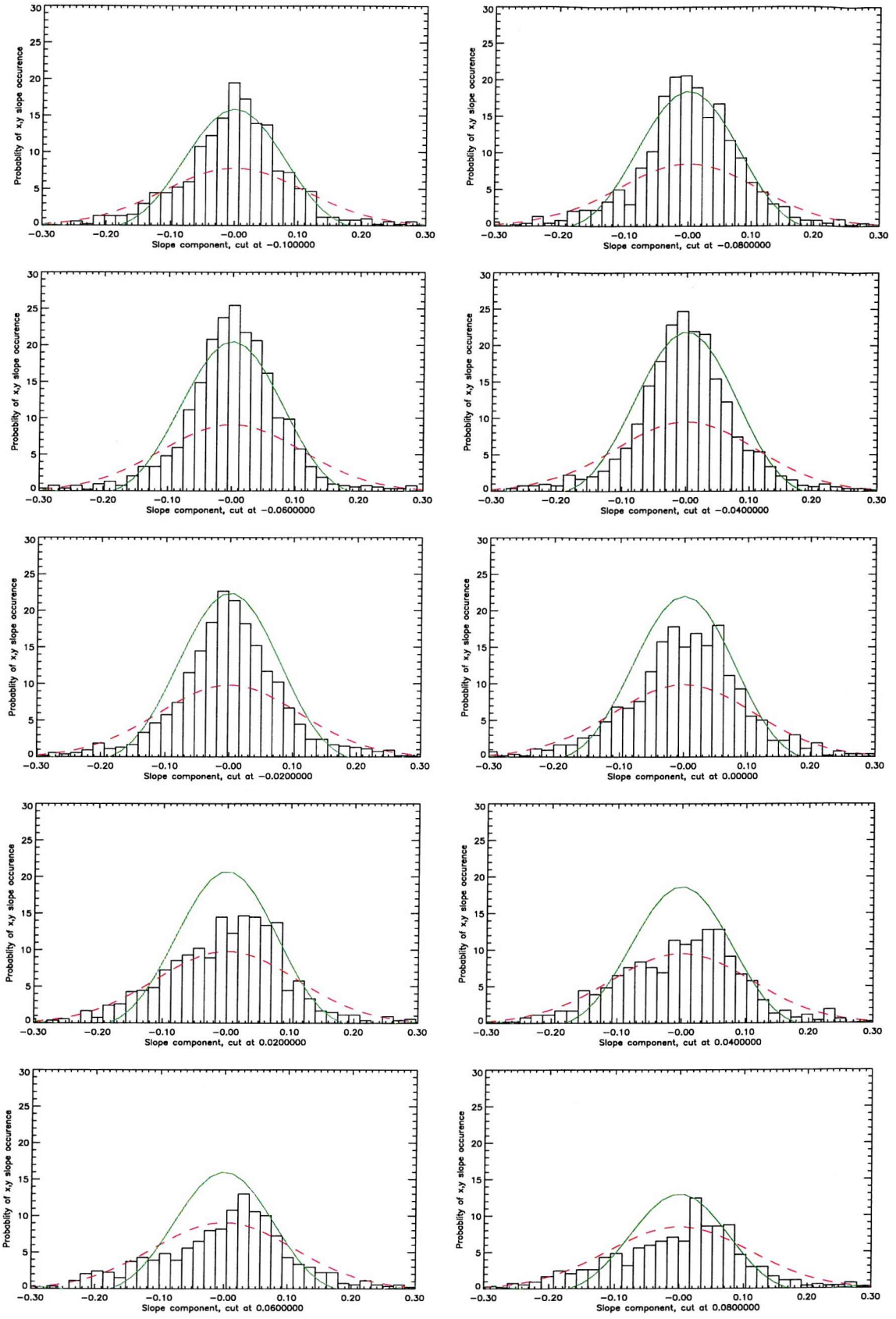

Figure 5-5: Gram-Charlier (green) and Gaussian (red) fits, sections parallel to cross wind direction for file section 26140928, 14.29-14.3, w=7.94m/s

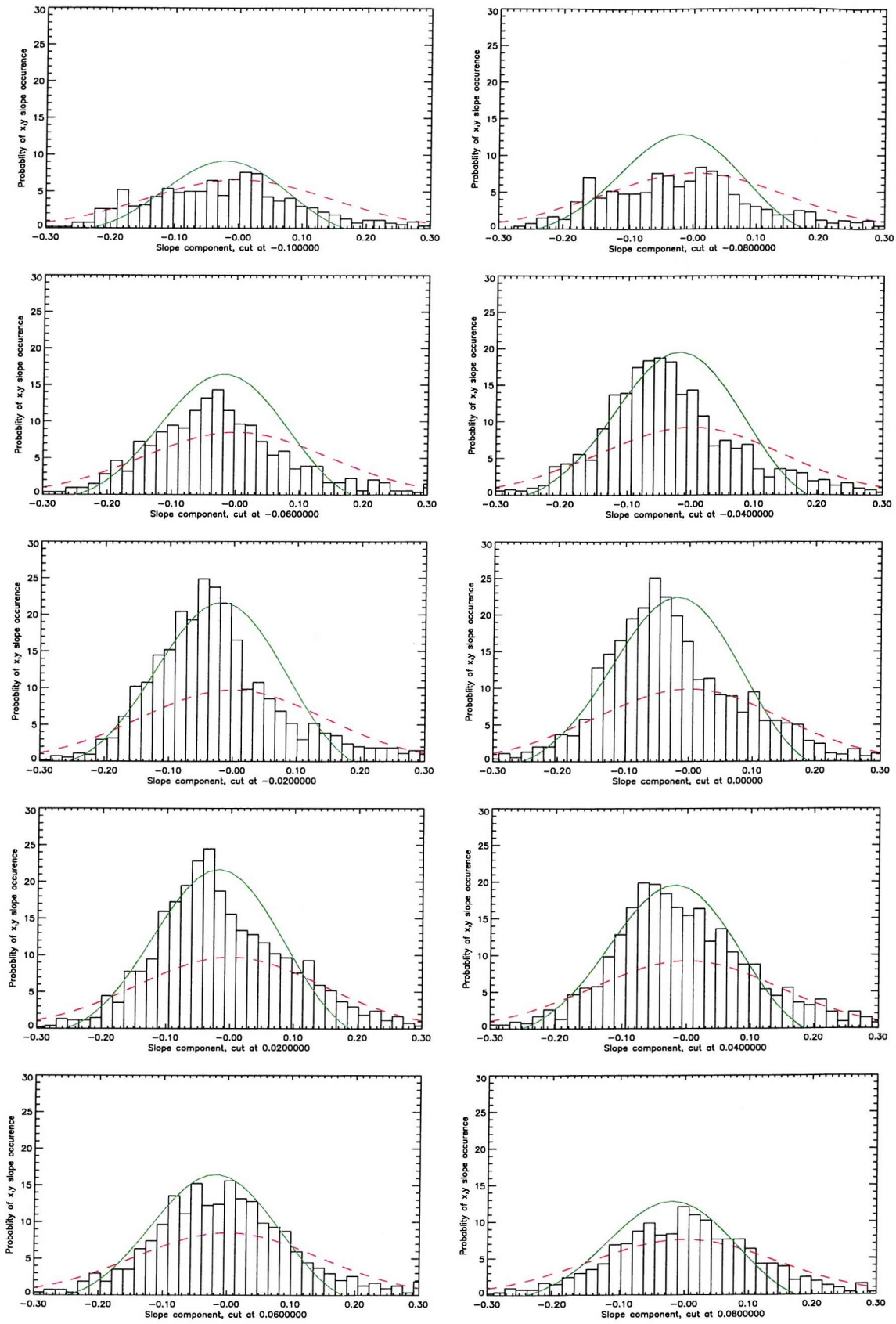

Figure 5-6: Gram-Charlier (green) and Gaussian (red) fits, sections parallel to along wind direction for the same data used in figure 5-5

their calculations were affected by this lack of large slope components making their distribution appear more Gaussian than it should have. Alternatively, the data from Loch Linnhe may have errors in the number of large slope values recorded, which would lead to errors in the rms slope. It is clear that the Gaussian fit generated from the rms slope value using all data points calculated for Loch Linnhe is not a good fit to the data, and therefore provides a poor start for the calculation of the Gram-Charlier coeffients.

Another possible difference is that Cox and Munk calculated their coefficients using a power series method, which permitted an analytic representation of the probability of a particular slope component even where data were missing. They, therefore, did not use moments to calculate their Gram-Charlier coefficients. Since moments of the distribution have been used in the TLS calculations, this may have led to different coefficients. However, given the difference in the fit of the basic Gaussian distribution, it seems likely that the differences in the data are more significant.

It is interesting that the Gram-Charlier coefficients calculated for random Gaussian number generator test cases were of a similar order to those calculated by Cox and Munk. This suggests that their data may have been almost purely Gaussian with only a small amount of non-linearity causing variations from a purely Gaussian distribution. It may also suggest that their variations from a Gaussian distribution were caused by an insufficient sample size rather than a true non-Gaussian behaviour. Although errors due to the measurement technique were discussed in their work, they did not consider the expected error on the coefficients resulting from discrete sampling of a continuous distribution.

A summary of the possible reasons for the differences between the Cox and Munk data and the data from Loch Linnhe is:

- data at limited fetch demonstrates different behaviour from the ocean as the wave field tends to consist of shorter wavelength, more highly peaked waves;
- the two-dimensional Gram-Charlier distribution calculated by Cox and Munk may not fit their data well at all points in the distribution, but this is not clear from their work.
- limitations in Cox and Munk's method of measuring large slope components may have made the distribution appear more Gaussian than it actually was;

- TLS instrument errors due to diode variations, data processing or contamination of the ambient wavefield by the catamaran;
- using moments to calculate the Gram-Charlier fit may produce different results for the Gram-Charlier coefficients;
- natural randomness of the wave field measured in the small sample by the TLS failed to demonstrate the full statistical characteristics of the data.

Considering variations of the coefficients with wind speed, Cox and Munk found that most of the coefficients they calculated had a large spread, although they did report that there appeared to be a slight correlation between skewness and wind speed. The peakedness (or kurtosis) coefficients were found to be independent of wind speed.

5.5 Variation of mean square slope with wind speed

5.5.1 Introduction

Another important parameter which is used in models of radar scattering from the ocean surface is the mean square slope. This value is a measure of the mean roughness of the surface, and varies according to the strength of the wave-generating wind. The relationship between the mean square slope and the wind is dependant upon other factors such as the fetch, the time for which the wind has been blowing, and shielding of the water by surrounding features such as hills which will modify the wind speed as a function of height.

The roughness of the water is expected to depend on the stress acting on it, since this is the force which generates the surface waves. The relationship between the stress at the water surface and the wind speed at a certain height has been the subject of much research and was described in detail in chapter 3. A lot of scatter has been found in simultaneous measurements of the stress and wind speed which makes it difficult to determine a single unique theory for all wind speeds in all types of ocean environments. In particular, the results for coastal waters have been found to differ from those measured in the open ocean. In order to make good comparisons between experiments performed in wind wave tanks and those in the field, it is important that the *wind stress* rather then the wind speed is related to the mean square slope.

In this section the mean square slope is calculated using the TLS data collected in Loch Linnhe, for each wind speed encountered. Different regions of the mean square slope versus wind speed graph are compared with observations of the surface conditions. Using the information presented in chapter 3 on wind stress, suitable methods are considered for converting the wind speed measured in Loch Linnhe into wind stress. The most appropriate method is selected for the conversion and the data are presented as mean square slope versus wind stress.

5.5.2 Method and initial results

The average mean square slope was calculated for each data file collected by the TLS during LL97. The errors in the slope data due to the instrument have been investigated in chapter 2.

The wind speed and direction were recorded on the towing vessel using a multi purpose AANDERAA meteorological station as reported in Knight (1997c). In order to make a correct comparison of the wind speed with variations in the data, the vessel motion has been removed from the wind data. The errors associated with the vessel motion removal have been investigated thoroughly and are presented in Taylor and Cooper (1999).

A plot of the calculated mean square slope versus corrected wind speed is given in figure 5-7. Here the "cross wind" component is the mean square slope of the slopes along the symmetric axis and the "along wind" component is the mean square slope of the slopes along the asymmetric axis. Error bars showing the calculated error in the wind speed are plotted on the total mean square slope points only, for reasons of clarity. Three distinct growth regions can be identified. At low wind speeds, the mean square slope is negligible until a critical velocity of approximately 2m/s is reached. The growth in mean square slope is then linear until approximately 4m/s whereupon the gradient changes and the data have a much greater spread.

Some insight can be gained into the behaviour of the mean square slope by matching the mean square slope of the water surface roughness in figure 5-7 with the visual observations of roughness. In order to do this, in figure 5-8, the total mean square slope is re-plotted so that each point is colour coded according to the average roughness observed during the run.

This roughness is a subjective measure made by the Authors' visual observation. It can be seen that there is a clear correlation between the wind speed and the visual observations. Of the three sections noted earlier, the initial section is found to be related to very smooth surfaces which contain just a few smooth patches of ripples. The middle steeper section seems to be related to the increase in the size of the ripples from being fairly smooth and sinusoidal, through becoming quite peaky, to wind waves which were just beginning to break (labelled as 'spilling' on the graph). Within the wind wave / spilling region there is a transition to the third section of the graph which is followed by a region that contains increasing numbers of more strongly breaking waves. In particular breaking waves were only observed for wind speeds equal to or greater than 4m/s. This coincides with the start of the third region and may be related to it.

Previous experimental measurements of the variation of the mean square slope with wind speed have been reviewed in chapter 3. In the ocean, in general a linear relationship has been found. In the presence of natural slicks within the ocean, there are differences between data sets, some of which still show a linear behaviour whilst other data sets show that no waves are generated below a certain threshold wind speed. This latter type of behaviour has been observed in data collected in wind wave tanks. The vast majority of these experiments show an initial region where no waves are generated until the wind reaches a minimum critical velocity. After this, in general the data do not have a linear trend, although there is sometimes a linear region.

During the experiment in Loch Linnhe, slicks due to internal waves were present on the surface as well as other natural slicks of unknown origin. These slicks were possibly caused by natural internal waves, bathymetry or surfactant deposits by vessels, or from rivers. These slicks were visible mainly at the lowest wind speeds, and may be responsible for the low measured mean square slope at low wind speeds.

Another possible explanation is that in the ocean there is often some residual swell which has not been created by the local wind. Therefore, at low wind speeds the mean square slope measurement may be dominated by the swell rather than by the true mean square slope. In addition to this, Miller *et al.* (1991) has found experimentally that the presence of swell is likely to increase the number of small waves that are generated on the surface at a

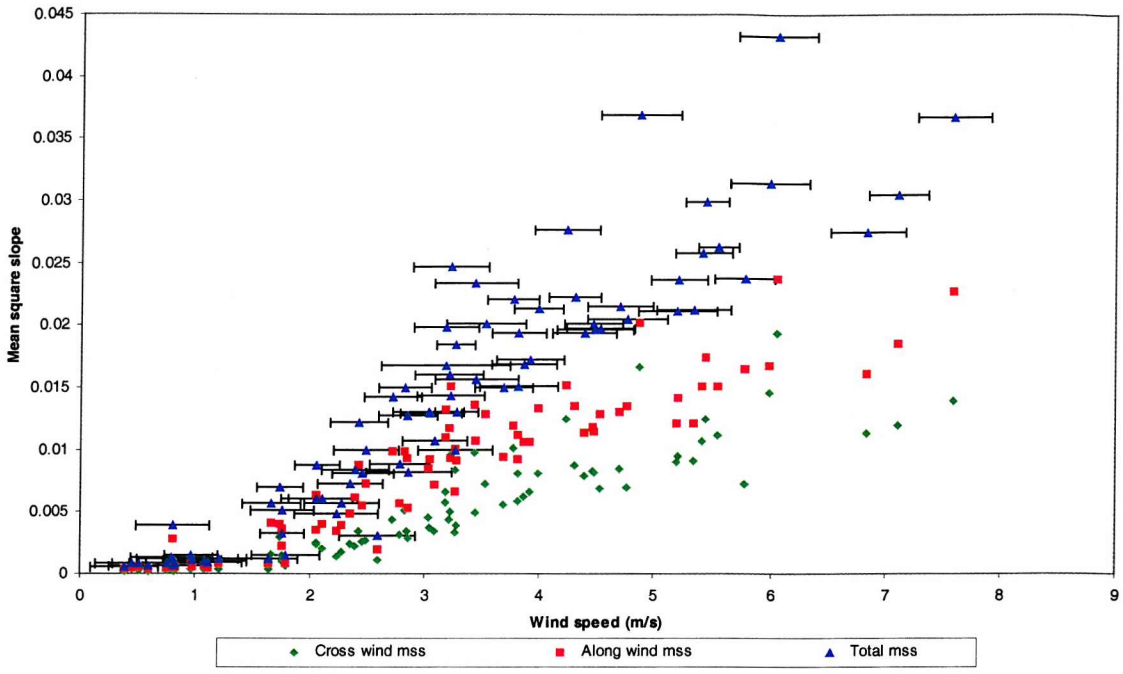

Figure 5-7: Total, cross wind and along wind mean square slope versus wind speed as measured by the TLS

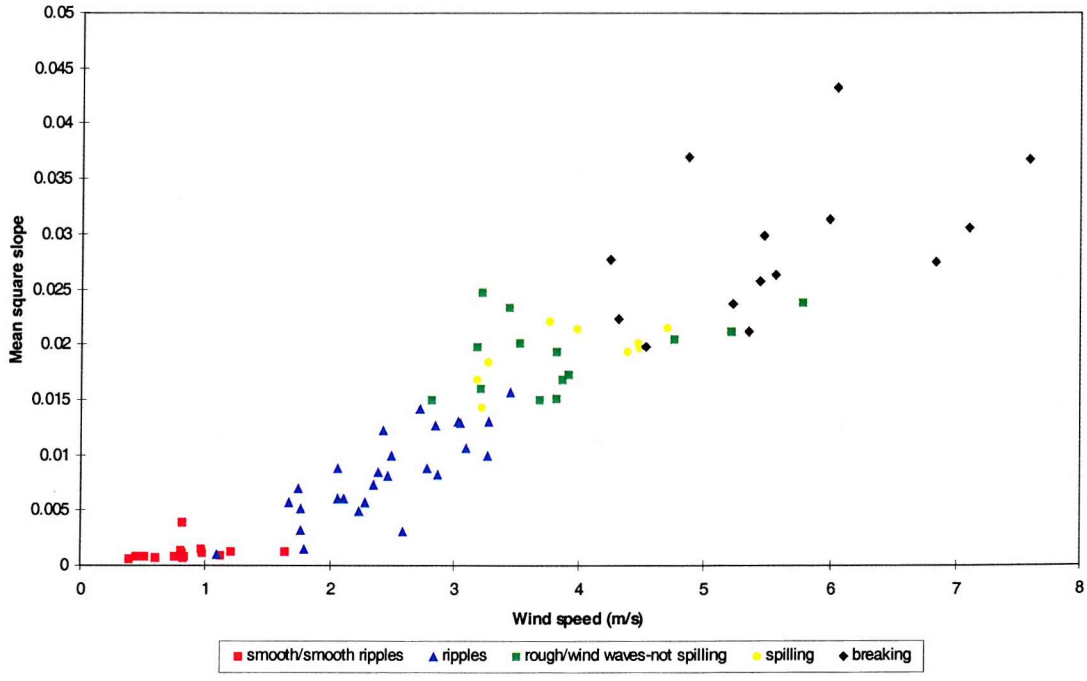

Figure 5-8: Total mean square slope versus mean wind speed with roughness categories from visual observations

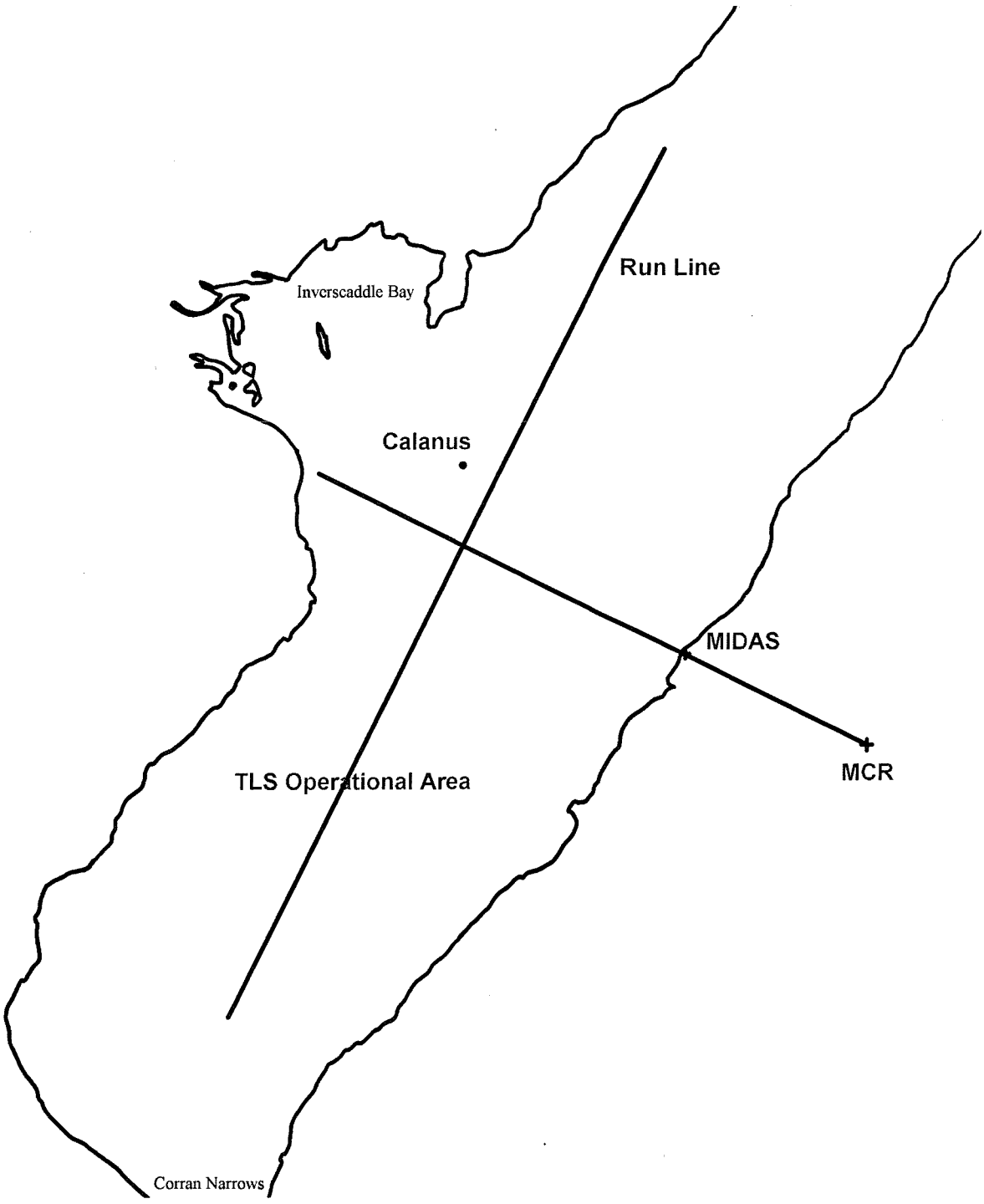

Figure 5-9: Schematic of Upper Loch Linnhe showing experimental area. Upper Loch Linnhe is approximately 14km long and 3km wide.

particular wind speed, thus increasing the mean square slope due to the short scale waves. The TLS measurements in Loch Linnhe were collected in the absence of swell, as there is not sufficient fetch for such waves to be generated. Therefore, the results would be expected to be similar in character to those collected in wind wave facilities, or other situations where swell is not present.

Other differences in the behaviour can not easily be attributed to individual factors. They may be due to equipment performance or to genuine differences between the ocean, coastal waters and different wind wave facilities. To allow a direct comparison of the mean square slope variations with wind speed with other experimental data sets, it is necessary to compare the mean square slope at similar wind stresses. This requires a relationship between the wind speed and wind stress which is appropriate for the location in which the data have been collected. In the next sub-section, the relationship between wind speed and wind stress is studied with reference to the material presented in chapter 3, and the most appropriate method is chosen to convert the Loch Linnhe wind speeds into wind stresses.

5.5.3 Discussion of wind friction velocity and application to TLS data

From the discussion in chapter 3, it can be seen that over the last half century a considerable amount of effort has been put in to determine the relationships between the wind stress and the wind velocity. The majority of these studies have concentrated on determining the variation either at sea or in the laboratory, and have little discussion of how to relate the two cases, or of how they apply to limited fetch ocean conditions. The latest, and currently most frequently cited, theory developed by Smith (1988) explicitly states that it is only applicable to open ocean conditions, and is therefore not applicable to the current data set.

Upper Loch Linnhe is approximately 14km long and 3km wide. The TLS data were collected at one end of the Loch about 2km from the Corran Narrows, see figure 5-9. In the figure, MIDAS and MCR represent the two radars whilst Calanus was a research vessel from which some of the in water measurements were made. The wind direction was variable during the experiment. Therefore, the fetch varied between experimental data runs. However, even for the longest fetch, this was still a limited fetch situation. The theory of Amorocho and DeVries (1980) has coefficients determined on the basis that waves start to

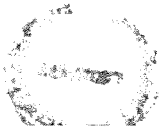

break at wind velocities of approximately 7m/s measured at 10m above sea level. In Loch Linnhe, wave breaking was first observed at wind velocities as low as 4m/s. This is possibly an indication of the effect of the limited fetch, in that the wind stress may have been higher, causing wave breaking earlier than for the same wind velocity in an unlimited fetch situation.

Wu (1969b) has considered how to take account of fetch limitation by developing a technique that involves placing the anemometer at a height which is dependent on the fetch. This height was not used in Loch Linnhe and so the results from Wu's study are not applicable to these data. The variability of the fetch in Loch Linnhe would also have caused complications as no single height would have been appropriate for all of the fetches.

After thorough searching of the literature, it has been decided that the most appropriate way in which to convert the wind speed measurements collected in Loch Linnhe into friction velocity is to use assume a logarithmic velocity profile defined in 3-5 and then use the values for the constants given by Garratt (1977). This was recommended by Smith (1988) for data collected in coastal regions. Therefore, the constants in equations 3-5 and 3-6 were taken to be, $a=0.0144$ and $\kappa=0.41$ (Garratt, 1977), but could have been used as $a=0.017$ with $\kappa=0.4$ (Smith, 1988). Wu (1980) also reviewed many of the same data and found a value of $a=0.0185$ with $\kappa=0.4$. These converted data are plotted in figure 5-10. Included for comparison are the mean square slope data of Hughes *et al.* (1977) who converted their wind velocity data via Wu's method and the data of Cox and Munk. Cox and Munk's wind measurements have been converted into wind friction velocity assuming a logarithmic profile, but this time using the constants, again recommended by Smith (1988), for open ocean conditions, i.e. $a=0.012$, $\kappa=0.4$. Their wind speed data collected at only 2.7m above sea level has not been used as the wind speed at this height can be affected by swell. Using this conversion, wind friction velocities have been obtained which are similar to values calculated by Wu when he converted the data of Cox and Munk using his own relationship.

This graph demonstrates quite clearly that within the limitations of the method employed, the variation of the mean square slope with wind speed, as measured by the TLS in Loch Linnhe, is very consistent with other similar data sets, provided the correct parameters are considered (wind stress rather than wind speed). The conversion into wind friction velocity

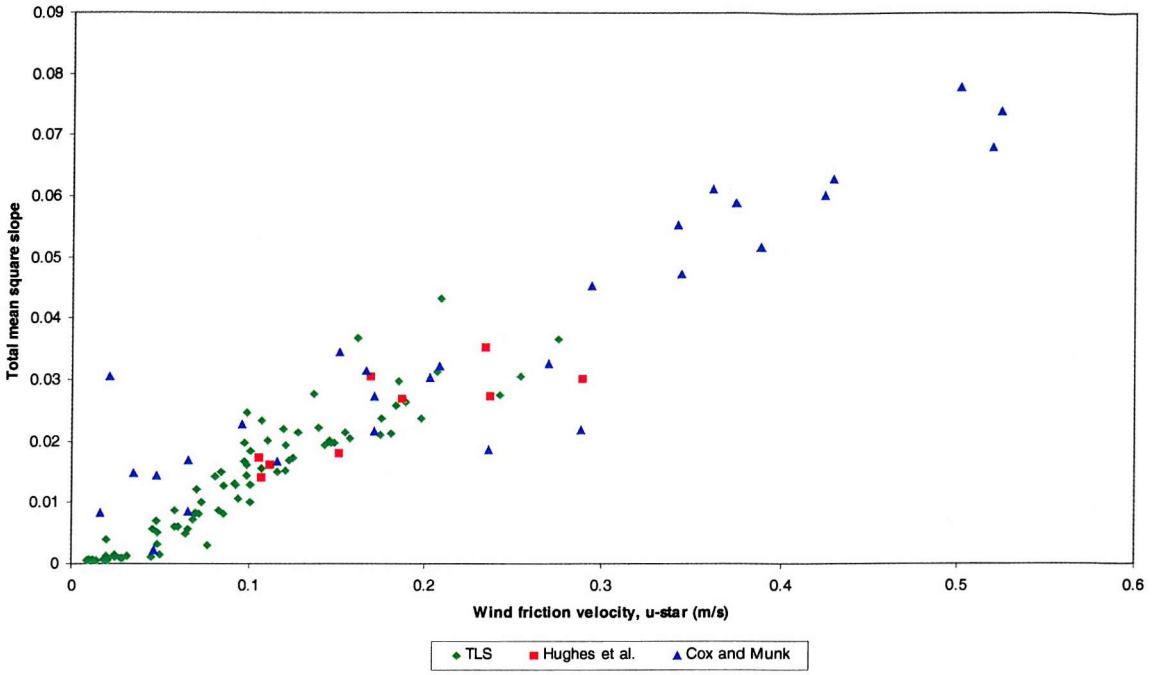

Figure 5-10: Wind friction velocity versus total mean square slope. Comparison of TLS data, data from Hughes et al and Cox and Munk's data

for the three data sets appears to allow a direct comparison of the data collected under different conditions.

This relationship will be revisited in chapter 6 where ambient wind wave fields generated in a wave tank are studied. There, an attempt will be made to discover if the stress relationship can be used to apply wave tank data to the open ocean.

5.6 Summary and conclusions

This chapter has concentrated on a number of areas. These are:

- the ability of the TLS to provide useful and reliable surface slope statistics;
- how well the two-dimensional surface slope distribution in Loch Linnhe conforms to a Gaussian hypothesis and how this compares with the well known work of Cox and Munk;
- the variation of the mean square slope with wind speed in Loch Linnhe;
- the computation of the wind stress from the wind speed in different locations to allow direct comparison between different experimental environments;

- discussion of the differences between coastal waters, the open ocean and wind wave tanks.

The capability of the TLS in providing useful reliable surface slope statistics has been discussed. It was concluded that the instrument should provide adequate and trustworthy statistics provided a long time sample of data is collected, the direction of travel is random with respect to the surface wind wave field and the wind variability is not too great spatially or temporally whilst the data collection is in progress.

Using these data, it has been shown that the two-dimensional distribution of surface wave slopes as measured by the TLS in Loch Linnhe does not seem to be fitted well by a Gaussian distribution, and thus that the Gram-Charlier coefficients needed to model the deviations from a Gaussian distribution are large. It has been found that the Gaussian fit can be improved if large slope components are ignored, and this leads to correspondingly smaller Gram-Charlier coefficients. However, the two-dimensional Gram-Charlier fit is not significantly improved in this case and the rms slope is modified from the true value for the distribution.

These results are in contrast to the results of Cox and Munk where the data was collected in the open ocean. For their data a Gaussian distribution was a reasonable fit and the Gram-Charlier coefficients were small. The differences between the results of Cox and Munk for the open ocean and the TLS data for Loch Linnhe may be due to a number of factors including:

- TLS instrument error;
- poor slope data for large slopes measured by Cox and Munk;
- differences between the wavefield in Loch Linnhe and that in the open ocean (possibly due to the short fetch in Loch Linnhe which does not allow the generation of ocean swell);
- large statistical fluctuations caused by the small data sample;
- different methods of calculating the Gram-Charlier coefficients.

It would seem appropriate that this should be investigated further as this model is widely used as a basis for the ocean slope statistics in theoretical models.

A study has been completed on how the mean square slope as measured by the TLS in Loch Linnhe varies with wind speed and observed surface roughness and has shown that there is a correlation between the mean square slope and the subjective visual observations of the surface roughness. At low wind speeds it has been observed that the mean square slope in Loch Linnhe is very low and there appears to be a critical wind speed below which waves are not generated. This type of behaviour has also been observed in wave tank experiments, although it has not been observed in ocean data except in the presence of slicks. This may be due to residual ocean swell, which is not present in wave tanks or Loch Linnhe, and has been observed to allow generation of surface waves at lower wind speeds than would otherwise be the case. The swell itself will also contribute to the mean square slope at these wind speeds even though it is not directly related to the local wind speed.

Arguments have been presented about how wind speed measurements should be converted into wind stress in different environmental conditions. These have resulted in the selection of a logarithmic wind profile with appropriate coefficients to convert our data and for the data of Cox and Munk. These data have been compared together and also with the data from Hughes *et al.*'s experiment and have demonstrated that the wind stress conversion appears to account correctly for these different conditions providing comparable mean square slope's at similar wind stresses.

Chapter 6

Loch Linnhe Experiment 1997: Spectral analysis

6.1 Introduction and scope of chapter

In this chapter the study is continued of the two-dimensional surface slope data that were collected using the TLS during the experiment in Loch Linnhe in 1997. In contrast to chapter 5, where only statistical properties of the surface wind wave field were studied, here the TLS data is analysed in a spectral sense. The overall objective of this chapter is to assess the usefulness of a device like the TLS, which can measure the two-dimensional surface slope at a single point along a line traverse, in determining the background wavenumber spectrum. In support of this objective, the occurrence of data ambiguities in the TLS data is examined, and a study is made of the way in which these ambiguities can be minimised or the data can be manipulated to calculate accurate surface height wavenumber spectra.

Data ambiguities caused by the following are investigated:

- instrument motion;
- wavefield motion;
- angular distribution of surface wave energy;
- bulk currents;
- aliasing.

It is shown that by using careful data collection techniques, it is possible to reduce the data ambiguities caused by the above effects. These techniques were used during the Loch Linnhe experiment and the resulting data are studied here.

Before the calculation of the wavenumber spectrum is described, methods, which have been used previously to calculate wavenumber spectra from similar data sets, are reviewed. The calculation proceeds by:

- using data sets collected specifically to reduce data ambiguities;
- making assumptions about the relative importance of each of the effects which may cause ambiguities;
- extending and simplifying one of the methods used by an earlier researcher to calculate a wavenumber spectrum.

Calculations are performed of the wavenumber spectrum in Loch Linnhe at four different wind speeds.

6.2 Spectral behaviour as a function of frequency of encounter

6.2.1 Introduction

The TLS was designed to be towed across a wave field at a finite speed to minimise wave field disturbance and so that it might partially bridge the gap between purely temporal measurements and purely spatial measurements. This technique was necessary since traditional techniques for making spatial measurements are not capable of providing the high resolution needed to accurately measure the short-scale ocean waves which are so important in radar imaging of the ocean. As the instrument is towed, the frequency at which the ocean waves are measured is dependent upon the velocity at which it is towed. This frequency will be referred to as the frequency of encounter, ω', and is related to the intrinsic frequency, ω by,

$$\omega' = \left|\omega - \underline{k}.\underline{v}\right| \qquad 6\text{-}1$$

where $\underline{v}$ represents the speed and direction at which the TLS is towed and $\underline{k}$ is the vector wavenumber of the surface wave at frequency, ω, related by the dispersion relation.

In order for the data from the towed instrument to be useful, it must be related to the real surface wavenumbers on the ocean surface. This means that 6-1 must be inverted to provide a solution for k in terms of ω'. This inversion is not trivial as the surface wave field

consists of a spectrum of waves that travel in all directions at different speeds. It is possible for many different wavenumbers travelling in different directions to all appear at a frequency of encounter, ω'. If the instrument was towed very fast, then the components of the wave field would not have been able to travel very far and it could be assumed that the velocities of the wavenumber components were negligible. The frequency of encounter could then be related directly to the wavenumber in the towing direction by,

$$\omega' = |\underline{v}.\underline{k}| \qquad 6\text{-}2$$

This provides a direct relationship which could be used to transform the data from the time domain to the wavenumber domain along the direction of travel. However, information would still be required about the angular distribution of the wave field in order to relate the frequency of encounter to the true surface wavenumber.

In practice, the TLS needs to be towed at a slow speed in order to gain sufficient sampling of the surface to provide the required resolution. This means that analysis of the data is not simple because the components of the wave field move at a speed that is comparable to the towing speed of the TLS. The precise way in which the TLS motion affects the measured spectrum is investigated in the next section of this chapter. Now, the form of the spectrum as a function of the frequency of encounter is considered.

6.2.2 Energy spectra as a function of frequency of encounter

Power spectral density plots of the measured time series for a number of the data runs collected in Loch Linnhe have been calculated. These data runs have been collected at a variety of angles to the wind direction and so at this stage no attempt will be made to understand them in terms of the wavenumber spectrum.

The estimates of the power spectra have been calculated from the autocorrelation of the data in order that the amount of noise can be minimised, and so that a sensible estimate of the error on the spectral estimate can be calculated (Papoulis, 1977). The estimate of the power spectral density (PSD) of a slope component is given by,

$$PSD = \frac{1}{2\pi}\int_{-\infty}^{\infty}\left[\left\langle s(t)s^*(t+\tau)\right\rangle - \overline{s(t)}^2\right]We^{-i\omega\tau}d\tau \qquad 6\text{-}3$$

Where s(t) represents the appropriate slope component and,

$$\left\langle s(t)s^*(t+\tau)\right\rangle = \int_{-\infty}^{\infty}\left|\frac{1}{2\pi}\int_{-\infty}^{\infty}s(t)e^{-i\omega t}dt\right|^2 e^{i\omega\tau}d\omega \qquad 6\text{-}4$$

is the autocorrelation function of the slope time series s(t). τ is a dummy variable of integration. W represents the window function; a Hanning window was used in these calculations. The window function was centred on zero of the time axis of the autocorrelation function. DFT's are used throughout. The PSD of the total slope is calculated from the sum of the along track and cross track PSD's.

By using this method, the number of degrees of freedom of the resulting power spectrum can be calculated (Blackman and Tukey, 1958).

$$\text{Degrees of freedom} = \frac{2\left(T_s - \frac{T_w}{3}\right)}{T_w} \qquad 6\text{-}5$$

where T_w is the time length of the window function and T_s is the time length of the time series used. The number of degrees of freedom can be related to the percentage of data points expected to be within a certain range of the estimated spectrum. The number of degrees of freedom used throughout this chapter was 100 which means that at least 90% of the data are expected to be within 2dB of the estimated spectrum.

Using the above method the PSD has been calculated for a noise file, figure 6-1. This has been created out of the water with the laser beam pointing directly upwards and not moving across the screen. It shows the power level below which no signal can be measured as the output will be dominated by noise. This noise arises through the electronics and communications links as well as in the signal from the laser.

In figure 6-2 the PSD is displayed for a number of data runs. It can be seen that the real data have a signal which is many dB's above the noise level and shows a variety of characteristics. As the wind speed increases, the spectral shape varies. Where smooth water was measured, the data display almost entirely noise characteristics; here the amount of signal is clearly of the same order of magnitude as the noise within the system. The remainder of the graphs show behaviour which is distinctly different from the noise file and which will be assumed to be the characteristic of the water slope distribution; the signal level tends to increase as the wind speed increases. The variation in spectral shape will not be studied as the data are not meaningful until they can be related to a physical property such as the wavenumber of the waves. As these spectra are evaluated with respect to the frequency of encounter, their shapes will depend on the direction of travel and velocity of the TLS with respect to the wind wave field.

6.3 Data ambiguities

6.3.1 Introduction

In this section the way in which the frequency of encounter is related to the real frequency and wavenumber of the surface wave field is studied. The effects of the following are investigated:

- the motion of the instrument;
- the motion of the ocean;
- the angular distribution of the wave field;
- bulk currents;
- aliasing.

6.3.2 Data ambiguities due to instrument and wave field motion

The relationship between the frequency of encounter and surface wavenumber was investigated by the Author in Taylor (1997a). These findings are presented below and the results of the research were used to determine the way in which data was collected during LL97. The spectral behaviour was also investigated in a slightly different fashion by Willoughby (1998), by looking at a quantity he defined as the compression ratio, $c_f = 1 - \omega/vk\cos\phi$, of the encountered wavenumber to the real wavenumber as a function of vessel velocity, v, and angle, ϕ, between vessel and wave directions.

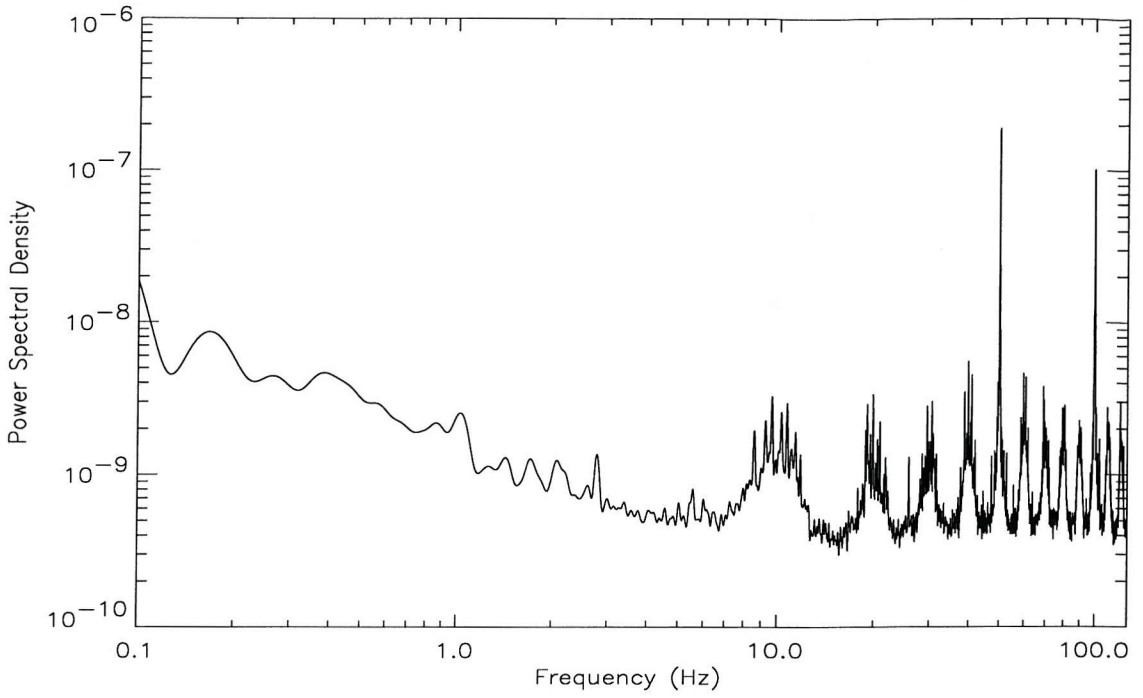

Figure 6-1: Power spectral density of noise file (data collected with the instrument and laser beam out of the water with the beam pointing directly at the screen without moving)

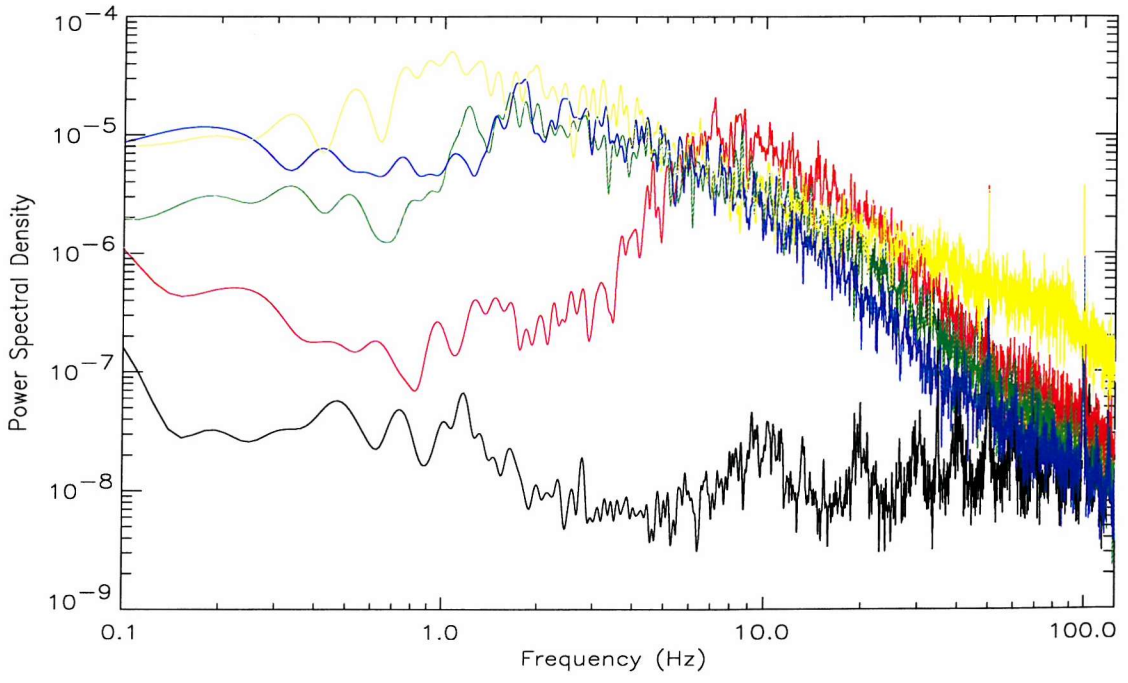

Figure 6-2: Variation of power spectral density with wind speed (in order of increasing wind speed, the colour order is black, red, green, blue, yellow)

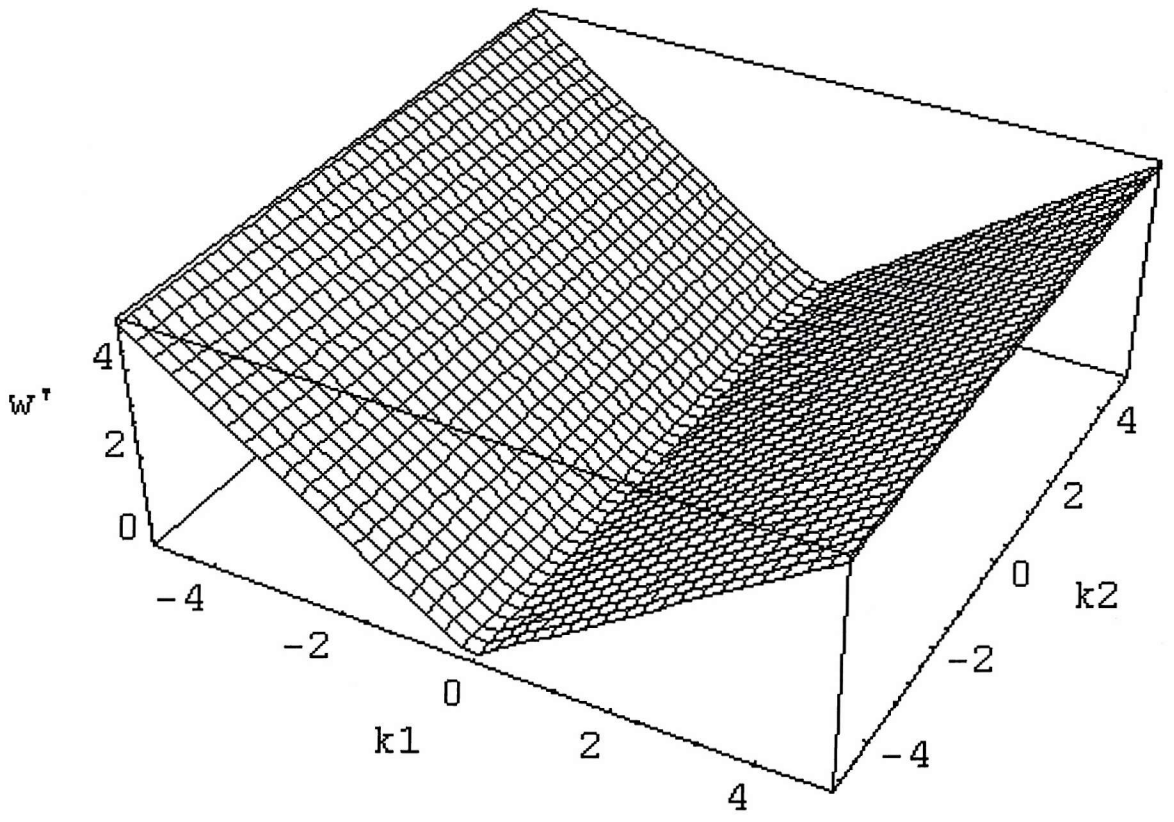

Figure 6-3:Pictorial representation of the functional relationship from wavenumber to the frequency of encounter given by 6-2, assuming a stationary wave field and that the Laser Slope meter is moving along the direction of k_1 at a speed of 1m/s.

If the TLS is considered to be moving much faster than any of the waves (i.e. assuming that the motion of the wave field is frozen) then the frequency of encounter will be related to the component of wavenumber along the direction of travel by 6-2. This is represented in k-space as shown in figure 6-3. In this three-dimensional diagram, the two horizontal axes are the components of the wavenumbers in the wave field; the component, k_1, is chosen to be along the direction of travel of the Laser Slope meter. The vertical axis is the frequency of encounter, ω'.

Even in this much simplified example it is still impossible to relate the frequency of encounter to the real wavenumber of the waves without prior knowledge of the angular distribution of the wind wave field. However, the spectrum of the wavenumber components along the direction of travel of the TLS could be studied. Theoretically, this

involves finding the contribution to the whole spectrum from those particular components. This work is presented in Phillips (1985).

If data of the wind wave field is collected whilst the TLS was stationary, then provided the gravity-capillary dispersion relation is assumed to be true, the frequency of encounter will simply be the intrinsic frequency of the surface waves,

$$\omega' = \omega = \sqrt{gk + \frac{Tk^3}{\rho}} \qquad 6\text{-}6$$

This relationship has also been displayed pictorially in k-space in figure 6-4. Here the surface tension, T, is taken to be to 75.7mN/m which is appropriate for fresh water at 0°C (approximately the temperature in Loch Linnhe) (Kaye and Laby, 1978) and ρ is the density of water equal to 1000kg/m^3. The dispersion relation is independent of direction and is therefore symmetrical about the vertical axis.

By studying figures 6-3 and 6-4 it can be seen that since the towing speed of the TLS is comparable to the wave speeds, it is not reasonable to assume that the TLS is travelling much faster than the waves within the wave field. This means that the frequency of encounter must include the terms for the finite wave speeds and the towing speed of the TLS, given in 6-1. This relationship has been displayed in k-space in figure 6-5 for v=1m/s.

In figure 6-6 a line cut through figure 6-5 along the k_1 axis at k_2=0 is shown. This allows a consideration of only those waves which are travelling parallel or antiparallel to the direction of travel of the TLS. It can be seen that for waves travelling parallel to the Laser Slope meter there are a number of solutions for k_1 for each value of ω'.

A maxima in the gravity wave regime is visible in this plot. There is another in the capillary wave regime, which is shown in figure 6-7. Therefore, for values of ω'<~3.5rad/s, there are six values of k_1 that satisfy the equations. The turning points occur at $\partial\omega'/\partial k$=0; at these points, the group speed of the wave is equal to the TLS speed and so the wave energy

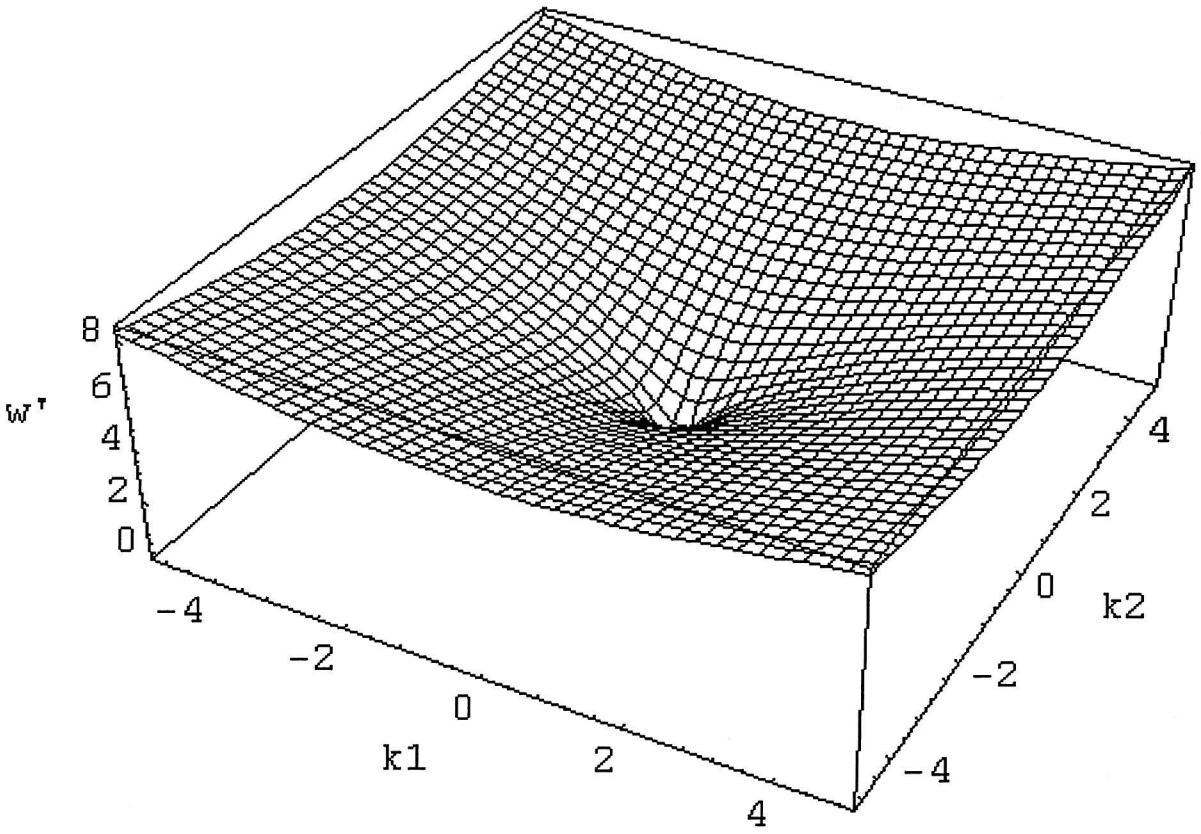

Figure 6-4:Pictorial representation of the functional relationship between wavenumber and frequency of encounter given by 6-6, for the gravity-capillary wave dispersion relation

is stationary with respect to the TLS (this occurs once in the gravity wave region and once in the capillary wave region). When $\omega'=0$, the TLS speed is equal to the phase speed of a particular wavenumber.

Therefore, there are six possible solutions for a particular frequency of encounter, which are for the following wavenumbers:

- waves travelling antiparallel to the TLS;
- wavenumbers in the gravity wave regime travelling in the same direction as the TLS which have group and phase speeds that are faster than the TLS speed;
- gravity waves travelling parallel to the TLS which have group speeds that are slower than the TLS speed but phase speeds which are faster than the TLS speed;

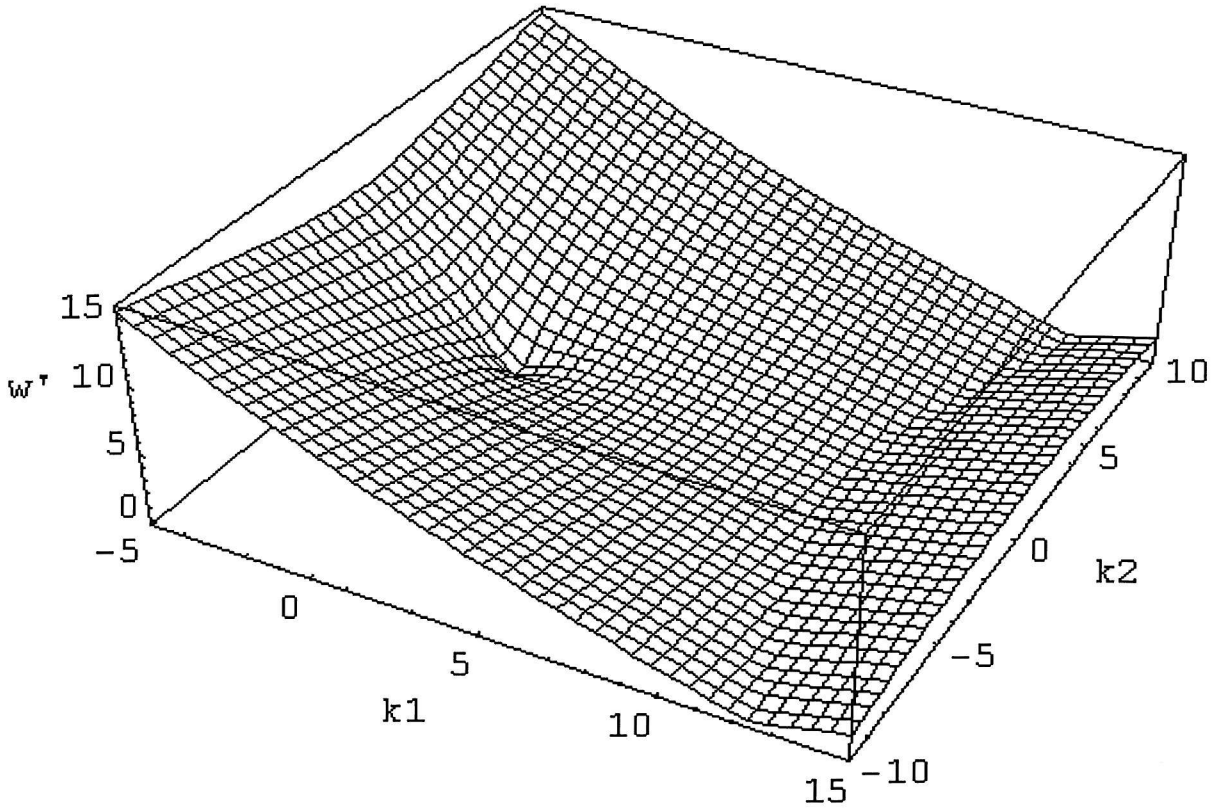

Figure 6-5:Pictorial representation of the functional relationship between wavenumber and the frequency of encounter given by 6-1, assuming the wave field has waves moving at finite speeds given by the gravity-capillary wave dispersion relation

- waves travelling parallel to the TLS which group and phase speeds which are slower than the TLS speed;
- capillary waves travelling parallel to the TLS which have group speeds faster than the TLS speed but phase speeds which are slower than the TLS speed;
- capillary waves with group and phase speeds which are faster than the TLS speed.

It must be emphasised that these multiple solutions are a consequence of the relative speeds of the waves and the Laser Slope meter and not due to aliasing resulting from the finite sampling. Even if continuous sampling was possible all of these solutions would still exist.

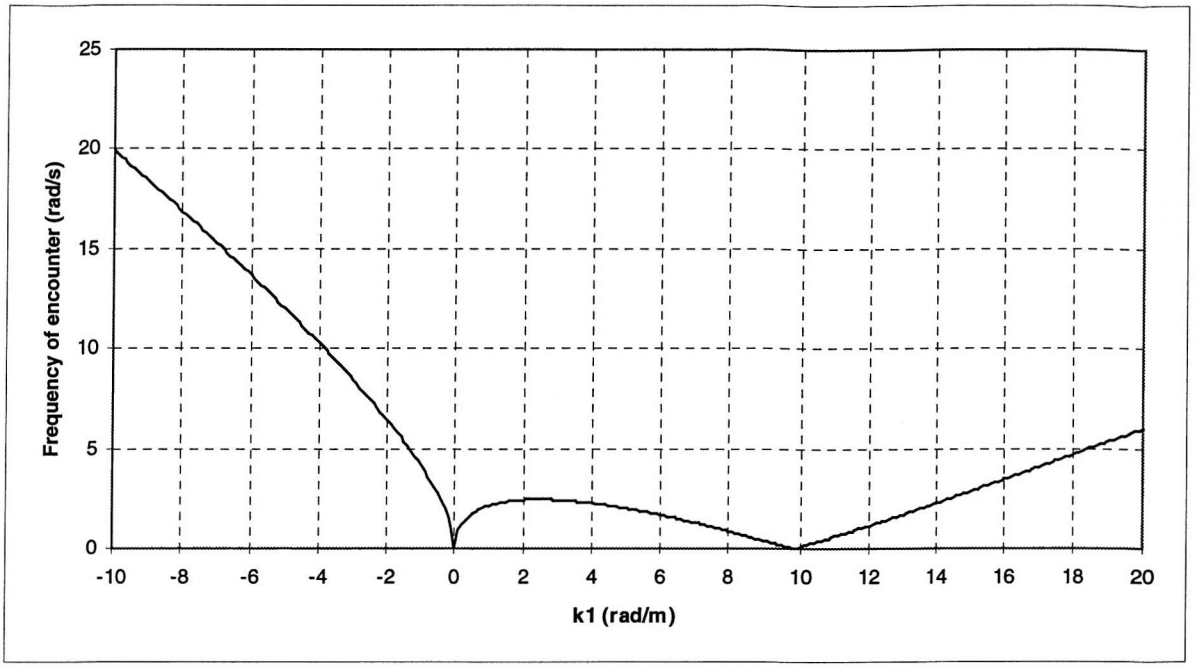

Figure 6-6:Line cut through figure 6-5 along the k_1 axis showing the multiple solutions of k_1 that may be obtained for one value of the frequency of encounter, due to the speed of gravity waves

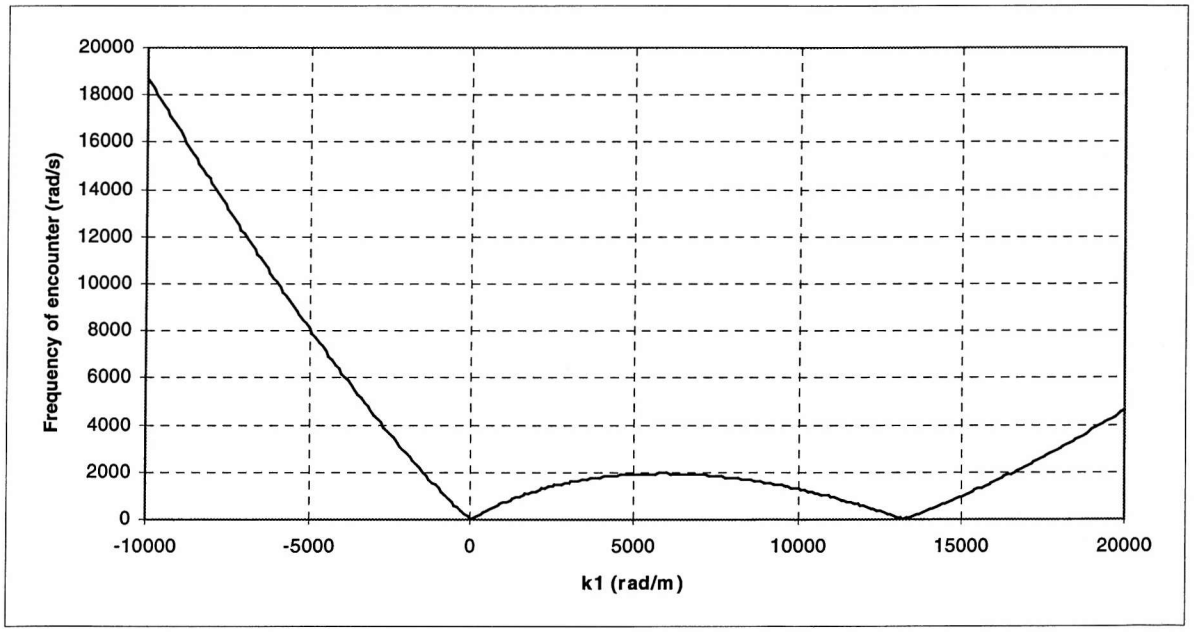

Figure 6-7:Line cut through figure 6-5 along the k_1 axis, for a larger range of k_1 than figure 6-6, showing the multiple solutions of k_1 for one value of the frequency of encounter, due to the speed of the capillary waves

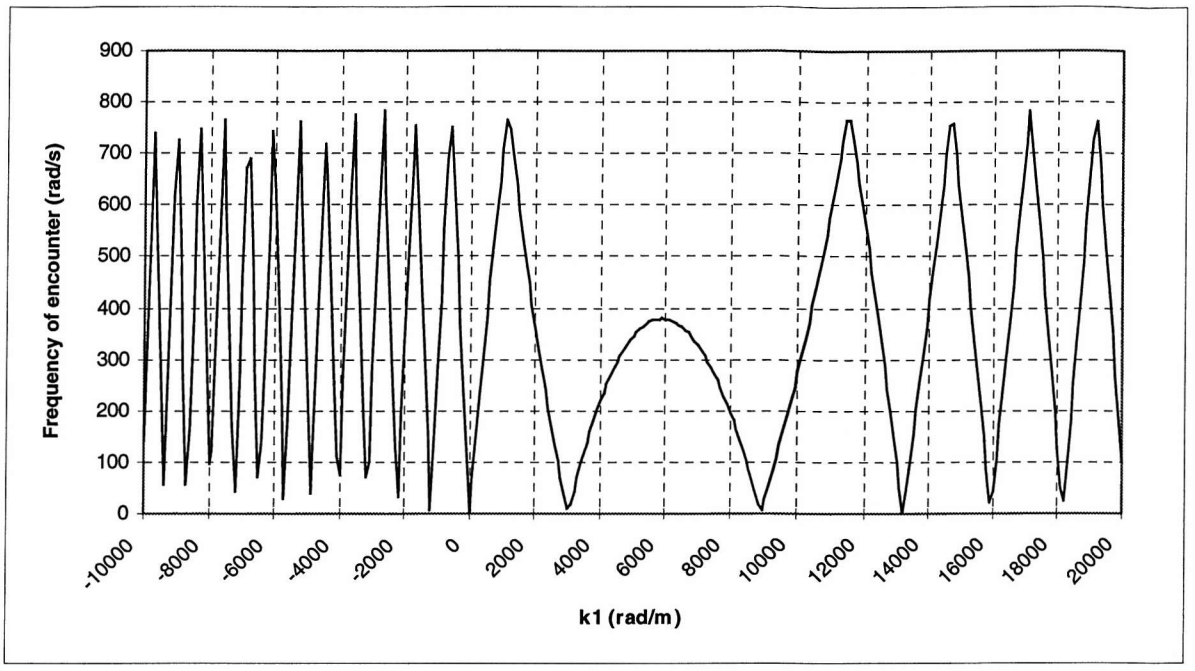

Figure 6-8:Reproduction of figure 6-7 showing the effects of aliasing for the Laser Slope meter moving at 1m/s and sampling at 250Hz

6.3.3 Bulk currents

The ambiguities can be further confused if the waves are travelling in the presence of a current. In this case the current causes velocity of all of the waves to change by the same amount relative to the TLS. This may be considered to be effectively causing the speed and direction of the Laser Slope meter to vary. 6-7 demonstrates how a current of magnitude and direction, $\underline{U}$, can be included in the relationship.

$$\omega' = \left|\omega - \underline{k}.\underline{v} + \underline{k}.\underline{U}\right| \qquad 6\text{-}7$$

The effect of a current will not be considered further here.

6.3.4 Data ambiguities caused by aliasing

In order to demonstrate the effect of aliasing, figure 6-6 has been redrawn in figure 6-8 with all frequencies above f_{max}=sampling frequency/2 mapping back onto smaller frequencies. f_{max} has been calculated for a sampling rate of 250Hz and a towing speed of 1m/s. It can be seen from this diagram that aliasing causes further ambiguities in the quest

for an $\omega' \rightarrow k$ transformation. This will only become important if a significant amount of energy is contained in those frequencies greater than f_{max} (i.e. in this case 125Hz).

6.4 Previous solutions to the problem

6.4.1 Introduction

The mapping between ω' and k is 1-many, which causes difficulties in transforming from the ω' spectrum to the k spectrum. If all the waves travelled directly towards the TLS then the mapping would be 1-1 and the transformation would be trivial. The mapping can be reduced to a form in which the transformation can be made if it is assumed that the angular distribution of the waves is known and their direction of travel is restricted to be within ±90° antiparallel to the TLS towing direction. It must also be assumed that no aliasing occurs. Recent experiments have shown that although a small proportion of the wave energy travels opposite to the wind direction, most of the energy travels within ±90° of the wind direction (Hara *et al.*, 1997). If the angular distribution for the waves with respect to the wind is assumed to be of a particular form and the TLS is driven antiparallel to the wind direction then, ignoring aliasing, it may be possible to determine a relationship between ω' and k. Previous attempts to convert the Doppler shifted spectrum to a real spectrum are reviewed here and the work is extended to the data from the TLS.

6.4.2 The method of Cartwright (1963)

Cartwright (1963) proposed a method for improving the accuracy of the measurement of the wavenumber energy spectrum measured by a wave recording buoy from a moving ship. Even when the ship was stationary, the limitations of the method meant that errors were introduced into the spectrum because of effects caused by the ship, which were a function of the wavenumber, k. These errors could be removed using a second spectral measurement taken with an accelerometer, assuming that $\omega'^2=\omega^2=gk$. When the ship was moving, this relationship was no longer valid and it was necessary to know the angular distribution of the wave field to convert between ω' and k. Cartwright's method involved assuming that the angular distribution was the same over a wide region of sea so that an angular distribution measured in a single location could be applied to the data taken from the moving ship. He used the angular harmonics of an accelerometer measurement at a single location to determine an estimate for the angular distribution, making the assumption that,

since only long wave were of interest, the energy would be confined to a fairly narrow angular band at each frequency. The angular distribution was then used to convert the frequency of encounter into wavenumber to determine an estimate of the wavenumber energy spectrum from the wave recording buoy.

6.4.3 The method of Hughes (1978)

Hughes and Grant (1978) deployed a single point surface slope measuring device to the TLS in the Georgia strait, Canada, through a ship generated internal wave field. They needed background wavenumber spectra in order to calculate the variations in the spectrum caused by the presence of the internal waves. During Hughes' analysis (Hughes, 1978) he did not specifically select data for which his laser slope instrument was heading into the wave direction. However, he found that the solutions to his equations were only stable for those runs where this was found to be true. The research presented in section 6.3 shows why this is the case.

Hughes showed that the frequency of encounter and wavenumber spectra for the along track slope, $S_1(\omega')$ and $k_1^2\Psi(k_1,k_2)$ respectively, can be related simply by assuming a modified dispersion relation which takes into account the motion of the TLS.

$$S_1(\omega') = \int_{-\infty}^{\infty}\int_{-\infty}^{\infty} k_1^2\Psi(k_1,k_2)\delta(\omega' - \omega + k_1 v)dk_1dk_2 \qquad 6\text{-}8$$

where $\omega = \sqrt{g\sqrt{k_1^2 + k_2^2}}$. This equation simply says that the energy in a frequency of encounter, ω', is equal to the sum of the energies contained in certain wavenumber components. These components are those which satisfy $\omega' = \omega - \underline{k}.\underline{v}$. It can be seen that this relationship is energetically consistent by integrating each side with respect to ω' (rearranging the order of the integrals on the right hand side of the equation.

$$\int S(\omega')d\omega' = \int_{-\infty}^{\infty}\int_{-\infty}^{\infty} k_1^2\Psi(k_1,k_2)\int \delta(\omega' - \omega + k_1 v)d\omega' dk_1dk_2 = \int_{-\infty}^{\infty}\int_{-\infty}^{\infty} k_1^2\Psi(k_1,k_2)dk_1dk_2 \qquad 6\text{-}9$$

Each side of 6-9 represents the total slope squared along the 1st axis within the wave field and so the equation balances.

Since a laser slope meter can only measure positive ω', the measured frequency component is actually the sum of the contributions from $\pm\omega'$. $+\omega'$ represents waves travelling opposite to the TLS or waves travelling in the same direction as the TLS but faster than it so that they overtake the instrument. $-\omega'$ represents waves which are travelling in the same direction as the TLS but slower than it so that the TLS is overtaking them. Therefore, the measured slope frequency spectrum $S_{ml}(\omega')$ is given by:

$$S_{ml}(|\omega'|) = S_1(\omega') + S_1(-\omega') = \int_{-\infty}^{\infty}\int_{-\infty}^{\infty} k_1^2 \Psi(k_1, k_2)\delta(\pm\omega' - \omega + k_1 v)dk_1 dk_2 \qquad 6\text{-}10$$

where $\delta(\pm\omega' - \omega - k_1 v) = \delta(+\omega' - \omega - k_1 v) + \delta(-\omega' - \omega - k_1 v)$.

Hughes continued by assuming a particular angular form for the background wavenumber spectrum,

$$\Psi(k,\phi) = A_q \psi(k)\cos^q\left[\frac{(\phi - \phi_w)}{2}\right] \qquad 6\text{-}11$$

where q can be obtained from solving 6-12, where σ_c, σ_u are the rms cross and along wind slopes, respectively,

$$\frac{\sigma_c^2}{\sigma_u^2} = \frac{\int_0^{\pi} \sin^2\phi\cos^q\left(\frac{\phi}{2}\right)d\theta}{\int_0^{\pi} \cos^2\phi\cos^q\left(\frac{\phi}{2}\right)d\theta} = \frac{4(q+1)}{q^2 + 2q + 4} \qquad 6\text{-}12$$

and,

$$A_q^{-1} = \int_0^{2\pi} \cos^q\left(\frac{\phi}{2}\right) d\phi \qquad 6\text{-}13$$

This leads to an equation for $S_{ml}(|\omega'|)$, 6-14, in terms of the wavenumber spectrum and the known quantity, $\Pi(k,\omega')$. It is a standard linear singular Fredholm integral equation of the first kind. The required wavenumber spectrum can be calculated from the inverse of this integral equation.

$$S_{ml}(|\omega'|) = \int_0^{\infty} \psi(k)\Pi(k,\omega')dk \qquad 6\text{-}14$$

6.4.4 The method of Willoughby (1998)

Willoughby (1998) suggested that a true wavenumber spectrum could be reconstructed from a frequency of encounter spectrum if both smoothed wave slope and wave height Doppler shifted spectra were measured. It was suggested that as the data ambiguities would be the same in both of these spectra due to the vessel motion, it would be possible to remove the ambiguities from one of the spectra using information provided by the other spectrum. Unfortunately, as the TLS does not provide wave height information, he was not able to investigate his method further.

Considering the method suggested by Willoughby, it does not seem possible that such a height measurement could provide sufficient information to extract a wavenumber spectrum from the two components of slope spectra. The height data will provide one-dimensional information which can not be used to extract two-dimensional variations from two-dimensional data. This is because there are insufficient equations for a solution of all the unknown quantities.

However, Willoughby (1998) did produce a wave slope spectrum simulation model that could be used to simulate the type of hybrid spectrum that would be measured by the TLS if the background spectrum was known and input into the model. In his investigations he used spectra suggested by Phillips (1958, 1985) to produce spectra along a TLS transect. This model could be used with varying input spectra to find the closest match to the spectra

measured by the TLS and thus estimate the true wavenumber spectrum in this reverse fashion.

6.5 Development of Hughes' method to calculate a wavenumber spectrum

Of the methods described above, the one most applicable to the TLS data is that of Hughes (1978). Here this method is extended and applied to the TLS data collected during the Loch Linnhe experiment. By selecting those TLS runs where the instrument was driven antiparallel to the wind direction, it is shown how this method can be simplified to extract an approximate wavenumber spectrum from a frequency of encounter spectrum.

The method consists of finding a solution for ψ and F in the equation,

$$S_{ml}(|\omega'|) = \int_0^\infty \int_0^{2\pi} k^3 (\cos^2\phi)\psi(k)F(\phi)\delta(\pm\omega' - \omega(k) + vk\cos\phi)d\phi dk \qquad 6\text{-}15$$

where,

$$\omega' = \omega(k) - vk\cos\phi \qquad 6\text{-}16$$

6-15 can be deduced from 6-10 under the assumption that $\Psi(k_1,k_2) = \psi(k)F(\phi)$. This equation is valid where $S_{ml}(|\omega'|)$ is the measured frequency of encounter along-track slope spectrum. If the total slope component frequency spectrum was used, the equation would take the same form but $k^2\cos^2\phi$ would be replaced simply by k^2.

This equation can be approximated by a matrix relation which allows the inversion of the equation in a relatively straightforward manner. Examination of the signal $S_{ml}(|\omega'|)$ shows that it tends to the noise level fairly rapidly as $\omega' \to \infty$. It is also expected that $\psi(k)$ will tend to zero as $k \to \infty$ and so interest can be restricted to a finite range of ρ and k without introducing significant errors. Between 0 and ω'_{max}, the Nyquist frequency determined by the sampling frequency of the TLS, the frequencies are divided naturally into a finite

number of equal sections, by the DFT, with each $S_{ml}(|\omega'|)$ representing the contribution to the slope squared along the 1st axis in a frequency range of $\Delta\omega'$. The k's can also be divided up into (unequal) sections allowing $\psi(k)$ to represent the energy in a wavenumber range Δk. In the given ranges of ω' and k, $S_{ml}(|\omega'|)$ is defined as,

$$S_{ml}\left(|\omega'|\right)_{\substack{\omega'_n\to\omega'_{n+1}\\ k_m\to k_{m+1}}} = \frac{1}{\Delta\omega'_n}\int_{\omega'_n}^{\omega'_{n+1}}\int_{k_m}^{k_{m+1}}\int_0^{2\pi} k^3\left(\cos^2\phi\right)\psi(k)F(\phi)\delta(\pm\omega' - \omega(k) + vk\cos\phi)\,d\phi\,dk\,d\omega' \qquad 6\text{-}17$$

where $\Delta\omega' = \omega'_{n+1} - \omega'_n$. The integral over ω' can be evaluated first and this defines the limits on the integral over ϕ in terms of the zeroes of the arguments of the delta function. Therefore,

$$S_{ml}\left(|\omega'|\right)_{\substack{\omega'_n\to\omega'_{n+1}\\ k_m\to k_{m+1}}} = \frac{1}{\Delta\omega'}\int_{k_m}^{k_{m+1}}\int_{R(\delta)} k^3\left(\cos^2\phi\right)\psi(k)F(\phi)\,d\phi\,dk \qquad 6\text{-}18$$

Where $R(\delta)$ represents the range of ϕ that satisfies $\pm(-\omega(k) + vk\cos\phi) \in (\omega'_n, \omega'_{n+1})$.

At this point, the method differs slightly from that used by Hughes. In order to evaluate the integrals over k and ϕ independently, it is necessary to approximate the value of k to be the central value, k_c, over the range of k in Δk. Therefore, it is assumed that,

$$S_{ml}\left(|\omega'|\right)_{\substack{\omega'_n\to\omega'_{n+1}\\ k_m\to k_{m+1}}} = \frac{\psi(k_c)k_c^{\,3}\Delta k_m}{\Delta\omega'}\int_{R(\delta)}\left(\cos^2\phi\right)F(\phi)\,d\phi \qquad 6\text{-}19$$

where k is taken equal to k_c in the definition of $R(\delta)$. This equation defines the elements to use in the matrix approximation of the integral that can be inverted to determine an estimate of the wavenumber spectrum. If,

$$I(\phi) = \int_{R(\delta)}\left(\cos^2\phi\right)F(\phi)\,d\phi \qquad 6\text{-}20$$

then,

$$\begin{pmatrix} S_{ml}(|\omega'|)_1 \\ S_{ml}(|\omega'|)_2 \\ \cdots \\ \cdots \end{pmatrix} = \begin{pmatrix} \frac{k_{c1}{}^3 \Delta k_1}{\Delta\omega'} I(\phi)_{11} & \frac{k_{c2}{}^3 \Delta k_2}{\Delta\omega'} I(\phi)_{12} & \cdots & \cdots \\ \frac{k_{c1}{}^3 \Delta k_1}{\Delta\omega'} I(\phi)_{21} & \cdots & \cdots & \cdots \\ \cdots & \cdots & \cdots & \cdots \\ \cdots & \cdots & \cdots & \cdots \end{pmatrix} \begin{pmatrix} \psi(k_{c1}) \\ \psi(k_{c2}) \\ \cdots \\ \cdots \end{pmatrix} \qquad 6\text{-}21$$

The elements of the left hand side of this matrix equation are obtained from the DFT of the along track surface slope data. The elements of the central matrix can also be obtained from the data, with an assumption for the angular distribution of the surface waves and once the k ranges have been defined. The right hand side vector consists of elements of the required wave height wavenumber spectrum.

Here, only angular distributions which allowed waves to travel within ±90° antiparallel to the direction of motion of the TLS are considered. This is in contrast to Hughes who considered an angular distribution of the form,

$$F(\phi) = A_q \cos^q\left(\frac{\phi}{2}\right) \qquad 6\text{-}22$$

for the full range of ϕ. In assuming an angular distribution of only ±90° from the wind direction, the number of ϕ ranges in $R(\delta)$ are reduced from four to two. These are assumed symmetrical about the wind direction, which is taken to be antiparallel to the course travelled by the TLS. Therefore, the calculation need only consider the ϕ range 0° to 90° with the result multiplied by two to provide the correct result.

A pictorial representation of the integration area can be drawn in k-space to show how the approximation relates to the real integral solution. This also helps to determine the optimum k-values for successful matrix inversion and the appropriate limits on the ϕ integrals. A schematic of this integration area is given in figure 6-9. The semi-circles represent lines of constant k and the horizontal lines represent lines of constant ω'. The integration area of any Δk, $\Delta\omega'$ is the overlapping region, shown in the diagram in red and

green. The area used by evaluating $R(\delta)$ for $k=k_c$ is given by the areas in red and blue. It seems likely that the approximation does not introduce a significant error into the calculation. The appropriate ϕ limits can be calculated from,

$$\phi = \cos^{-1}\left(\frac{\omega - \omega'}{vk}\right) \qquad 6\text{-}23$$

using (ω'_{min}, k_c) and (ω'_{max}, k_c) for each interval. The exception for this is for waves moving directly towards the TLS where the upper limit should be replaced by 180°.

For any range of ω', the smallest wavenumber that will contribute will be travelling directly opposite to the TLS. A successful matrix inversion is made more likely if the largest elements are placed along the diagonal elements. The k-values to use in the inversion can be chosen so that they are centred between the ω' values along ϕ=180°. A successful matrix inversion is guaranteed by choosing the angular distribution so that the majority of waves travel opposite to the TLS. This makes the matrix upper triangular with no zeros on the diagonal. Such a matrix always has an inverse.

Three types of angular distribution have been considered:

- a unidirectional wave field with all the waves heading antiparallel to the direction of motion of the TLS;
- a uniform wave field with the energy equal in all directions within ±90° of the wind direction;
- a $\cos^2\phi$ distribution centred antiparallel to the direction of motion of the TLS.

None of these distributions is expected to model accurately the actual wave field. However, they do provide some insight into the amount of error that is likely to be caused by choosing an incorrect angular distribution. This differs from Hughes method where he used knowledge of the ratio of the along wind to cross wind mean square slope to help determine the form of the angular distribution. This has not been used here as the clarity of along wind to cross wind results is not good, as discussed in chapter 5.

A program was written in IDL to calculate the wavenumber spectrum from the TLS data collected at LL97. The matrix formation given above was implemented, and IDL's inverse matrix routine was used to invert M. A similar technique was employed to calculate the wavenumber spectrum from the total slope spectrum instead of the along track slope spectrum. The frequency of encounter power spectrum was calculated using the method described in section 6.2. Again, the number of degrees of freedom used was 100. Graphs displaying the results of the calculations for a number of different wave fields for each angular distribution are shown in figures 6-10 to 6-13. These graphs are plotted as k^4 multiplied by the PSD versus the wavenumber. The gravity wave dispersion relation has been used in the matrix conversion and so the solutions are valid only for gravity waves, up to k≈150rad/m. This type of matrix inversion technique is not always a good representation of the integral inversion and so care must be taken when considering the results.

Only four data files were collected in ambient conditions with the TLS motion antiparallel to the wind direction. However, these covered a wind speed range from 0.83m/s to 4.47m/s and thus provide information on the variation of the behaviour of the spectrum and the effectiveness of the technique with wind speed.

Considering the differences between the two forms of wave height wavenumber spectra produced by each form of angular distribution, can indicate whether or not the angular distribution may be similar to the actual angular distribution of the wave field. If the distribution and frequency of encounter spectra were perfect than the two forms of wave height wavenumber spectra would be identical. It can be seen that a uniform angular distribution does not provide consistent wave height spectra for the along wind and total slope calculations which suggests this distribution is not similar to the actual distribution. The unidirectional distribution wave height spectra for the along track and total slope components are more similar than when a uniform distribution was considered. However, the estimated wave height spectra from the $\cos^2\theta$ distribution are very similar which suggests this may be a reasonable estimation of the angular distribution of the wind wave field, and appears to be the most physical out of the three distributions considered. This type of distribution is fairly directional along the wind direction but does allow some component of the wave field to travel at an angle to the wind direction.

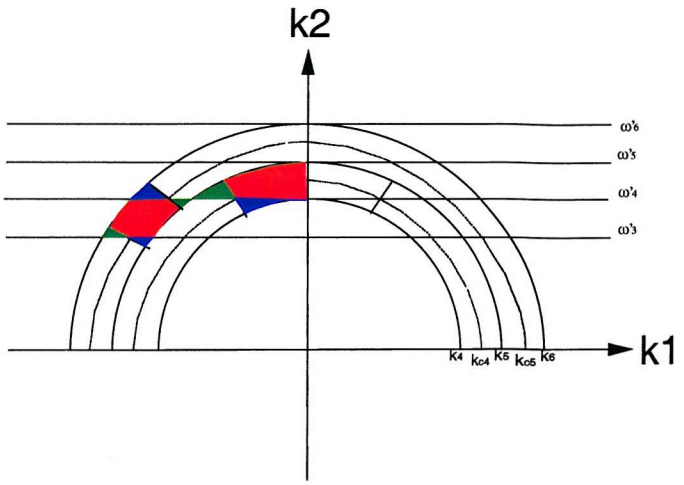

Figure 6-9: Representation of integration areas in k-space. The semi-circles represent lines of constant k and the horizontal lines represent lines of constant ω′. The integration area of any Δk, Δω′ is the overlapping region, shown in the diagram in red and green. The area used by evaluating R(δ) for k=k_c is given by the areas in red and blue.

At the three highest wind speeds, a clear spectral peak can be seen in the plots of the frequency of encounter spectra in both the total slope and the along wind slope component. The lowest wind speed has a frequency of encounter spectrum characteristic of pure noise.

Cross wind slope frequency of encounter spectra were not used alone in this calculation as the matrix inversion was found to be unstable. The spectral peak is translated into the wavenumber spectrum. The fall off of the spectrum is easily demonstrated by this plotting method to follow approximately a k^{-4} law over the central region. Small wavenumber behaviour is dominated by residual DC errors in the spectral calculation. Large wavenumber behaviour, above approximately 150rad/m, are not valid results of this method as the gravity wave dispersion relation was assumed, which is not applicable for such short wavelengths.

The approximate position of the peak of the wavenumber spectrum has been studied and wavelength at the peak versus wind speed has been plotted for the higher three wind speeds considered. The precise position of the peak is difficult to distinguish and so an

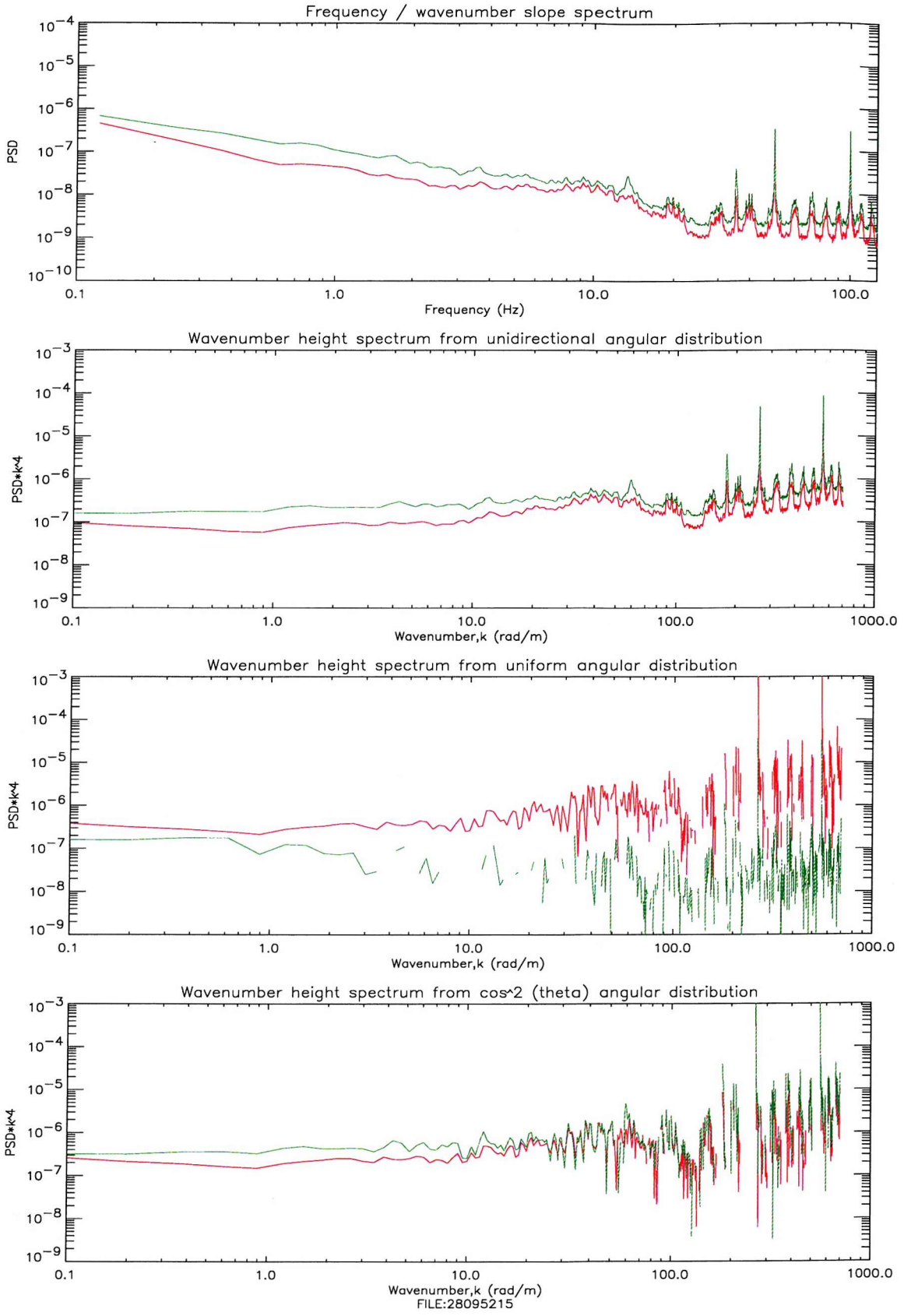

Figure 6-10: Frequency / wavenumber spectra and estimated wave height spectra assuming a unidirectional angular distribution (second graph), a uniform angular distribution (third graph) and a $\cos^2\phi$ distribution (fourth graph) for file 28095215 with average wind speed of 0.83m/s, total slope in green and along-track slope in red

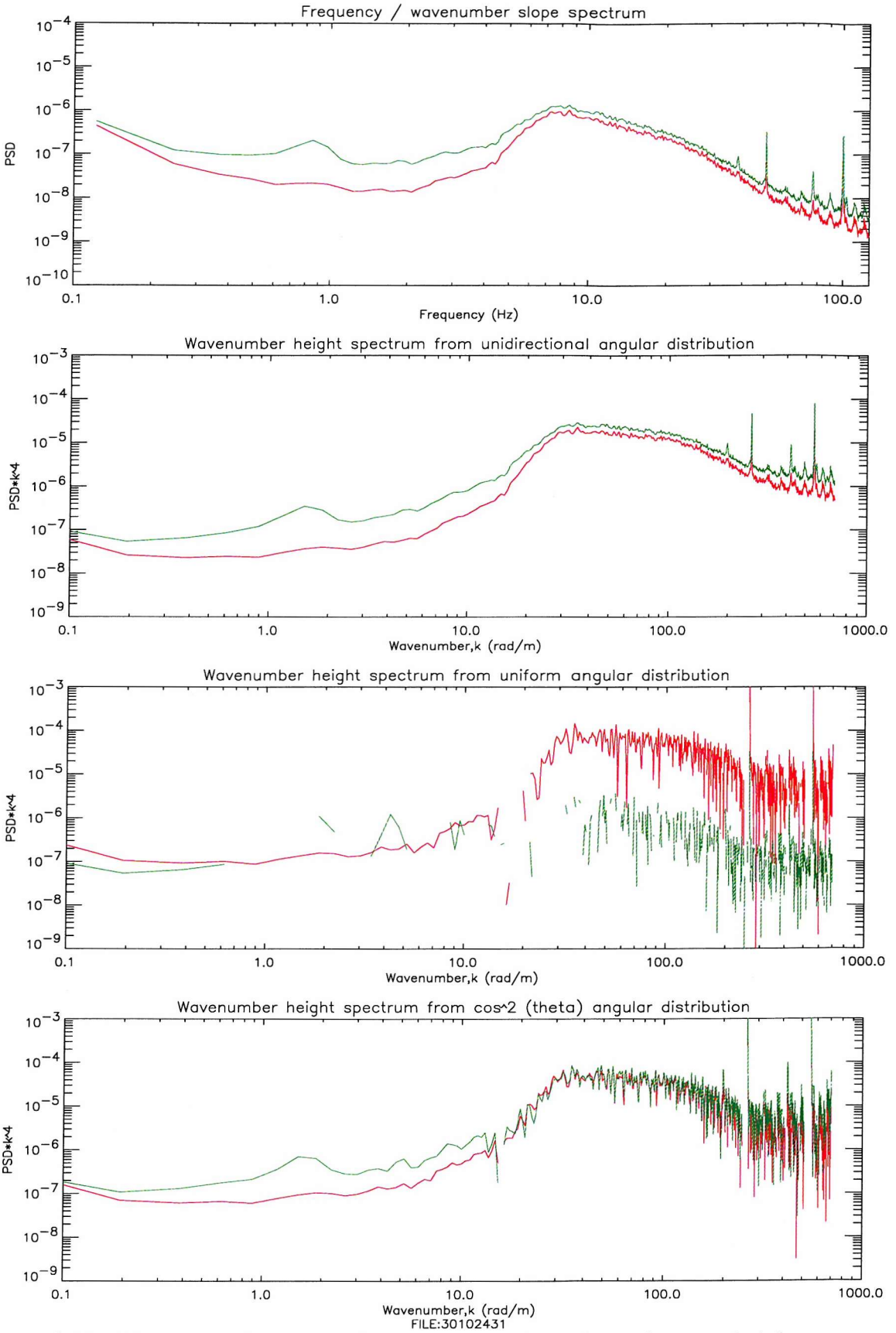

Figure 6-11: Frequency / wavenumber spectra and estimated wave height spectra assuming a unidirectional angular distribution (second graph), a uniform angular distribution (third graph) and a $\cos^2\phi$ distribution (fourth graph) for file 30102431 with average wind speed of 2.86m/s, total slope in green and along-track slope in red

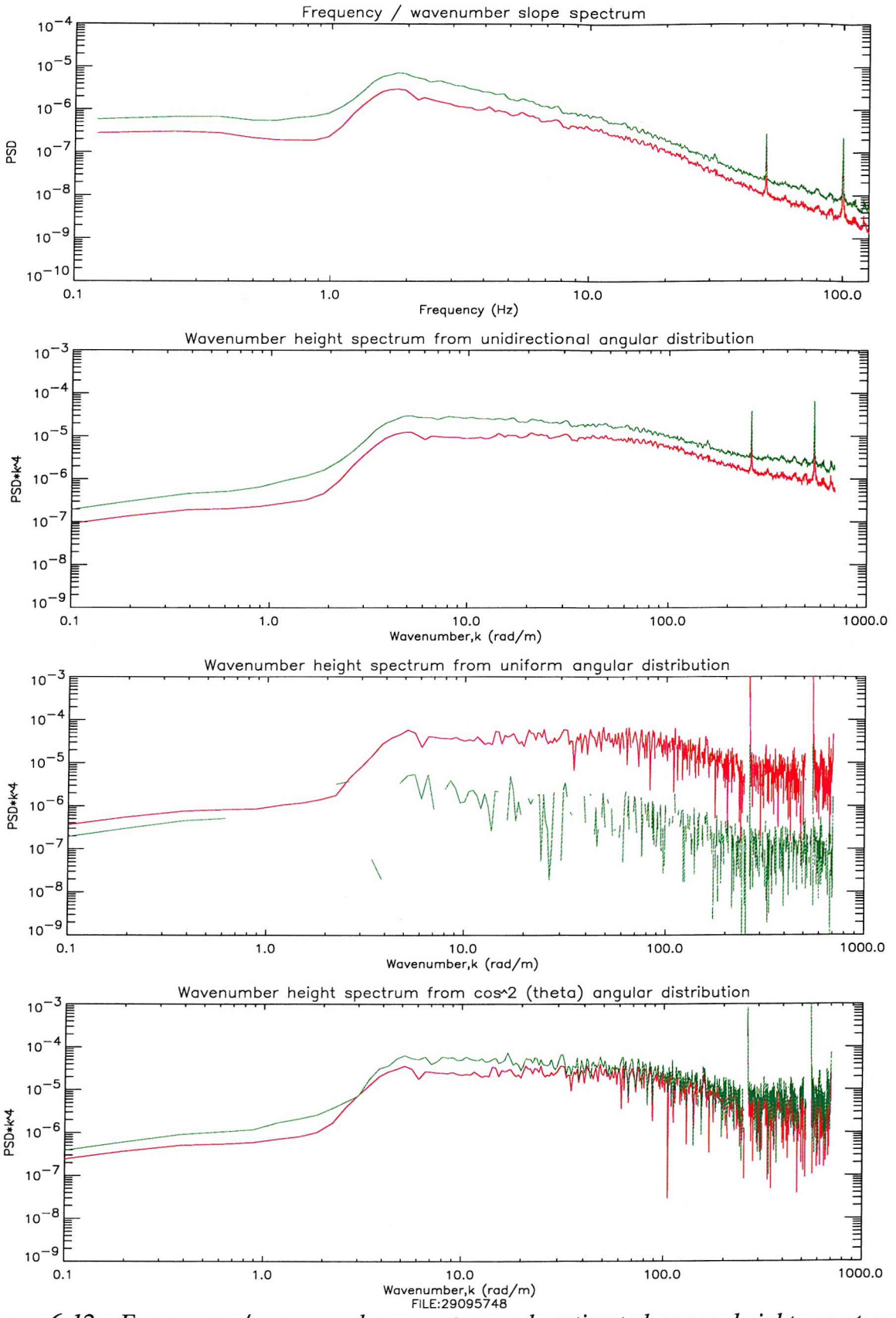

Figure 6-12: Frequency / wavenumber spectra and estimated wave height spectra assuming a unidirectional angular distribution (second graph), a uniform angular distribution (third graph) and a $\cos^2\phi$ distribution (fourth graph) for file 29095748 with average wind speed of 3.22m/s, total slope in green and along-track slope in red

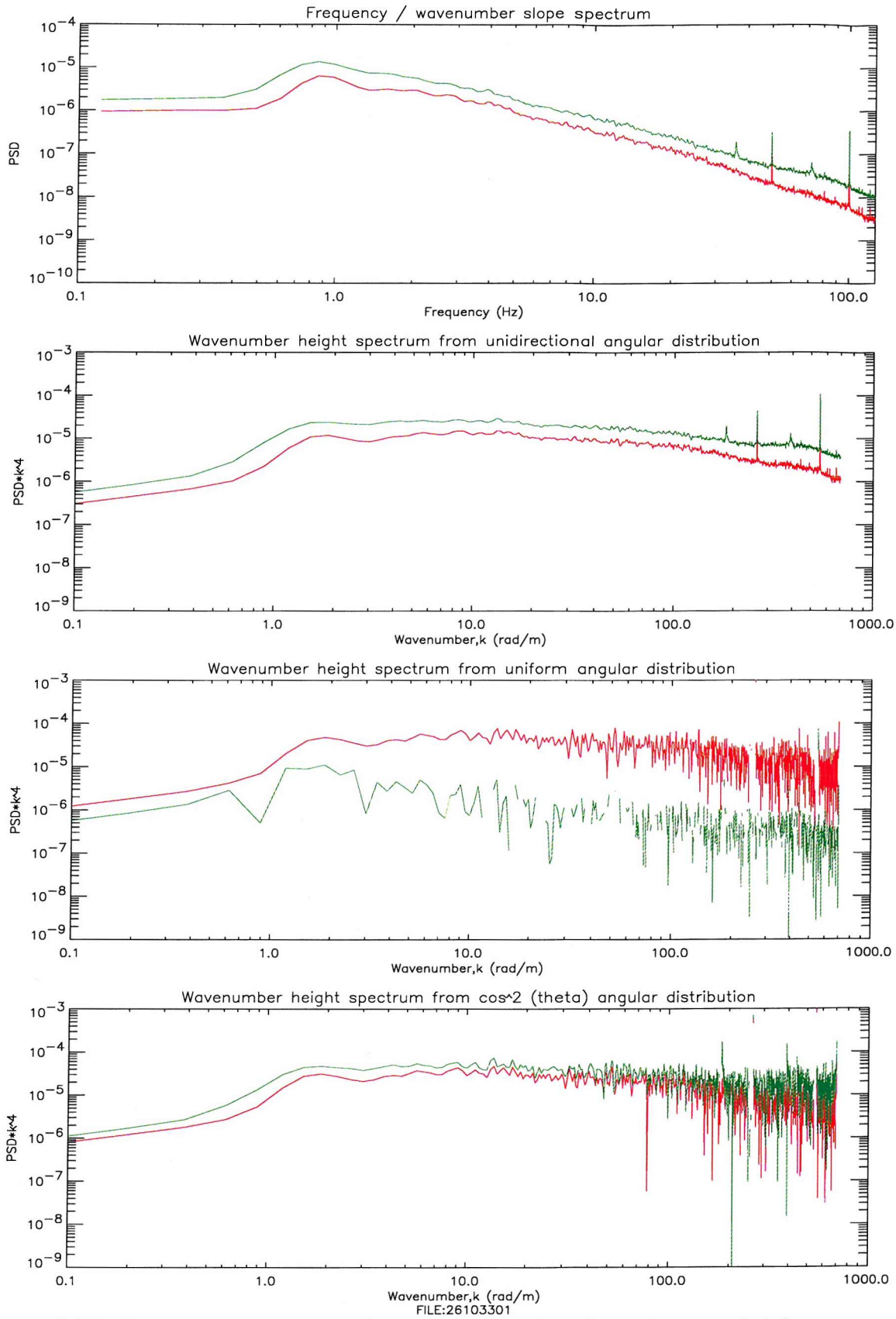

Figure 6-13: Frequency / wavenumber spectra and estimated wave height spectra assuming a unidirectional angular distribution (second graph), a uniform angular distribution (third graph) and a $\cos^2\phi$ distribution (fourth graph) for file 26103301 with average wind speed of 4.47m/s, total slope in green and along-track slope in red

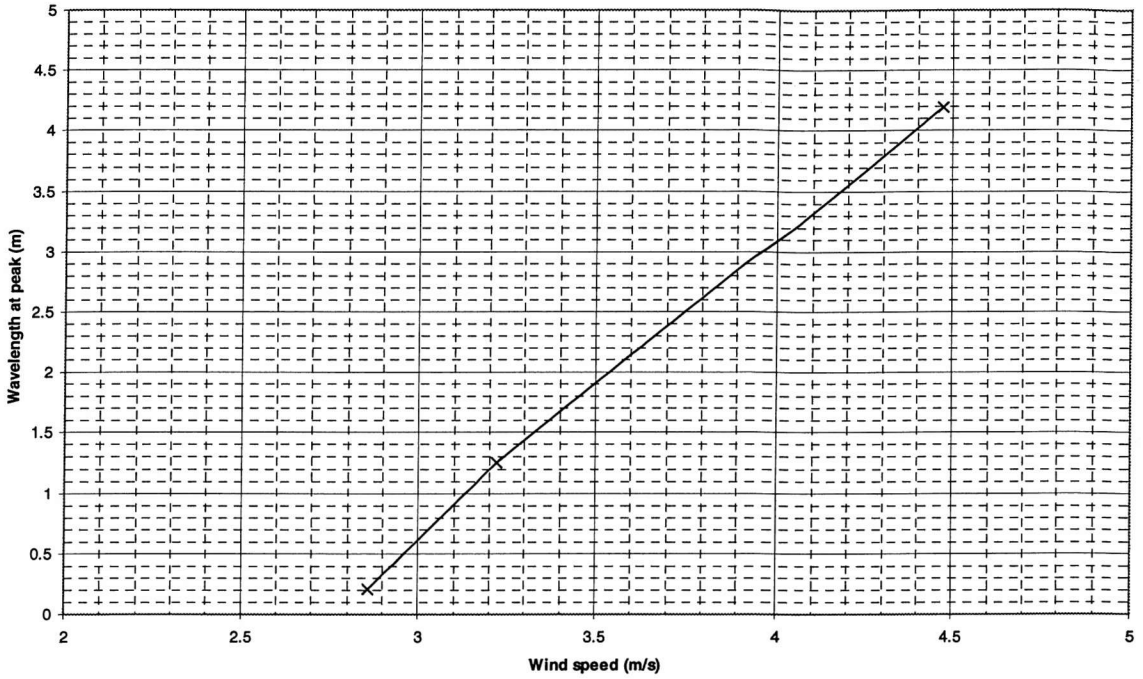

Figure 6-14: Variation of wavelength at peak of wavenumber spectra versus wind speed. Peak of spectra measured from graphs 6-10 to 6-13.

approximate position has been selected visually from the graphs. This is displayed in figure 6-14. The three available data points show a straight line behaviour. However, extrapolation of the fit would not go through the origin. With only three data points and the errors associated with the assumptions and method involved in the estimates of the wavenumber spectra, it is not realistic to form strong conclusions about the behaviour of the peak of the spectrum.

There has been considerable effort invested, both theoretically and experimentally, in determining the form of the wavenumber spectrum of the ocean. Many of the papers are reviewed in chapter 3 and so the work is just summarised here. Theoretically, most notably there have been two forms suggested for the decay of the wavenumber spectrum; k^{-4} and $k^{-3.5}$. The k^{-4} distribution was determined by Phillips (1958) on dimensional grounds by postulating that the spectrum would be determined by the physical parameters that governed the discontinuity of the surface at the breaking point, and would therefore depend only on g and k. This same result was reached by Toba (1972, 1973) based on the concepts of local balance and spectral similarity. Kitaigorodskii (1983) suggested that there may be a

Kolmogoroff subrange (where the gravitational instability is not important) where the spectrum varies as $k^{-3.5}$; where gravitational instability was important, the k^{-4} spectrum would remain. Phillips (1985) later considered an action balance approach which led to the $k^{-3.5}$ spectrum found by Kitaigorodskii. However, later Banner *et al.* (1989) showed this same energy balance could also lead to other spectra one of which was the original k^{-4} spectrum. Belcher and Vassilicos (1997) also found a wavenumber spectrum of k^{-4} based on their theory, which is described in chapter 3.

Experimentally, Banner *et al.* (1989), Stilwell and Pilon (1974), Lubard *et al.* (1980) and Jahne and Reimer (1990) have all made measurements of the ocean wavenumber spectrum which were consistent, at least in part, with a k^{-4} spectrum.

The results presented here cover a wind speed range of 0.87 to 4.47m/s. As only four data sets were collected in ambient conditions with the TLS motion antiparallel to the wind direction, it is difficult to be sure about the consistency of the results. However, similar files collected where internal waves were present but where they were not obvious on the water surface, demonstrate similar behaviour to the files shown here. It can be seen that, as the wind speed increases, the spectrum increases from below the instrument noise level to well above it. The peak of the spectrum shifts to larger wavelengths. Each estimated wavenumber spectrum, except for the lowest wind speed, has a section of data where the spectrum varies as k^{-4}, which appears as a horizontal section on these graphs. This section increases to include lower wavenumbers as the wind speed increases. At the high k-end of the spectrum the behaviour changes. This is not unexpected as data above approximately 150rad/m is well into the gravity-capillary range and so is not valid for this method, which assumes a gravity dispersion relation.

The observed behaviour of a spectrum varying as k^{-4} is consistent with many of the results of other experiments as summarised above. As various theories are split in their support of a spectrum varying as k^{-4} or $k^{-3.5}$, this latter form should also be investigated here. Although no graph is drawn here explicitly to determine whether these results could support a $k^{-3.5}$ spectrum, it should be noted that if this was the case, there would be a region on these graph with a gradient of $k^{-3.5}k4=k^{0.5}$. This is clearly not the case as no part of the spectra

show a positive gradient in the expected range. Therefore, these data also support the theoretical results which suggest the spectrum decays as k^{-4}.

6.6 Summary and Conclusions

In this chapter the capability of the Laser Slope meter for measuring the wavenumber spectrum of the ocean surface wave field has been investigated. In order to gain some form of spatial information, the instrument has been towed through the wave field. The possibility of calculating a wavenumber spectrum from two-dimensional surface slope data collected by the TLS along this transect has been presented and discussed. Consideration has been given as to whether or not useful information can be gained from the spectrum with respect to the frequency of encounter. It has been shown that, unless the towing speed is much faster than the wave speeds, the frequency of encounter can not be related with certainty to any component of a naturally formulated surface property such as the wavenumber, and so does not provide useful material on the way in which the energy is distributed at the ocean surface.

Data ambiguities which arise from towing the TLS slowly across a moving wave field have been considered. It has been shown that those ambiguities can be reduced by towing antiparallel to the wind direction. This information has been used to collect suitable data sets for a trial calculation of the wavenumber spectrum. This is an improvement over previous attempts, for example Hughes and Grant (1978), where the data were not collected with the instrument moving anti-parallel to the wind direction, leading to ambiguities.

Hughes' matrix method has been extended and simplified and used to convert between a frequency of encounter spectrum and a wavenumber spectrum. This method has been used to convert four data sets over a range of wind speeds. The lowest wind speed has not provided much information as its spectral level is similar to the noise level of the instrument. However, the other three files have produced wavenumber spectra which show a k^{-4} behaviour in the saturation range of the spectrum. As the wind speed increases, the peak of the spectrum moves to lower wavenumbers, as expected. For this small data sample, there is a straight line relationship between the wavelength at the peak of the spectrum and the wind speed. In this analysis, the angular distribution of the wave field has

been assumed, rather than measured. It is likely that none of the distributions used is a true description of the angular distribution of the wave field as other experiments (Hara *et al.*, 1997) have shown this to vary with wavenumber, sometimes to become double peaked and that a small portion of the energy does move against the wind direction. However, these assumptions have allowed an exploration of the method of using such data to determine a wavenumber spectrum.

The majority of the research presented in this chapter is applicable to many towed slope measuring instruments. There are several laser slope meters of this kind which have been built, and this research is potentially of use to all of them. The calculated wavenumber spectrum appears to be consistent with that from many other experiments and theoretical results. This gives confidence in the method used here. However, at present, the spectra are only applicable for gravity waves and do not use all the information that is available about the angular distribution. The method is also reliant upon the dispersion relation and may therefore not be appropriate for extension to capillary waves until they are researched further, as will become apparent in chapter 7. The matrix inversion techniques used are known to not always be a good representation of the integral inversion. Therefore, despite the promising results, the method is viewed with caution and needs considerable further investigation before being relied upon, particularly at short length scales. It may be more efficient in future, rather than investigating this further, to move to scanning laser slope meters which can provide the spatial information directly.

Chapter 7

Measurements of ambient wind wave fields in a wave tank

7.1 Introduction and scope of chapter

In this chapter measurements are presented of unmodulated wind wave fields made by the Laser Slope meter at a very high frequency. The experiments were conducted at the wind wave facility at the University of California, Santa Barbara. The Laser Slope meter was situated over the centre of the wave tank in a stationary location situated a few metres from the wind tunnel exit. Under conditions of positive stability, waves generated by wind speeds in the range from 1.6m/s to 12m/s have been measured. The objective of the research was to collect high quality data products which could then be analysed to provide further information about the ambient wave field, and simultaneously to assess the capability of the Laser Slope meter in this type of environment for providing the research results of interest. What distinguishes these experiments from previous measurements of this type is the objective of achieving both a level of accuracy and a data rate which exceed the performance of other equipment reported in the literature.

These data have been collected with the improved instrument described in chapter 2. It should be made clear that two data sets were collected at the wind wave facility. Data set 1 was collected during July and August 1998 and constitutes a very high accuracy set, but with a laser spot size of approximately 2mm. These data are presented throughout the majority of this chapter. Data set 2 was collected during February and March 1999. Although this set was collected with the same instrument, which should have been of the same data quality, poor shipping of the equipment from the UK to the USA caused considerable damage to the instrument and resulted in the laser being completely unusable. A new laser was hired for the experiment, but was old and provided a noisy output. This, together with instrument damage, unfortunately led to data set 2 containing much higher noise and variability than data set 1. However, the data were collected with a laser spot size

of 0.5mm, a significant improvement over the first experiment. Therefore, investigations are presented of the changes in the data caused by the laser spot size and the noise and it is discussed how this affects the data products. This is necessary in order that the results of data set 2 in the surface wave - surface current interaction experiment can be analysed in chapter 9. At each stage of the analysis it will be made clear whether the data presented is from set 1 or 2.

Initially, the statistical and spectral characteristics of the tank data are compared with field measurements taken using the Laser Slope meter and other equipment. They are also compared with theoretical results. The variation of the mean square slope with wind speed and wind friction velocity is investigated, and histograms of the along- and cross-tank components of slope, including a Gram-Charlier analysis of these data, are presented. The effect of the finite laser spot size on the data is examined both theoretically and experimentally, and it is discussed how this may affect the presentation of high frequency spectra. The two data sets were collected in slightly different regions of the wave tank and this factor is discussed with reference to theory and other experiments. Information which may be contained about the angular distribution of the wave field is investigated by considering the cross- and along-tank components of the surface slope spectra. Using this method an attempt is made to estimate the full wavenumber spectrum. Finally, the character of raw time series of the data is studied, examples of capillary waves are identified, and simultaneous data and photographs showing particularly good resolution of group wave features are displayed.

7.2 Variation of mean square slope with wind speed and wind friction velocity

The variation of the mean square slope with wind speed was measured in the wind wave tank using the laser slope meter. The data presented here are from set 1. They were collected throughout the production of the wind wave field to ensure it had reached equilibrium. Measurements were made for approximately 20 minutes at each wind speed and the final section of each data set (approximately 300s of data) were averaged to produce the mean square slope values presented in figure 7-1. The magnitude of the wind

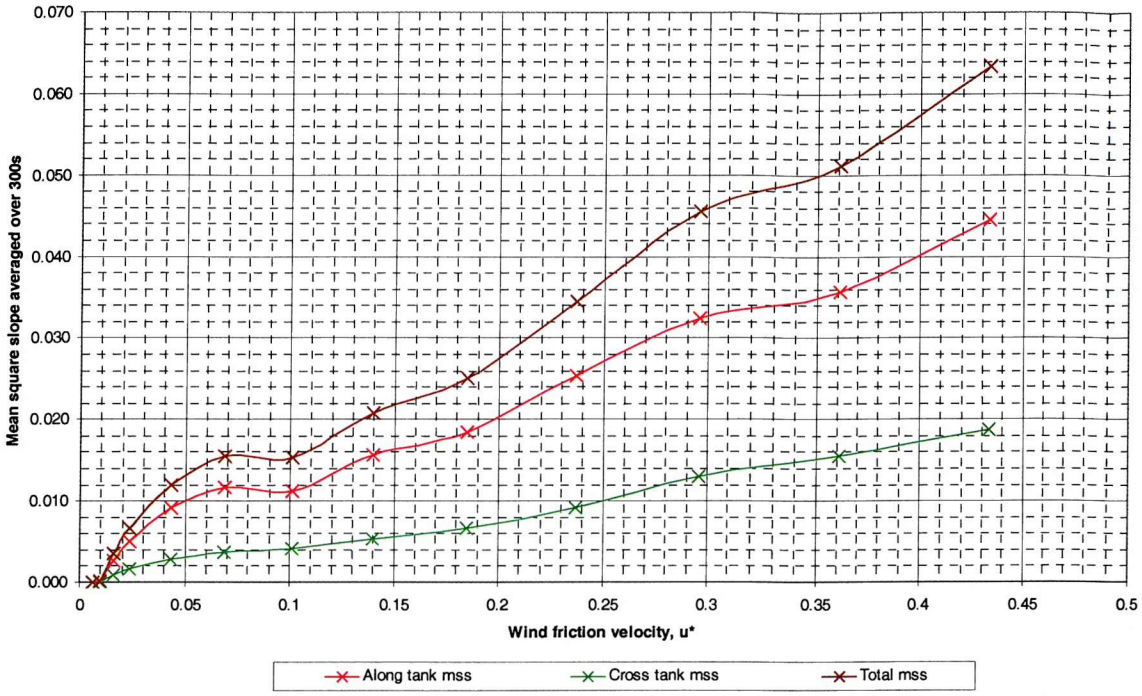

Figure 7-1: Mean square slope versus wind friction velocity.

speed generated in the wave tank was adjusted by means of a wind dial. This has been calibrated so that the wind speed in metres/second is approximately 1/5 of the wind dial reading. Where the term 'wind speed' is used with reference to the wind wave tank this actually means 1/5 of the wind dial reading rather than being measured independently. The wind friction velocity was measured by Barter *et al.* (1998) during a separate experiment at the wave tank using warm wire anemometers. Although there was some scatter in their data, they concluded that the wind friction velocity in the wave tank could be related to the wind speed, w, via equation 7-1.

$$u^* = \left(8.0 \times 10^{-5}\right)(5w)^{2.1} \qquad 7\text{-}1$$

By applying this relationship to the recorded values of w, the laser slope meter measurements of the mean square slope have been plotted against u* as the independent variable in figure 7-1.

It can be seen that the mean square slope along and across the wave tank is negligible at low wind stress values until the wind friction velocity reaches approximately 0.01m/s

(which is equivalent to a wind speed of 2m/s). There is then a sharp increase to a wind friction velocity of 0.07m/s (equivalent to 5m/s wind speed). Following this, there is a large and unexplained decrease in the mean square slope at wind friction velocity of 0.1m/s (6m/s wind speed) in the along tank slope component. From there, the mean square slope again increases approximately linearly up to the maximum wind friction velocity considered of approximately 0.0435m/s or 12m/s wind speed.

The initial part of the mean square slope versus wind speed behaviour is consistent with previous observations, such as those of Cox (1958) and Wu (1971), although as the wind speed increases the along tank mean square slopes are much lower than those measured by Cox. Wu (1971) believed that in his measurements below 1.9m/s there was laminar flow which was not sufficient to overcome the forces of surface tension and produce waves on the water surface. In the data sets presented here, this is a possible reason, although an alternative is that this region may have been caused by some residual surfactants / slicks left on the water surface. This behaviour, of a threshold wind velocity below which no waves are observed, is different from that observed at sea, except where slicks are present (Cox and Munk, 1954, Khristoforov *et al.,* 1992), where it is thought that the presence of swell waves causes sufficiently turbulent flow for waves to be formed. This is also consistent with observations of wind waves generated on the top of mechanical waves. Miller *et al.* (1991) observed that wind waves were generated in the presence of mechanical waves at wind speeds where no wind waves were generated without the mechanical waves.

For comparison with the Loch Linnhe data presented in chapter 5, figure 5-10 is reproduced here with the data from UCSB overlayed, in figure 7-2. This shows that the mean square slope values produced in the wind wave tank are similar to those in the field when similar stresses are exerted. This gives good confidence that at least the statistical characteristics of the wave tank wind waves are very similar to the open ocean ambient statistics. This allows the research to proceed with conviction that the wind wave tank statistics will be useful in understanding real ocean phenomena provided the correct wind stress forces are considered.

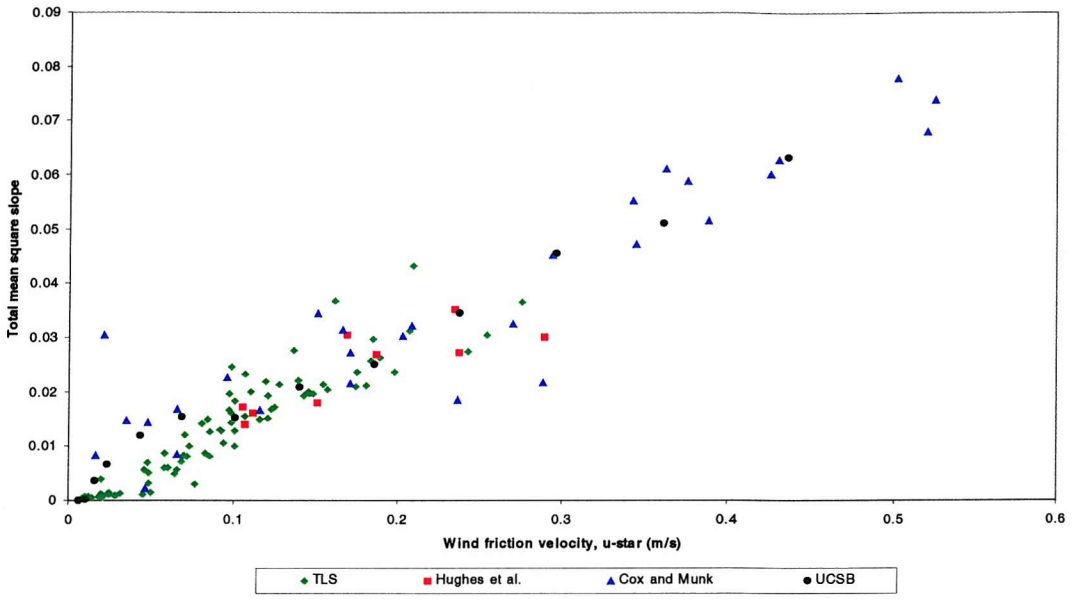

Figure 7-2: Figure 4-10 reproduced to include UCSB data

Information on the mean square slope of the ocean surface wave field is very useful for radar specialists attempting to model radar backscatter from the sea surface. Scientists at DERA are doing this by using the UCSB wave tank to produce sample wind wave fields. One of the radar models being considered by DERA is the Composite Scattering model. This model assumes that the scattering surface is modulated by a long wave that causes the scattering surface to be tilted as the wave goes past. For this model it is necessary to know the mean square slope of the long waves present in the wave field. This information has been provided by the Laser Slope meter (Walker, 1999).

By Parseval's theorem, it is possible to calculate the mean square slope from the data as a time series or as a frequency spectrum. In this case, as the mean square slope of only low frequency components was required, the frequency domain was used for the calculation. To determine an appropriate frequency to use as the maximum frequency in a low pass filter, the component of the radar wavelength on the water surface was used. Any waves with wavelengths shorter than half the component of the radar wavelength would not be 'seen' by the radar and so should not contribute to the mean square slope calculation. A frequency value was calculated from this wavelength component by relating frequency to wavelength via the gravity-capillary dispersion relation. The resulting value of frequency used as the upper limit in the low pass digital_filter function in IDL was 8Hz. The same value of

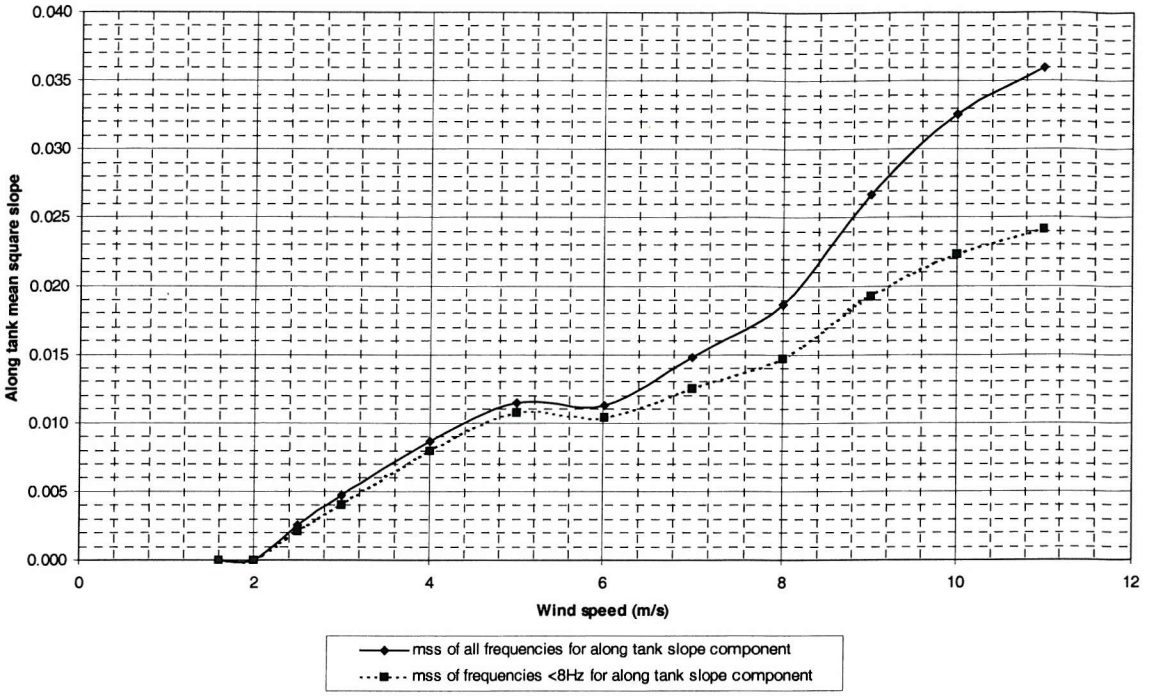

Figure 7-3: Comparison of total and filtered along tank mean square slope

frequency was used for each wind speed. The resulting mean square slope for the along tank slope component for the low frequency components is plotted in figure 7-3. For comparison, the mean square slope of the along tank slope component for the full spectrum of frequencies is also plotted.

It is interesting to see that there is very little difference between the mean square slope of frequencies <8Hz and the mean square slope of all frequencies when measured at wind speeds up to approximately 6m/s. This means that the high frequency behaviour at these wind speeds does not contain much energy in comparison to the spectral peak. However, as the wind speed increases, the amount of mean square slope in the high frequency components increases significantly as a proportion of the total mean square slope.

7.3 Variation of histograms with wind speed

Using data set 1, the dominant axes of each data set have been calculated (expected to be across and along the wind direction) by the method described in chapter 5 and Appendix B. The rotation angles are given in table 7-1. In general the rotation has been very small. It is

Wind speed	Rotation angle (°)
1.6	28.5
2.0	-40.9
2.5	8.67
3.0	7.31
4.0	0.867
5.0	1.90
6.0	1.34
7.0	-1.26
8.0	-1.27
9.0	1.22
10.0	2.63
11.0	1.87
12.0	-0.723

Table 7-1: Angle between principal axes of slope data and the wind direction

largest at the lowest wind speeds where data errors are greatest and the skew of the wind wave field is likely not to be so large.

Histograms of the slope components along these axes are displayed in figures 7-4 to 7-8. For the lowest two wind speeds a bin size of 0.001 has been used; a bin size of 0.02 is used for all other wind speeds. It can be seen that for wind speeds of 1.6 and 2.0m/s there is almost no spread either along or across the wave tank. i.e. no significant wave slopes were generated at all. As the wind speed increases, the cross tank slope component remains approximately symmetrical whilst the along tank slope component becomes slightly positively skewed. This means that the modal slope value moves from zero slope to small negative slopes (on the back face of the waves, assuming they travel parallel to the wind direction) and the tail of the positive slopes increases as higher slopes are experienced on the front face of the waves.

Some small irregularities can be seen in the histograms, for example at wind speeds of 9,10 and 11m/s, there are small depressions in the histograms in the along tank slope component between approximately –0.05 and –0.1 and between 0.05 and 0.1 in slope component. These have been investigated and are associated with instrument performance. Some areas of the wavelength shifting screens are prone to errors resulting from differences between the laser power during calibration and the experiment. These areas include regions of slight scratching and diode reflections. At these positions, the processing software erroneously finds the majority of data points to lie on either side of the poor patch, causing more points to be found in these areas and fewer points directly over the bad patch. These patches are not thought to affect spectral calculations significantly but may slightly increase high frequency noise.

The one-dimensional Gaussian distribution having the same rms slope as the data has been calculated as have the corresponding one-dimensional Gram-Charlier coefficients using the moments of the distribution. The Gram-Charlier equation used is the one-dimensional form of 3-25. These curves are overplotted on the histograms, the Gaussian curve in red and the Gram-Charlier curve in green. In general the one-dimensional fit is good and the Gram-Charlier fit is an improvement on the Gaussian fit. A graph of the variation of the coefficients with wind speed is shown in figure 7-9a.

The two-dimensional Gram-Charlier coefficients have also been calculated and an attempt has been made to fit these to the data as was done in chapter 5. Excluding the lowest two wind speeds, the coefficients calculated are plotted in figure 7-9b. It is clear that C_{21}, C_{03}, C_{22} and C_{04} are approximately constant. C_{40} increases with increasing wind speed approximately linearly. A study of the actual fit to the data is quite poor, although, in most cases the Gram-Charlier model does seem to be an improvement over the Gaussian. As was seen in chapter 5, certain areas of the distribution fit well, whilst other areas do not. Graphs of the 1-dimensional and 2-dimensional standardised moments corresponding to the Gram-Charlier coefficients are also included in figure 7-10a and 7-10b.

It is concluded from the findings here and those in chapter 5, that it is very difficult to produce a simple two-dimensional fit to a whole data set. A one-dimensional fit may be more useful in these circumstances. This may be because of the differing numbers of

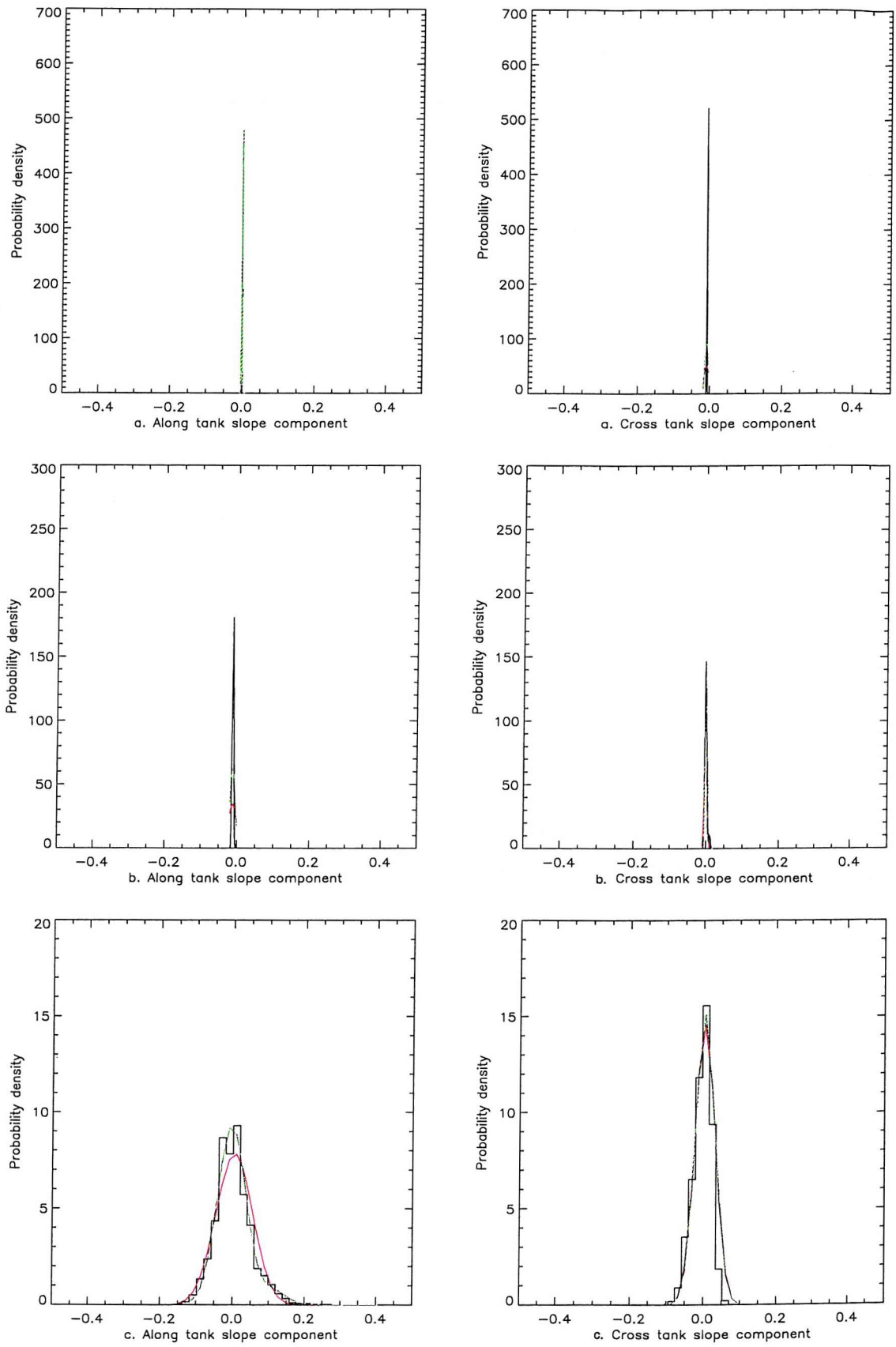

Figure 7-4: Wind wave histograms for a. 1.6m/s, b. 2.0m/s, c. 2.5m/s

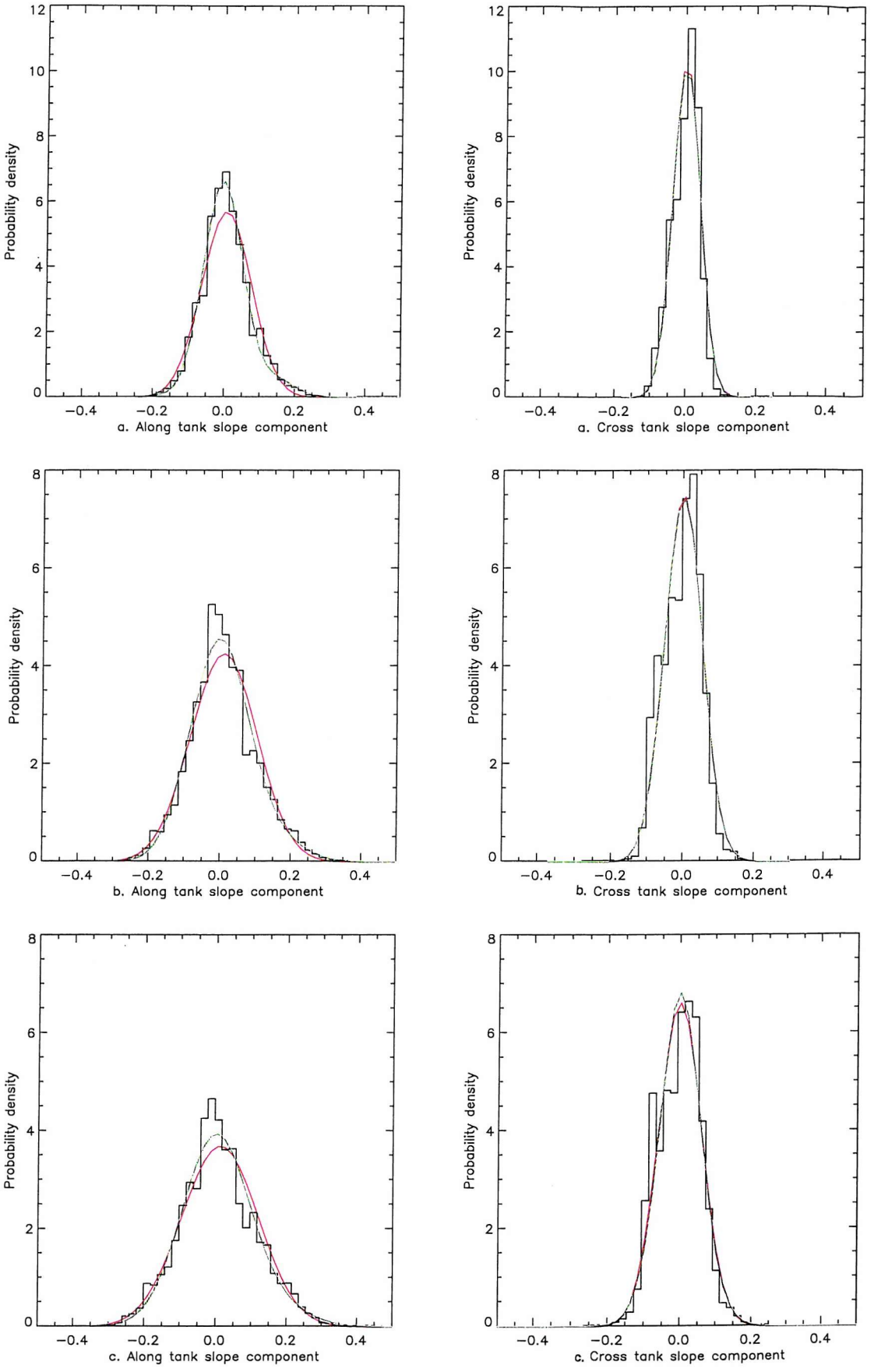

Figure 7-5: Wind wave histograms for a. 3.0m/s, b. 4.0m/s, c. 5.0m/s

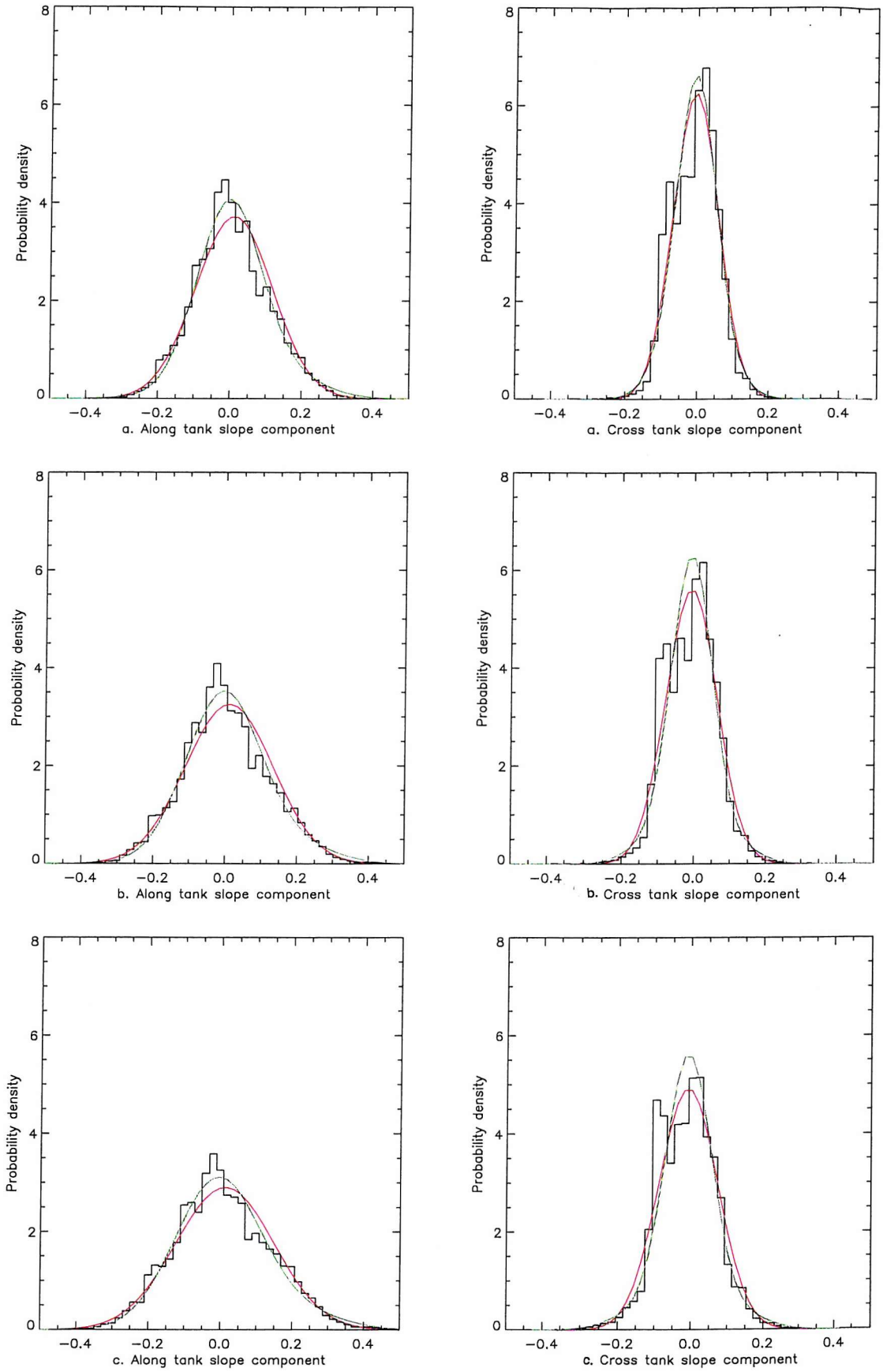

Figure 7-6: Wind wave histograms for a. 6.0m/s, b. 7.0m/s, c. 8.0m/s

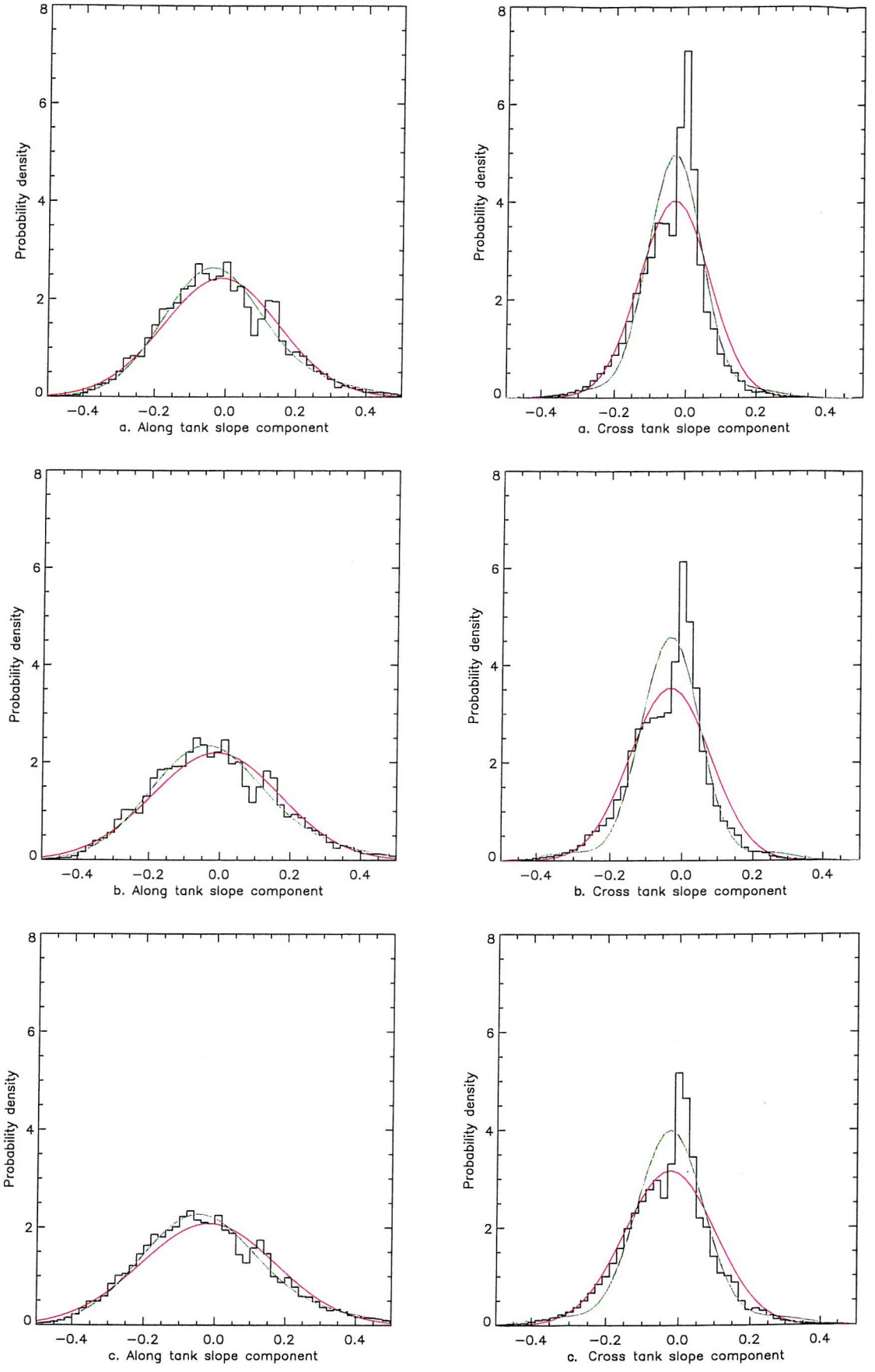

Figure 7-7: Wind wave histograms for a. 9.0m/s, b. 10.0m/s, c. 11.0m/s

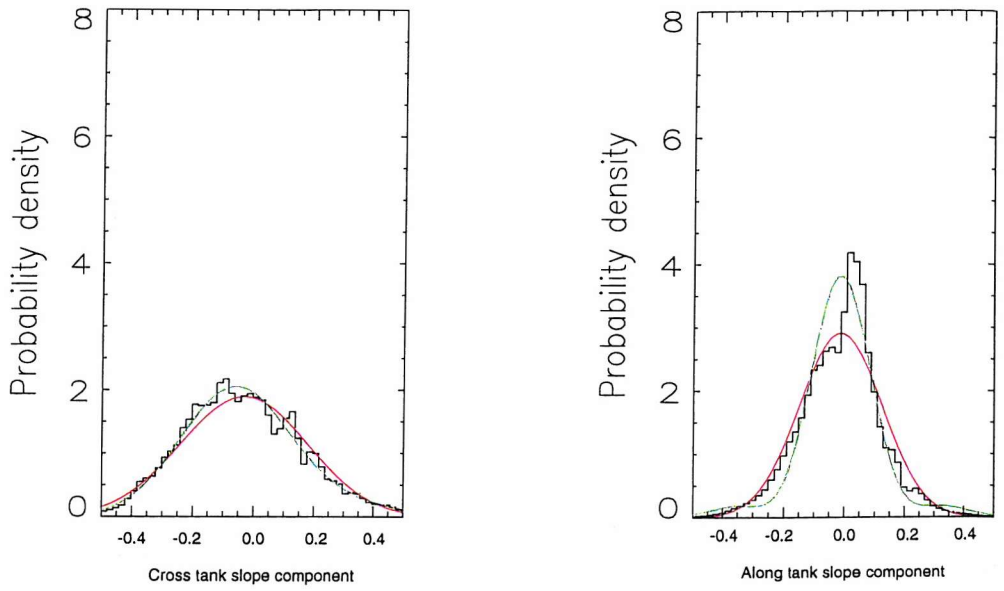

Figure 7-8: Wind wave histograms for 12.0m/s

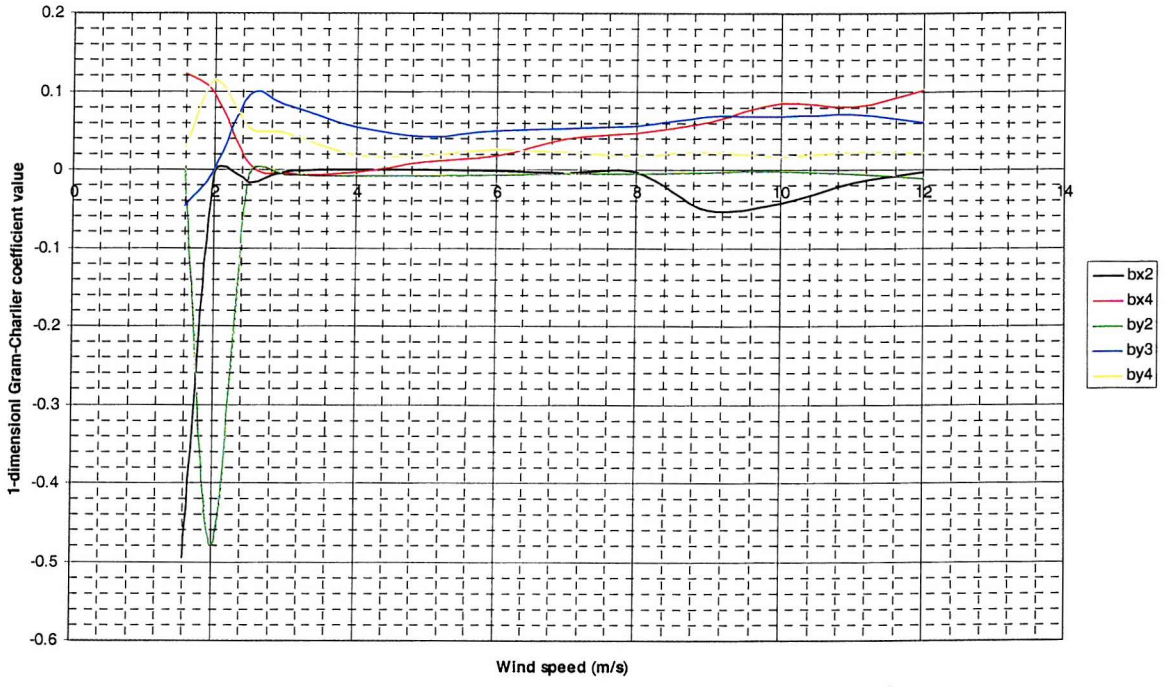

Figure 7-9a: 1-dimensional Gram-Charlier coefficients

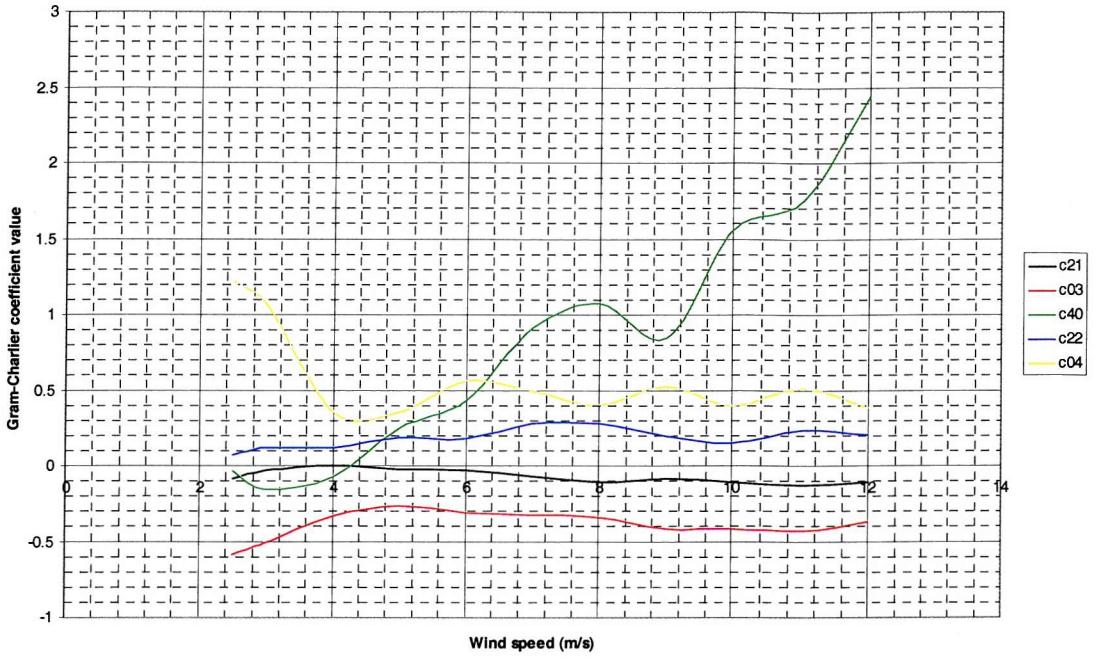

Figure 7-9b: 2-dimensional Gram-Charlier coefficients

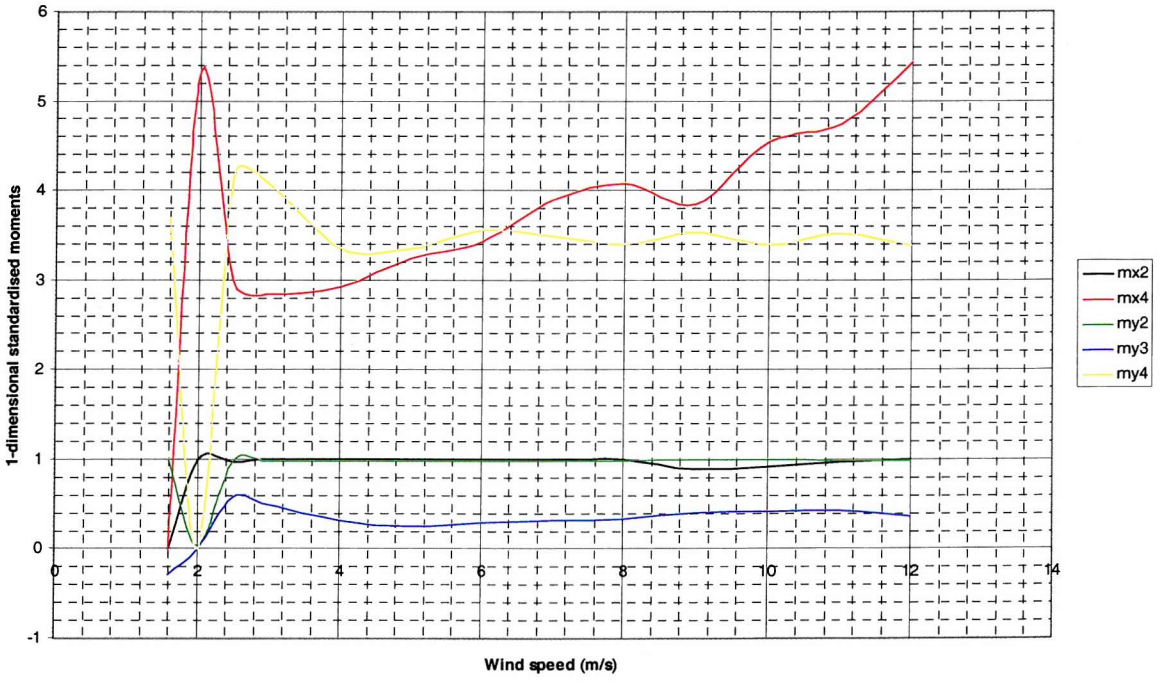

Figure 7-10a: Standardised moments for the 1-dimensional histograms

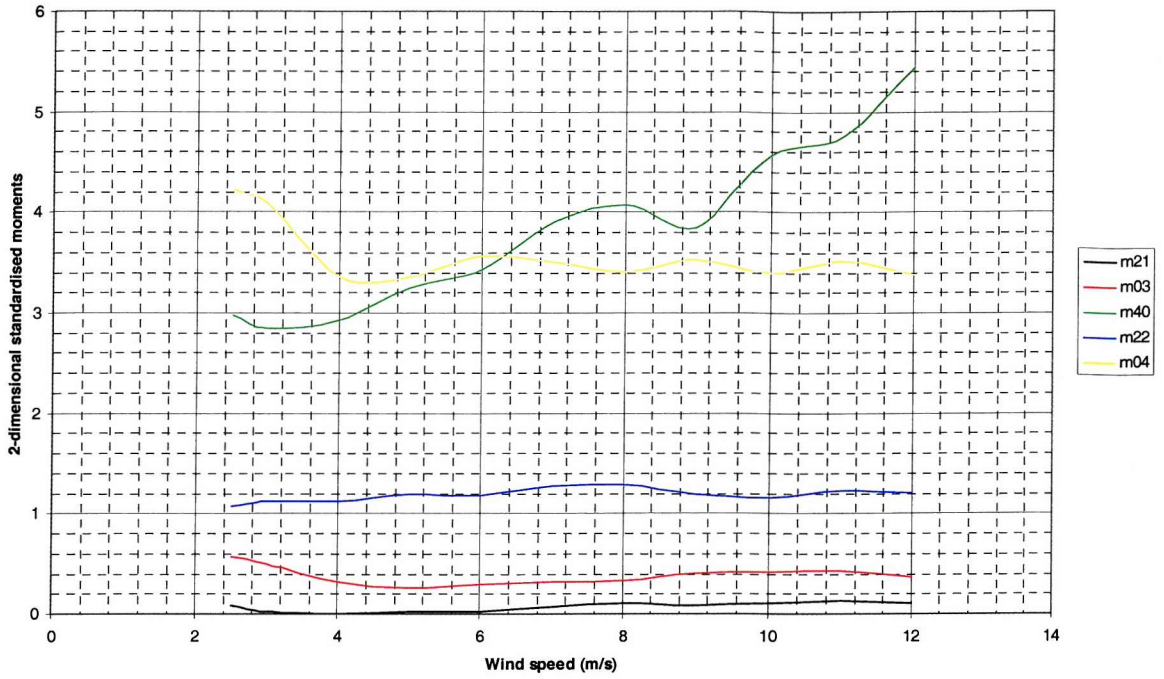

Figure 7-10b: Standardised moments for the 2-dimensional histograms

degrees of freedom between the two types of fit which give more scope for a better fit in the one-dimensional case.

7.4 Effect of laser spot size on high frequency measurements

7.4.1 Introduction

The finite size of the laser spot at the water surface can have a seriously degrading effect on any high wavenumber waves. If the spot is similar in size to the waves, it acts as a low pass filter and the very short wave energy will not be recorded. Therefore, for an instrument which is attempting to measure high wavenumber waves, it is crucial to know the size of the laser spot and to fully understand the effects of the finite size on any resulting data products. The aim of this section, therefore, is to study this both theoretically and experimentally and to apply the results to the measurements presented below.

7.4.2 Theoretical effects of spot size on high frequency measurements

The effect of a finite spot size on the resulting measurement of slope with increasing wavenumber can be simulated by assuming that the output slope is an average of slope

within the bounds of the laser spot. In practice this will not be perfectly accurate because the conversion from spot position on the wavelength shifting screens into surface slope is a non-linear process. However, for the purposes of this exercise, it is considered that this assumption is valid.

It will be assumed that the laser spot has an even intensity over its entire area and is perfectly cylindrical. The surface wave being measured will be assumed to be perfectly two-dimensional (i.e. uniform in the cross tank, or y, direction) and linear (sine or cosine in the along tank, or x, direction). If the slope of the wave is represented by $S(x,y) = ak\cos(kx + \vartheta)$, ϑ is an arbitrary phase constant and A represents the area of a cross section of the laser beam, then,

$$\text{Resulting averaged slope} = \frac{\mathrm{Re}\left[\int_A ake^{i(kx+\vartheta)}dxdy\right]}{\int_A dxdy} = \frac{\mathrm{Re}\left[e^{i\vartheta}\int_A ake^{ikx}dxdy\right]}{\int_A dxdy} \qquad 7\text{-}2$$

Integrating with respect to y over the range $\left[-\sqrt{r^2-x^2}, \sqrt{r^2-x^2}\right]$ where r is the radius of the laser spot,

$$\text{Resulting averaged slope} = \frac{\mathrm{Re}\left[e^{i\vartheta}\int_{-r}^{+r} ake^{ikx}\,2\sqrt{r^2-x^2}\,dx\right]}{\int_{-r}^{+r} 2\sqrt{r^2-x^2}\,dx} \qquad 7\text{-}3$$

The integral in the numerator takes the form of a Fourier transform, which will be real. Therefore,

$$\text{Resulting averaged slope} = ak\cos\vartheta\frac{\int_{-r}^{+r} e^{ikx}\,2\sqrt{r^2-x^2}\,dx}{\pi r^2} \qquad 7\text{-}4$$

It can be seen that the resulting measured slope will also be sinusoidal in the same way as the original wave form. For a wave which had slope amplitude ak, the slope amplitude would be measured as 7-4 with $\vartheta=0$.

Dividing 7-4 by the original slope, $ak\cos\vartheta$, the ratio of the measured slope to the real slope can be calculated.

$$\text{Ratio of measured slope to actual slope} = \frac{\int_{-r}^{+r} e^{ikx} 2\sqrt{r^2 - x^2}\,dx}{\pi r^2} \qquad 7\text{-}5$$

Writing the ratio of the laser beam diameter to the water wavelength as $r_a=rk/\pi$, 7-5 becomes,

$$\text{Ratio of measured slope to actual slope} = \frac{\int_{-r}^{+r} e^{\left(\frac{ir_a\pi x}{r}\right)} 2\sqrt{r^2 - x^2}\,dx}{\pi r^2} \qquad 7\text{-}6$$

Making a change of variables so that $x=r\cos\theta$, 7-6 can be written as,

$$\text{Ratio of measured slope to actual slope} = \frac{2}{\pi}\int_0^{\pi} e^{ir_a\pi\cos\theta} \sin^2\theta\,d\theta \qquad 7\text{-}7$$

This integral can be written in terms of a Bessel Function and Gamma Functions (Watson, 1958) so that,

$$\int_0^{\pi} e^{ir_a\pi\cos\theta} \sin^2\theta\,d\theta = \frac{2J_1(r_a\pi)\Gamma\left(\frac{1}{2}\right)\Gamma\left(\frac{3}{2}\right)}{r_a\pi} \qquad 7\text{-}8$$

Therefore, evaluating the Gamma functions (Boas, 1966),

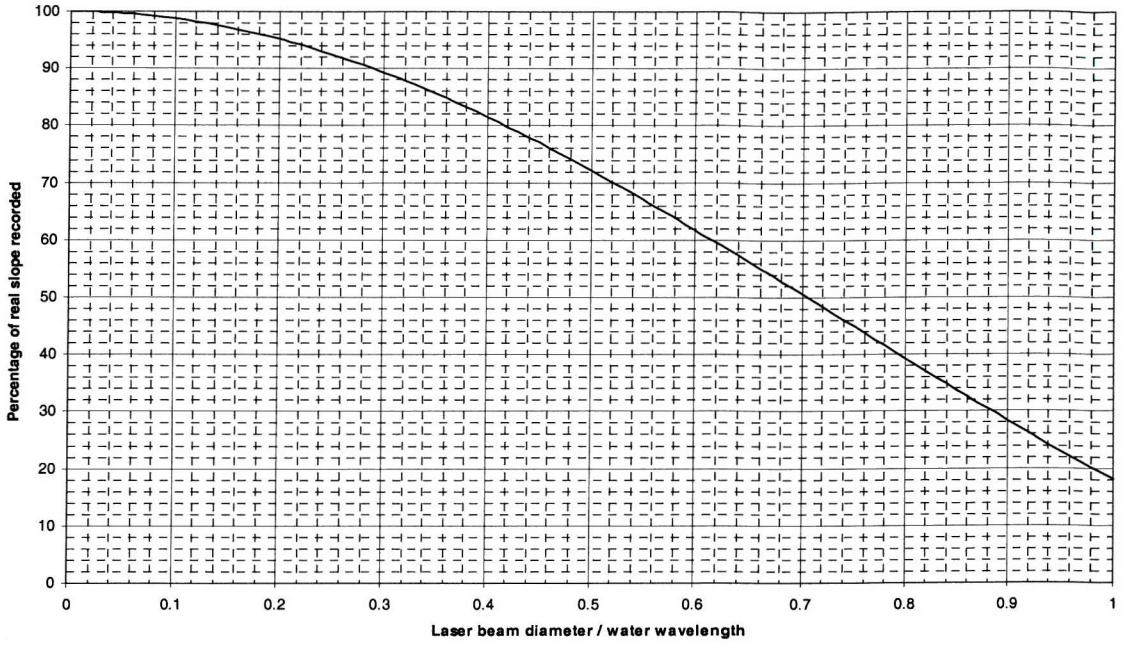

Figure 7-11: Variation of measured slope with laser spot size

$$\text{Ratio of measured slope to actual slope} = \frac{2J_1(r_a\pi)}{r_a\pi} \qquad 7\text{-}9$$

This ratio is displayed in figure 7-11 as the percentage of the real water slope recorded as the measured slope.

It can be seen that for a laser spot size of 2mm, water waves of wavelength twice this length will be recorded as having slopes of ~72% of the actual slope magnitude. To stay within 10% of the actual slope magnitude, waves can only be accurately measured down to ~7mm. These wavelengths of 4mm and 7mm correspond in the gravity-capillary dispersion relation to frequencies of 87 and 39 Hz respectively.

What is important about these findings is that the magnitude of the slope is reduced in a consistent fashion as the laser spot size becomes comparable with the wavelength of the water waves being measured, rather than a random behaviour. However, any frequency fluctuations will be preserved but will be measured at a lower energy. This means that wave spectra may have their energy reduced, but some signal will remain in this region

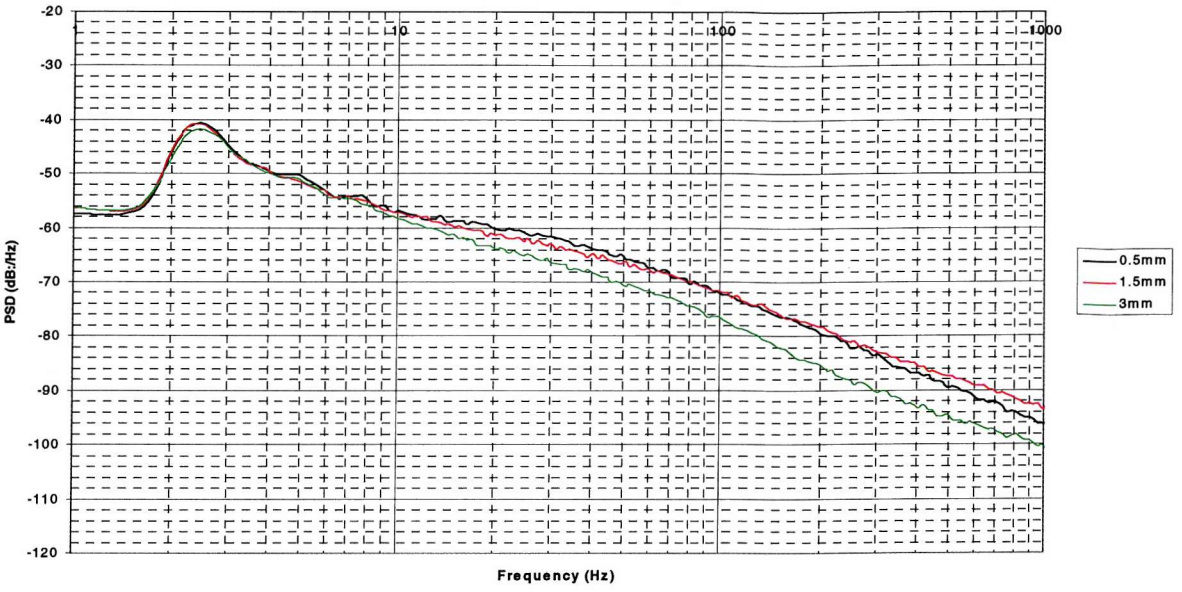

Figure 7-12: Frequency spectra of total slope component for 6m/s wind speed for different laser spot diameters

providing at least some information. The spectrum will be underestimated as described by figure 7-11.

7.4.3 Experimental measurements of effect of laser spot size on high frequencies

During the second experiment at the wind wave tank in Santa Barbara, experiments were conducted on the effect of varying the size of the laser spot incident upon the mean water level. This was achieved by varying the distance between two lenses situated in a specially manufactured tube directly at the end of the fibre optic cable. Three different spot sizes were used of approximately 0.5mm, 1.5mm and 3mm in diameter to measure slope data for a 6m/s wind wave field. Frequency spectra have been plotted for the resulting data and are presented in figure 7-12.

It can be seen that there are some significant differences between the frequency spectra at different laser spot sizes. Apart from variations caused by the laser spot size, some of these differences may also be attributed to different noise levels in the data sets. When each wind wave file was collected, a file was taken with the laser beam pointing directly upwards through flat water. As there were no waves on the water, these results can be used to assess the level of noise in the data at that particular time. These files have been investigated and

show that in order, the noise levels were highest for the 1.5mm spot diameter, followed by 3mm and then 0.5mm. This may well explain why the data for 1.5mm become greater in magnitude than the data for 0.5mm at the higher frequency end of the spectrum.

A study of the spectra created using these different spot sizes shows that at low frequencies the spectra are very similar. This suggests that the spot size has not affected these results. They begin to differ around 9Hz for the 3mm spot size and around 15Hz for the 1.5mm spot size. Theoretically, a larger spot should have the effect of filtering out higher frequency components. This will tend to put less energy into the high frequency components and so their spectral level will be reduced. However, the spectral level at high frequencies may be increased if there are high noise levels.

7.4.4 Discussion

Taking the theoretical and experimental results together, it must be assumed that at higher frequencies, the spectral level will be slightly reduced over its real value due to the laser spot size. This effect may, to some extent, be compensated for by noise. For set 2 it is reasonable to assume that the data are not significantly affected by the laser spot size up to an observed wave frequency of approximately 300Hz. After this point, it can be seen that noise levels on different days may start to affect the measured slopes, although all the data were collected with a spot size of 0.5mm. For data set 1, the laser spot size was approximately 2mm as the focussing equipment was not yet available. Assuming the dispersion relation, it can be deduced that waves up to ~4mm can be considered to be measured with up to 70% accuracy (frequencies of up to approximately 100Hz) from the theoretical study. However, a 4mm wave may not appear at a frequency of 100Hz due to advection by the orbital velocities of longer waves, or because it may be a parasitic capillary wave, and so it is possible that much higher intrinsic frequencies may have been measured accurately.

7.5 Wind spectra

7.5.1 Introduction

For each wind speed in data sets 1 and 2, wind wave spectra have been calculated for the total, along tank and cross tank slope components; these are presented below. Set 1 was

Height Spectrum	Slope Spectrum
$H(\omega)$	$S(\omega)=k^2H(\omega)$
$\psi(k)$	$S(k)=k^2\psi(k)$
$H(\omega)\propto\omega^{-5}$	$S(\omega)\propto k^2\omega^{-5}\propto\omega^{-1}$
$H(\omega)\propto\omega^{-4}$	$S(\omega)\propto k^2\omega^{-4}\propto\omega^{0}$
$\psi(k)\propto k^{-4}$	$S(k)\propto k^2k^{-4}=k^{-2}$
$\psi(k)\propto k^{-7/2}$	$S(k)\propto k^2k^{-7/2}=k^{-3/2}$

Table 7-2: Table showing relationships between slope and wave height frequency and wavenumber spectra

collected at 5.77m from the wind tunnel exit whilst the second set was collected at 2.12m from the wind tunnel exit. Here, the similarities and differences in the data sets are studied at the two positions, and an attempt is made to attribute the differences to some factor such as location or noise. Additionally, the spectra are compared with ocean wave spectra at similar wind stresses and it is discussed how well results from the wave tank may apply to the real ocean in the spectral sense. To aid understanding of the relationships between the slope and wave height frequency and wavenumber spectra, table 7-2 lists the relationships between the spectra and the expected spectral forms in the gravity wave range for some of the most commonly assumed spectral forms.

As a separate exercise, the possibility of estimating an ambient wavenumber spectrum from the frequency spectrum data is considered. The same method is used to determine information about the angular distribution by considering the cross- and along-tank components of the surface slope. A wavenumber spectrum estimate is produced at each wind speed and its shape is discussed with reference to ocean spectral theories.

7.5.2 Wind spectra measured in the wind wave tank

Power spectral density plots have been computed for each of the wind wave field data files collected. For computational reasons, 4194304 data points were used in total selected from near the end of each data set. This data stream was divided into two equal parts of 2097152 points (a power of 2 so that a Fast Fourier Transform could be computed). The power

spectrum was calculated for each part and then the two results were averaged to form the final power spectral density. The method presented in chapter 6 was used to calculate each power spectrum.

The size of each data section used was 196.6s and the size of the window function was 5.6s. This corresponds to 70 degrees of freedom. Therefore, each individual estimate of the power spectrum has a confidence interval of 80% within a 2dB interval (Blackman and Tukey, 1958). By averaging two independent estimates of the power spectrum this error is reduced by a factor of $1/\sqrt{2}$. Errors lines have not been drawn on the graphs for reasons of clarity. However, the error lines are very close to the data estimate.

The variation of the along tank, cross tank and total slope power spectra with wind speed have been plotted for both data sets in figures 7-13 and 7-14.

Studying the spectra visually, the following are the most obvious features that can be seen:

- there is a large peak in the gravity wave region of the spectrum;
- the main peak moves to lower frequency as the wind speed increases;
- the main peak has more mean square slope than the spectra at higher wind speeds at the same frequency;
- there is a bulge in the spectrum at much higher frequencies between approximately 10 and 200Hz (exact frequencies depend on the wind speed);
- the overall magnitude of the spectrum increases at all frequencies as the wind speed increases;
- there is a sharp drop in the spectrum at 3.5kHz;
- there are spikes in data set 1 in the two smallest wind spectra at the American mains electricity frequency of 60Hz and at harmonics of this frequency.

Between the two locations in the wave tank there are a number of differences (data set 2 was collected closer to the wind tunnel exit than data set 1):

- the energy in the spectral peak decreases more quickly with decreasing wind speed in data set 1;

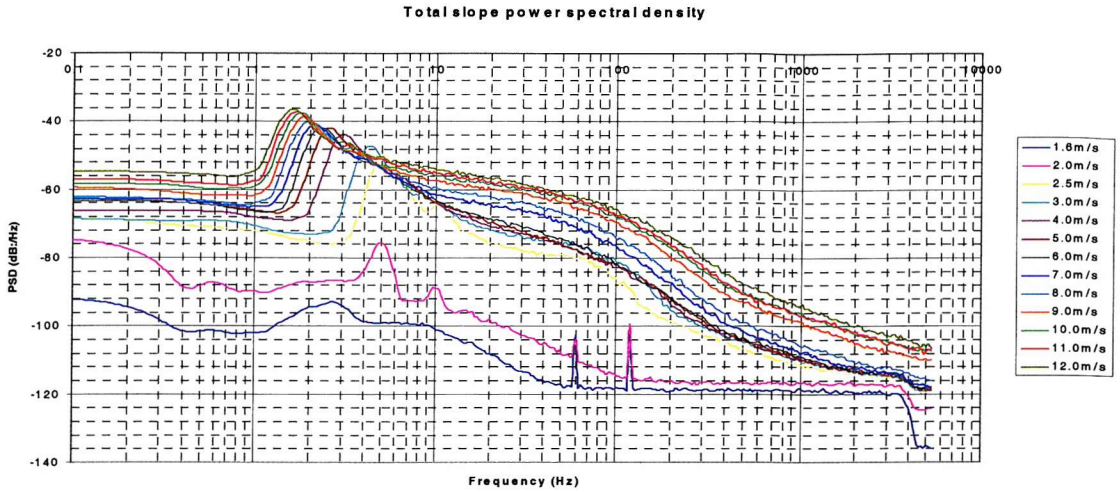

Figure 7-13a: Power spectrum of total slope at 5.77m from wind tunnel exit (data set 1)

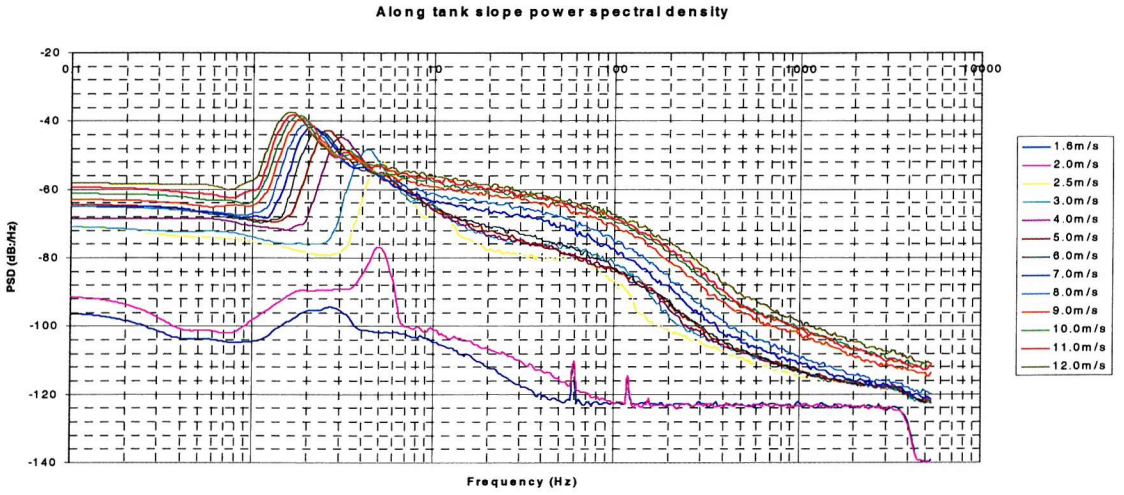

Figure 7-13b: Power spectrum of along tank slope component at 5.77m from wind tunnel exit (data set 1)

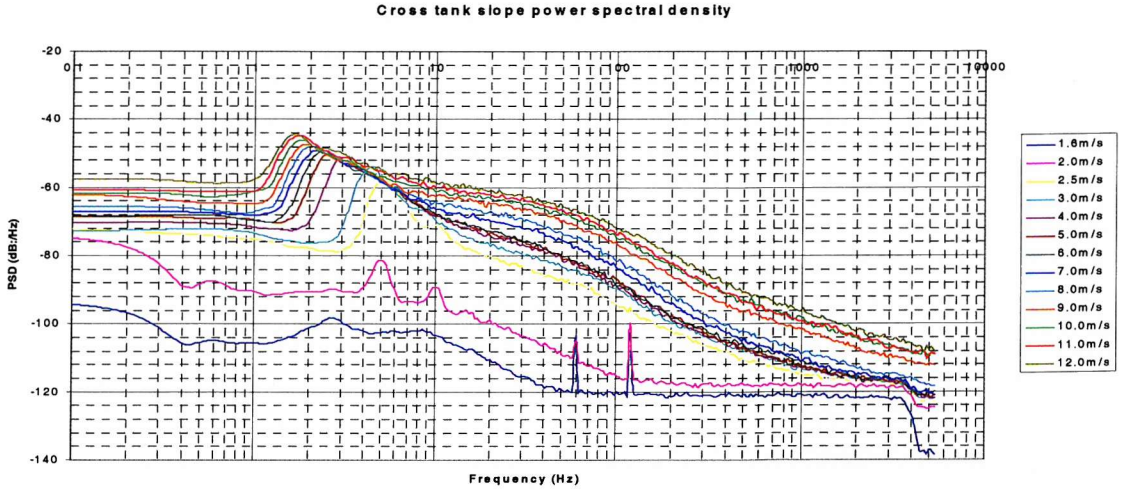

Figure 7-13c: Power spectrum of cross tank slope component at 5.77m from wind tunnel exit (data set 1)

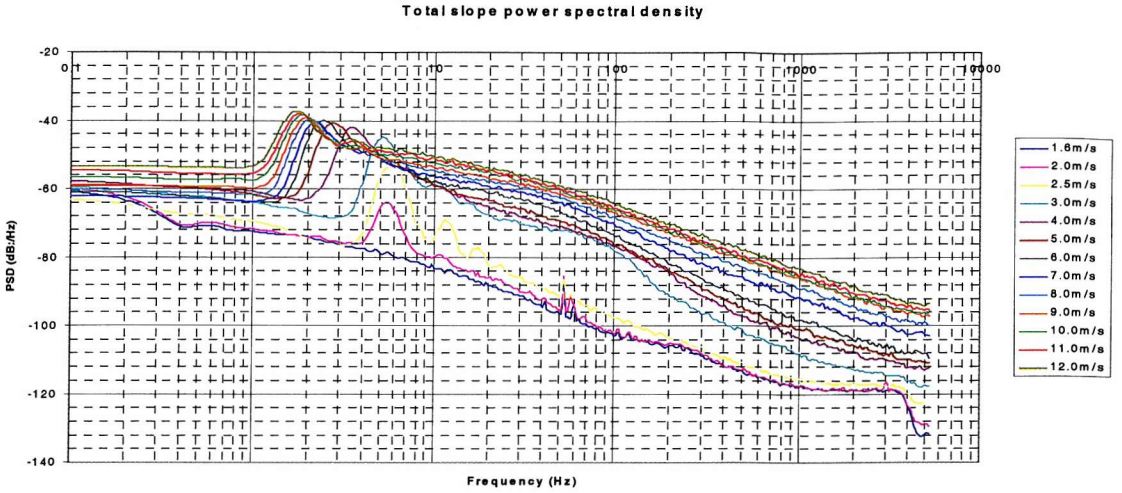

Figure 7-14a: Power spectrum of total slope at 2.12m from wind tunnel exit (data set 2)

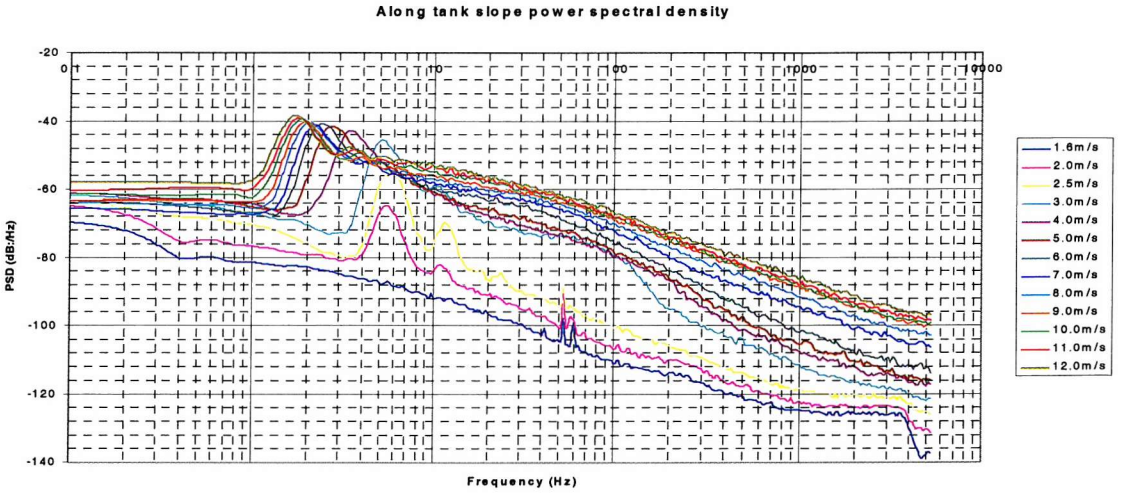

Figure 7-14b: Power spectrum of along tank slope at 2.12m from wind tunnel exit (data set 2)

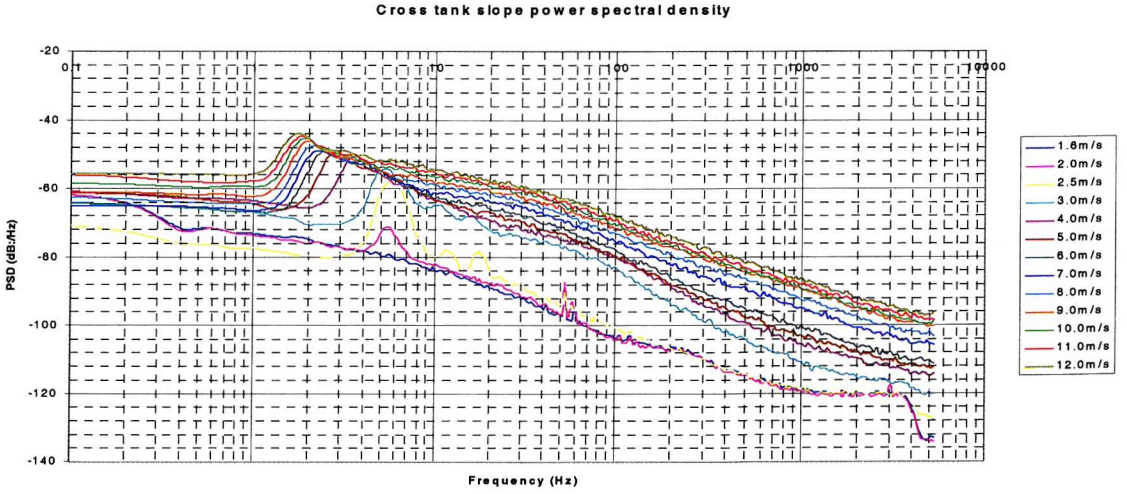

Figure 7-14c: Power spectrum of cross tank slope component at 2.12m from wind tunnel exit (data set 2)

- considering frequencies around 30Hz higher than the spectral peak, there is less energy in these frequencies in data set 1 compared to data set 2 which makes the high frequency bulge more pronounced.
- there is a much lower signal in data set 1 at high frequencies;there are spikes in data set 1 in the two smallest wind spectra at the American power frequency of 60Hz and at harmonics of this frequency whereas similar spikes are seen at approximately 55Hz and 60Hz in data set 2.

Initially, considering the differences between the data sets, it is likely that most of the differences can be attributed to damping of the wave motion in data set 1 over the increased fetch without the continued action of the wind. This would explain the reduced spectral value at and beyond the spectral peak. As expected, an increase of the energy at the spectral peak with wind speed is observed. Since shorter waves decay faster, this increase is more prominent in the data set taken further away from the wind tunnel exit (data set 1). The lower energy at high frequencies in set 1 as compared to set 2 may not be purely due to the fetch, but instead is likely to be due to a combination of the following factors:

- less noise in data set 1;
- the increased laser spot size in data set 1 causing filtering of the high frequencies;
- the higher frequencies decaying more quickly and therefore being reduced in energy by this position in the wave tank.

The peak in the spectra at 55Hz is not understood, but may be related to the frequency of oscillation of the lights used in the photography of the waves.

Studying the general shape of the spectra, it can be seen that the wind waves are generated over a very large frequency range with a cut-off frequency at the low frequency end of the wind wave spectrum (an attempt has been made to remove DC errors which cause confusion at the low frequency end of the spectrum, although some effect remains). In the open ocean where the fetch is unlimited, it is likely that this cut off frequency would correspond approximately to waves moving with a phase velocity equal to the wind speed. At limited fetch, such as in the laboratory, the wind wave field never becomes fully developed but instead reaches an equilibrium level at the fetch being considered. Within an area of the wind wave field, this equilibrium is due to a balance between the net wave energy transferred into the area and the physical processes occurring within it.

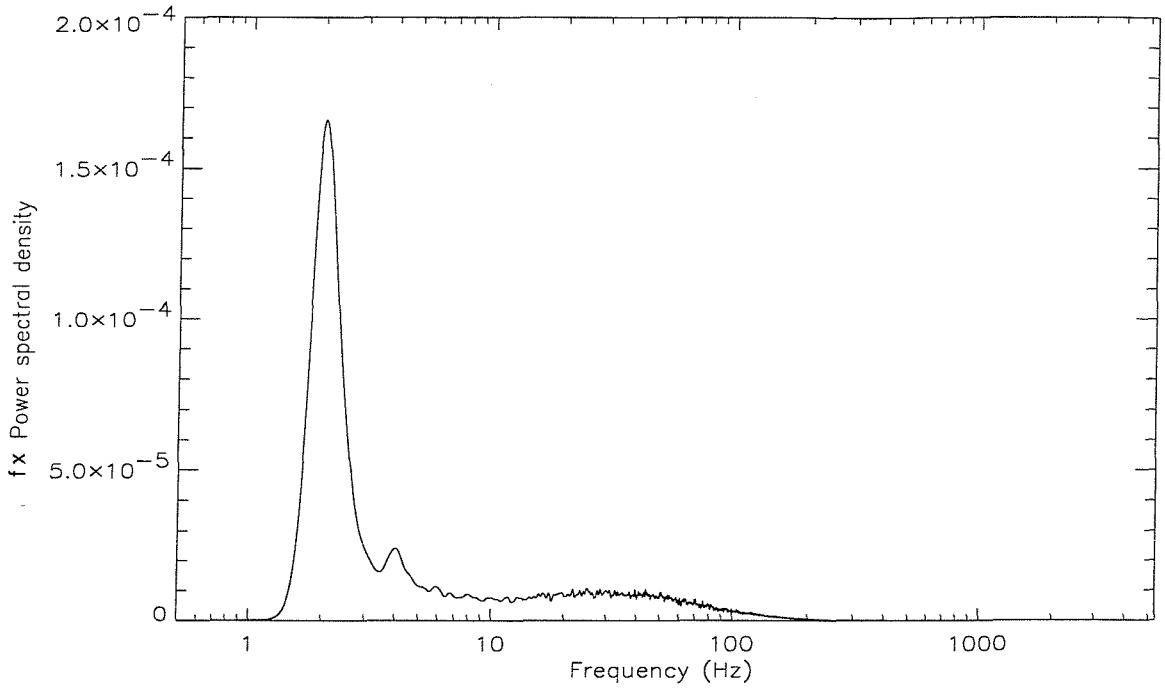

Figure 7-15: Plot showing areas of high energy over the frequency spectrum. Data from set 1 at 8m/s

If the x-axis only of the spectral graphs is plotted on a log scale, the mean square slope contained within the wave field can be represented by area if the spectrum is multiplied by the frequency, as this takes into account the increasing frequency range represented by each point at higher frequencies. A graph of this form from data set 1 at a wind speed of 8m/s is plotted in figure 7-15. This shows that the mean square slope in the wave field is mainly concentrated around the spectral peak. There is a second surge in mean square slope at much higher frequencies between approximately 10 and 100Hz. The reason for this bulge may be due to parasitic capillary waves on wavelengths at the spectral peak. These waves would be generated by the underlying gravity wave rather than by the wind. If this was the case, the spectrum would be enhanced at these frequencies over the spectral level expected if the waves were generated purely by the wind. As the capillary waves would have a range of wavelengths, the increased energy would appear over a large frequency range. There is evidence from other experiments (Cox, 1958, Ebuchi *et al.*, 1987) to suggest that such waves do exist. In addition to these waves, Hara *et al.* (1997) have measured an unexpected high level of short wind waves that travel bound to the dominant gravity wave which may be due to some non-linear interaction. Since these waves are advected by the underlying gravity wave they will travel at the speed of the dominant wave

rather than at their intrinsic speed as given by the gravity-capillary dispersion relation. These waves may also add to the spectral bulge.

If the majority of the spectral bulge is in fact due to capillary waves which are travelling very much faster than would be expected from the dispersion relation, this lessens the limitations caused by the laser spot size. Instead of these waves being of very short wavelength, they may, in fact, have much longer wavelengths which are not so highly filtered by the finite laser spot size. For example, from the dispersion relation, a 1mm wave would register at a frequency of 676Hz. If that same wave was bound to a gravity wave travelling at 1m/s it would register at a frequency of 1kHz. Thus, in this way, some of the high frequency measurements may be more accurate than would otherwise be the case.

If this type of behaviour is also seen in the ocean, the amount of energy contained in these high frequency waves may potentially have a large effect on the radar backscatter from the ocean surface. Assuming for now that only Bragg scattering occurs, then the particular wavelength of these waves will be very important in determining how much effect they may have for any particular radar wavelength. As discussed above, if these waves do not travel at the speeds given by the dispersion relation then their wavelength can not be calculated. This leads to uncertainty in the amount of energy in a particular surface wavelength and hence will lead to inaccuracies in radar scattering models of the ocean.

The variation of the spectral peak with wind speed will now be investigated. For reasons of brevity, only data set 1 will be studied here. The value of the slope spectrum and the frequency at the peak of each spectrum has been calculated. Also calculated is the corresponding wavelength at the peak (using the gravity-capillary dispersion relation). These values have been plotted versus wind speed in figures 7-16 and 7-17. At wind speeds above approximately 2.5m/s, a single trend is followed in the variation of the wavelength / frequency at the peak in the wind wave spectrum. As the wind speed increases, the peak moves to a longer wavelength or lower frequency, with a linear behaviour with wind speed in the wavelength at the spectral peak. For data set 1, the variation of the slope power spectrum at the peak in the spectrum with wind speed behaves in a similar manner to the variation in the mean square slope.

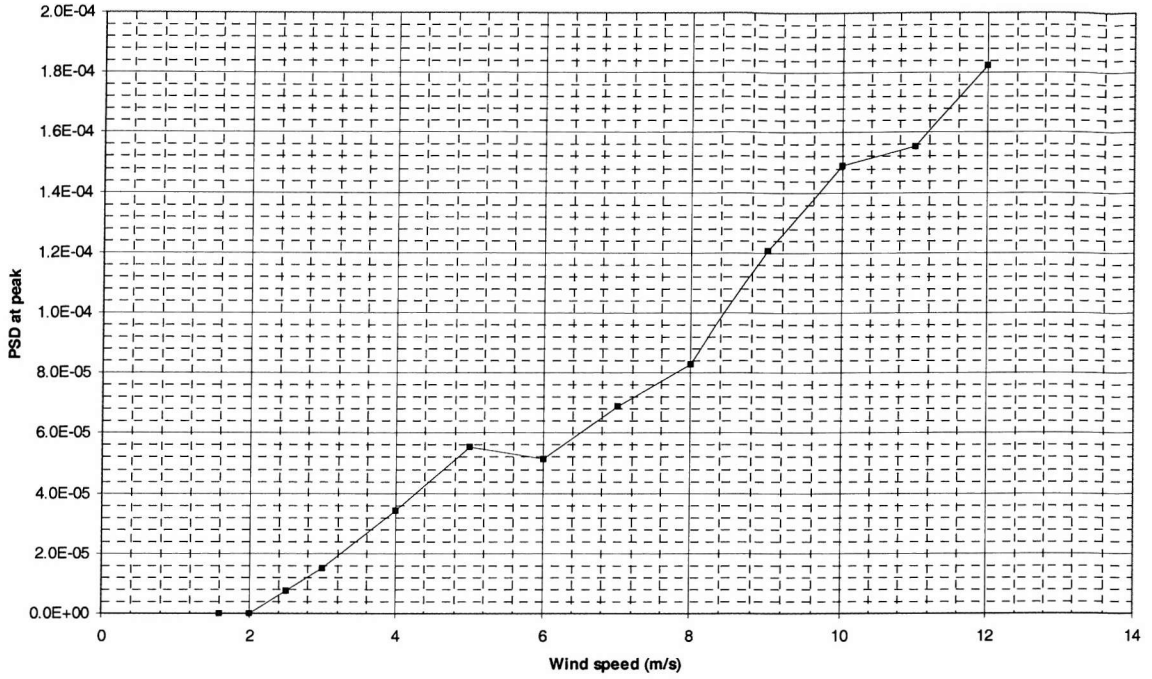

Figure 7-16: Magnitude of slope power spectrum at peak

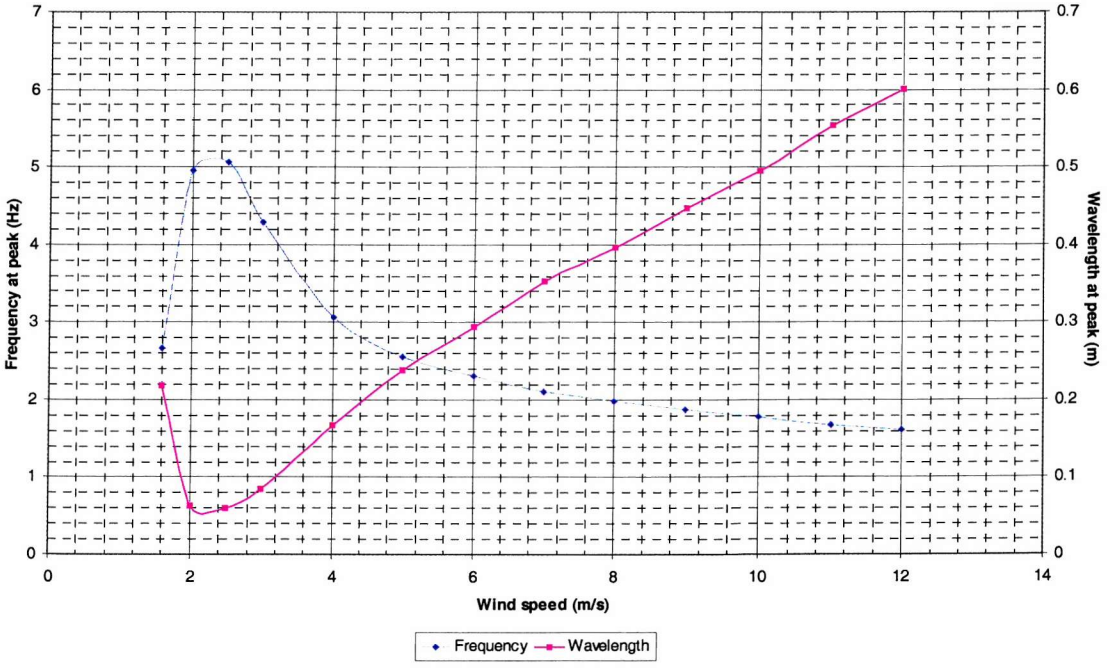

Figure 7-17: Frequency and wavelength at peak in slope frequency power spectrum

Still considering the behaviour of the spectral peak, the overshoot effect is investigated. In the open ocean, growth of wave components is thought to be exponential (Plant, 1982) until the growth is limited by breaking or by wave-wave interactions. As the fetch increases, shorter waves saturate and start to break whilst longer waves continue to grow. The longer waves also gain energy from the higher frequency end of the wave spectrum via wave-wave interactions. This causes a peak in the spectrum near to the maximum wavelength generated at a particular fetch. As the fetch increases further the same effect occurs which moves the peak of the spectrum to lower frequencies and tends to cause the energy at the earlier peak to be reduced. This phenomenon is known as the overshoot effect (*Komen et al.,* 1994, Hasselmann *et al.* 1973). When the wave field is fully developed, all the frequencies are at saturation and an energy and momentum balance between wave growth, wave-wave interactions and breaking results.

This overshoot phenomenon is also observed in the current data sets. Here, as the wind speed is increased, longer waves are generated in the wave field at a single fetch. The shorter waves reach saturation and start to break whilst the longer waves interact with the shorter waves reducing their energy and increasing the spectral peak. As the wind speed increases further the effect continues moving the spectral peak to lower frequencies and reducing the energy at the frequency of the original peak in the spectrum. Thus, there is more energy at the peak of the spectrum at a particular wind speed than at the same frequency at a higher wind speed. For the results of the JONSWAP experiment (Hasselmann *et al.*, 1973), the relationship between overshoot for one wind speed and increasing fetch and for one fetch and increasing wind speed was explained using Kitaigorodskii's similarity theory (Kitaigorodskii, 1962), where the appropriately non-dimensionalised wave spectrum should be a universal function of the of the non-dimensionalised fetch $x_{nd} = xg/u_*^2$, where x_{nd} is the non-dimensionalsed fetch and x is the dimensionalised fetch.

Looking to the right of the spectral peak, as the wind speed increases, it can be seen in figures 7-13 and 7-14 that the sharp change in the gradient of the spectrum following the spectral peak, moves closer and closer in energy to the energy at the spectral peak. This suggests that if the wind field was fully developed, the spectral peak would not be so prominent, although it would always remain, as it is related to the overshoot effect. The

region around the spectral peak will not be in equilibrium as the wave-wave interactions in this region will be unusual as there is not much energy in the waves which are longer than those at the spectral peak. Very short waves will also not be in equilibrium as capillary effects will become important. Therefore, the equilibrium region will be between the spectral peak and the region affected by capillarity. In these data this region is where there is a shallow gradient after the sharp fall off from the spectral peak (Cooper, 1998).

The gradient of the log plot of the total frequency spectra for both data sets is plotted in figures 7-18 and 7-19 except for wind speeds of 1.6m/s and 2m/s. It can be seen that this region of the spectrum following the spectral peak has a gradient of between –1 and –1.5. This is equivalent to the power of the height frequency spectrum being between –5 and –5.5.

Phillips (1958) predicted on dimensional grounds that in the equilibrium range this power should be –5 and so these data show a similar result in this region. This power is also the basis for the spectrum proposed by Pierson and Moskowitz (1964) which fitted their data well. Their theory was based in part on Kitaigorodskii's (1961) results for assuming similarity between wave spectra at different wind speeds. Since then there have been many other theories and experimental results some indicating this result and others tending to support Phillips' later hypothesis based on an energy balance which suggested that the power of the height frequency spectrum should be –4. The recent theory of Belcher and Vassilicos (1997) also supports this form of frequency spectrum. In their theory, waves of all frequencies within a breaking wave travel at the same speed and so in the dispersion relation, $\omega \propto k$. Therefore, the power of the slope frequency spectrum, which is equivalent to a height frequency spectrum with a power of -4, is -2, which is not incompatible with the measurements presented here. As these data are for limited fetch, they are not directly applicable to the spectral form in the equilibrium range.

Qualitatively, for the higher wind speeds the overall shape of the along tank spectrum measured here is very similar to that measured by Lange *et al.* (1982). In their data there is a dominant peak in the spectrum followed by a 'bulge' in the frequency of gravity-capillary waves. They showed that, as the laser spot size used in the measurements increased, the

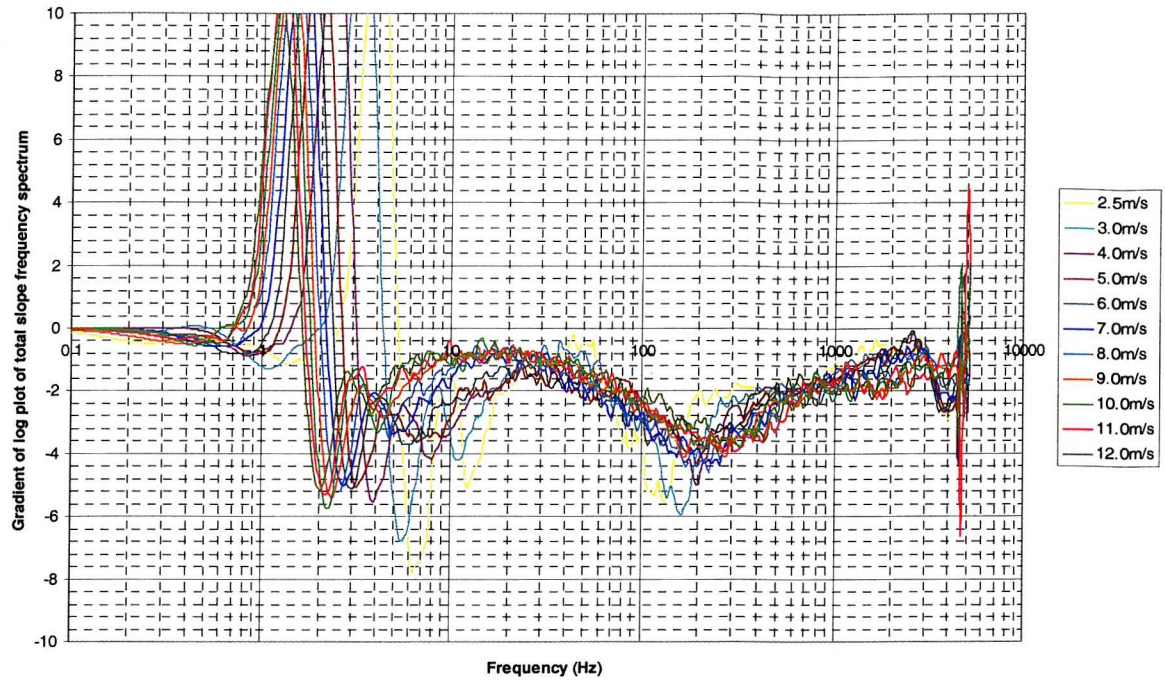

Figure 7-18: Gradient of log plot of total slope frequency spectrum versus frequency for data set 1

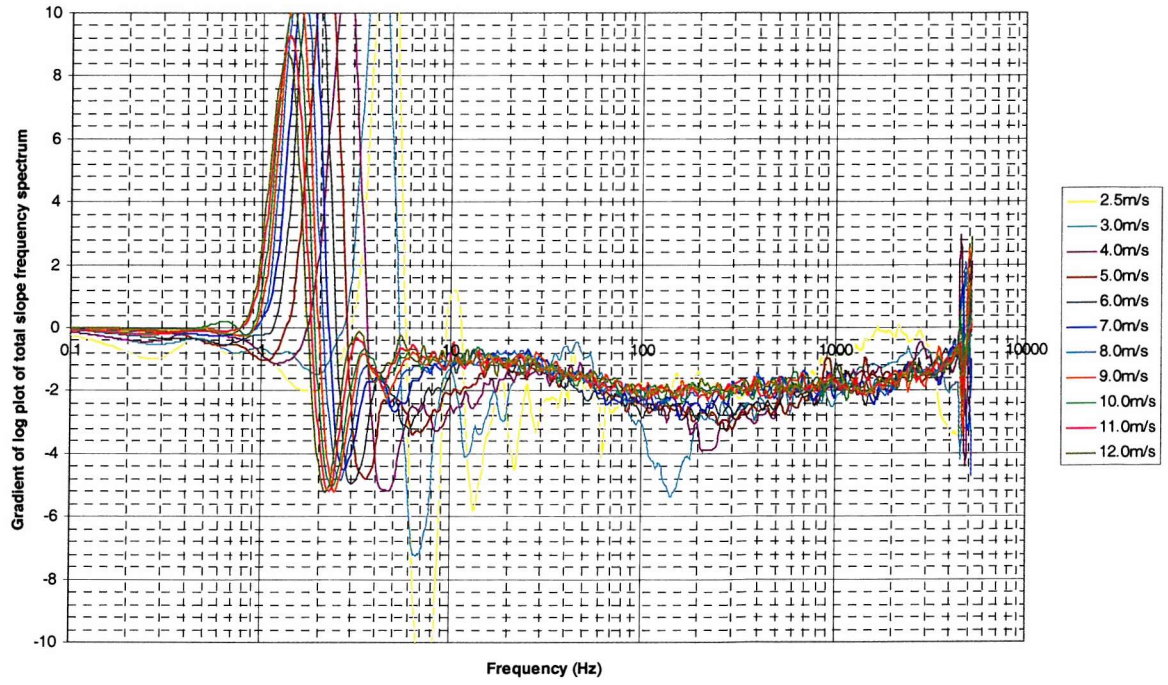

Figure 7-19: Gradient of log plot of total slope frequency spectrum versus frequency for data set 2

magnitude of the energy measured at each frequency in the gravity-capillary range reduced increasingly towards higher frequencies. Data set 1 qualitatively seems very similar to Lange's spectrum measured with a laser spot size of 1.8mm. The results of Long and Huang (1976) also show similar behaviour with a peak followed by a bulge in the gravity-capillary range. Below wind speeds of 7m/s the spectral shape of the DERA laser slope meter data changes slightly. There is then a distinct difference for wind speeds below 3m/s. This may be caused by some change in the interaction mechanisms present for the wavelengths generated in the tank at these wind speeds.

7.5.3 Overall effect of laser spot size on measurements

It is difficult to quantify precisely what effect the finite size of the laser spot may be having upon the measurements. As was discussed above, the differences seen between data sets 1 and 2 may be due to the laser spot size but may also be due to a number of other factors. The experimental tests have been inconclusive due to increased noise in the system. Frequency regions where one might assume the spot size is important may not be affected due to the short scale waves being either bound or parasitic, and with this laser slope meter it is impossible to distinguish between such waves and short scale waves following the gravity-capillary dispersion relation. Overall, it is reasonable to assume from the theoretical studies that data up to 100Hz is believable from data set 1 and up to 300Hz from data set 2.

7.5.4 Information on angular distribution of wave field

The cross and along tank components of the surface slope frequency spectrum can be written in terms of the full wavenumber height spectrum, $\Psi(k,\phi)$, as,

$$S_x(\omega) = k^2 \int_0^\infty \int_0^{2\pi} \Psi(k,\phi) \sin^2\phi \, k \, dk \, d\phi \, \delta(\pm\omega - \omega(k)) \qquad 7\text{-}10$$

$$S_y(\omega) = k^2 \int_0^\infty \int_0^{2\pi} \Psi(k,\phi) \cos^2\phi \, k \, dk \, d\phi \, \delta(\pm\omega - \omega(k))$$

It is assumed that the wavenumber spectrum takes the following form,

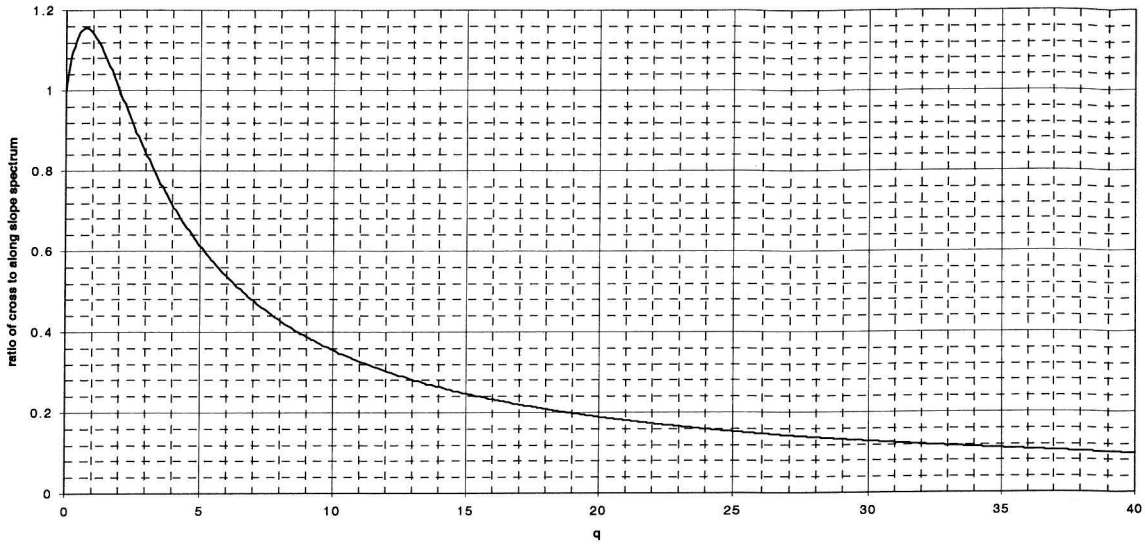

Figure 7-20: Relationship between cross to along tank spectral ratio and q.

$$\Psi(k,\phi) = \psi(k) A_q \cos^q\left(\frac{\phi}{2}\right) \qquad 7\text{-}11$$

where,

$$A_q^{-1} = \int_0^{2\pi} \cos^q\left(\frac{\phi}{2}\right) d\phi \qquad 7\text{-}12$$

Transforming dk to dω via the dispersion relation and integrating over the delta function then,

$$S_x(\omega) = \frac{2k^3}{\partial\omega/\partial k} \psi(k) \int_0^{\pi} A_q \cos^q\left(\frac{\phi}{2}\right) \sin^2\phi \, d\phi \qquad 7\text{-}13$$

$$S_y(\omega) = \frac{2k^3}{\partial\omega/\partial k} \psi(k) \int_0^{\pi} A_q \cos^q\left(\frac{\phi}{2}\right) \cos^2\phi \, d\phi$$

for those wavenumbers and frequencies that satisfy the dispersion relation. Taking the ratio of the spectra leads to an expression in q (Hughes, 1978),

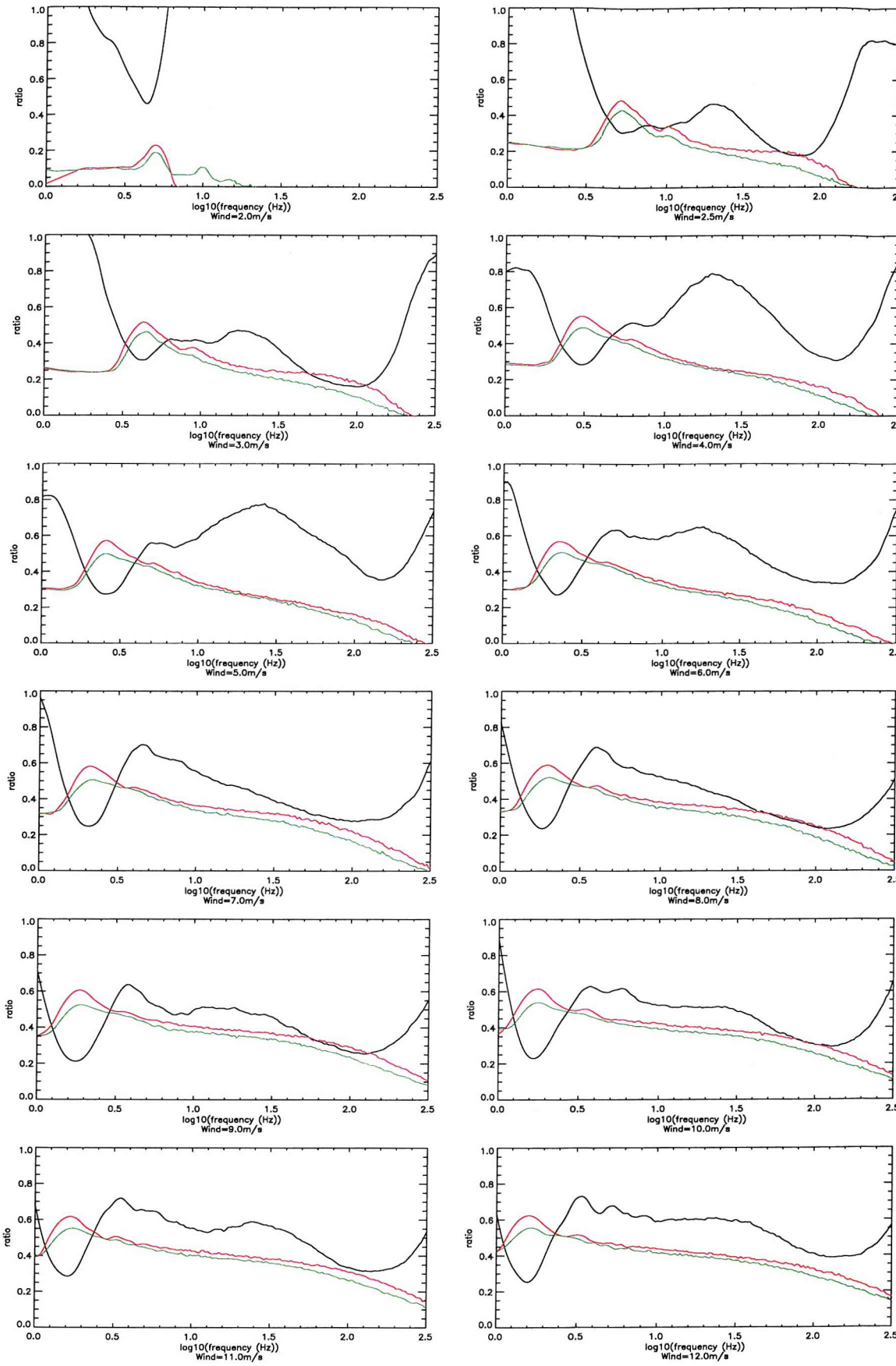

Figure 7-21: Ratio of cross to along spectra for data set 1

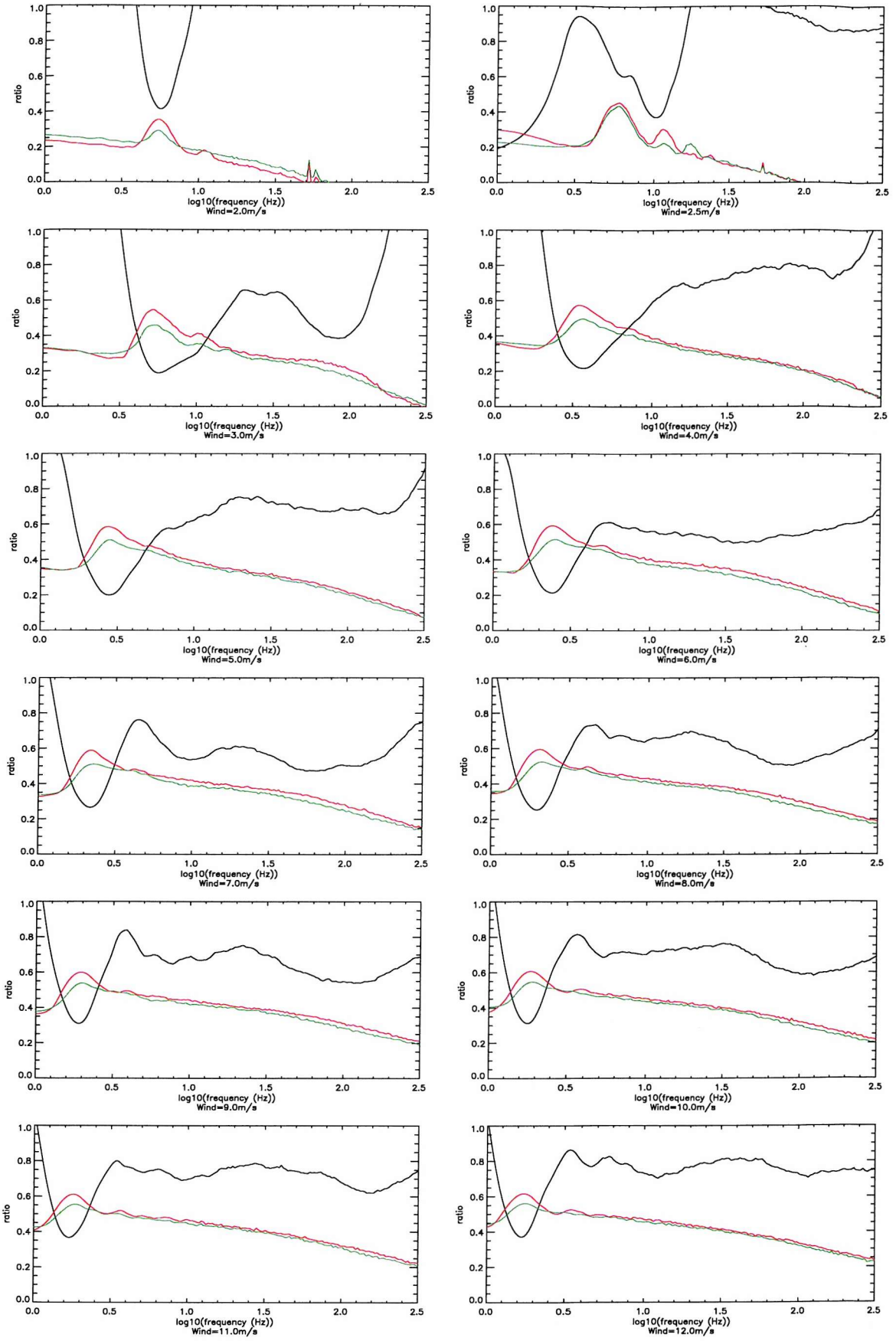

Figure 7-22: Ratio of cross and along spectra for data set 2

$$\frac{S_x(\omega)}{S_y(\omega)} = \frac{\int_0^{\pi} \cos^q\left(\frac{\phi}{2}\right)\sin^2\phi d\phi}{\int_0^{\pi} \cos^q\left(\frac{\phi}{2}\right)\cos^2\phi d\phi} = \frac{4(q+1)}{q^2+2q+4} \qquad 7\text{-}14$$

A graph of the relationship between the ratio and q is plotted in figure 7-20.

The ratios of the cross to along tank spectra have been calculated for each of the data sets presented above (except for the lowest wind speed where no waves are created) and are plotted for each wind speed in figures 7-21 and 7-22. Log plots of the cross (green) and along (red) tank spectra have been superposed as this helps to show how the variation in the ratio is related to the different spectral components in each wind wave field. The y-scale for the spectra is arbitrary.

It can be seen that there are strongly different characteristics between the data sets. Set 1 in general shows the wave field to be highly directional about the peak. Then there is an interim region where the wave field is less directional followed by a more directional region at higher frequencies. This may be evidence of parasitic capillary waves riding on the dominant wavelengths. In set 2 a similar behaviour is seen except that the directionality is reduced overall (the ratio is high) at the high frequencies except at 3m/s. The regions of reduced directionality often have a ratio of approximately 0.7, equivalent to q=4, which is characteristic of open ocean data within the equilibrium range (Apel, 1994).

These observations could be explained in the following way. Since set 1 was collected further from the wind tunnel exit than set 2, the majority of wind-driven capillary waves may have dissipated to a large extent except for those which are being locally generated by the longer gravity waves. Therefore, the high frequency waves would show a much greater directionality. Alternatively, these differences may be associated with the differing noise levels and laser spot sizes between the experiments.

7.5.5 Estimation of wavenumber spectrum

An estimate of the wavenumber spectrum can be calculated by summing the two expressions in 7-13 and rearranging. This leads to a relationship between $\psi(k)$ and $S(\omega)=S_x(\omega)+S_y(\omega)$,

$$\psi(k)=\frac{S(\omega)\partial\omega/\partial k}{2k^3\int_{-\pi}^{\pi}A_q\cos^{q(k)}\left(\frac{\phi}{2}\right)d\phi}=\frac{S(\omega)\partial\omega/\partial k}{2k^3} \qquad 7\text{-}15$$

Alternatively, either component of the slope frequency spectrum can be used with the appropriate angular term.

The above calculation assumes that the dispersion relation for gravity and capillary waves is valid for the full range of wavenumbers. This ignores wind drift at all wavenumbers, which was not measured. Additionally, for short waves, there may be advection of the short waves by the longer surface waves.

Recently, there has been extensive research into the background frequency-wavenumber spectra using scanning and imaging devices in wind wave tanks (Hara *et al.,* 1997, Zhang, 1995, Klinke and Jahne, 1992). In particular, Hara *et al.* have made measurements of the full wavenumber frequency slope spectra using a scanning laser slope meter. Their data show that these effects are important, although they were not able to find any simple relationship to adequately describe the data in terms of these effects for all wind speeds. Along the wind direction, energy was usually between the normal dispersion relation curve and a curve plotted for the waves being advected by both surface drift and the phase speed at the peak of the spectrum. Different frequencies had energy on different curves, suggesting that the dominant effect modulating the standard dispersion relation was wavenumber dependent. Across the wind direction, the standard dispersion relation fitted the measured data very well.

As there is currently no way of taking these effects into account, 7-15 has been used to calculate an estimate of the wavenumber spectrum relating to the frequency spectra collected in the wind wave facility at UCSB. Here data set 2 has been used as the results

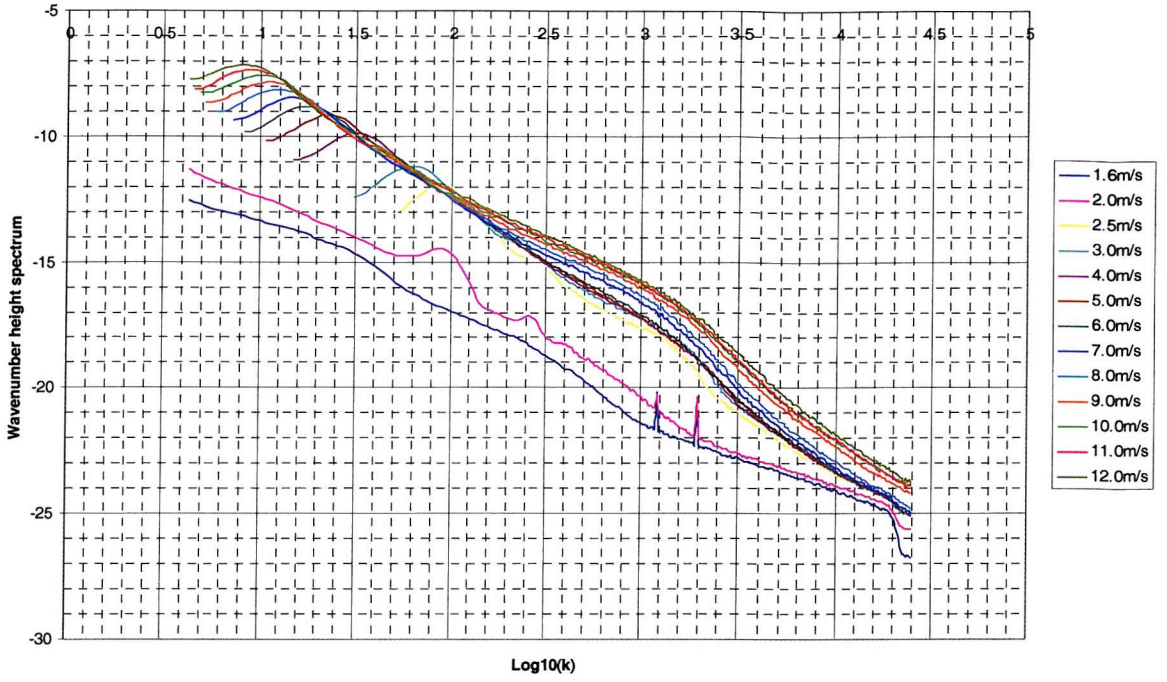

Figure 7-23: Wavenumber spectra calculated from slope frequency spectra

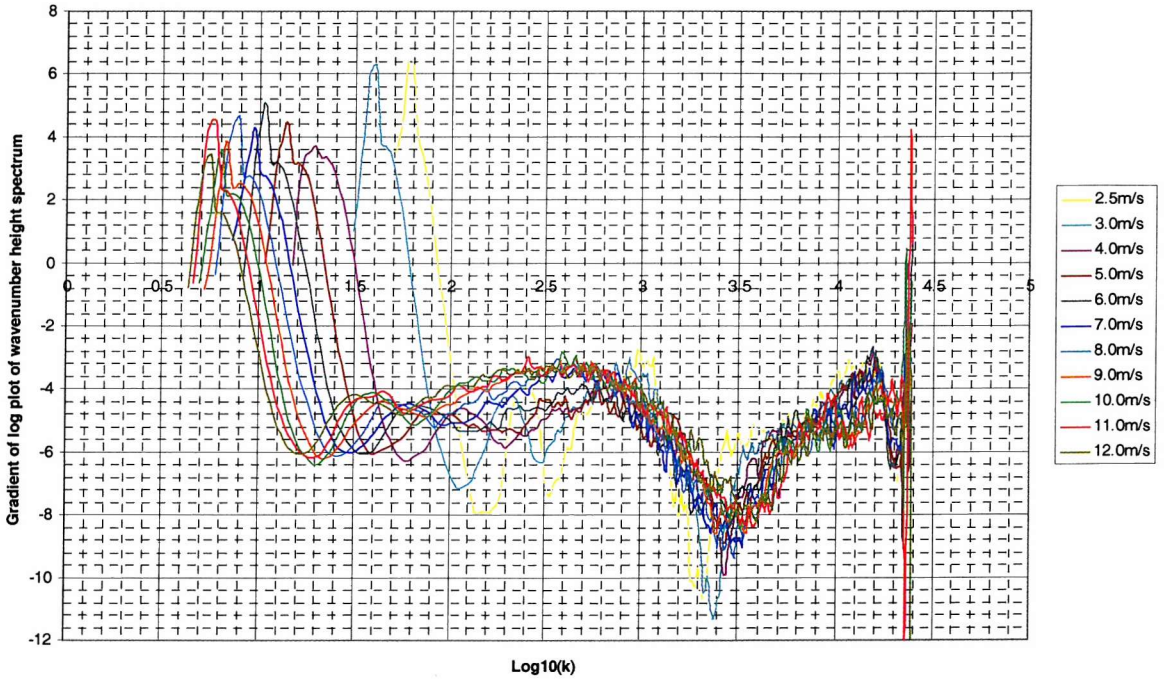

Figure 7-24: Gradients of wavenumber spectra shown in figure 7-21 except wind speeds of 1.6m/s and 2.0m/s which have been omitted for reasons of clarity

will be used in the analysis in chapter 9. The total slope frequency spectrum has been calculated from the sum of the along and cross tank slope frequency spectra, and has been used directly in 7-15 along with the gravity-capillary dispersion relation connecting ω and k. The resulting spectra are displayed in figure 7-23.

It can be seen that these spectra show a spectral peak and then decay with an approximately constant power law down to short wavelengths. There is a small bulge in each spectrum around 1000rad/m in approximately the capillary wave regime. This has been observed in other experimental data summarised in Apel (1994). In figure 7-24 the gradients of the above wavenumber spectra are displayed. These graphs show that between the spectral peak and the capillary wave section, the mean gradient is between –3 and –5. A value of –4 was predicted on dimensional grounds by Phillips (1958) and also by Belcher and Vassilicos (1997), and this basic form of the wavenumber spectrum is used widely for modelling purposes (Holliday *et al.*, 1987). However, these data do not distinguish between this form of the wavenumber spectrum and Phillips (1985) later spectral form of $k^{-3.5}$. The overall shape and character of these resulting wavenumber spectra give confidence in the method.

7.6 High frequency wave profiles

7.6.1 Wind waves

In figure 7-25 are some data examples of the slope time series measured in the wave tank from data set 1. Wind speeds of 2m/s, 4m/s, 6m/s, 8m/s 10m/s and 12m/s have been selected to provide coverage of the full range of data collected. The change in data character can be seen very clearly as the wind speed increases. In these graphs, positive slopes represent the front faces of the wind waves.

At 2m/s it can be seen that the signal to noise ratio is poor as the slope amplitudes are very small. The apparent dominant wavelength is quite short.

At 4m/s small capillary waves are visible on the surface with the remaining wave field quite smooth in character. The capillary waves are generally situated on the front faces of the waves although, in the example, one patch is on the back face of the wave. It was

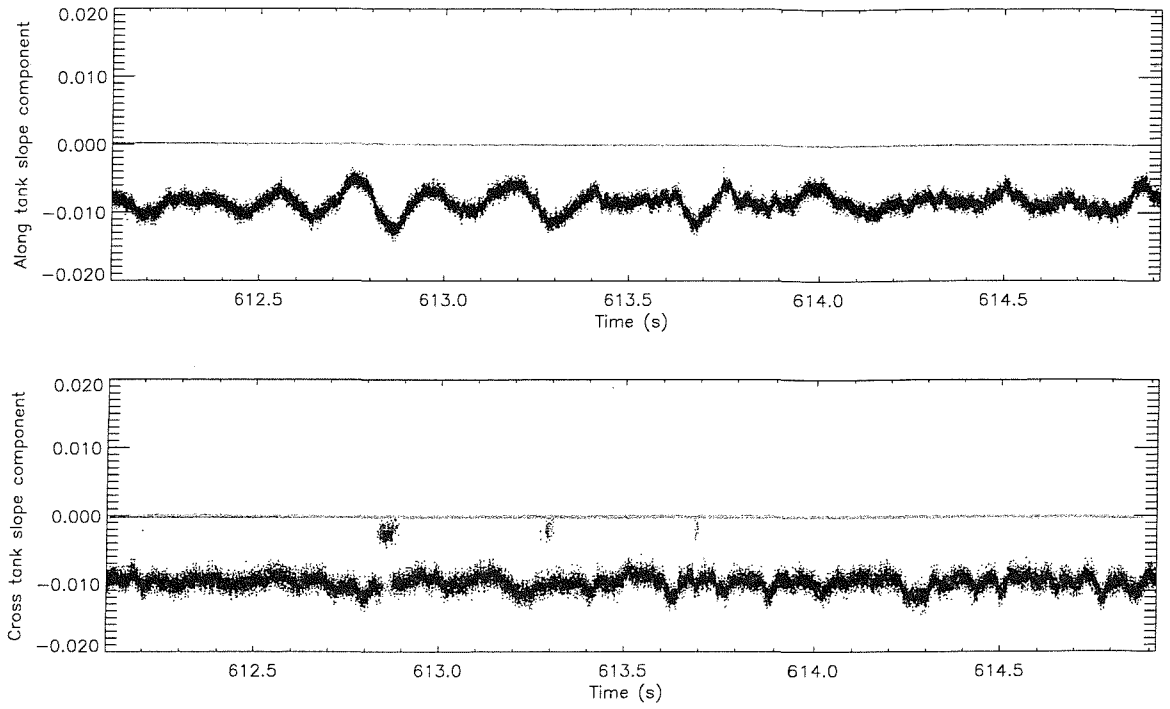

Figure 7-25a: Laser slope meter measurements of wind waves generated in the UCSB wind wave facility at w=2m/s

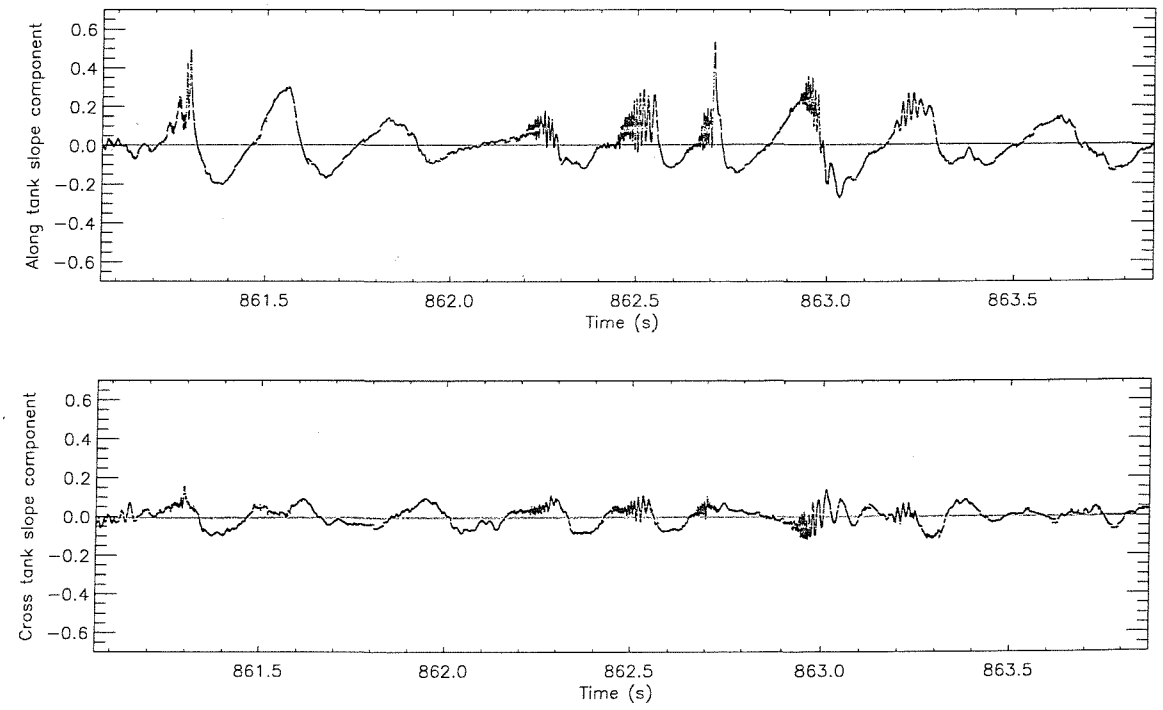

Figure 7-25b: Laser slope meter measurements of wind waves generated in the UCSB wind wave facility at w=4m/s

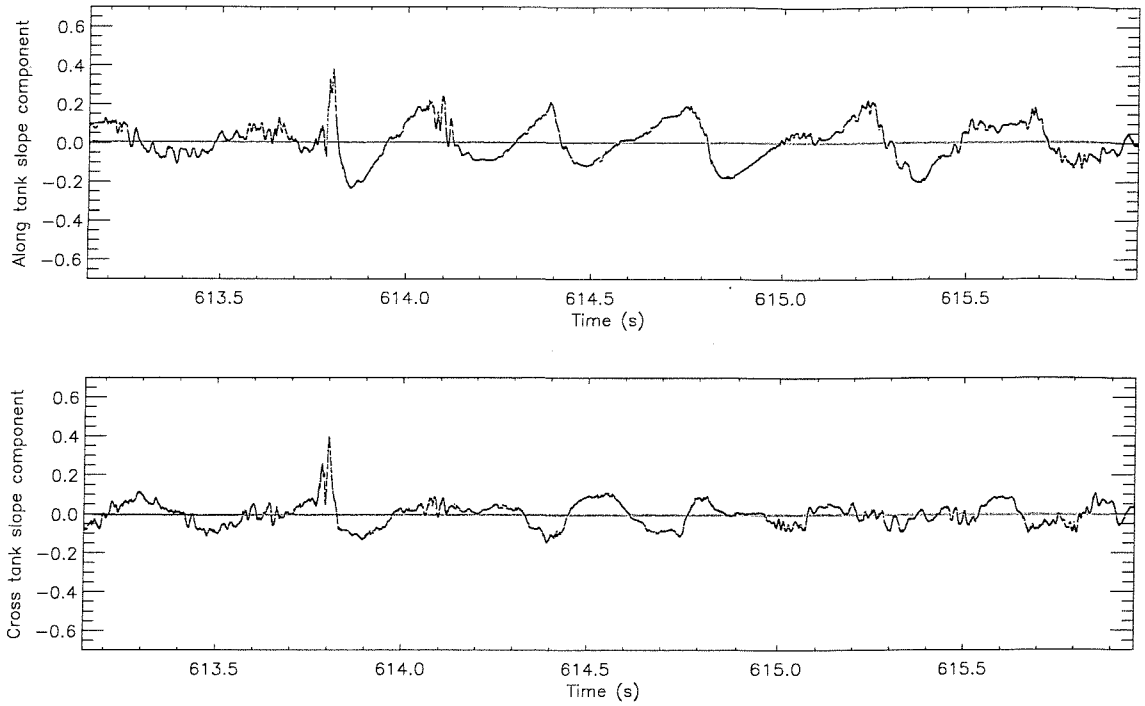

Figure 7-25c: Laser slope meter measurements of wind waves generated in the UCSB wind wave facility at w=6m/s

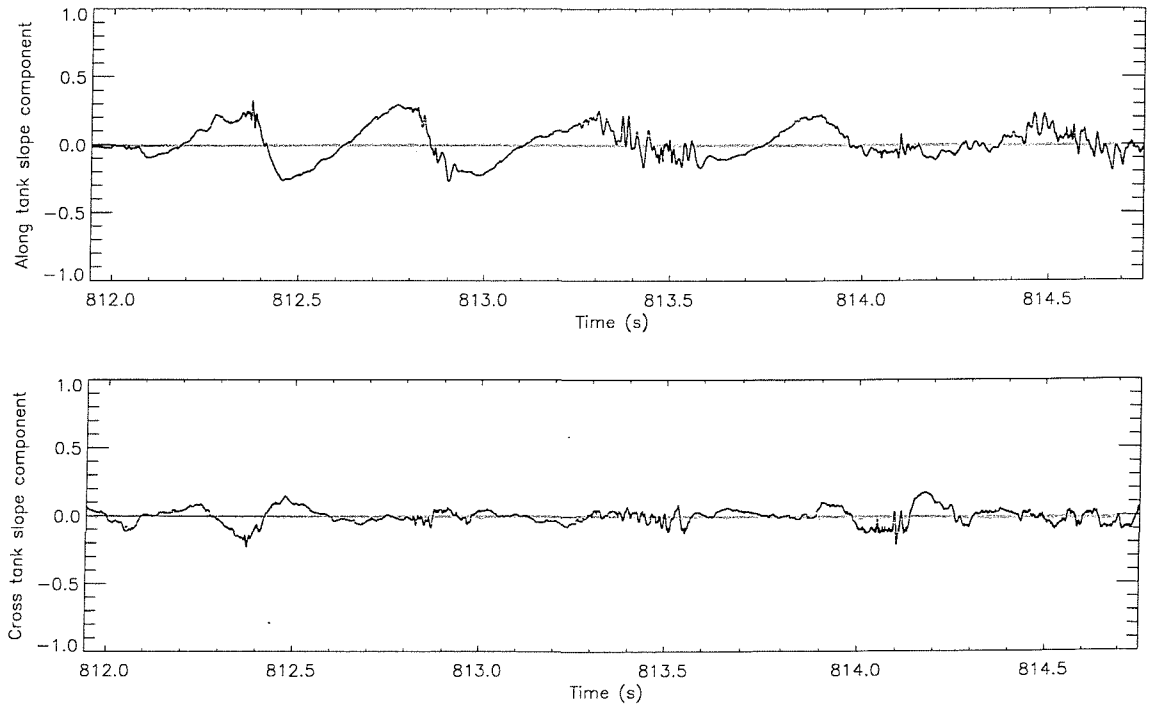

Figure 7-25d: Laser slope meter measurements of wind waves generated in the UCSB wind wave facility at w=8m/s

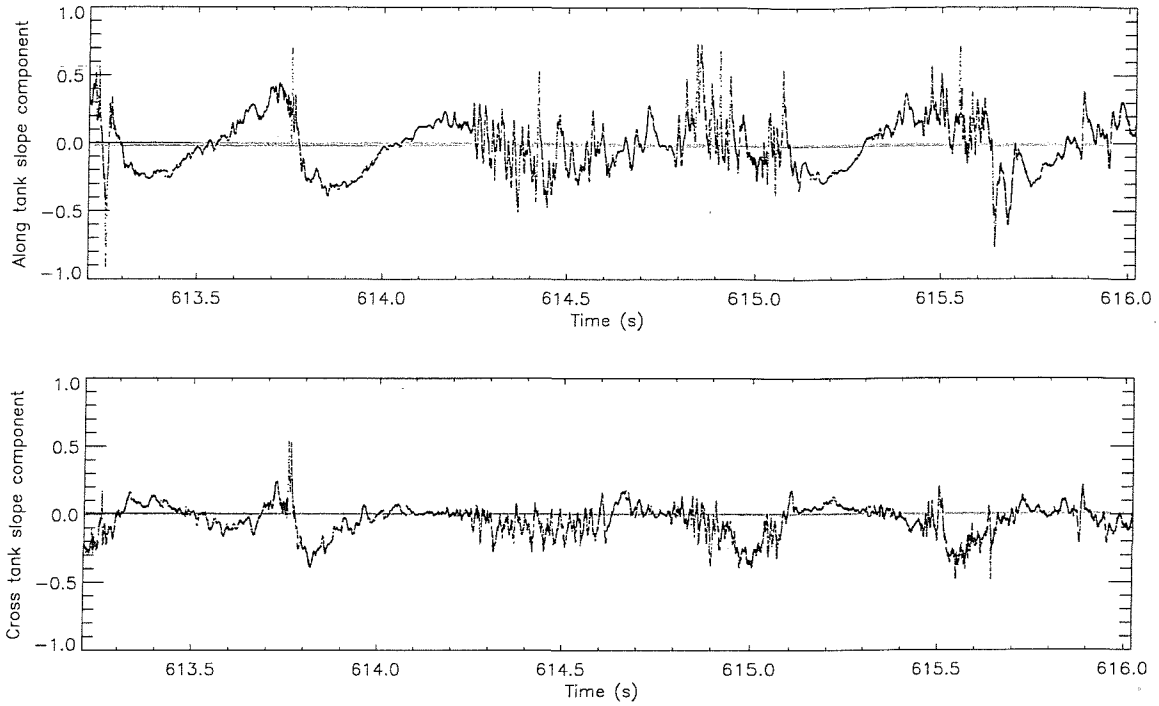

Figure 7-25e: Laser slope meter measurements of wind waves generated in the UCSB wind wave facility at w=10m/s

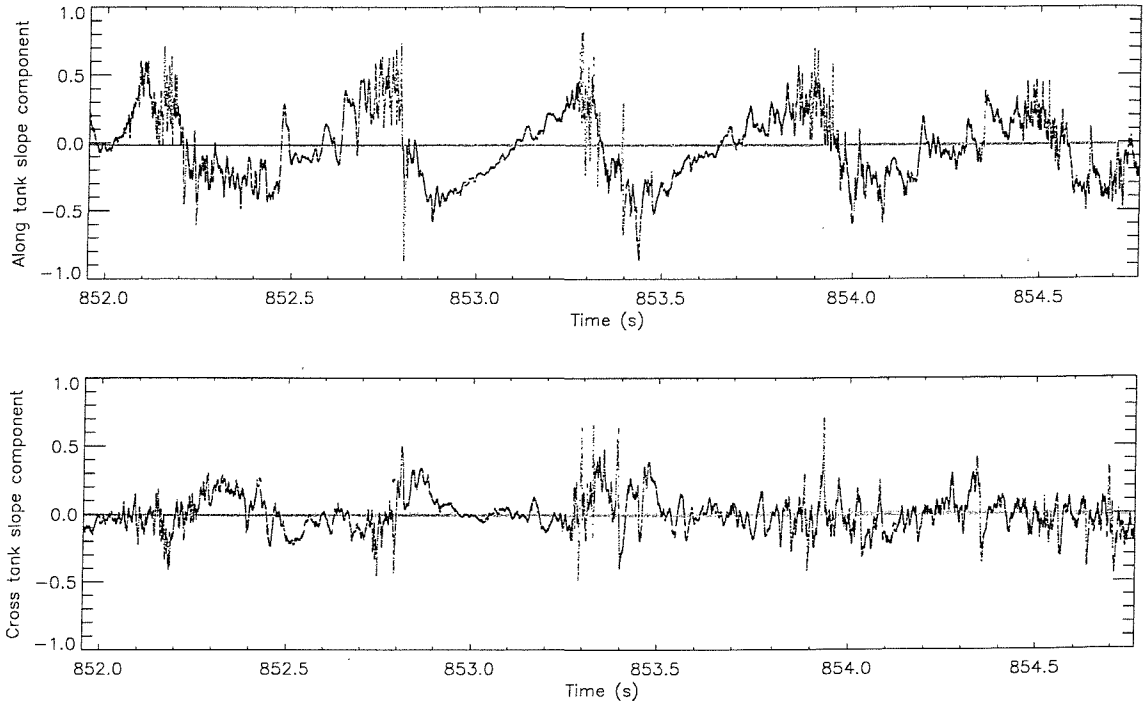

Figure 7-25f: Laser slope meter measurements of wind waves generated in the UCSB wind wave facility at w=12m/s

observed visually, that once the capillary waves were generated on the front face, on some occasions the dominant wave appeared to pass by the capillary waves which would travel backwards over the crest of the dominant wave and over its back face, relative to the speed of the dominant wave.

Throughout the rest of the wave fields, the surface gets gradually rougher and the dominant wind wavelength increases. Most of the roughness is associated with the crests of the dominant waves. It can also be seen that the crests of the dominant waves (where the slope goes from +ve to –ve with increasing time) are much sharper than the troughs (where the slope goes from -ve to +ve with increasing time), signified by the difference in gradient of the slope between the two areas. The crests and troughs also appear parabolic as the slope has a constant gradient. It is noticed, however, that as the wind speed increases, the range of slope values has not changed significantly, indicating that at all wind speeds above the critical value for wave generation, large slope values are generated.

7.6.2 Investigation of the capillary waves

The time axis for the along and cross tank slope components have been expanded for of a number of capillary wave features observed when the wind speed was 4m/s. The time axis shows when the data were collected. The enlargements are shown in figure 7-26a-7-26f.

The suggestion is made here that these waves are parasitic capillary waves. In support of this suggestion, it is noted that these capillary waves are clearly apparent to the eye, on the gravity waves at some distance from the end of the wind wave tunnel. Normally, short waves such as these would dissipate quickly suggesting that the source of these waves is not the wind, but may be the gravity waves themselves, as would be the case for parasitic waves. In addition to this argument, the directional analysis performed earlier indicated that many of the high frequency wave components were almost as directional as the spectral peak. This would suggest that the short waves may be related to the longer waves in some way, such as being generated by them rather than by the wind. It can be seen from these plots of the along tank and cross tank slope components that in some cases the waves do appear to be travelling directly down the tank, whilst in other cases there is a cross tank component to the capillary waves. In the following analysis, only the along tank slope component will be considered.

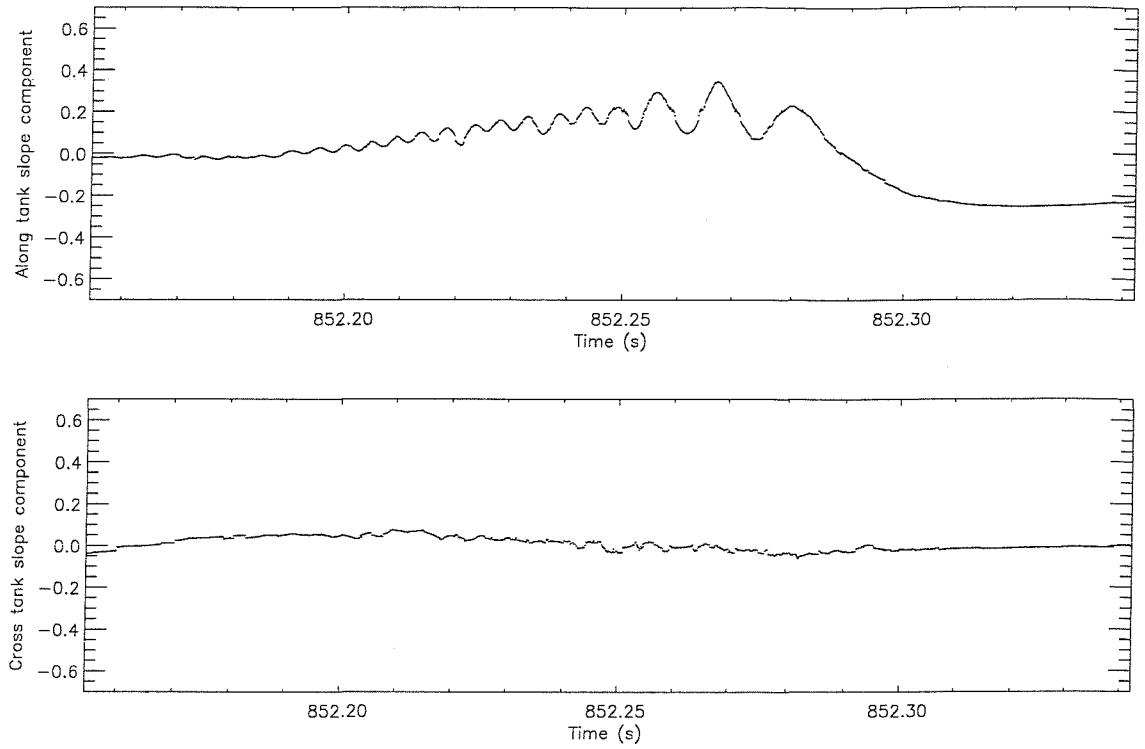

Figure 7-26a: Detail of capillary wave packet number 1

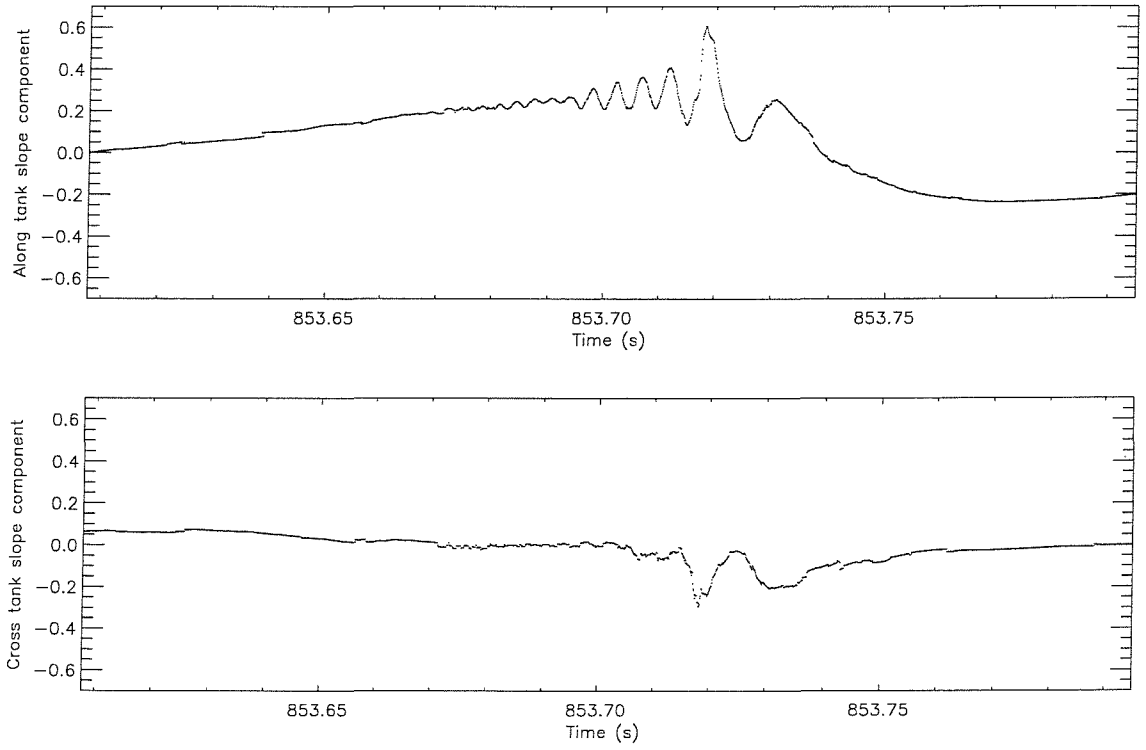

Figure 7-26b: Detail of capillary wave packet number 2

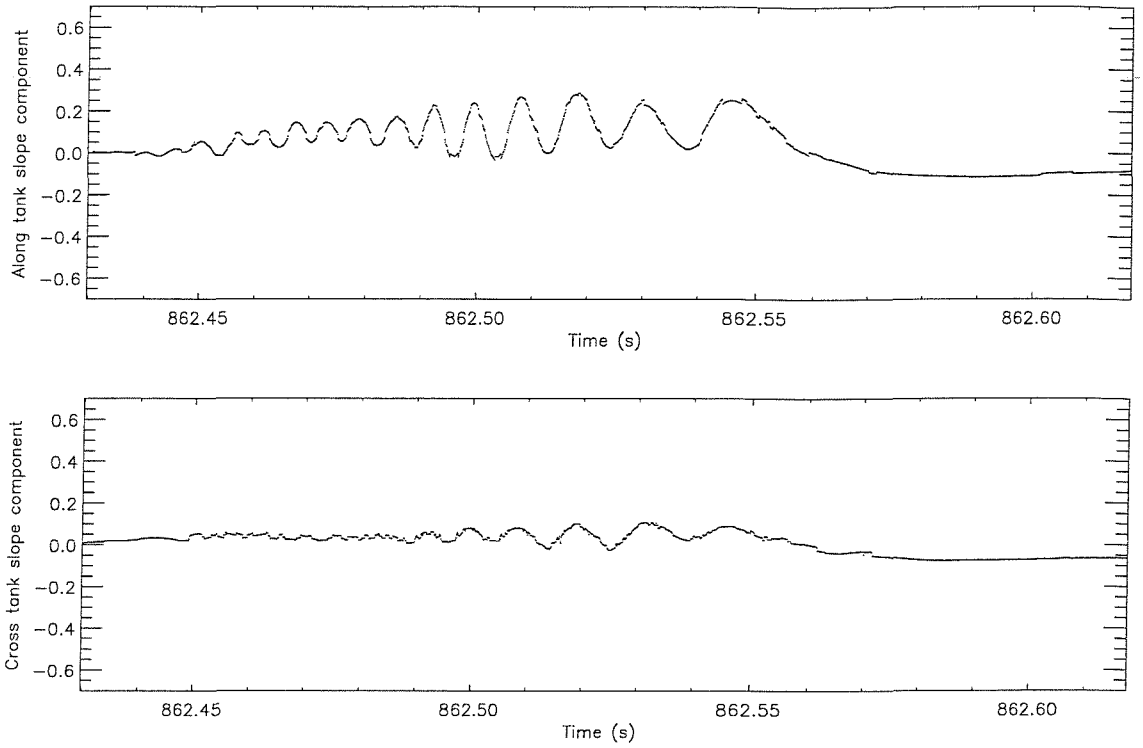

Figure 7-26c: Detail of capillary wave packet number 3

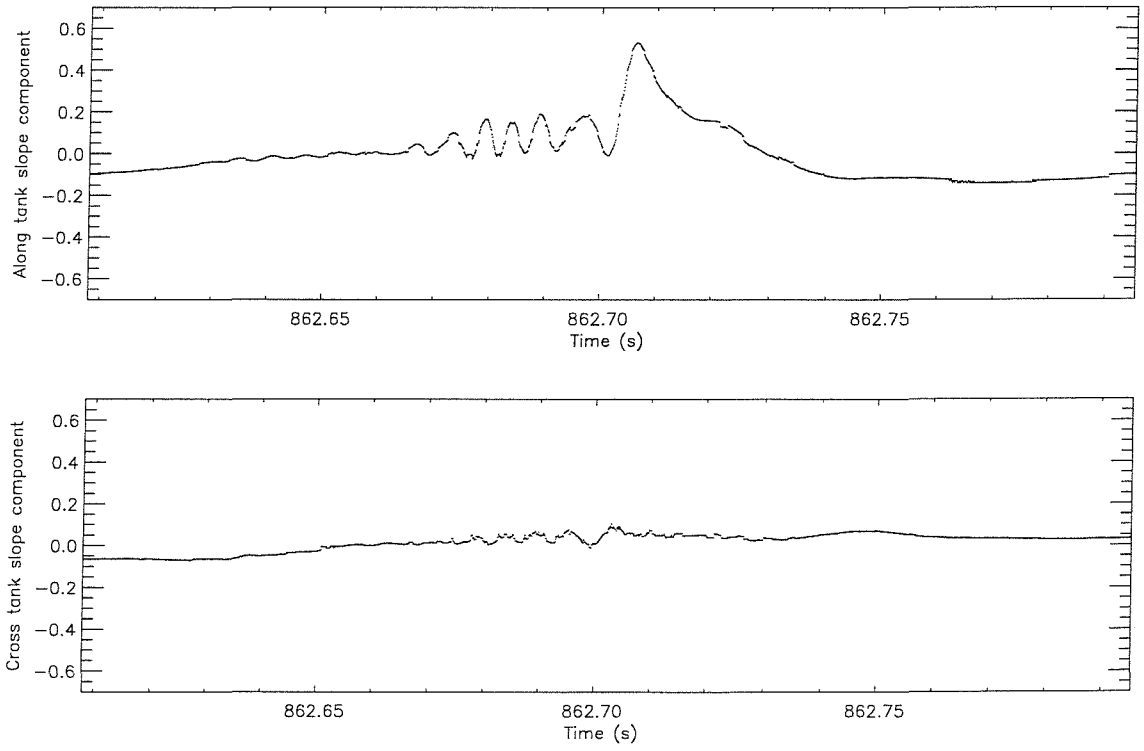

Figure 7-26d: Detail of capillary wave packet number 4

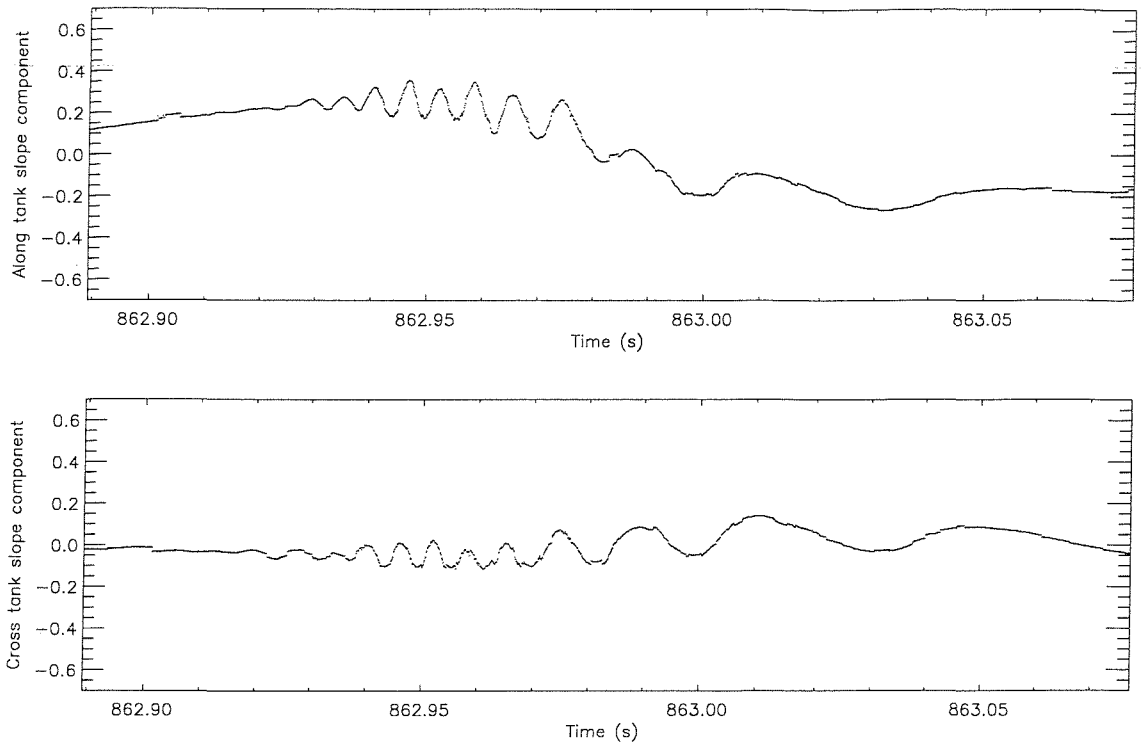

Figure 7-26e: Detail of capillary wave packet number 5

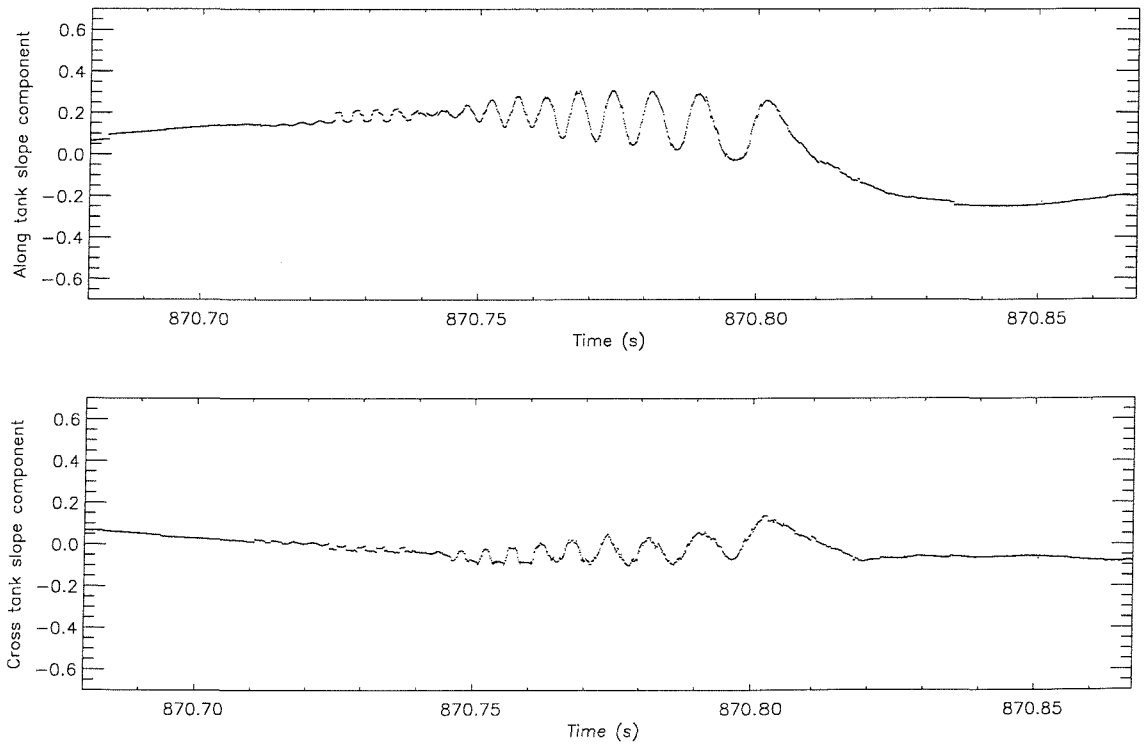

Figure 7-26f: Detail of capillary wave packet number 6

If these waves are parasitic waves, they may be compared with the theory of Longuet-Higgins (1995). This theory assumes that the capillary waves are generated by the uneven pressure distribution set up by the varying surface tension over the wave surface. It shows that it is possible for there to be two types of region on the wave surface relating to where the wavenumber of the possible capillary waves is either real or imaginary. If the wavenumber is real, that part of the wave is "resonant" and capillary waves can exist. If the wavenumber is imaginary, that part of the wave is "non-resonant" and capillary waves cannot exist. At low steepnesses, all parts of the gravity wave are resonant. However, as the wave steepness increases, for all wavelengths there becomes a critical wave steepness, $(ak)_c$ beyond which there are non-resonant regions near to the wave crests. The capillary waves are trapped between two caustic points located either side of the wave crest. Gravity waves with $ak<(ak)_c$ are known as subcritical whereas waves with $ak>(ak)_c$ are known as supercritical.

The theory shows that the maximum amplitude of the parasitic capillary waves occurs for gravity waves of near critical steepness rather than at maximum steepness as might be expected. The amplitude of the capillary waves decreases as the steepness moves away from the critical value in both directions. In terms of slope, this is characterised by large amplitude oscillations in the slope magnitude near critical steepness. For the steepest supercritical waves, a "toe" feature appears near the wave crest characterised in wave slope by the first ripple being of much smaller magnitude than the subsequent ripples.

Longuet-Higgins' theory shows that if T_p is the period of the gravity wave then the corresponding wave speed is given by,

$$c_p = \frac{1.069 g T_p}{2\pi} \qquad 7\text{-}16$$

and the wavelength by,

$$\lambda = c_p T_p \qquad 7\text{-}17$$

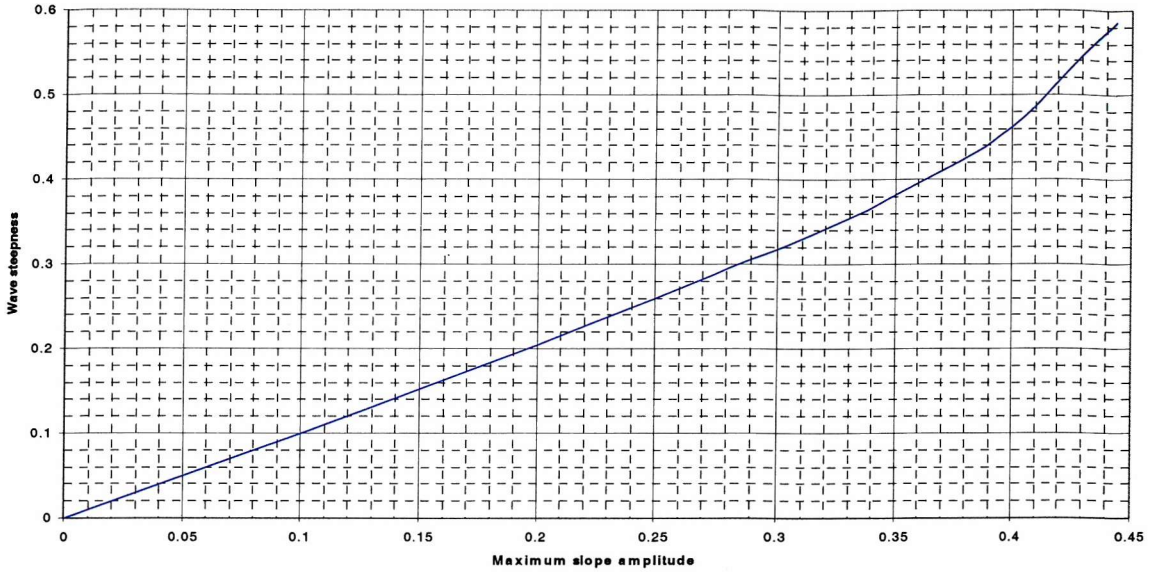

Figure 7-27: Relationship between the maximum slope amplitude and the wave steepness

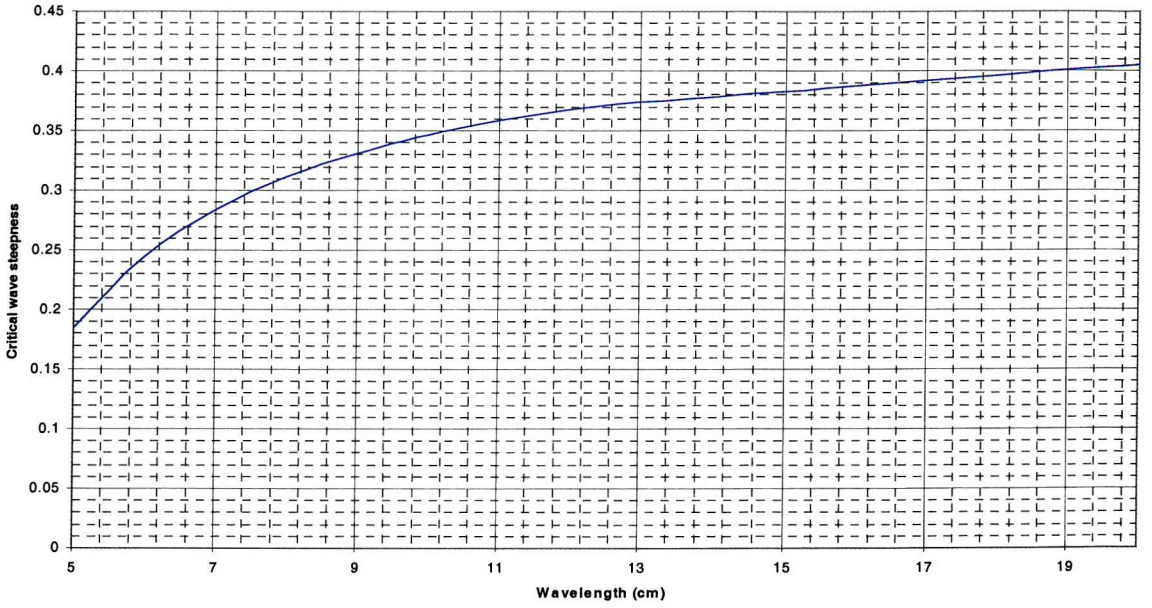

Figure 7-28: Relationship between the wavelength and the critical wave steepness

In order to calculate the wave steepness from experimental data, Longuet-Higgins suggests drawing a smooth trace through the experimental profile of the gravity waves containing parasitic capillary waves to obtain the slope amplitude (this is half the difference between the maximum and minimum slopes). Using the theory Longuet-Higgins calculated a series of numbers, plotted graphically in figure 7-27, which relates the slope amplitude to the

wave steepness, ak. A second list of numbers, plotted in figure 7-28, relates the wavelength to the critical steepness.

In this analysis, the theory is used in an attempt to determine the type of capillary waves that may have been measured. For comparison with the theory, it is necessary to know the average period of the long waves, T_p. This may be measured approximately from figure 7-25b as T_p=0.297s. This leads to c_p=0.50m/s and λ=0.15m. It will be assumed that this is the same for all the wave packets presented here.

Using figure 7-28, the critical wave steepness for the experimentally measured waves is approximately 0.38. Drawing a smooth line through the data is quite subjective and can alter whether or not a wave packet appears to be subcritical or supercritical. It is not clear whether the line should take the central point of the capillary waves, or follow the line of the peaks or troughs. Because of this uncertainty, it is difficult to compare the theory accurately with the data. Assuming a central line, using this process, all of the waves appear to be subcritical. However, it is noted that for those wave packets with the largest slope, shown in figures 7-26b and 7-26d, there is a smaller toe in the slope amplitude before the largest slope. This is also true to some extent for figure 7-26a. This shape is consistent with Longuet-Higgins supercritical waves.

These results are inconclusive as to the type of capillary waves measured, as the comparison of the data with the theory is not good. Reasons for this may be that the waves are not in fact parasitic, or because some of them are travelling at an angle across the wave tank. However, what these results do demonstrate is the clarity with which the laser slope meter has been able to capture the wave profile, showing that the noise level of the instrument is far below that which would hide such small features. In fact, the noise level is so low that the small areas of screen damage are visible in the data time series. The high sampling rate shows clearly that there is no small scale behaviour other than the capillary waves, and that the water surface is quite smooth to either side of the packet as well as over the capillary waves themselves. These data are presented here as they demonstrate clearly the capability of this instrument compared to other wave recording devices to measure detailed wave profiles.

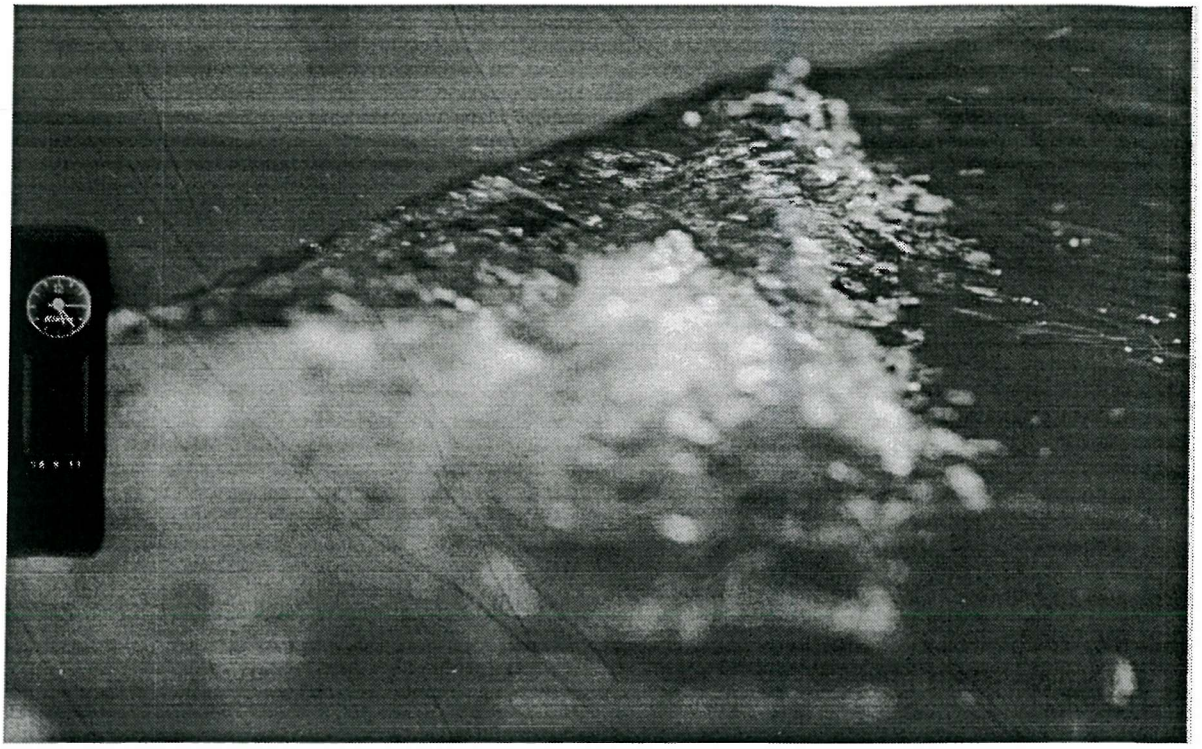

Figure 7-29a: Photograph of a breaking 2.0m group wave at 129.4720

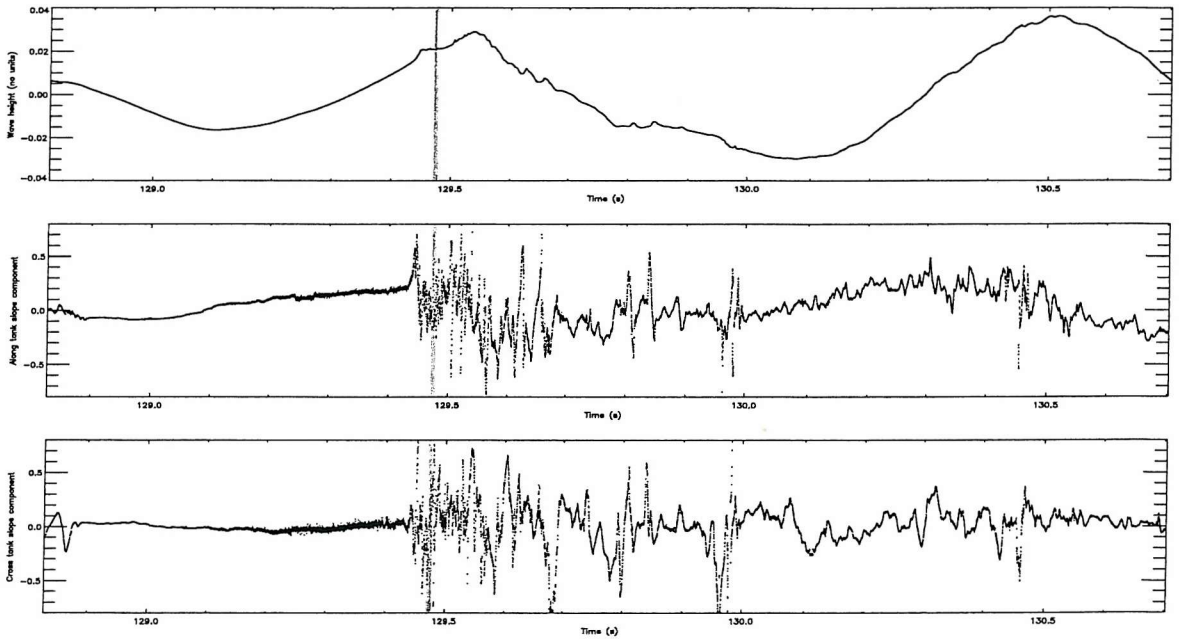

Figure 7-29b: Slope and integrated slope data of 2.0m breaking group wave in figure 7-29a. Vertical line represents when photograph was taken.

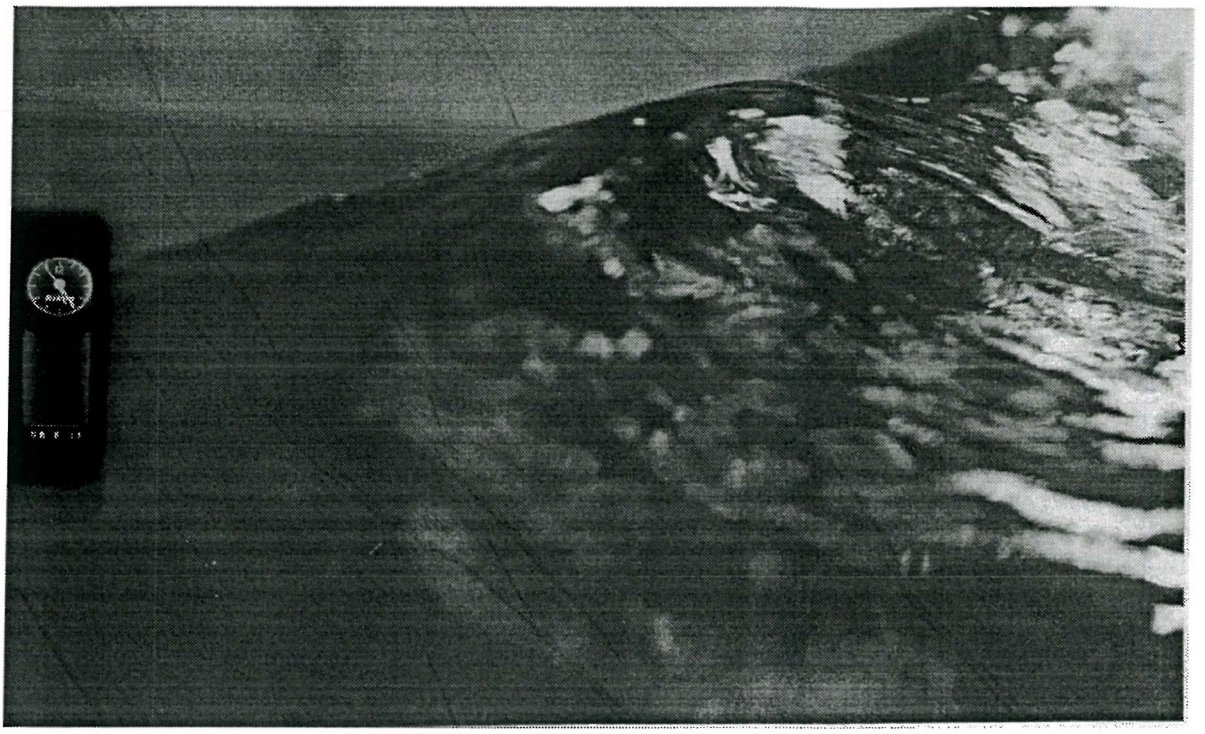

Figure 7-30a: Photograph of a 2.0m group wave on the verge of breaking at 167.9696

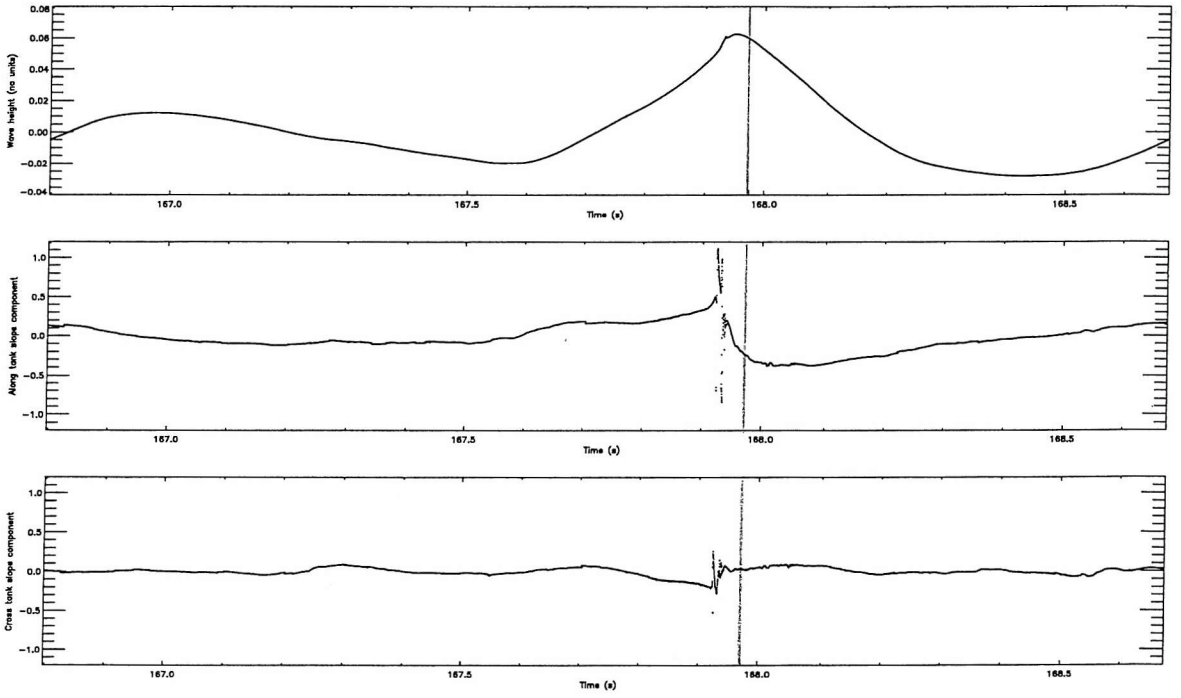

Figure 7-30b: Slope and integrated slope data of 2.0m group wave on the verge of breaking in figure 7-30a. Vertical line represents when photograph as taken.

7.6.3 Group waves

In addition to the wind wave field shown above, the Laser Slope meter was also used to make detailed measurements of the slope profiles of some groups of waves generated using a fully programmable mechanical wave making device. These waves were centred on a particular frequency and contained smaller amplitude frequency side bands. Two examples have been selected to demonstrate the detailed measurements which are possible with this instrument.

In figures 7-29b and 7-30b, the top graph is the time integration of the along tank slope which is an approximate representation of the wave height profile. In the first example, figure 7-29b, the data are very smooth between the trough and half way up the front face of the wave. Here, the froth created by the breaking group wave reaches the laser slope meter just as the photograph is taken. Observations showed that the froth tended to remain fairly static and the wave would pass through whilst the froth gradually reduced in more or less the same position within the tank. This can be seen here as the froth is recorded through the peak and following trough and peak of the group wave (see 7-29b).

In the second example, figure 7-30b, the laser slope meter has captured a very steep wave just on the point of breaking. The crest of the wave is just about to turn as it passes beneath the instrument, as is captured beautifully in the photograph.

7.7 Conclusions and discussion

In this chapter a number of distinct topics have been studied. The main objectives of the chapter were:

- to compare and contrast similarities and differences between data collected in the wave tank and data collected in other environments and to discuss how applicable measurements in this wind wave tank may be to the open ocean;
- to investigate the effect of the laser spot size on high frequency measurements and determine the limit of accurate measurements, given a particular laser spot size;
- to determine how it may be possible to estimate the wavenumber spectrum from the frequency spectrum and compare this with other experimental and theoretical results;

- to demonstrate the capabilities of the instrument to provide highly detailed measurements of the slope features of waves;
- to use all the data and analysis presented to make an assessment of the ability of the instrument to provide useful research results, but also to determine its limitations.

It has been shown that, provided wind stress is used rather than wind speed, the statistics of data collected both in the field and in wave tanks is comparable in terms of the variation of mean square slope with wind speed. As the wind speed increases, the along wind component becomes more skewed. Further to the studies presented in chapter 5, a second investigation is presented into whether a Gram-Charlier distribution is better than a Gaussian for fitting to histograms of the slope data. It is shown that a one-dimensional Gram-Charlier fit is an improvement and all of the Gram-Charlier coefficients except one, C_{40}, are approximately independent of wind speed. C_{40} increases approximately linearly with wind speed. A two-dimensional Gram-Charlier fit has also been studied and found in general to be better than a Gaussian, but it is still not a good representation of the actual distribution. The variation of the two-dimensional Gram-Charlier coefficients with wind speed was found to behave differently to those calculated by Cox and Munk.

The theoretical investigations into the laser spot size have shown that at high frequencies, the measured slope magnitude decreases in a known fashion. Thus spectral energies will be reduced, but provided the amount of reduction can be calculated, the original signal may be retrieved from the data. The practical investigations were not entirely conclusive because of additional noise in the data. Although the main trend is as expected, this exercise should be repeated to confirm the results.

The two components of surface slope frequency spectra, along- and cross- tank, for two different experimental data sets have been studied. Set 1 was collected with a low noise instrument with a large laser spot size several metres from the wind tunnel exit, whilst set 2 was collected with a noisy instrument but with a small laser spot size close to the wind tunnel exit. The high frequency components were found to be significantly reduced in energy in set 1 compared to set 2. This may be due to filtering of high frequencies by the larger spot size, reduced energy at these frequencies due to viscous dissipation during the

extra distance from the wind tunnel exit, or increased high frequency noise in data set 2 due to the noisy laser.

In the gravity wave region the spectra show similar characteristics to those measured in the open ocean and to theoretical predictions. Following the initial decay from the spectral peak (which is an artefact of a short fetch) the spectra decay approximately as f^{-1} to $f^{-1.5}$ which is broadly equivalent to $\psi(k) \sim k^{-4}$ (as is demonstrated by the estimation of the wavenumber spectrum). In this region, the angular distribution is similar to $\cos^4(\theta/2)$. The variation of the wavelength of the spectral peak with wind speed is linear. An effect similar to the overshoot effect is observed. At low wind speeds, where capillary waves were observed, the data were found to be more directional at high frequencies in set 1 than in set 2. This could be due to those short waves remaining at this position being generated by the longer gravity waves (i.e. being parasitic capillary waves).

The details of the slope wave profiles have highlighted some interesting features:

- the wave crests are much sharper than the troughs;
- in general, the wave crests and toughs are approximately parabolic leading to constant temporal rate of change of slope;
- the majority of the high frequency behaviour occurs on the front face of each wave (mainly in the top half of the wave);
- the second wave in a capillary wave packet has the largest slope magnitude on its front face;
- the period of the capillary waves is longest at the peak of the dominant wave and decreases down the front face.

These observations confirm the work of Stokes (1847, 1880) for parabolic troughs and crests and for crest sharpening, even at high wind speeds where the waves are fairly non-linear. Since most of the high frequency behaviour is on the front face of each dominant wave, it is likely to be caused by gravity as the wave crest turns and breaks rather than directly by the wind. Qualitatively, the capillary waves show features similar to Longuet-Higgins' theoretical parasitic capillary waves.

In this chapter the Laser Slope meter has shown itself to be a very worthwhile tool for exploring the characteristics of tank wind wave fields. In particular, the potential for high accuracy measurements of the smallest features has been demonstrated, including showing that capillary waves are the smallest features that occur on the water surface at low wind speeds, and that the waves are genuinely smooth around the capillary wave packets. Limitations caused by instrument noise and laser spot size have been investigated and it has been shown that improved performance could be achieved if these areas were improved. However, the limitations caused by sampling at a single spatial point can not be overcome, even when using special mathematical techniques to extract information about the surface. In order to obtain genuine short scale spatial information, including the speed of travel of the shortest waves, data will have to be collected with other devices, for example a scanning laser slope meter. Such instruments have become more common throughout the duration of this research project and it is now time to accept the limitations of the information available from the single point laser slope meter for certain types of measurements, and move onto the new technology. Nevertheless, there are still many research questions which can be answered adequately with this simplest type of laser slope meter, and due to the ease of processing and data analysis of this instrument compared to a scanning device, it should be used where more advanced information in not needed. Examples of this include statistical information on wave slopes at a single point, any temporal information, for example frequency spectra information and wave profiles, where spatial information is not required.

As a final remark for this chapter, it should be noted in future experiments that the combined effect of reduced laser noise and improved laser spot size should lead to the production of very high frequency and high accuracy data products which will provide significantly enhanced results even over those presented in this chapter. Thus, the full capability of the instrument has not yet been exploited.

Chapter 8

A numerical model to solve the action balance equation

8.1 Introduction and scope of chapter

In this chapter the work changes emphasis from the ambient wave fields studied in chapters 5, 6 and 7, to modulations of these ambient wave fields. The objective of this chapter is to describe the production and testing of a computer program which is capable of solving the full action balance equation for any reasonable form of background wind wave spectrum and any reasonable form of modulating one-dimensional horizontal current.

The program has been written in IDL and uses a numerical technique to solve the full action balance equation. The results from the programme will be valid for the full gravity and capillary range of wavenumbers provided the ambient spectrum used is valid for the entire range and if appropriate terms are inserted for growth, dissipation and wave-wave interactions. However, the gravity-capillary dispersion relation is assumed to provide wave speeds and this will also have to be corrected for the true speeds of capillary waves for the model to be fully applicable to the full range of wavenumbers.

The numerical method used in the solution of the action balance equation is presented and tested, and some sample results are included where functional forms have been used for the surface current and the surface wind wave spectrum. The modulated action value at individual wavenumbers within the wind wave field has been calculated as has the variation to the surface slope variance caused by the surface current. Although only a one-dimensional current is allowed, it may be at any angle to the dominant wind direction and the wind wave field may include an angular distribution as well as a variation of energy with wavenumber.

This work has been completed in preparation for the results presented in chapter 9. There, experimentally measured wind wave spectra and surface currents are input into the program and are used to produce theoretical results, which are compared with experimental data. This allows the experimental results to be compared with a theory using inputs which are specific to the data set. In doing this, limitations in both the theory and experimental method can be explored. This may help to assess the suitability of the Laser Slope meter for such measurements so that its full potential might be exploited.

8.2 Full solution of equation using a numerical method

8.2.1 Introduction

In this section, a description is given of how the full action balance equation can be solved using numerical techniques. The derivation of the action balance equation was discussed in chapter 4 and was shown to be,

$$\frac{dN}{dt} = \frac{\partial N}{\partial t} + \frac{\partial N}{\partial x}\frac{dx}{dt} + \frac{\partial N}{\partial k}\frac{dk}{dt} = N\left(1 - \left(\frac{N}{N_B}\right)^p\right) \qquad 8\text{-}1$$

It will be assumed that there is a two-dimensional region in space in which there exists a varying one-dimensional current pattern along the 'x'-direction which is modulating an underlying wind wave field. For the purposes of this analysis, and so that the results here are directly applicable to chapter 9, it is assumed that the current pattern is generated by the motion of a sub-surface carriage. This carriage can be driven at velocity, v, beneath the surface waves at any angle to the wind direction (although only parallel and anti-parallel directions will be considered in chapter 9). The current pattern generated by the carriage is stationary with respect to the carriage. Therefore, if the frame of reference of the carriage is used in 8-1, the temporal variations will be incorporated into dx/dt where this is the velocity of the surface wave packets relative to the carriage. Thus,

$$\frac{dN}{dt} = \frac{\partial N}{\partial x}\frac{dx}{dt} + \frac{\partial N}{\partial k}\frac{dk}{dt} = N\left(1 - \left(\frac{N}{N_B}\right)^p\right) \qquad 8\text{-}2$$

Solving the equation in this way would be similar to the cases when the current is generated by an internal wave or long surface wave. If bathymetry was the cause of modulations to a tidal current pattern, the equations would be the same in the reference frame of the bathymetry.

The technique used to solve 8-2 numerically is a 4^{th} order adaptive step size Runge-Kutta algorithm (Press *et al.*, 1986). It is used to step along the characteristics, i.e. the energy trajectories, beginning at points which are in a uniform grid in x,k, space around the region affected by the surface current, back in time using the kinematic equations until each point has reached its equilibrium value. The routine then steps forwards in time using the dynamic equations along the same characteristic line until the original start point is reached. The accumulation of numerical errors throughout this stepping procedure is carefully monitored throughout.

For each of the points in the x,k grid, the action is presented as the value of action at that point as modulated by the current normalised against the equilibrium action value at that wavenumber. Values of p=1 and 2 in equation 8-1 are considered along with ambient wavenumber spectra of the forms k^{-4} and $k^{-7/2}$ in the test cases. An angular distribution of $\cos^2\phi$ is used unless otherwise specified, where ϕ is the angle between a particular wavenumber and the wind direction. The modulation of the action of a particular wavenumber component is investigated in cases where the wavenumber is along the wind direction but the wind is at an angle to the current, and where the wavenumber is at an angle to the wind direction but the wind is parallel to the current direction. In the majority of cases, a current pattern of $U(x)=A\mathrm{sech}^2(x/4)$ is used. The shape of this current pattern is displayed in figure 8-1, with A=-0.1. This current form was selected for these tests as it is similar to the current pattern generated by carriage shape used in chapter 9, and it represents the surface current generated by a soliton internal wave (Perry, 1988). It has also been measured as the shape of the internal wave generated surface current during the SARSEX experiment (Thompson and Gasparovic, 1986). It is, therefore, typical of the type of current that might cause straining to wind wave fields in the open ocean. The surface slope variance is calculated by summing over the contributions from many different wavenumber components.

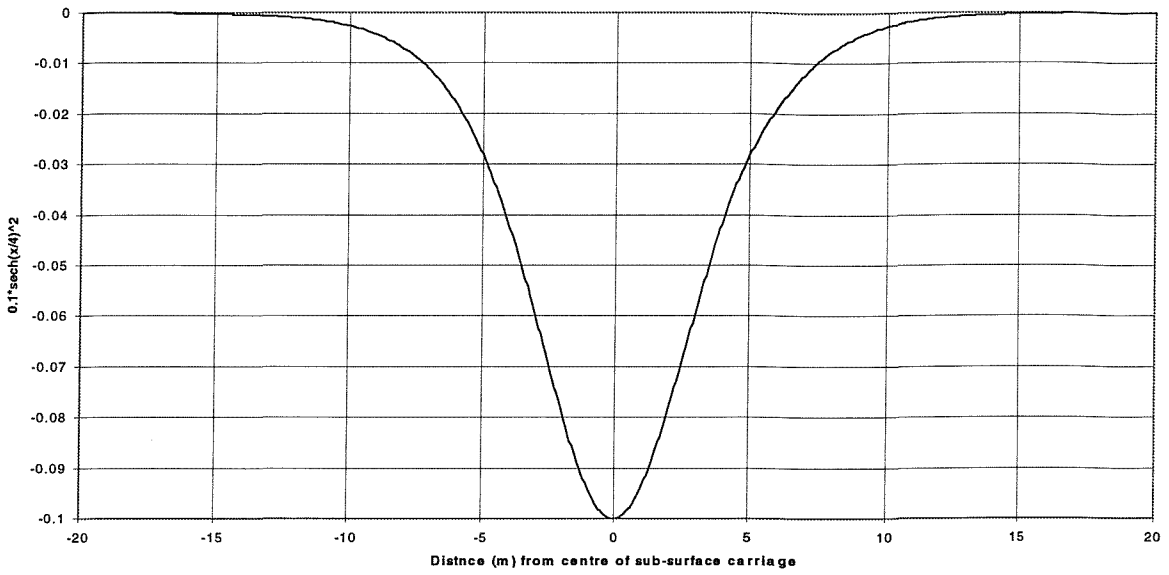

Figure 8-1: Current shape used in first three tests

8.2.2 Explanation of basic technique

Numerical methods may be used to solve a variety of differential equations for which there are no analytical solutions. Here, a 4^{th} order Runge-Kutta algorithm is employed to solve the characteristic equations for current modulated surface wind wave fields, which are a pair of linked differential equations, followed by the action balance equation along the line of the characteristics. The objective is to determine how the normalised action varies across the current pattern. To do this, it is necessary to know the initial value of the action in the equilibrium spectrum, which depends upon the initial value of the wavenumber of that action parcel. The initial wavenumber, and hence action value, are determined by tracing the action parcel backwards in time using the characteristic equations. Once these values are known, the action balance equation can be solved, tracing the action parcel forwards in time to the position at which the normalised action is required over the current pattern.

In this numerical program, the wave spectrum is allowed to be at an angle to the current direction and to have an angular spread. Therefore, any particular wavenumber k will be at an angle, θ, to the direction of a one-dimensional current and at an angle, ϕ, to the wind direction. The wind is at an angle, φ, to the current direction. This is shown in figure 8-2.

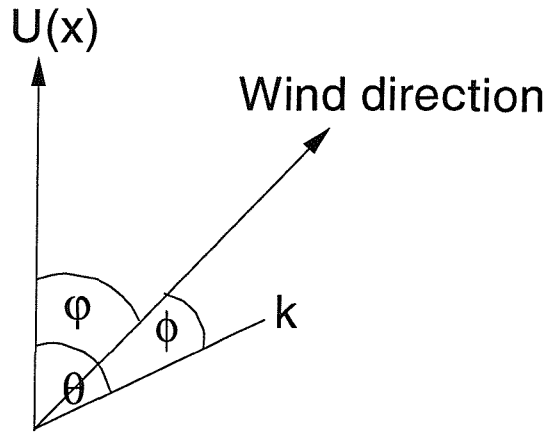

Figure 8-2: Diagram showing angles between current direction, wind direction and a wavenumber component in the wind wave field

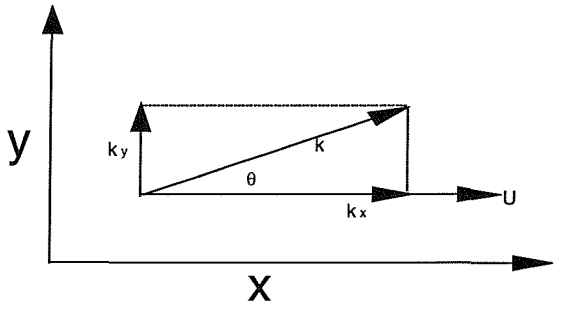

Figure 8-3: Diagram of wavenumber components parallel and perpendicular to current direction

An arbitrary wavenumber vector will have two components which are respectively directed parallel, k_x, and perpendicular, k_y, to the current direction, as described in 8-3 and displayed in figure 8-3.

$$k_x = k\cos\theta \qquad 8\text{-}3$$
$$k_y = k\sin\theta$$

Since the current does not vary in the y-direction, only the x-component of each wavenumber will be altered by the surface current. Therefore, k_y=constant at all times. A pair of parametric equations can be written which are the characteristic equations for the system,

$$\frac{dx}{dt} = \frac{\partial \omega}{\partial k_x} + U(x) - v \qquad 8\text{-}4$$

$$\frac{dk_x}{dt} = -k_x \frac{dU(x)}{dx}$$

where ω is the intrinsic frequency of the surface waves and is taken to be,

$$\omega = \sqrt{gk + \frac{Tk^3}{\rho}} \qquad 8\text{-}5$$

The frequency of encounter, ω', is defined as the actual frequency at which the wind waves are encountered by the carriage.

$$\omega' = \omega + (U - v)k \qquad 8\text{-}6$$

It is necessary to calculate the modulation of the action at all points along the current pattern and at all wavenumbers within the wind wave field. Initially, a grid of x,k points is chosen in order to simplify the results. It is possible to visualise what is happening during the solution of the equation by considering the wavenumber variations caused by the interacting current as a function of position. An example of this is given in figure 8-4. Starting at the required finishing values in x,k and then stepping both backwards and forwards in time allows the final action density at these points to be calculated. If it were not done in this way, the final action values would depend only on the chosen start values and would be an irregular grid in x,k space which would then need interpolating. This may cause further errors if the grid was found to be sparse in a particular area.

In the example shown in figure 8-4, the initial start point for the reverse stepping is (x_1,k_1). If the current was not present, there would be no variation in wavenumber, k, going back in time and the characteristic line shown would be horizontal. However, in the presence of the current, the wavenumber is modulated and so the characteristic traces out a curve in x,k, space as the routine steps back in time. Once a region has been reached that contains a wind wave field which is unaffected by the current, the action at this point is taken from the background spectrum, and the Runge-Kutta algorithm is used again to step

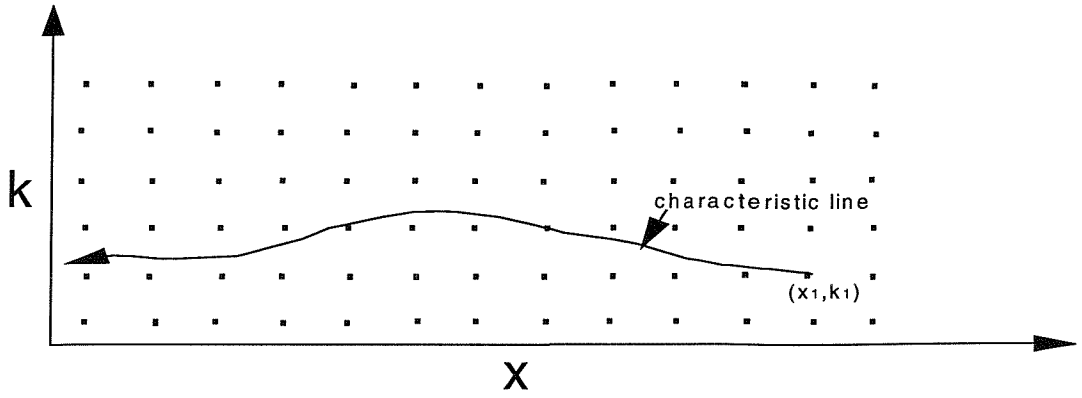

Figure 8-4: Grid pattern used in stepping procedure in solution of action balance equation

forwards in time using the wind growth and decay term, calculating the variation to the action along the characteristics.

The characteristic lines drawn out by this process show the path taken by the parcel of action as its wavenumber is refracted and its velocity altered by the current. If a sample current of,

$$U(x) = -0.1\,\mathrm{sech}^2\left(\frac{x}{4}\right) \qquad 8\text{-}6$$

is used with the current pattern moving at a velocity of v=0.5m/s then the characteristic lines can be drawn out for the full range of wavenumbers. It can be shown that the characteristics are along lines of constant ω'. Figure 8-5 shows the ray paths for a selection of wavenumbers in the gravity wave region for the above current shape and value of v, whilst figure 8-6 shows the paths in the capillary wave region.

It can be seen that in the gravity wave region, the group speeds of some of the wave packets are altered sufficiently that the direction of travel of the wave packet is reversed relative to the speed of travel of the current pattern. At the change of direction, the wave packet would be momentarily stationary. The stopping position is called the region of resonance and is given by,

$$\frac{\partial \omega'}{\partial k} = \frac{\partial \omega}{\partial k} + U - v = 0 \qquad 8\text{-}7$$

This has been investigated extensively by Gargett and Hughes (1972). Wave packets travelling in the same direction as the current, which have negative or small positive k-values, have minor modifications to their speed and wavenumber but do not have their direction of travel altered. In the capillary wave region, some of the waves become trapped and the current causes them to travel in circles in x,k space, travelling back and forth over the current region.

In this solution of the action balance equation, an initial x,k grid from –30m to +30m in x and for k-values specified by wavelength of 1mm to 1m (evenly spaced in x and wavelength) was selected. In x, this covers the full region affected by the current, plus a margin to either side to allow for wind effects. In k-space, this provides full coverage of all waves likely to be in the wind wave field and allows a reasonable estimate of the modulated variance as was shown in chapter 4.

For each point in the x,k grid, for both of the characteristic equations given in 8-4, the 4th order Runge-Kutta algorithm was used to step backwards in time. As the stepping occurs in time, t is used as the stepping variable with dt the step size. When stepping backwards, Ξ represents the vector (x,k). When stepping forwards in time, Ξ represents N. The Runge-Kutta algorithm is as follows:

$$\Xi_{i+1} = \Xi_i + \frac{dt}{6}(Q_1 + 2Q_2 + 2Q_3 + Q_4) \qquad 8\text{-}8$$

$$Q_1 = \left.\frac{\partial \Xi}{\partial t}\right|_{t=t_i, \Xi=\Xi_i}$$

$$Q_2 = \left.\frac{\partial \Xi}{\partial t}\right|_{t=t_i+\frac{dt}{2}, \Xi=\Xi_i+\frac{dtQ_1}{2}}$$

$$Q_3 = \left.\frac{\partial \Xi}{\partial t}\right|_{t=t_i+\frac{dt}{2}, \Xi=\Xi_i+\frac{dtQ_2}{2}}$$

$$Q_4 = \left.\frac{\partial \Xi}{\partial t}\right|_{t=t_i+dt, \Xi=\Xi_i+dtQ_3}$$

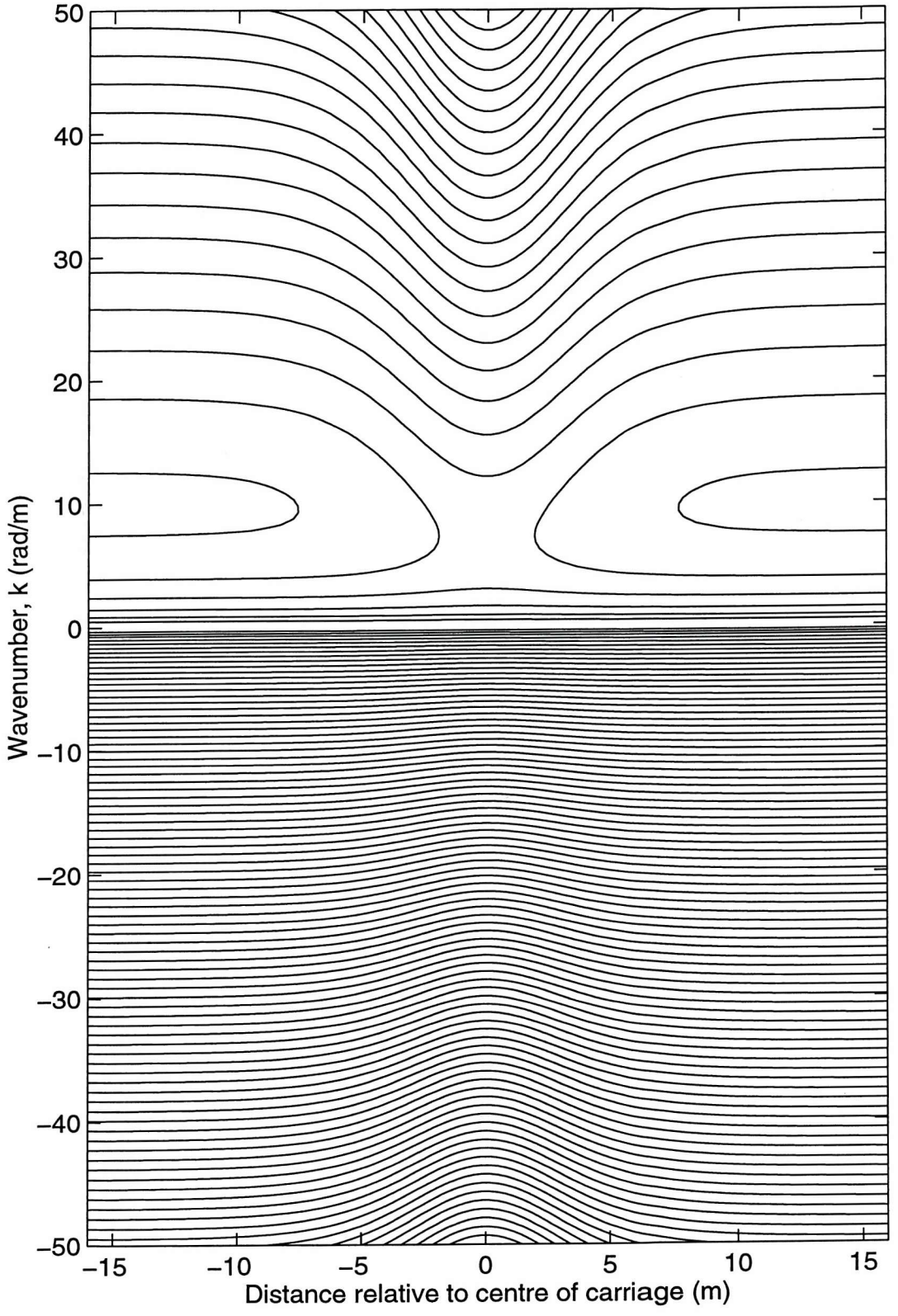

Figure 8-5: Ray paths in the gravity wave region

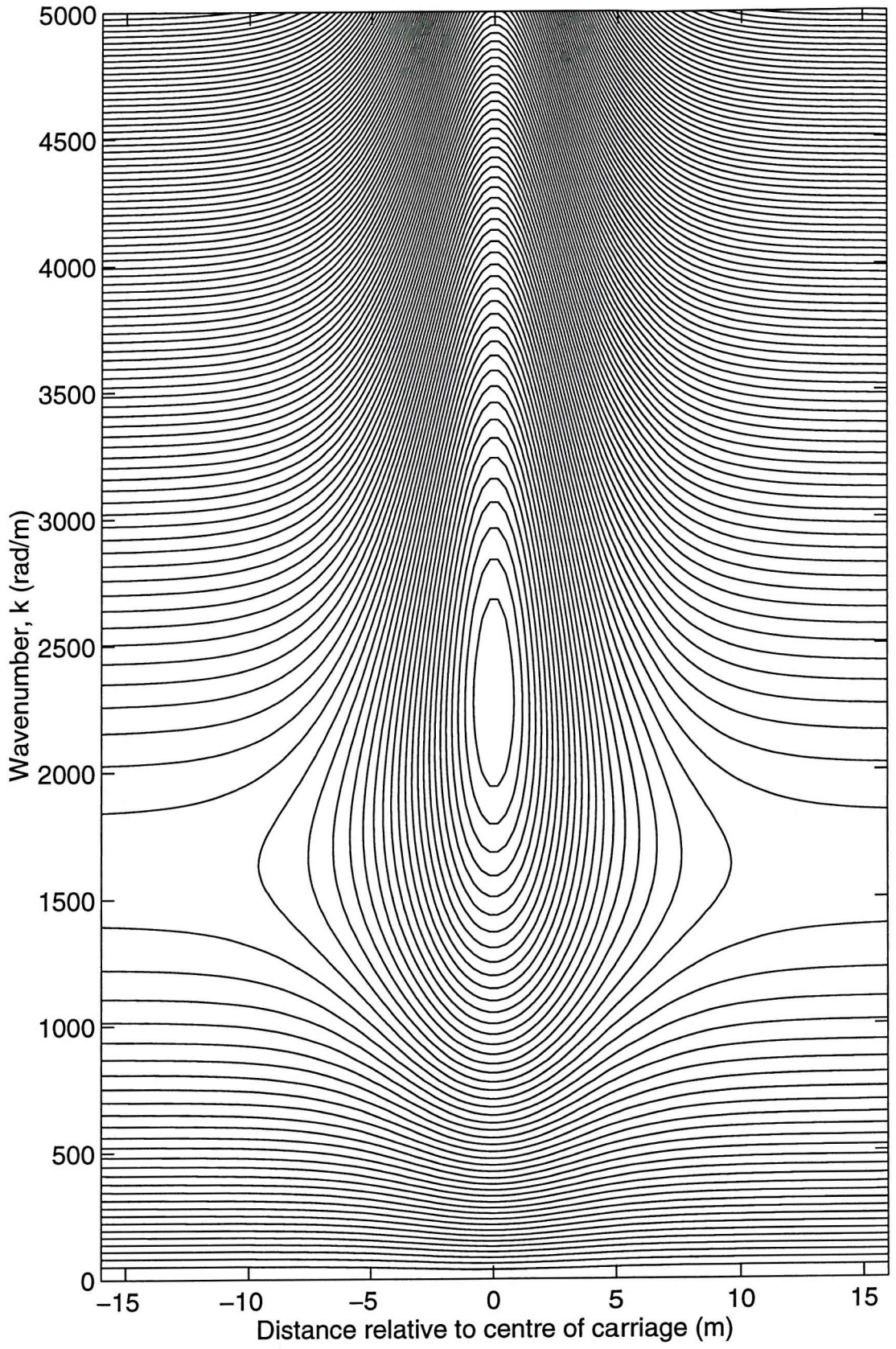

Figure 8-6: Ray paths in the capillary wave region

The stepping is continued until the equilibrium spectrum area is reached. This is a region outside the effect of the current perturbation. For those positions in the gravity-capillary range where the waves are forced around in circles, a length of time was used to determine when to stop stepping. This time was taken to be approximately 100 times greater than the relaxation time at that wavenumber. By allowing a long length of time in comparison to the relaxation time, the resulting action level at that wavenumber after the forward stepping process has been completed will be dependent only on the current magnitude at that x location, and not on the initial action value, as any growth or decay of the waves will have reached an equilibrium level.

Errors introduced by the Runge-Kutta algorithm are 5^{th} order in the step size. This error is per step and, therefore, the total error is 4^{th} order in the step size where the error has been added cumulatively over the number of steps. Initially, when this program was written, a constant step size was used. At this stage the cumulative error was recorded and checked and was found to agree with theory.

From these equilibrium st rt points reached after the stepping backwards in time along the characteristic lines, the 4^{th} order Runge-Kutta algorithm was used to step forwards using the action balance equation (with p to be defined),

$$\frac{dN}{dt} = \beta N\left(1-\left(\frac{N}{N_B}\right)^p\right) \qquad 8\text{-}9$$

where β is the wave growth parameter given by Plant's formula for wave growth (Plant, 1982),

$$\beta = \frac{0.04 u_*^{\,2}\omega\cos\phi}{c_p^{\,2}} \qquad 8\text{-}10$$

p determines how quickly the wind wave field decays due to dissipative effects, and N_B is the value of the equilibrium action spectrum at the current wavenumber of the action parcel. The step length used was twice that for the reverse case so that intermediate values

of k were known for use in the Runge-Kutta algorithm. N_B is the full angular wavenumber background spectrum with angles, ϕ, measured relative to the wind direction.

The final values of N(k) were normalised against the equilibrium value at the same wavenumber. These could be plotted for each wavenumber, k, versus x to describe how the action was modulated by the surface current at a constant wavenumber. Equations describing how the action at each wavenumber may be summed to provide an estimate of the modulated slope variance were given in chapter 4. This is discussed further in section 8.3.

8.2.3 Improvements to the basic routine

To enhance the performance of the algorithm, an adaptive step size routine was implemented (Press *et al.*, 1986). This involves taking each step twice: once as two half steps and then again as one full step as described by equations 8-11. The difference between the end values is a measure of how much error is introduced by the full step as opposed to the two half steps and provides a number which can be used to determine the appropriate step size to produce a predefined required maximum error.

$$\Xi(t+2dt) = \Xi_1 + (2dt)^5\phi + O(dt^6) + \ldots$$
$$\Xi(t+2dt) = \Xi_2 + 2(dt^5)\phi + O(dt^6) + \ldots \qquad 8\text{-}11$$

The truncation error is given by,

$$\Delta \equiv \Xi_2 - \Xi_1 \qquad 8\text{-}12$$

Equations 8-11 can also be solved to improve the numerical estimate,

$$\Xi(t+2dt) = \Xi_2 + \frac{\Delta}{15} + O(dt^6) \qquad 8\text{-}13$$

Although equation 8-13 now provides an improved estimate, there is no way of monitoring its truncation error. Therefore, it is sensible to assume that its truncation error will be no more than that given by 8-12. This has been used here.

The above adaptive step size method has been applied when stepping back in time in x,k using the characteristic equations. The k-value at each half step has been recorded along with x and k at each full step for use in the forward stepping process. Adaptive step size is not used when stepping forward in time as it is necessary to know the value of x and k at each step and half step which are known from backward time stepping in x,k. Therefore, the same step sizes must be used to step forwards in time.

To determine the new step size, an error in x and k must be calculated which can be compared with Δ. In each case, these errors have been selected so that there is an absolute x error (i.e. the position is estimated to be accurate to 0.01mm at its furthest point from the current field) and a fractional error in k (since k varies over several orders of magnitude throughout the x,k grid). Since,

$$d(\log k_x) = \frac{dk_x}{k_x} \qquad 8\text{-}14$$

the error comparison has been made between the difference in the log of the end point values in 8-14 which leads to a fractional error comparison in k.

In order to keep the cumulative error below a certain threshold value, an algorithm was developed to determine an estimate for the number of steps that would have to be taken to keep the cumulative error within a set upper limit. Additionally, to reduce errors in the forward stepping routine, the maximum step size was limited to be no greater than the relaxation time for that wavenumber. The relaxation time was defined to be the reciprocal of the gradient of the growth/decay term at the equilibrium spectrum value in a graph of dN/dt versus N. This was to allow appropriate growth and decay characteristics to develop appropriately in the action balance equation.

8.3 Testing the numerical programme

8.3.1 Introduction

The numerical program was tested for individual wavenumbers, assuming that the wavenumber is along the wind direction, so ϕ=0. A number of techniques were used which include:

- comparing the results of the program to an analytical approximation at high wind speed;
- comparing the results of the program to an analytical case with exponential wind growth only;
- comparing two sides of an equation where the numerical program has been used in different ways to calculate each side of the equation. This is known as studying the residuals.

The validity of the program for wavenumbers at an angle to the wind direction was tested by studying the way in which the spectrum returned to the equilibrium value, and to what value, after the straining by the current stopped acting. The results from these tests are presented below.

8.3.2 High wind speed case

Perry (1988) has shown that if an action spectrum of,

$$N_B(k,\phi)=\begin{cases} k^{-4} & -\frac{\pi}{2}<\phi<\frac{\pi}{2} \\ 0 & \text{elsewhere} \end{cases} \qquad 8\text{-}15$$

is assumed and if k is at an angle of θ with respect to the current direction, which is directed along the x-axis then, using equations 8-3 and 8-4, equation 8-2 can be written as,

$$\begin{aligned} &(U+c_g\cos\theta-v)\frac{\partial(N/N_B)}{\partial x} \\ &+\left(4\frac{N}{N_B}\cos^2\theta+\frac{\sin 2\theta}{2}\frac{\partial(N/N_B)}{\partial\theta}-k\cos^2\theta\frac{\partial(N/N_B)}{\partial k}\right)\frac{\partial U}{\partial x} \\ &=\beta\frac{N}{N_B}\left(1-\left(\frac{N}{N_B}\right)^p\right) \end{aligned} \qquad 8\text{-}16$$

If it is assumed that in the high wind speed case, N/N_B can be written as,

$$\frac{N}{N_B}=1+\frac{f(x,t,\theta)}{\beta} \qquad 8\text{-}17$$

then considering terms up to $1/\beta$ only in 8-17, Perry (1988) has shown that,

$$\frac{N}{N_B} \approx 1 - 2\frac{\cos^2\theta}{\beta}\frac{\partial U}{\partial x} \qquad 8\text{-}18$$

A wind speed exerting approximately 30 times the stress exerted at a wind speed of 5m/s in the wind wave tank has been used to test the program with $\varphi=0$. The results from the numerical method, the analytical form at high wind speed and the ratio and difference of the two are presented in figure 8-7. The results show that the error from the numerical program over the analytic result is never more than 0.3%.

8.3.3 Exponential case

The program was tested by setting the growth / decay term in the action balance equation, 8-2, as an exponential.

$$\frac{dN}{dt} = \beta N \qquad 8\text{-}19$$

This equation was also solved analytically so that,

$$N = N_B e^{\beta t} \qquad 8\text{-}20$$

The value of t in 8-20 was the time taken by the wave packet in the numerical program to move from the equilibrium value N_B to the final action value, N at each x,k. The results are presented in figure 8-8. In this example a wavenumber of 10rad/m was used (equivalent to 63cm wave) and $\beta=0.001$. The results show that the error from the numerical program over the analytic result is never more than 0.4%.

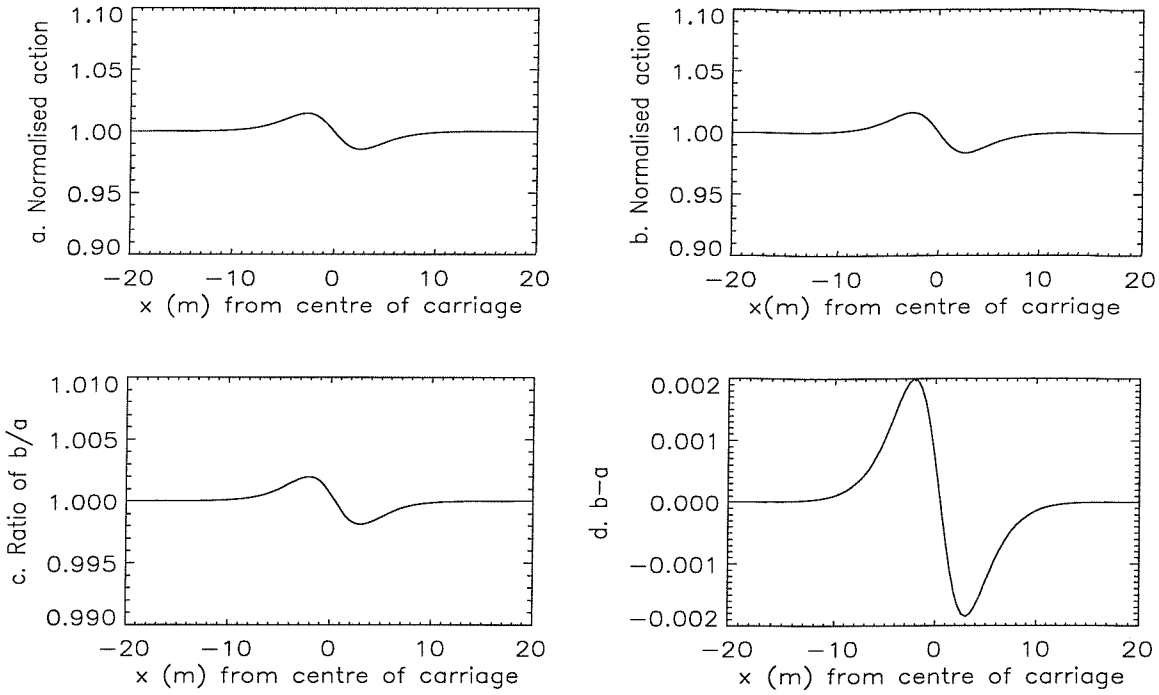

Figure 8-7: Results from high wind speed case. a.analytic case, b.output from numerical program, c.ratio of numerical result to analytic result, d.numerical result minus analytic result.

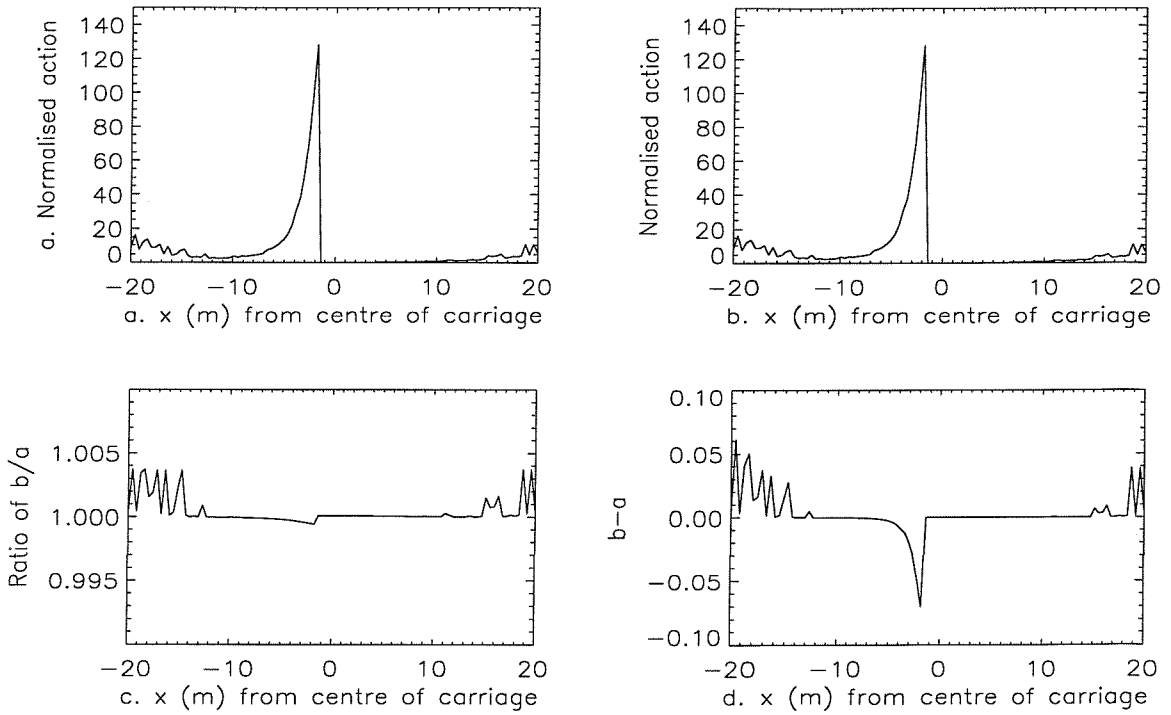

Figure 8-8: Results from the exponential case. a.analytic case, b.output from numerical program, c.ratio of numerical result to analytic result, d.numerical result minus analytic result.

8.3.4 Residuals

The program was also tested using the method of residuals, described briefly in section 8.3.1. θ was set to zero in equation 8-17 to simplify the test, so that the equation being considered was 8-21.

$$(U+c_g-v)\frac{\partial(N/N_B)}{\partial x}+\left(4\frac{N}{N_B}-k\frac{\partial(N/N_B)}{\partial k}\right)\frac{\partial U}{\partial x}=\beta\frac{N}{N_B}\left(1-\left(\frac{N}{N_B}\right)^p\right) \qquad 8\text{-}21$$

The action ratios at a number of points in an x,k grid were calculated using the numerical program. The right and left sides of the equation were compared, with $\partial(N/N_B)/\partial x$ and $\partial(N/N_B)/\partial k$ calculated approximately by differentiating across the x,k grid. Provided a fine grid is used to reduce errors in the differentiation across the grid, then for each x,k grid point, the two sides of the equation were found to be the same within 4%.

8.3.5 Test of angular part of spectrum

The relationship between the direction of the current, the wind and a particular wavenumber is given in figure 8-2.

For this test, a single wavenumber and angle relative to the wind direction were selected. An angular distribution of $\cos^2\phi$ was assumed, with ϕ=-53.5°. A current field of 0.1*tanh(x/5)+0.1, displayed in figure 8-9, was selected so that initially there was zero current and zero strain. This was followed by a zone of current and strain, which ended with a zone of current but no strain. In this final region, the wave field should return to its ambient value at each wavenumber as there is no straining, but the frequency of the waves will be altered by the remaining constant surface current. This type of current was selected as it allows a full test of the program.

The ratio of the energy in a wavenumber which is at an angle to the wind direction to the energy of that wavenumber directly in the wind direction should be $\cos^2\phi$ in the ambient spectrum. The energy should be returned to be this ratio after the current has stopped acting on the wave field. Stronger wind fields should return the spectrum to the ambient level

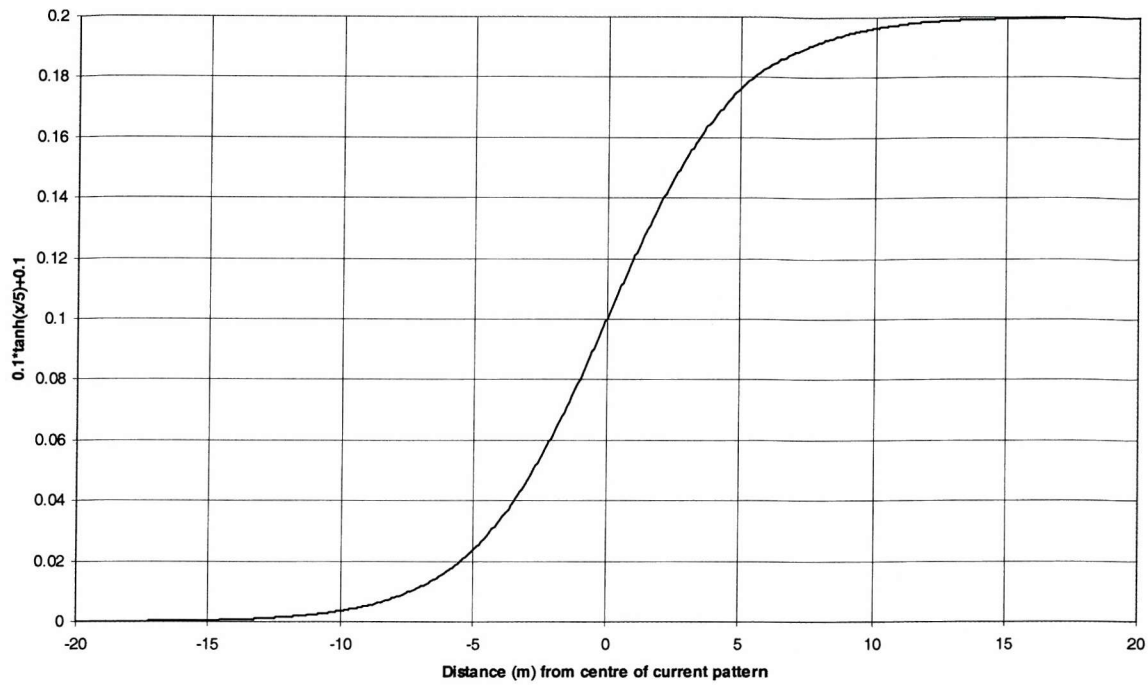

Figure 8-9: Example of current used in angular test

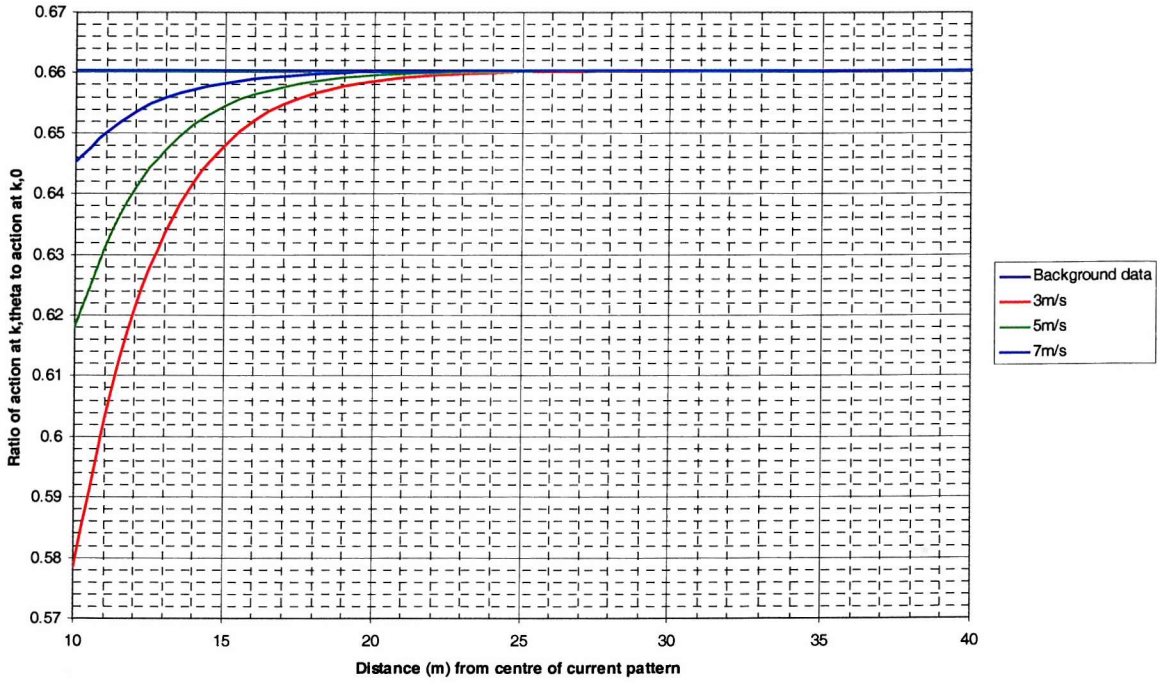

Figure 8-10: Test of angular part of wind field structure

more quickly than weak wind fields. In order to demonstrate that the program is working correctly, three wind speeds were selected. The ratio between the action at the angle, ϕ, to the wind direction and the action at 0° was calculated at a number of positions in the current pattern, moving gradually further away from the region affected by the current. These values are plotted in figure 8-10. The ambient wave field ratio is also plotted.

The results show that the action ratio does tend to the expected equilibrium value for all three wind speeds. The ambient wave field is restored faster at the higher wind speeds as expected.

8.4 Calculation of slope variance

The surface slope variance can be calculated from the action spectrum by summing over all the wavenumber components in an appropriate manner. By Parseval's theorem, the mean square slope (mss) is given by the integral of the total slope spectrum, $S(k,\phi)$, over all wavenumbers.

$$mss = \iint S(k,\phi)kdkd\phi \qquad 8\text{-}22$$

The slope spectrum can be related to the action spectrum via 8-23, assuming that the action spectrum can be separated into a term depending on k and a term depending on ϕ.

$$S(k,\phi) = \frac{\omega k^2}{\rho g} N(k) f(\phi) \qquad 8\text{-}23$$

Therefore,

$$mss = \iint \frac{\omega k^2}{\rho g} N(k) f(\phi) kdkd\phi \qquad 8\text{-}24$$

If the mean slope is zero (as is expected for a flat water surface) then the mean square slope is equal to the slope variance. Normalised slope variance can be found by dividing by the variance in the absence of currents.

Starting at equation 8-23, this equation can be used to calculate the variance from action wavenumber spectral density. Since the action density will only be known at a finite number of wavenumbers and angles, the integral can be estimated via a summation. In order to provide a good representation of the contribution to the variance from each wavenumber component, it is important that a full spread of wavenumbers throughout the spectrum are chosen in the summation so that there are not large gaps in areas such as around resonance. This can be adequately fulfilled if the wavenumbers are evenly spaced in wavelength with a spacing no greater than 1mm. The angular separation was chosen to reduce the length of time needed for the calculation to run. A 5° spacing was considered sufficient. To ensure that the final integral represents the required output from this spacing, and since,

$$dk = \frac{-k^2}{2\pi} d\lambda \qquad 8\text{-}25$$

then,

$$\int S(k,\phi) k dk d\phi = \int \frac{-k^2}{2\pi} S(k,\phi) k d\lambda d\phi \qquad 8\text{-}26$$

Using 8-26 to take account of even spacing in wavelength in the summation, the integral in 8-24 can be re-written in summation terms as,

$$mss = \sum_{n,m} \frac{-k_n^{\,2}}{2\pi} S(k_n, \phi_m) k_n \Delta\lambda_n \Delta\phi_m \qquad 8\text{-}27$$

Therefore, using 8-23,

$$mss = \sum_{n,m} \frac{-\omega k_n^{\,5}}{2\pi\rho g} N(k_n) f(\phi_m) \Delta\lambda_n \Delta\phi_m \qquad 8\text{-}28$$

In the calculations that follow, this form of summation is used to produce the graphs of the surface slope variance. Since k^5N has a fairly flat graph, the important regions of the spectrum are not undersampled.

8.5 Solutions for theoretical spectra and currents

In this section, a number of parameter sets are chosen to demonstrate how the output from the program, and hence the solution to the action balance equation, varies as certain parameters are varied. A spectrum of the form,

$$\Psi(k,\phi) = k^{-s_p}\cos^2\phi \qquad 8\text{-}29$$

is used, with,

$$\frac{dN}{dt} = N\left(1-\left(\frac{N}{N_B}\right)^p\right) \qquad 8\text{-}30$$

Different values of s_p, p, ϕ and φ are considered and variations with these parameters examined. Graphs displaying the results of the tests are displayed in figures 8-11 to 8-24. Below each graph is a caption which lists the parameter set used in the generation of the graph from the solution to the action balance equation. It also lists whether the current pattern was moving with or against the wind direction. Where the current and wind direction are parallel, the front of the carriage is on the right hand side of the figure. This part of the carriage would reach a particular location earlier in time than the left hand side. Where the current and wind direction are anti-parallel, the left hand side of the figure represents the front of the carriage, which would reach a particular location earlier in time than the right hand side.

Figures 8-11 to 8-14 show the variation caused by altering s_p with p=2, ϕ=0 and φ=0. It can be seen that the general trend is with the carriage and wind parallel for there to be a decrease in the action ratio in regions containing a current divergence and an increase of action ratio in regions containing a current convergence. Studying the action rays in figure 8-5 can help to interpret these results in terms of the way in which the action ratio at a

particular location will vary. In regions where the ambient action from which a wave packet has started is greater than the ambient action at its final wavenumber within the current pattern, the ratio will be greater than 1. The ratio will be smaller than 1 when the reverse is true. The resonance effect can be seen clearly in figure 8-11 where the action ratio changes rapidly from more than 1 to less than 1.

Comparing figure 8-11 with figure 8-13 and figure 8-12 with figure 8-14, it can be seen that altering the power of the spectrum, s_p, between the two commonly used forms of s_p=-4 and s_p=-3.5, has only a small effect on the action spectral density ratios.

Figures 8-11, 8-12 and 8-15, 8-16 show the variation caused by altering p. It can be seen that varying the power of the decay term has a very large effect. This is especially noticeable near resonance where with p=1 the action values are up to 27 times greater than the corresponding action values with p=2.

Figures 8-17 and 8-18 show how the ratio varies as the wind angle, φ, is altered, with the wavenumber, k, directed along the wind direction. As the angle of the wind direction, φ, is increased with respect to the direction of travel of the sub-surface carriage, the ratio of the action at a wavenumber k after modulation by the current to the background value decreases. This is expected because the magnitude of the component of k being modulated decreases as φ increases, and thus the action ratio would be expected to decrease with increasing φ.

Figures 8-19 and 8-20 show how the contribution to the modulated normalised action spectral density varies from different initial parts of the angular distribution of the wind wave field. This modulation of the wavenumber is different to figures 8-17 and 8-18 only in that the growth of the wavenumbers will be different depending on their angle with respect to the wind direction. The same spectral component at different angles within the wind wave field has a very different behaviour as the angle changes. Where most of the wavenumber component is along the wave direction, the effects are similar to those seen in figures 8-17 and 8-18. Where the angle between the wind direction and the wavenumber is large, the greatest effect will be due to the fact that at a slightly increased wavenumber angle to the wind direction, there is a lot more action in the background spectrum because

of the $\cos^2\phi$ factor. For these cases, the initial amount of action at a particular wavenumber before stepping forwards is greater than the value of the ambient spectrum at the final wavenumber value and so the action ratio is greater than one, in regions where a decrease in action might be expected.

As the value of p was found to be most important in determining the variation of the spectrum due to the surface current, the way in which this affects the surface slope variance was investigated. The variance graphs shown in figures 8-21 to 8-24 were generated for the current pattern moving parallel and anti-parallel to the wind direction with $\varphi=0$ and p=1 or p=2. The variance is up to 2% larger for the p=1 cases as compared to those cases with p=2.

The results produced here are in agreement with those presented by Perry (1988) except near resonance. Perry's model made the assumption that changes in the normalised action with wavenumber and angular direction are small. It seems likely that this approximation is not valid near to resonance.

8.6 Discussion of results

A numerical model has been developed to solve the full action balance equation. This chapter has described how the model works, the way in which it was tested and some preliminary results using prescribed background wind wave spectra and surface currents. The variation of the output of the model has been considered as parameters are altered. It has been shown that the power of the ambient spectrum, s_p, has little effect on the output which is normalised by the ambient values. However, the power of the decay term, p, has a large effect and needs to be determined correctly.

The model is a significant improvement over some previous action balance equation solvers as it has been written so that any reasonably well behaved ambient spectrum and surface current can be used. In the next chapter, this model will be used with real experimental data to predict changes in the spectrum caused by the current and to compare the theoretical output with real data from the laser slope meter. As this model is written

very generally, the growth and decay parameters can be varied, or indeed the whole functional form of the term can be changed, in an attempt to reproduce the observed data.

Limitations of the numerical model at present are that no progress has been attempted in terms of introducing new forms for the growth, dissipation and wave-wave interaction terms. Those included are appropriate for the gravity wave range but will not be valid for capillary waves where direct generation by gravity waves may occur and viscous dissipation is the over-riding factor for the wave decay. It is likely that the dispersion relation is not valid for many capillary waves which have been observed to travel at the speed of the gravity wave peak of the spectrum (Bock *et al.* 1997). This will lead to inaccuracies in the values of the frequencies and wave speeds used in the calculations. The particular forms of wave-wave interactions may also be different in the capillary wave regime as compared to gravity waves. Although no terms for wave-wave interactions are included in this model, they may be significant for capillary wave generation and should therefore be considered.

No attempt has been made to include terms for other effects in this model as it is an initial attempt at a full solution of the action balance equation. Here, the emphasis has been on producing a model which is capable of accepting experimentally measured ambient wave spectra and surface current patterns. For simplicity, previously used terms for growth and dissipation are used so that the effect of the new program can be assessed without the additional complications of new terms. Information from new scanning laser slope meters could be used to provide enhanced knowledge of the dispersion relation for capillary waves, and this information could be used to improve this model.

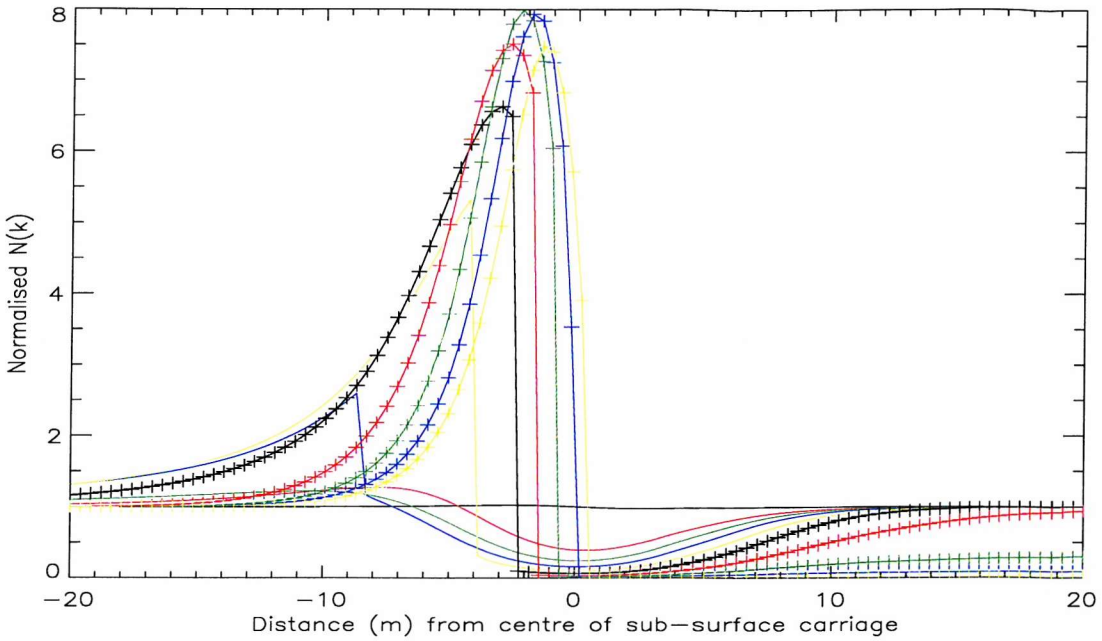

Figure 8-11: Normalised action with current motion and wind direction parallel for the following parameters: $\Psi(k,\phi)=k^{-4}\cos^2\phi$, $\phi=0$, $\varphi=0$, $p=2$, $v=0.5$, $k=6283.2$ (black-), 56.1 (red-), 28.2(green-), 18.8 (blue-), 14.1 (yellow-), 11.3 (black+), 9.42 (red+), 8.08 (green+), 7.07 (blue+), 6.28 (yellow+)

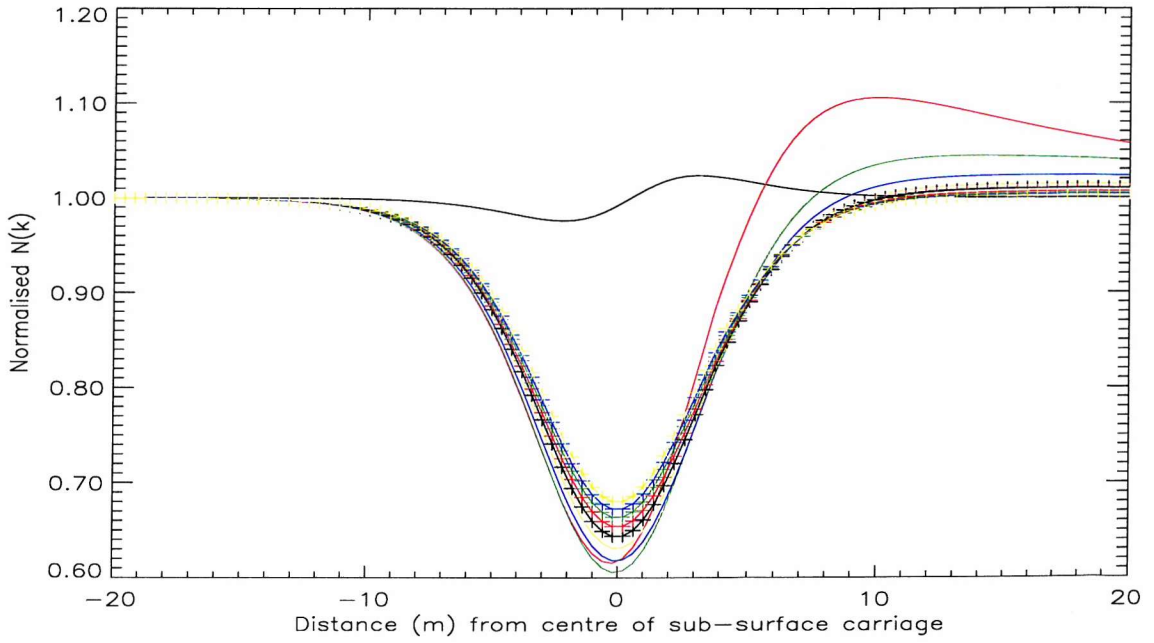

Figure 8-12: Normalised action with current motion and wind direction anti-parallel for the following parameters: $\Psi(k,\phi)=k^{-4}\cos^2\phi$, $\phi=0$, $\varphi=0$, $p=2$, $v=0.5$, $k=6283.2$ (black-), 56.1 (red-), 28.2(green-), 18.8 (blue-), 14.1 (yellow-), 11.3 (black+), 9.42 (red+), 8.08 (green+), 7.07 (blue+), 6.28 (yellow+)

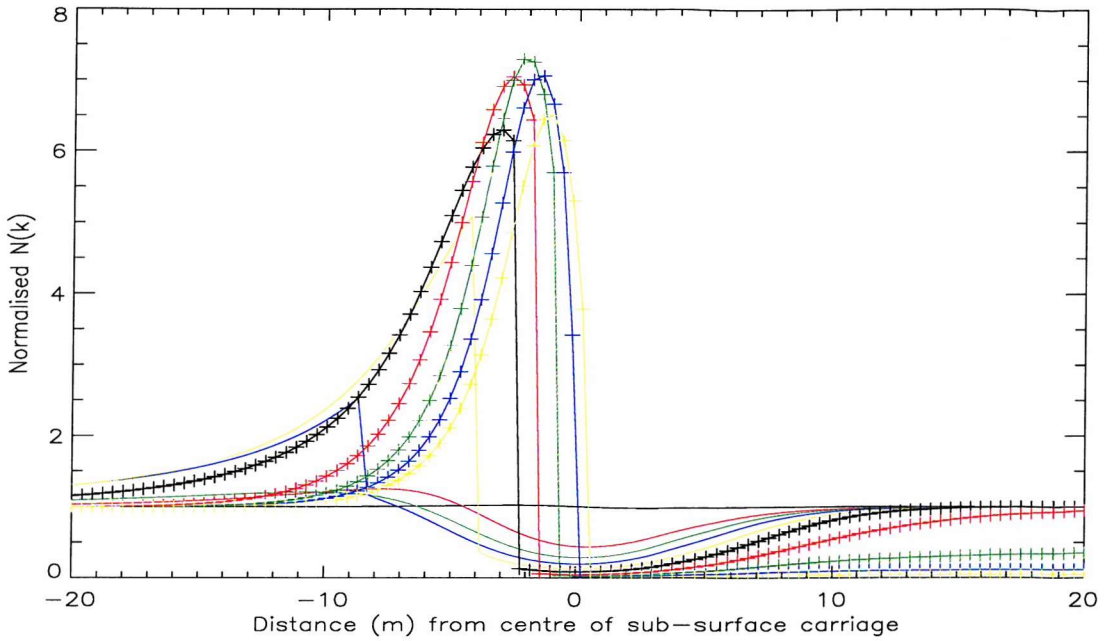

Figure 8-13: Normalised action with current motion and wind direction parallel for the following parameters: $\Psi(k,\phi)=k^{-3.5}\cos^2\phi$, $\phi=0$, $\varphi=0$, $p=2$, $v=0.5$, $k=6283.2$ (black-), 56.1 (red-), 28.2(green-), 18.8 (blue-), 14.1 (yellow-), 11.3 (black+), 9.42 (red+), 8.08 (green+), 7.07 (blue+), 6.28 (yellow+)

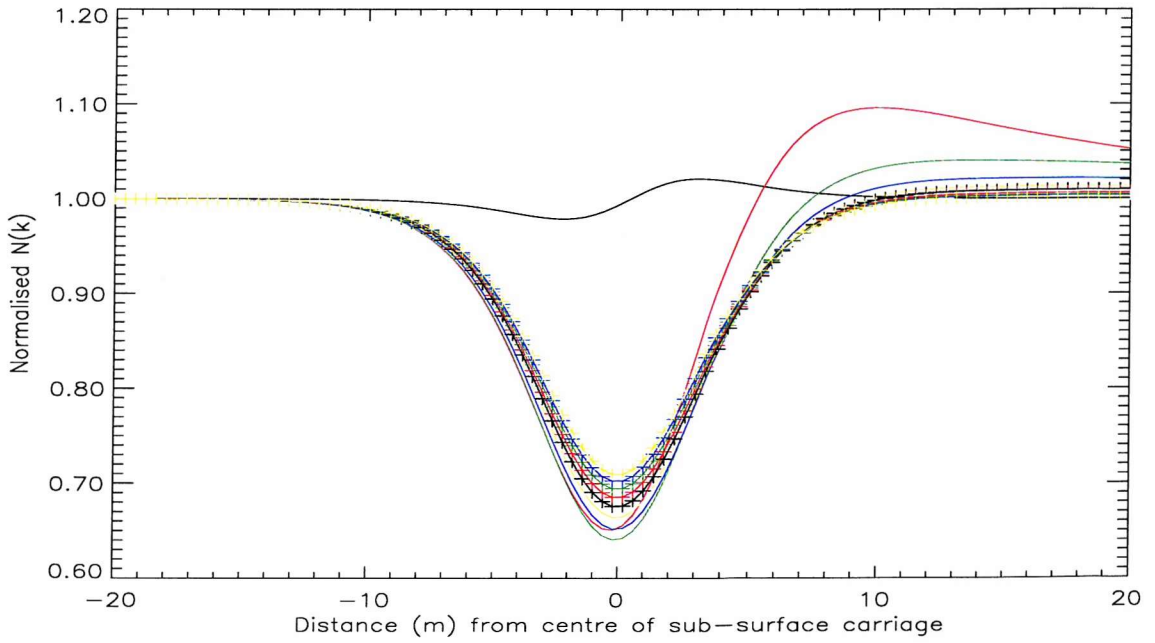

Figure 8-14: Normalised action with current motion and wind direction anti-parallel for the following parameters: $\Psi(k,\phi)=k^{-3.5}\cos^2\phi$, $\phi=0$, $\varphi=0$, $p=2$, $v=0.5$, $k=6283.2$ (black-), 56.1 (red-), 28.2 (green-), 18.8 (blue-), 14.1 (yellow-), 11.3 (black+), 9.42 (red+), 8.08 (green+), 7.07 (blue+), 6.28 (yellow+)

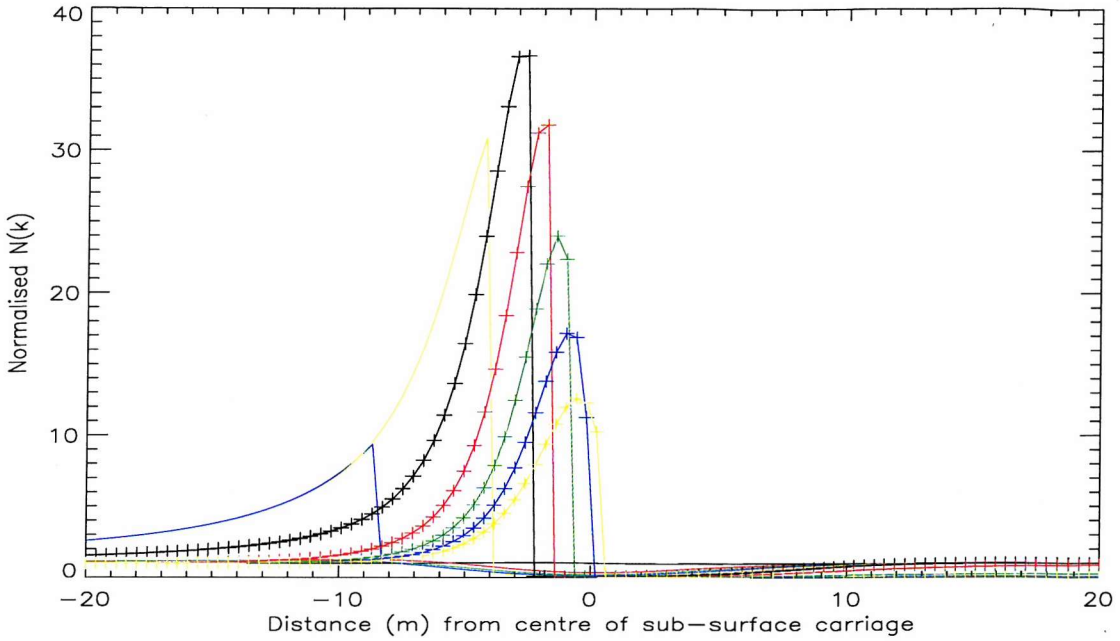

Figure 8-15: Normalised action with current motion and wind direction parallel for the following parameters: $\Psi(k,\phi)=k^{-4}\cos^2\phi$, $\phi=0$, $\varphi=0$, $p=1$, $v=0.5$, $k=6283.2$ (black-), 56.1 (red-), 28.2(green-), 18.8 (blue-), 14.1 (yellow-), 11.3 (black+), 9.42 (red+), 8.08 (green+), 7.07 (blue+), 6.28 (yellow+)

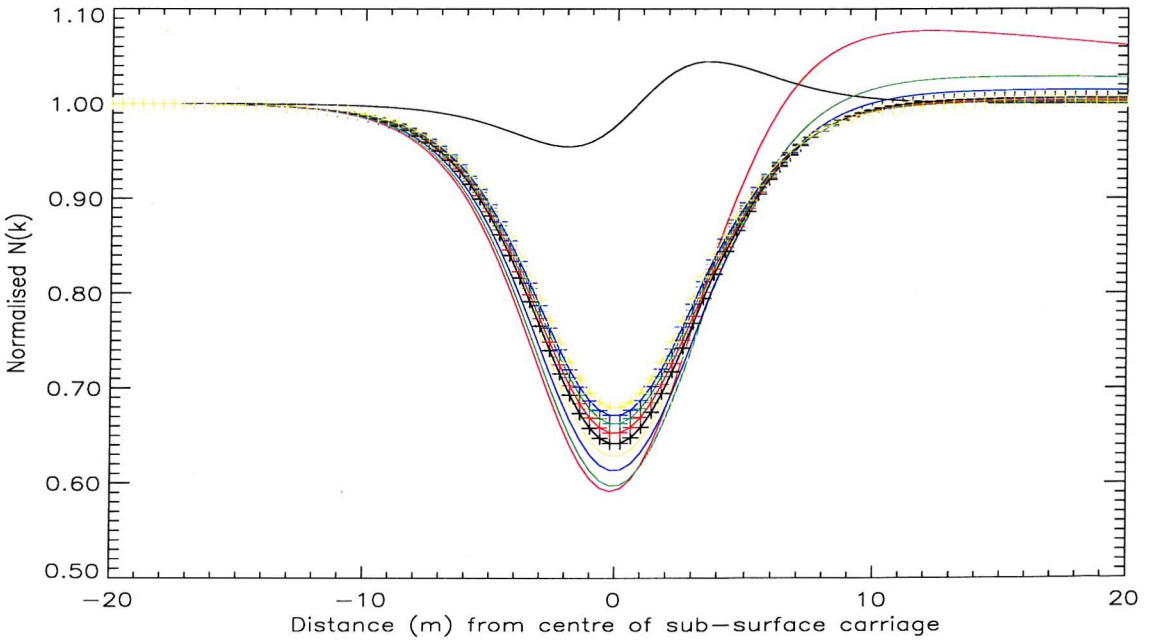

Figure 8-16: Normalised action with current motion and wind direction anti-parallel for the following parameters: $\Psi(k,\phi)=k^{-4}\cos^2\phi$, $\phi=0$, $\varphi=0$, $p=1$, $v=0.5$, $k=6283.2$ (black-), 56.1 (red-), 28.2 (green-), 18.8 (blue-), 14.1 (yellow-), 11.3 (black+), 9.42 (red+), 8.08 (green+), 7.07 (blue+), 6.28 (yellow+)

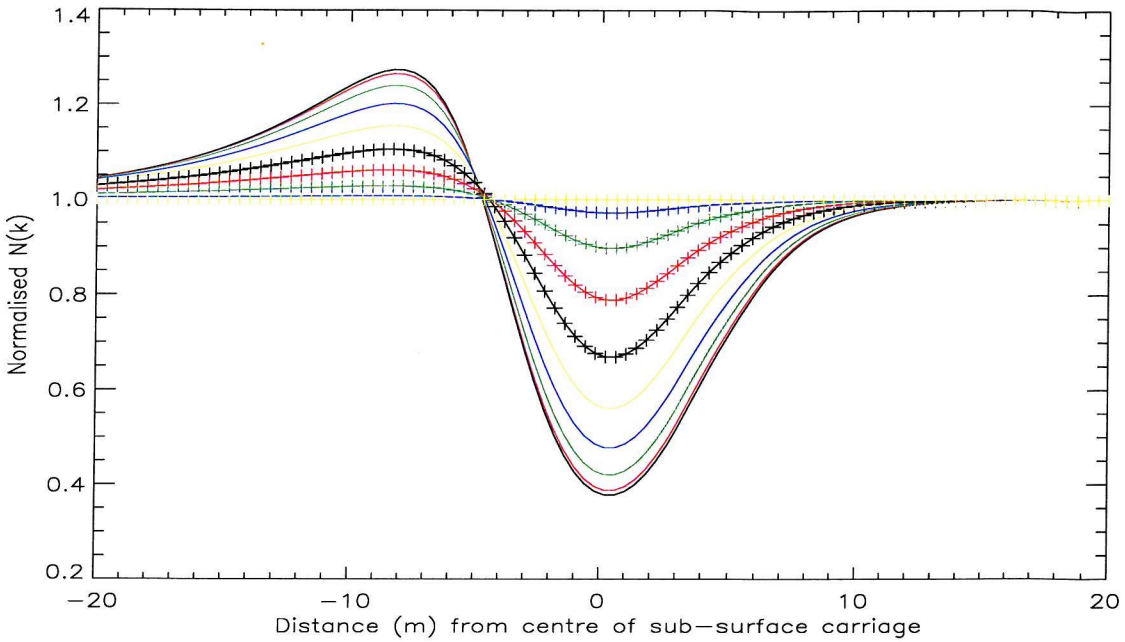

Figure 8-17: Normalised action with current motion and wind direction parallel for the following parameters: $\Psi(k,\phi)=k^{-4}\cos^2\phi$, $\phi=0$, $p=2$, $v=0.5$, $k=52.4$rad/m, $\varphi=0$ (black-), $0.11\pi/2$ (red-), $0.22\pi/2$ (green-), $0.33\pi/2$ (blue-), $0.44\pi/2$ (yellow-), $0.55\pi/2$ (black+), $0.66\pi/2$ (red+), $0.77\pi/2$ (green+), $0.88\pi/2$ (blue+), $0.99\pi/2$ (yellow+)

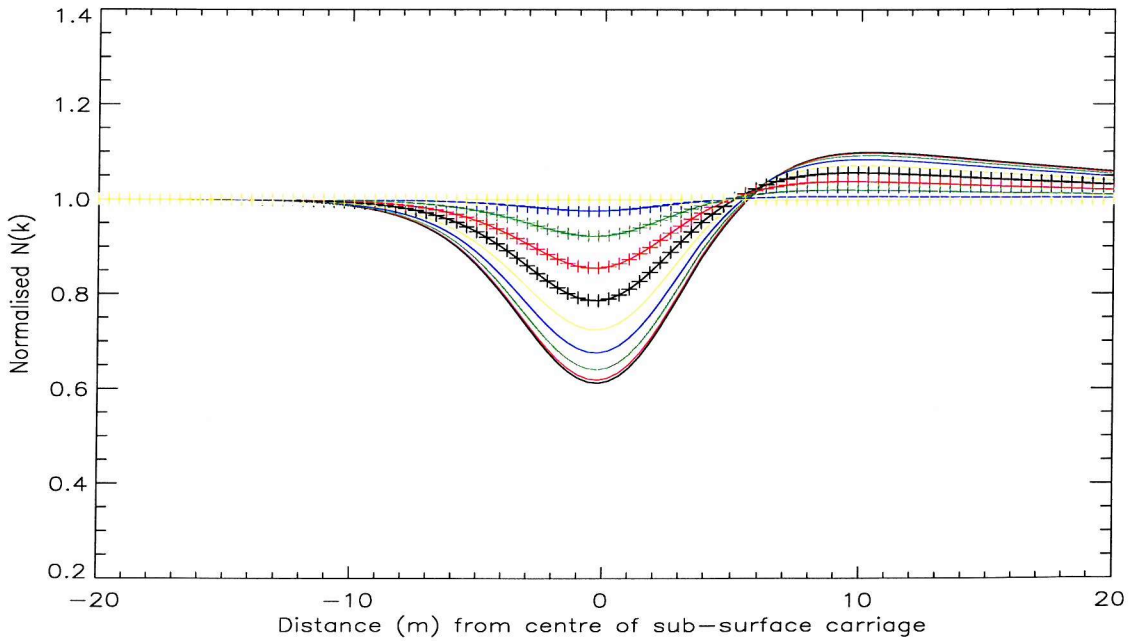

Figure 8-18: Normalised action with current motion and wind direction anti-parallel for the following parameters: $\Psi(k,\phi)=k^{-4}\cos^2\phi$, $\phi=0$, $p=2$, $v=0.5$, $k=52.4$rad/m, $\varphi=0$ (black-), $0.11\pi/2$ (red-), $0.22\pi/2$ (green-), $0.33\pi/2$ (blue-), $0.44\pi/2$ (yellow-), $0.55\pi/2$ (black+), $0.66\pi/2$ (red+), $0.77\pi/2$ (green+), $0.88\pi/2$ (blue+), $0.99\pi/2$ (yellow+)

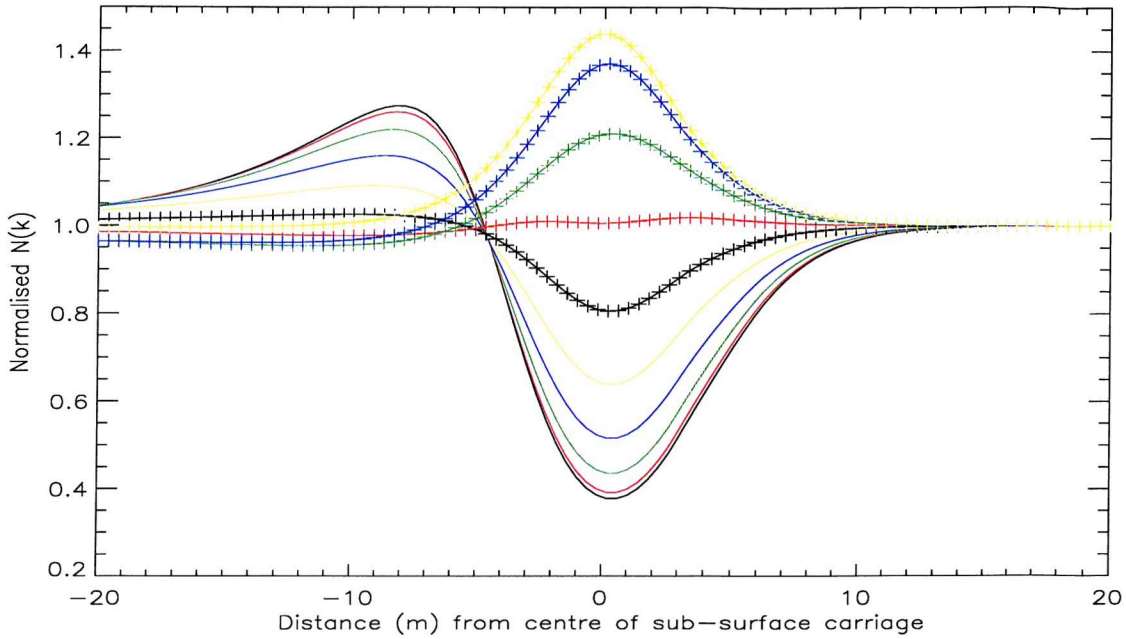

Figure 8-19: Normalised action with current motion and wind direction within ±90° following parameters: $\Psi(k,\phi)=k^{-4}\cos^2\phi$, p=2, v=0.5, k=52.4rad/m, φ=0, ϕ=0 (black-), 0.11π/2 (red-), 0.22π/2 (green-), 0.33π/2 (blue-), 0.44π/2 (yellow-), 0.55π/2 (black+), 0.66π/2 (red+), 0.77π/2 (green+), 0.88π/2 (blue+), 0.99π/2 (yellow+)

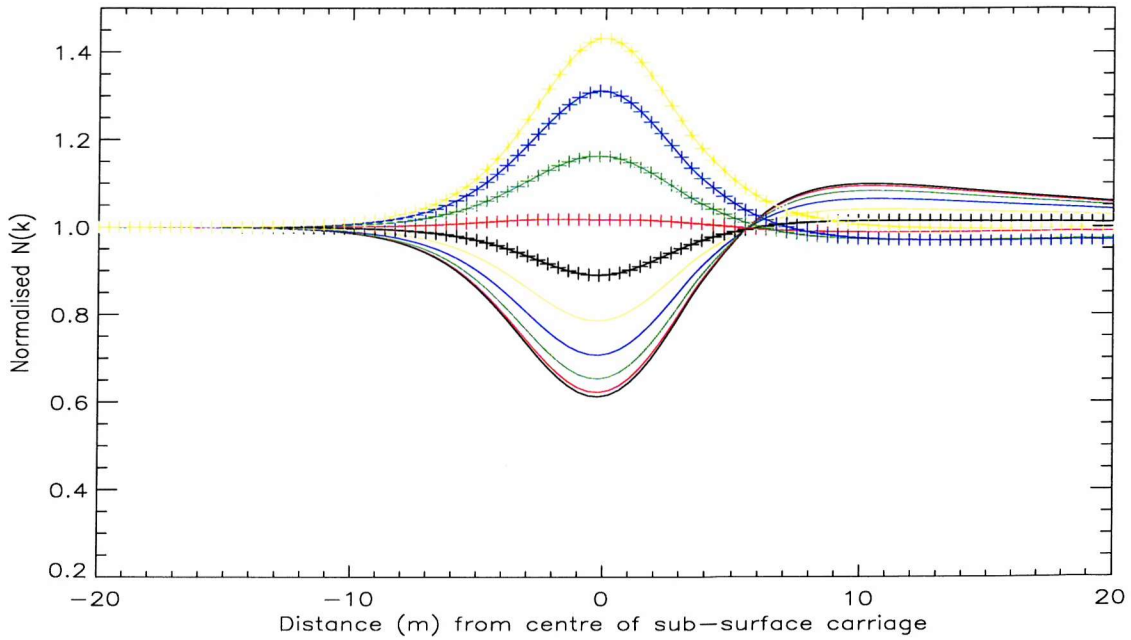

Figure 8-20: Normalised action with current motion and wind direction between ±90° to ±180° the following parameters: $\Psi(k,\phi)=k^{-4}\cos^2\phi$, p=2, v=0.5, k=52.4rad/m, φ=0, ϕ=0 (black-), 0.11π/2 (red-), 0.22π/2 (green-), 0.33π/2 (blue-), 0.44π/2 (yellow-), 0.55π/2 (black+), 0.66π/2 (red+), 0.77π/2 (green+), 0.88π/2 (blue+), 0.99π/2 (yellow+)

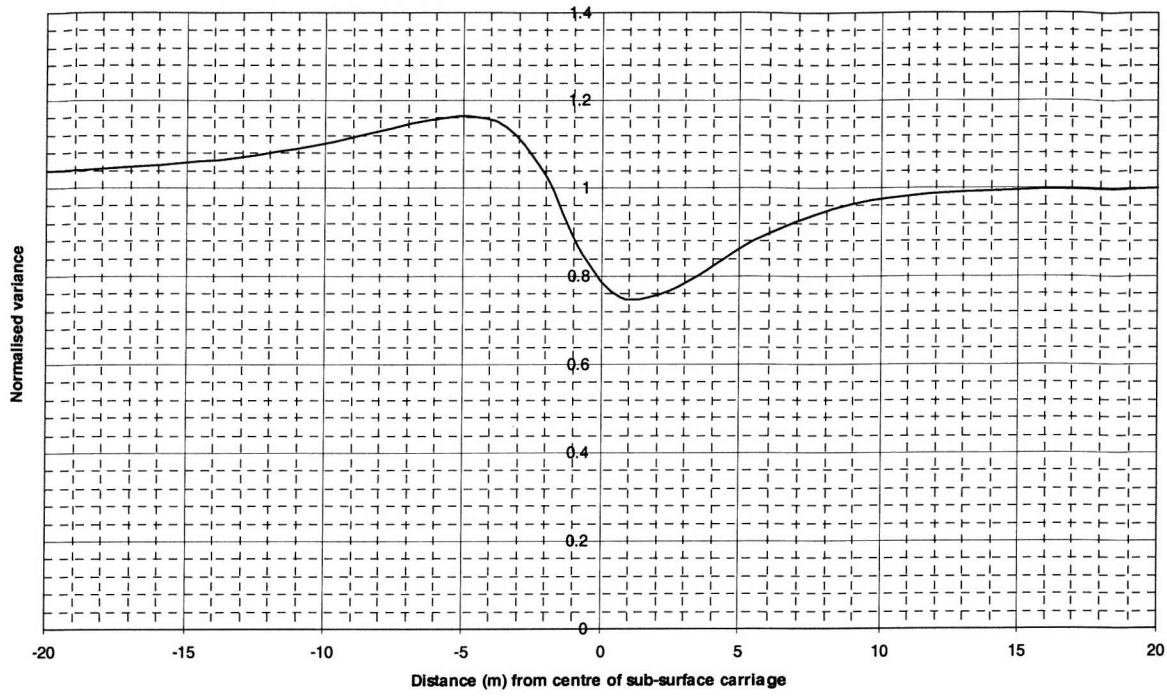

Figure 8-21 Normalised variance with current motion and wind direction parallel for the following parameters: $\Psi(k,\phi)=k^{-4}\cos^2\phi$, $p=2$, $\varphi=0$, $v=0.5$

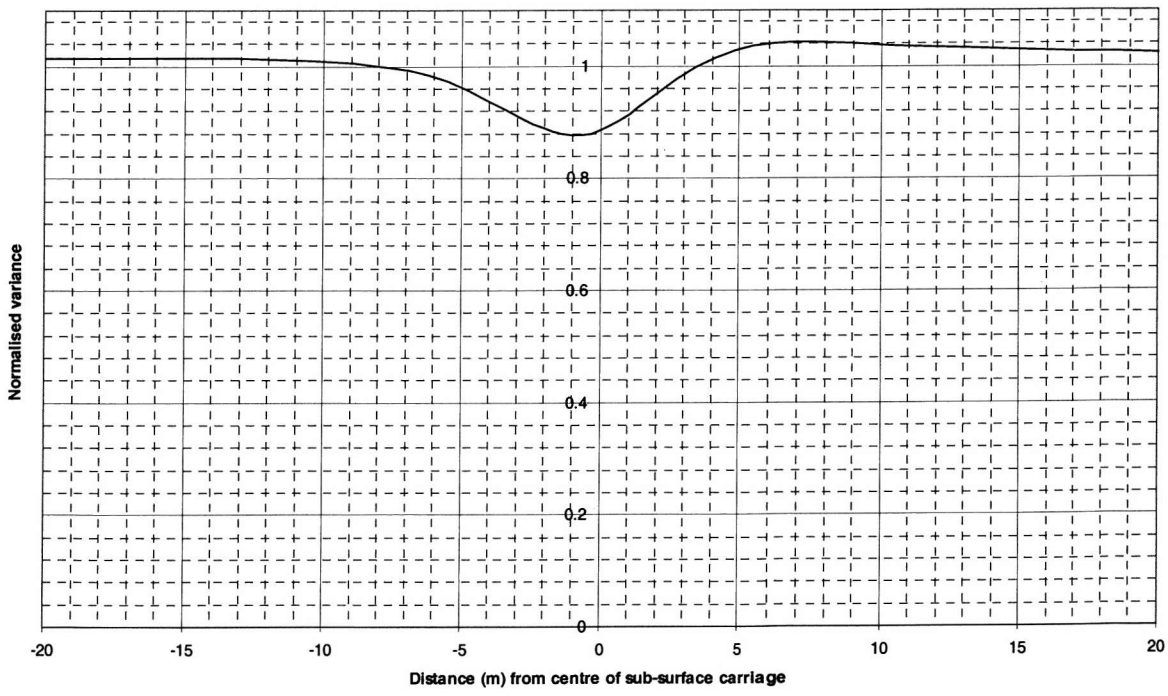

Figure 8-22 Normalised variance with current motion and wind direction anti-parallel for the following parameters: $\Psi(k,\phi)=k^{-4}\cos^2\phi$, $p=2$, $\varphi=0$, $v=0.5$

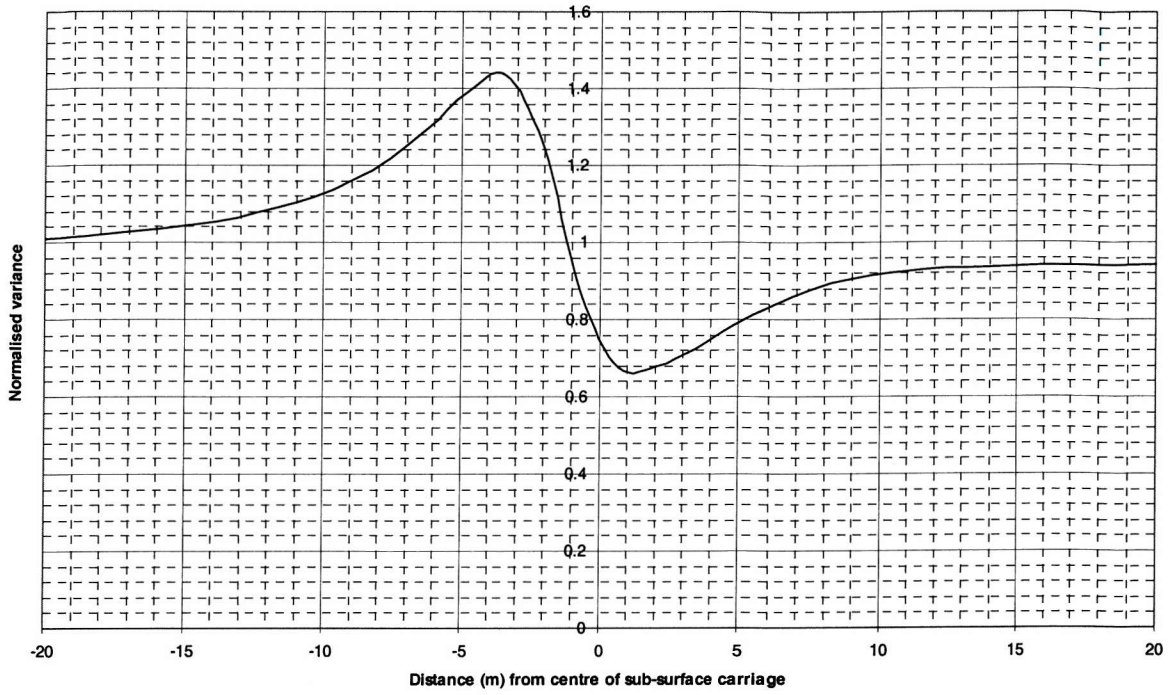

Figure 8-23 Normalised variance with current motion and wind direction parallel for the following parameters: $\Psi(k,\phi)=k^{-4}\cos^2\phi$, $p=1$, $\varphi=0$, $v=0.5$

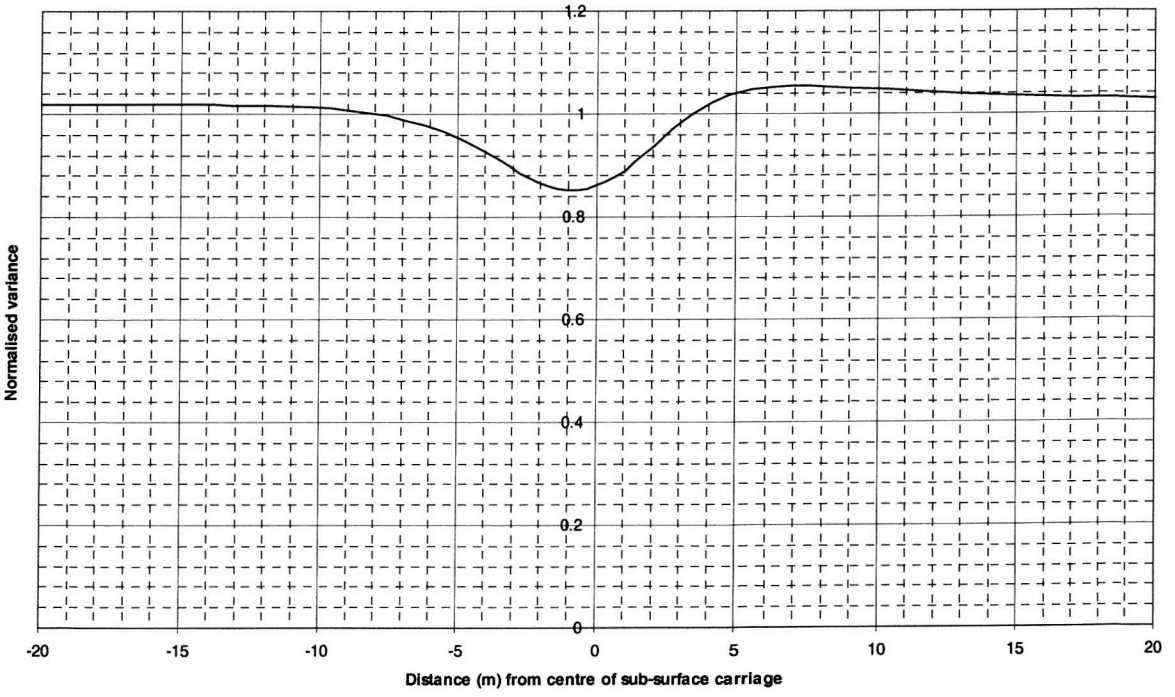

Figure 8-24 Normalised variance with current motion and wind direction anti-parallel for the following parameters: $\Psi(k,\phi)=k^{-4}\cos^2\phi$, $p=1$, $\varphi=0$, $v=0.5$

Chapter 9

Measurements of surface wave – surface current interactions

9.1 Introduction

This chapter presents experimental work with the Laser Slope meter aimed at investigating its capability in providing data which is useful for furthering understanding of the interaction between surface waves and a horizontally varying surface current. Data of such interactions have been collected by the Laser Slope meter and analysed in terms of the variation caused by the interaction, in the surface slope variance and slope frequency spectra. Ambient wind wave fields measured by the instrument have been used along with experimentally measured surface currents as inputs into the theoretical model presented in chapter 8. Careful consideration has been given to the way in which the model can be used to generate a theoretical version of the modulation of the surface wave field, which can then be compared directly with the experimental measurements. DERA planned to run a series of experiments with the Laser Slope meter to make such measurements, so that these data can be used to verify and further theoretical modelling techniques and to assist in understanding radar measurements of these types of interactions. The experimental design, results and analysis of the data from the first experiment are presented in this chapter. The particular objectives of this experiment were to determine:

- the capability of the Laser Slope meter for making measurements of the interaction between surface waves and a horizontally varying surface current ;
- the most effective way of designing such experiments to provide the necessary results;
- the most effective way of analysing the data to provide the required information;
- the most effective way of using frequency information about the wave field to compare with theoretical models designed to study wavenumber changes.

Therefore, the emphasis of the research presented in this chapter is on the role of the Laser Slope meter in providing the results and the way in which this affects the experimental design and data analysis.

9.2 Experiment overview

The Laser Slope meter data were collected at the wind wave tank at the OEL, UCSB. The experiment simulated the surface effect of underwater topography or an internal wave by creating a weakly varying one-dimensional horizontal current at the water surface. This current was used to modulate surface wind wave fields, and the effects of the current on the wind waves were measured using the Laser Slope meter.

To generate the surface current, a sub-surface carriage was towed either parallel or anti-parallel to the wind direction on the bed of the wind wave tank, at speeds ranging from 0.1m/s to 0.78m/s. The shape of the carriage is shown graphically and approximately to scale in figure 9-1. The shape of the surface current pattern produced by the carriage was calculated theoretically using a linear inviscid theory (Taylor, 1998) and also measured experimentally using particle tracking (Hall, 1999), without a wind wave field being present. An example of one of the experimentally measured current patterns is given in figure 9-2, and examples of the theoretical forms of the surface current and resulting surface strain rate are given in figures 9-3 and 9-4. Note that the current flow is opposite to the direction of travel of the carriage. The magnitude of the surface current, and the shape of the pattern, can be varied by altering the speed at which the carriage is towed. The most significant alterations to the shape of the pattern will be because of separation of the flow from the body of the carriage.

To make measurements of the surface wave field, the Laser Slope meter was situated over the wave tank as described in chapter 7. Initially, data were collected of the ambient wind wave fields which were to be modulated by the surface current; these results were presented in chapter 7. The current patterns were reproduced in conjunction with the wind wave field of interest by driving the sub-surface carriage beneath the wind generated waves. The surface slopes were measured at a single point throughout using the Laser

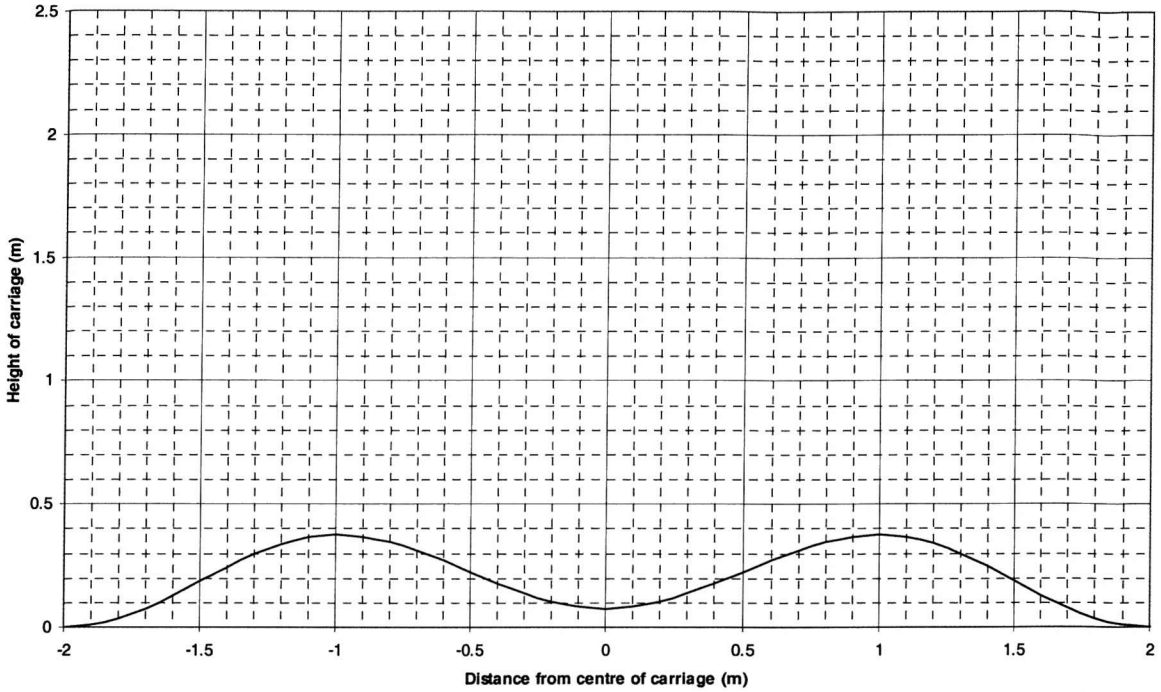

Figure 9-1: The profile of the sub-surface carriage (approximately to scale)

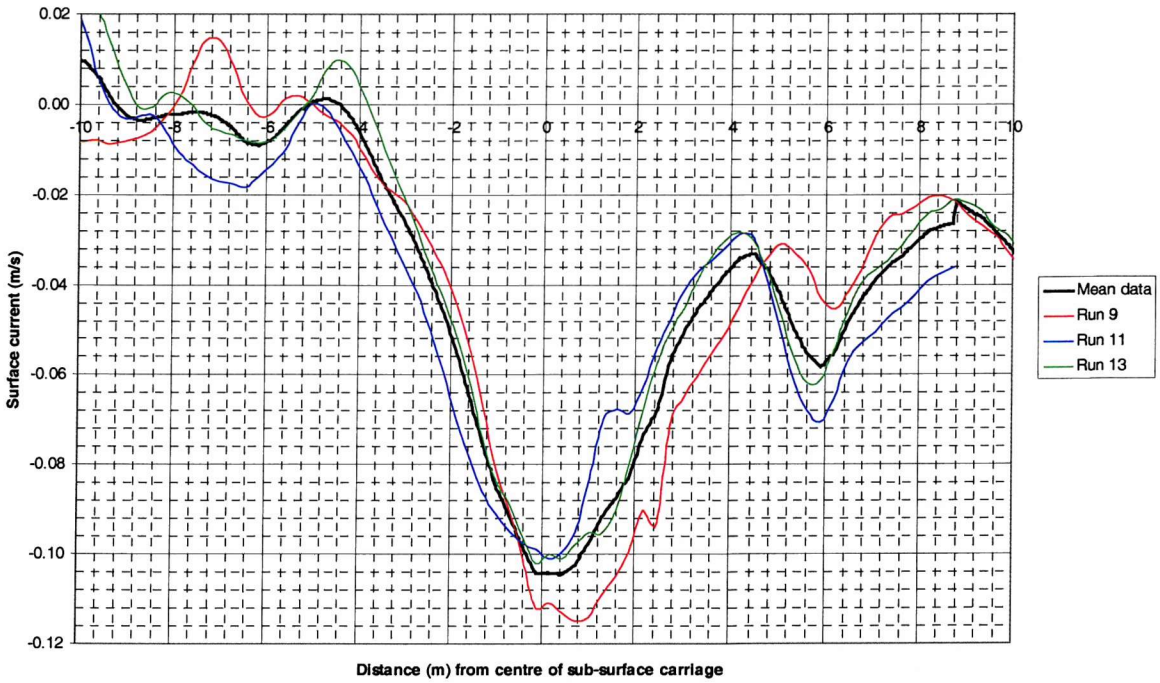

Figure 9-2: Surface current measured using particle tracking for the sub-surface carriage travelling at 0.57m/s. Carriage travelling in the direction which would be parallel to the wind direction.

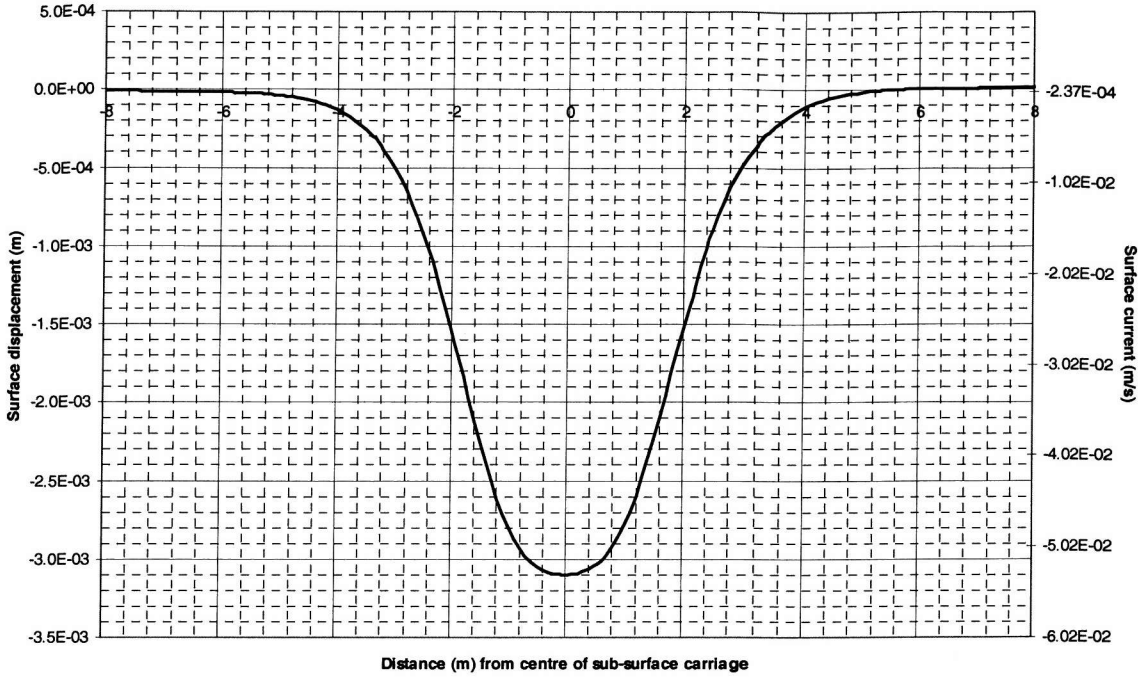

Figure 9-3: Theoretical surface displacement and surface current produced by sub-surface carriage moving at 0.57m/s

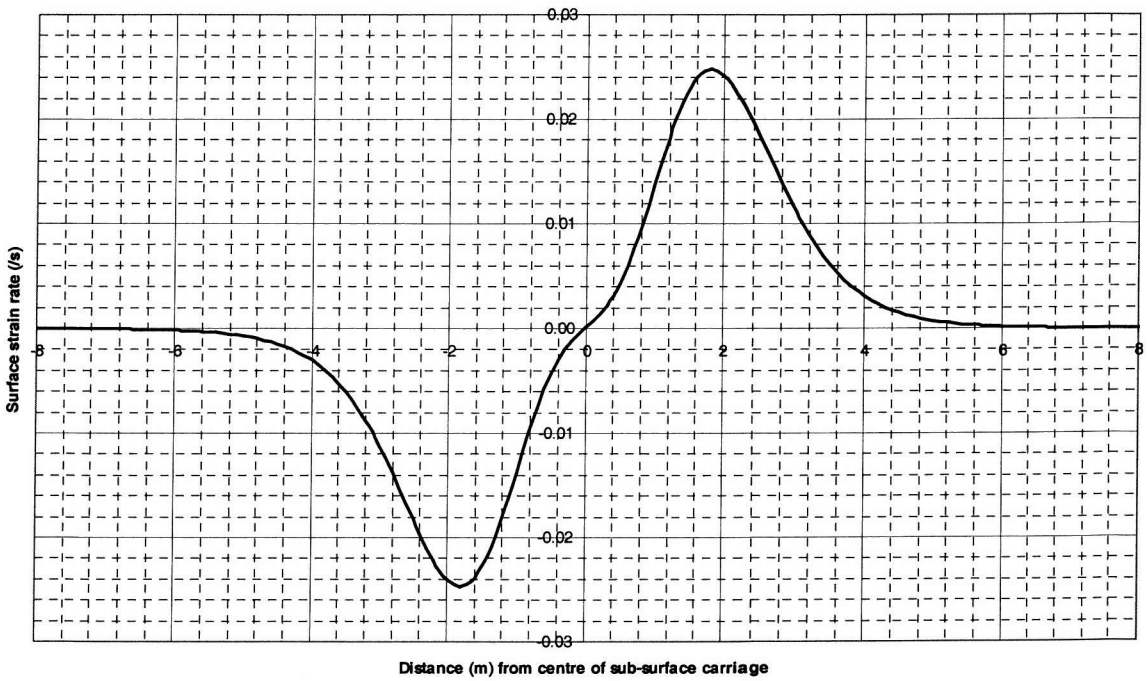

Figure 9-4: Theoretical surface strain rate produced by sub-surface carriage moving at 0.57m/s

Wind speed (m/s)	Sub-surface carriage speed (m/s)	Direction	No. of runs
5	0.10	Parallel	18
5	0.11	Anti-parallel	18
5	0.26	Parallel	18
5	0.27	Anti-parallel	18
5	0.57	Parallel	36
5	0.58	Anti-parallel	36
5	0.77	Parallel	14
5	0.78	Anti-parallel	14
3	0.26	Parallel	18
3	0.27	Anti-parallel	18
3	0.57	Parallel	12
3	0.58	Anti-parallel	12

Table 9-1: Wind wave fields and sub-surface carriage speed combinations

Slope meter. In this experiment, only two different wind wave fields were considered; one in combination with four different carriage speeds and one in combination with two carriage speeds. The carriage was run both parallel and anti-parallel to the wind direction in each case. Table 9-1 lists the combinations of wind wave fields, carriage speeds and wind / carriage directions. These data do not provide a very extensive parameter set, however, it is entirely sufficient to meet the objectives of this first experiment.

As the Laser Slope meter only measures data at a single point in the surface wave field, one experimental technique used in data analysis so that the statistical errors, arising from the natural fluctuation of the wave field in the data, could be reduced, was to make repeated measurements for each parameter set. This allows the data to be averaged at the same phases in the surface current pattern over many independent measurements. Without this, the statistical variations in the surface wave energy due to the stochastic nature of the wind wave field would hide any modulation effects. The aim was to collect 18 runs of each parameter set. This was not achieved for all the parameter sets due to repeated failure of the carriage pulley mechanism. Two data sets were taken with 36 runs, so that the effect of an

increased number of runs in reducing the statistical error in the averaged data, could be assessed. Each time the carriage was driven beneath the Laser Slope meter, data collection was continued for approximately a further 2 minutes after the carriage had passed the instrument, to allow the ambient wind wave field to regenerate. The carriage was then driven back in the opposite direction.

The carriage speeds were chosen so that it could be seen if there were differences in the experimentally measured variations that were consistent with resonant behaviour. The lowest carriage speed was chosen so that it was slower than the slowest possible wave group speed, whilst the fastest speed was chosen to be faster than any of the wave packets expected to be present in the wave tank at the wind speeds considered. The two middle speeds are comparable to the speeds of some of the wave packets in the wind wave fields. The kinematics of the surface wave packets for each sub-surface carriage speed have been investigated using ray diagrams (Ballard, 2000). These clearly show regions of wavenumbers for which resonance might occur. They also show regions in which the surface waves are trapped and travel back and forth over the top of the carriage.

An important issue in the design of the experiment is whether it accurately reproduces conditions which might be expected in the ocean. This can be considered in terms of the relative importance of the local time (how fast the modulating system moves past a stationary point), the advection time (how long it takes the surface waves to move the scale length of the modulation) and the relaxation time (how quickly the surface waves return to their equilibrium value). These terms are different depending on the ocean phenomenon and this experiment will certainly not be accurate for all situations. The local time is, for example, the period of the internal or surface wave, or the time it takes the carriage to pass a point in the wave tank. These timescales are long for internal waves, but quite short for swell waves and for the sub-surface carriage generated surface current to travel through one full cycle. For natural internal waves the local time and advection time are generally very much longer than the relaxation time. However, for surface swell waves, the local time is much shorter than the other two terms. In the wave tank, all three terms are of a similar magnitude. Therefore, careful consideration would need to be given in applying the results to ocean phenomena.

A second issue in the data analysis is whether or not the action balance equation is an appropriate equation to solve for the conditions of the experiment. For this to be the case, the current must be slowly varying over the wind wave field. As the current pattern moves directly above the carriage, it may be moving at up to 0.78m/s. However, the current pattern extends over a much greater distance than the carriage length with the entire pattern covering approximately 10m centred on the carriage centre. Since the wavelengths under investigation are at most 1m in wavelength, the current pattern was considered to be slowly varying.

9.3 Experimental results

9.3.1 Introduction

From visual inspection of the surface slope measurements made during the experiment, it has been observed that insufficient time was left for the wind wave field to fully recover in between separate sub-surface carriage runs. It is clear from the data that the mean square slope values do not recover to the values measured for the ambient wave fields. Although the water was visually inspected during this experiment, it was not possible for this to be detected by this method. However, as far as it is possible to tell, the character of the data does not appear different, but the slopes are of lower magnitude than for a fully generated surface wave field. It is clear that this will affect the results to some extent, although how much is not known. It seems reasonable to assume that results obtained from modulations to fully generated wave fields may be stronger versions of those presented below.

9.3.2 Surface slope variance calculations

The time variation of the surface slope variance along and across the wind wave tank was calculated for each parameter set collected. The time segments over which a single variance point was calculated overlapped significantly so that each sample point was included in 8 of these. Each segment width used 32768 data points; equivalent to approximately 3 seconds of data. A Hanning window was applied prior to the calculation of the variance. For each set of experimental parameters, the data sets were co-located to a particular position of the sub-surface carriage under the Laser Slope meter so that variance results from each independent measurement could be averaged over equal phases in the surface current pattern. This technique was used to reduce the fluctuations due to the

statistical errors and therefore to enhance any interaction effect due to the carriage. During the analysis of the data, it was noted that it was not possible to see any variance modulations in just one data run, even for those data sets where the modulation is strongest. A minimum of five runs averaged together were needed to make the effects become just visible above the noise level.

Some examples of the calculated variance for each slope component, normalised by the mean value of the data presented, are plotted in figures 9-5 to 9-8, relative to the nominal position of the sub-surface carriage (this is actually the position where it would have been had it travelled at a constant velocity over the entire measurement period). A section of data before and after the carriage is included for comparison with the perturbed data section. Negative distance represents data before the carriage arrived at the Laser Slope meter and positive distance represents data after it had passed by. It is noted that a significantly longer section of data would have made the results much clearer and would also have allowed a greater amount of time for the recovery of the wind wave field. The profile of the surface current measured using particle tracking is overlayed on the data (without any magnitude or direction information) so that its location and length-scales can be compared with the slope variance measurements.

9.3.3 Surface slope variance results

An overview of all the variance measurements is given below. The examples included in figures 9-5 to 9-8 show the carriage moving parallel and anti-parallel to the wind direction for two of the parameter sets used. These examples displayed the strongest modulations measured.

- at 5m/s wind speed, a sub-surface carriage speed of ~0.1m/s is insufficient to cause a significant perturbation to the surface wind wave field in either the parallel or anti-parallel cases;
- of the remaining 5 carriage and wind parallel combinations, a similar effect is seen in 4 of the 5 data sets (seen most strongly in the two examples shown). This effect is a decreased surface roughness at or slightly before the passing of the centre of the sub-surface carriage followed by an increase in surface roughness. In general the extent of any large variation in slope variance from the mean level lasts for the duration of the significant current. The decrease and increase in the variance also correspond

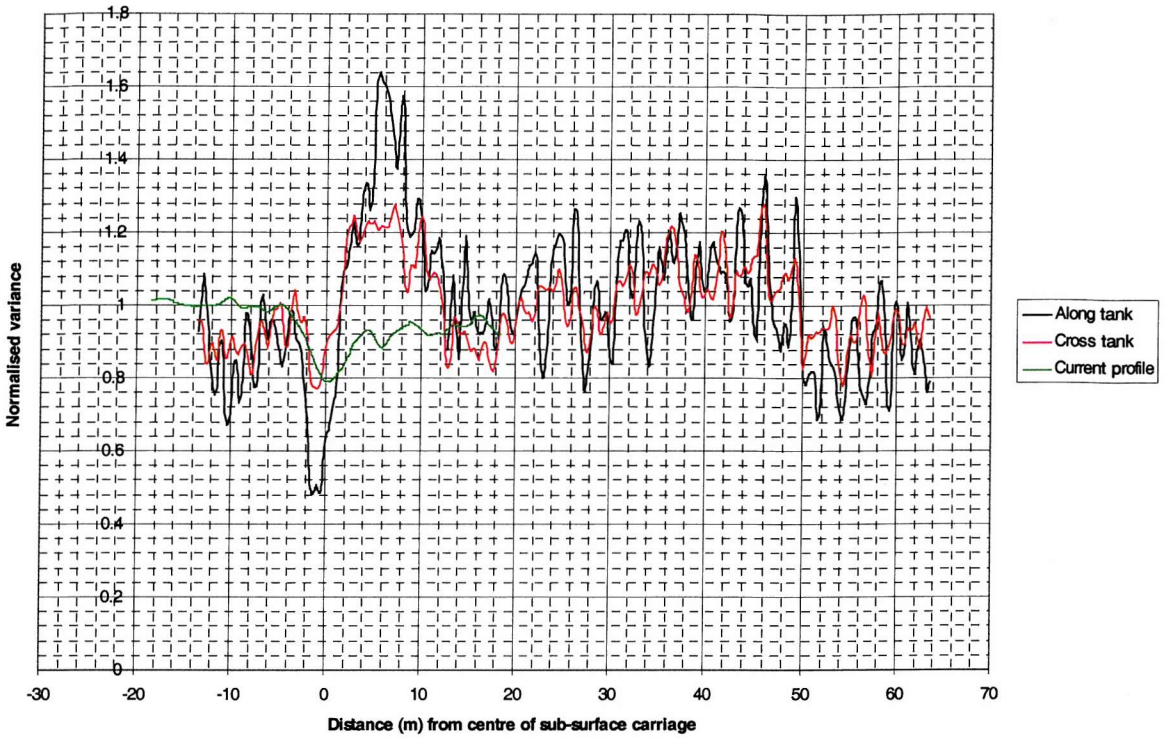

Figure 9-5: Surface slope variance for wind=5m/s, sub-surface carriage speed=0.57m/s, carriage and wind parallel. Peak value of current=0.104m/s.

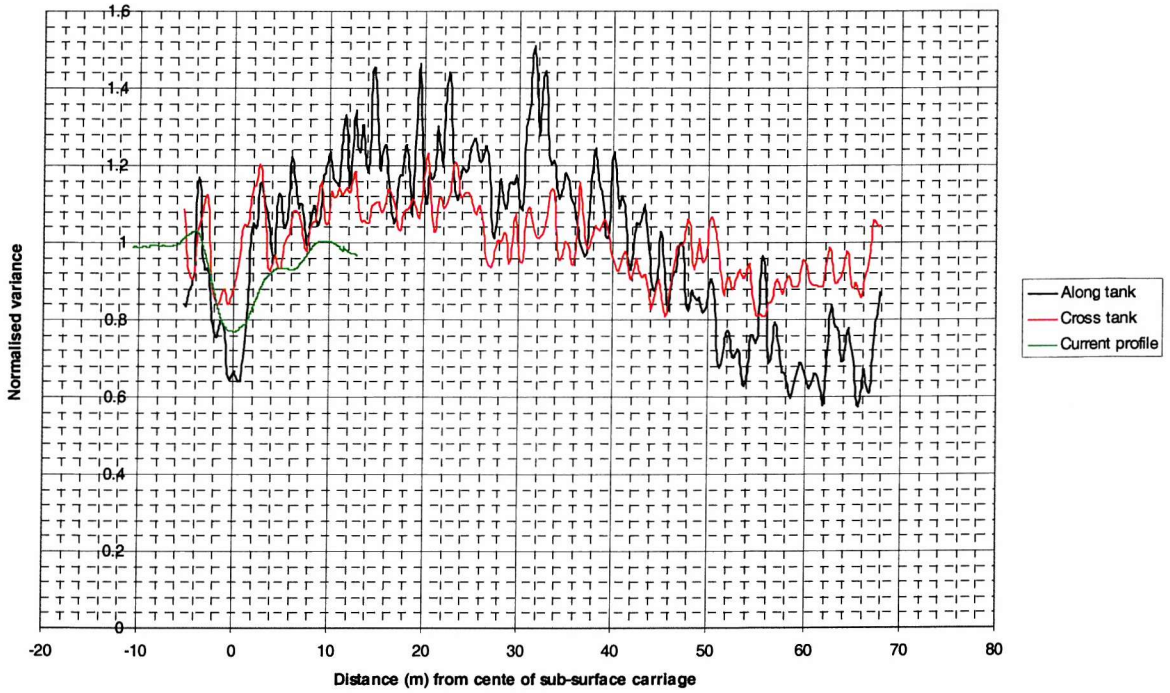

Figure 9-6: Surface slope variance for wind=5m/s, sub-surface carriage speed=0.58m/s, carriage and wind anti-parallel. Peak value of current=0.092m/s.

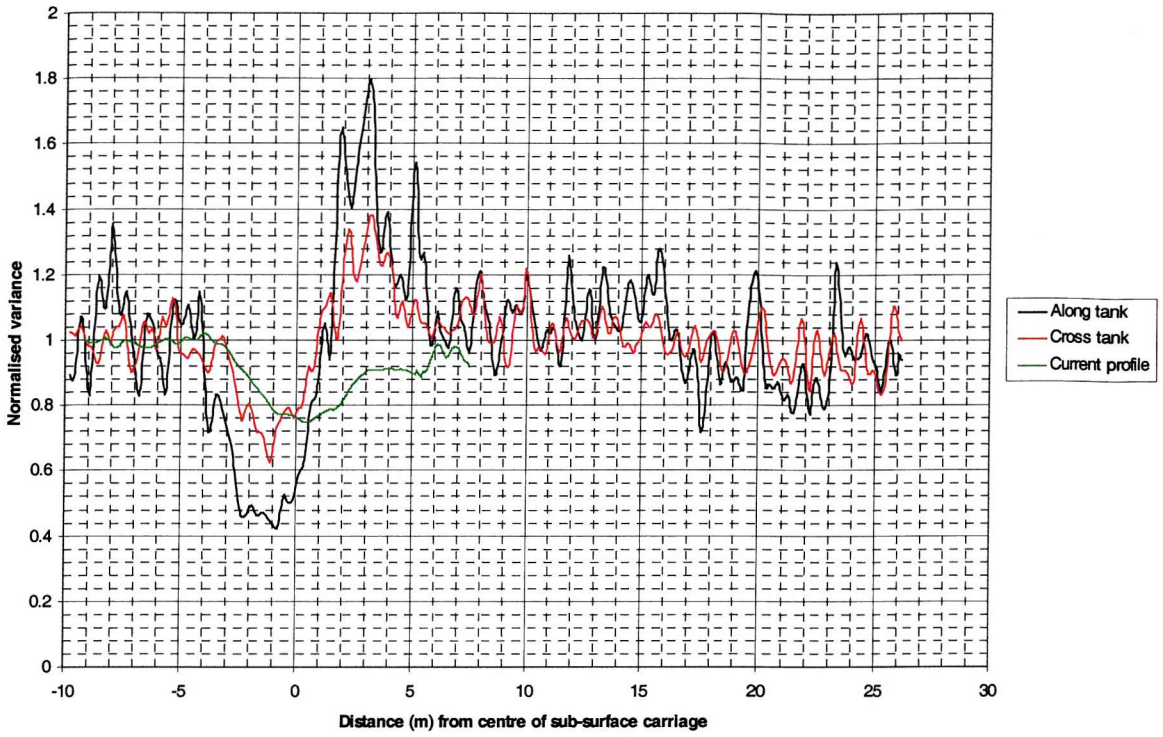

Figure 9-7: Surface slope variance for wind=3m/s, sub-surface carriage speed=0.26m/s, carriage and wind parallel. Peak value of current=0.05m/s.

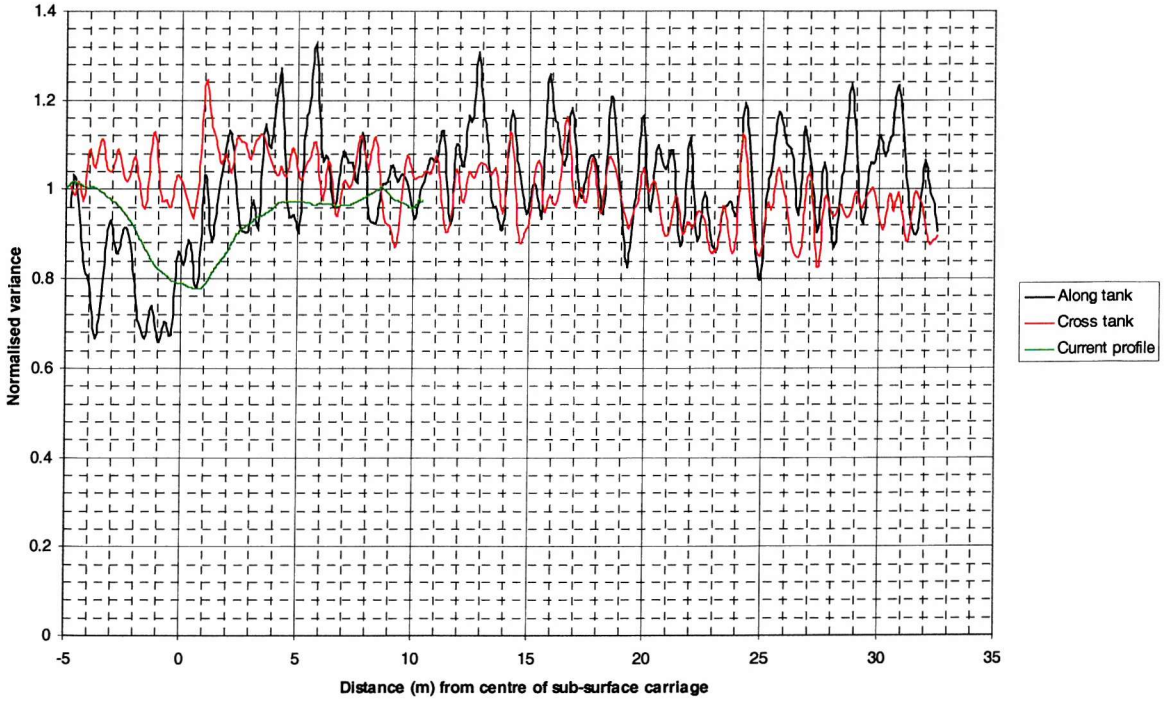

Figure 9-8: Surface slope variance for wind=3m/s, sub-surface carriage speed=0.27m/s, carriage and wind anti-parallel. Peak value of current=0.044m/s.

approximately to the current divergence and convergence. It seems likely that there may be some residual current oscillations set up in the tank which affect the surface wind wave field for some time after the carriage has passed. However, after the modulations caused by the current pattern created directly above the sub-surface carriage, further variations in surface roughness are much more random in nature;

- the results for the carriage and wind anti-parallel are less clear then those with the carriage and wind parallel. However, for the runs displaying the clearest modulations, it is found that there is a decrease in the surface roughness with its minimum value at or slightly earlier than the centre of the sub-surface carriage. This is followed by a long low increase in the surface roughness. It seems likely that when the carriage and wind are anti-parallel, surface roughness variations may persist for longer as the carriage will continue to affect the surface wave field throughout its journey back down the tank. These perturbed waves will continue to travel towards the Laser Slope meter where measurements of the surface roughness are made;
- at a carriage speed of 0.57m/s and a wind speed of 3m/s, the surface roughness displays complicated behaviour which can not be explained at this stage.

It is clear from these results that using the technique of averaging the surface roughness of many independent runs over equal phases of the surface current pattern, the Laser Slope meter has proved capable of detecting the modulations of the surface wind wave field. This is a valuable result which clearly demonstrates the potential of the Laser Slope meter for such measurements.

9.3.4 Calculation of spectral changes in experimental data

In the same way as for the variance calculations, along tank surface slope frequency spectra have been calculated for each segment of data. Each data segment was multiplied by a Hanning window before the spectral calculation to reduce side band errors. Again, the data segments overlapped significantly so that each sample point was included in 8 such segments. A spectrogram was generated for each parameter set by plotting the spectra from successive times side by side and plotting log10 of the magnitude of the spectrum as a colour code to form one image. For each parameter set, the data from many independent runs have been averaged over the same phase of the surface current pattern. In the examples displayed in the 'b' figures of 9-9 to 9-12, the mean level of the spectrum at

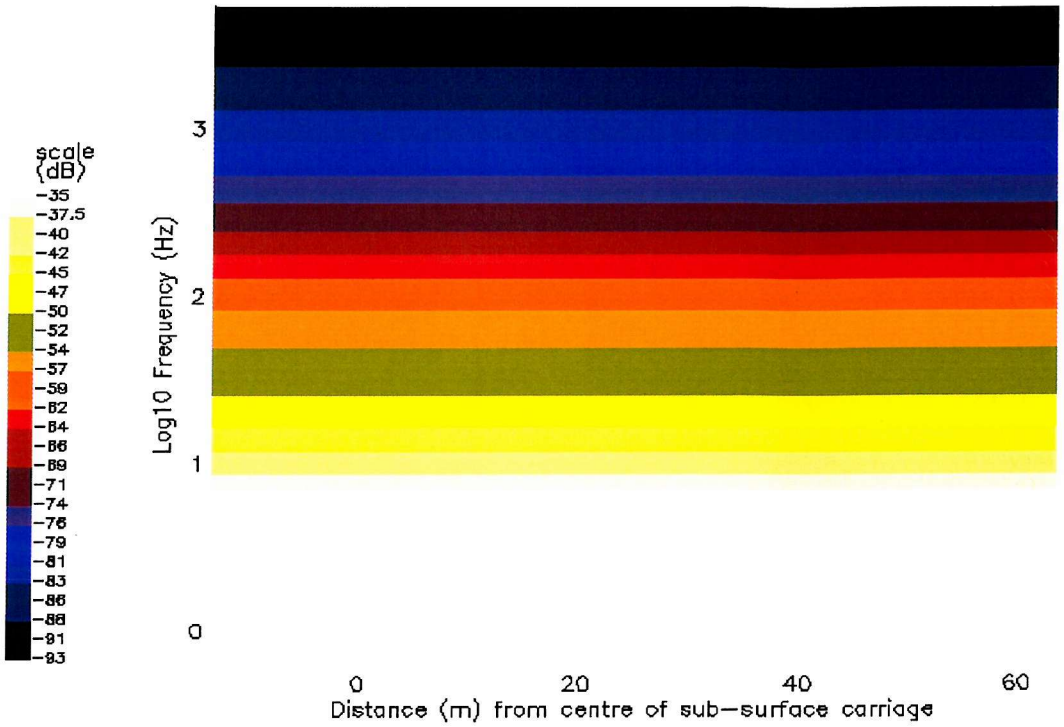

Figure 9-9a: Mean level of spectrum at each frequency for along tank surface slope spectrograms for wind=5m/s, sub-surface carriage speed=0.57m/s, carriage and wind parallel. Peak value of current=0.104m/s.

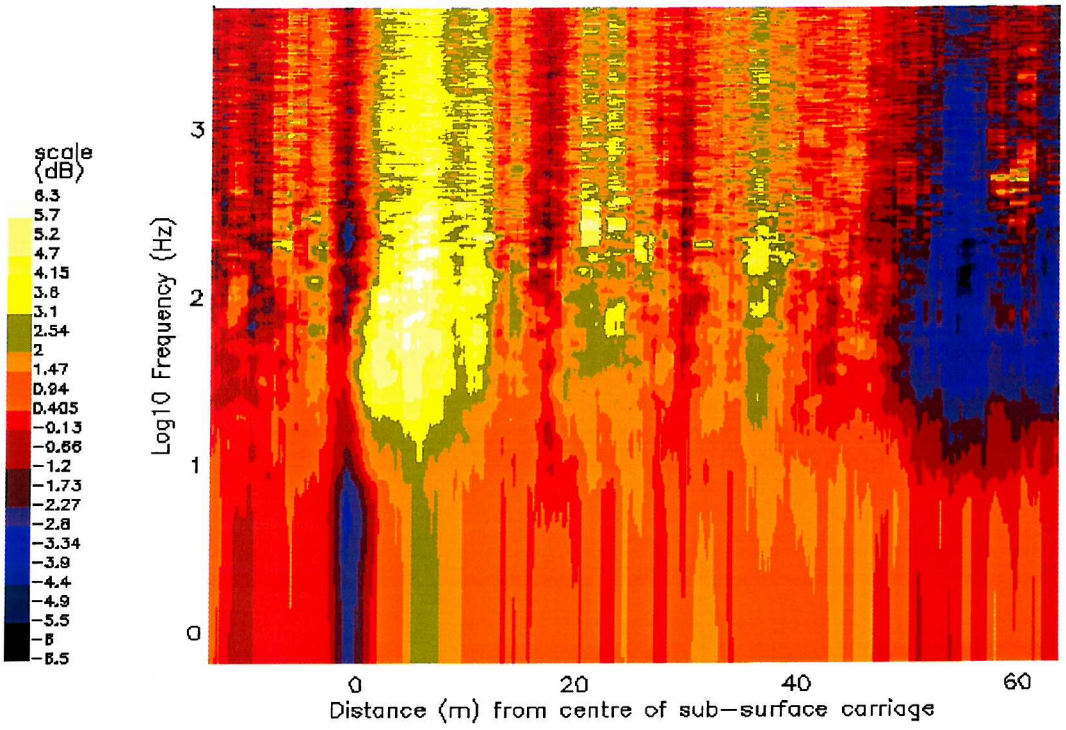

Figure 9-9b: Along tank surface slope spectrograms for wind=5m/s, sub-surface carriage speed=0.57m/s, carriage and wind parallel. Peak value of current=0.104m/s.

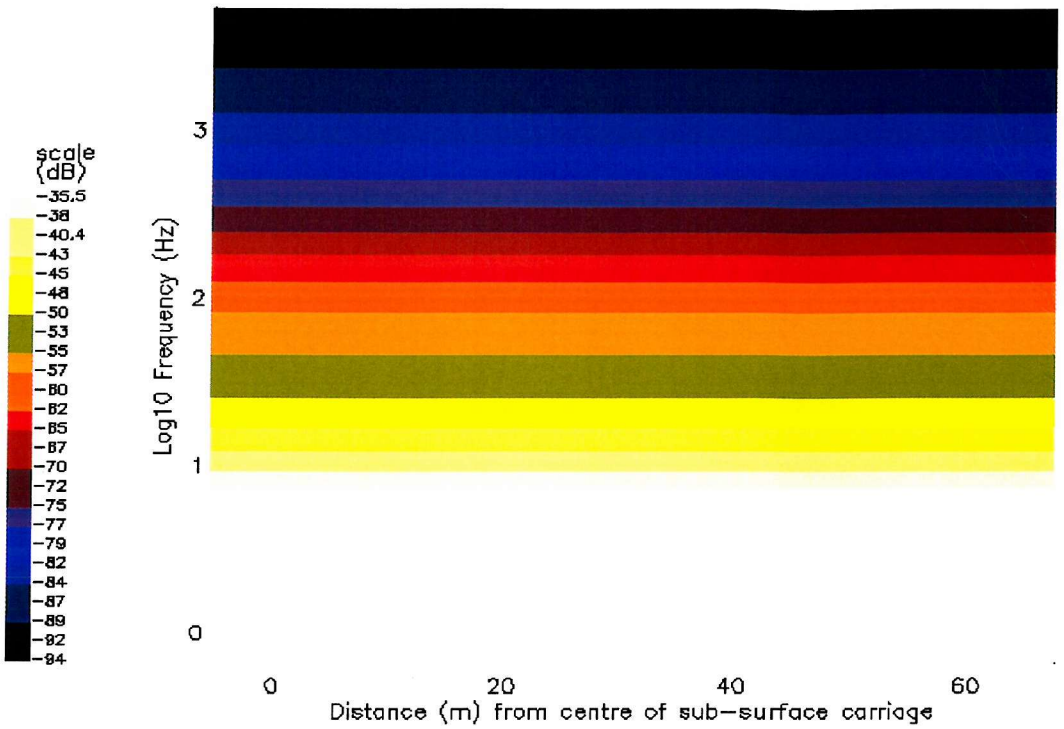

Figure 9-10a: Mean level of spectrum at each frequency for along tank surface slope spectrograms for wind=5m/s, sub-surface carriage speed=0.58m/s, carriage and wind anti-parallel. Peak value of current=0.092m/s

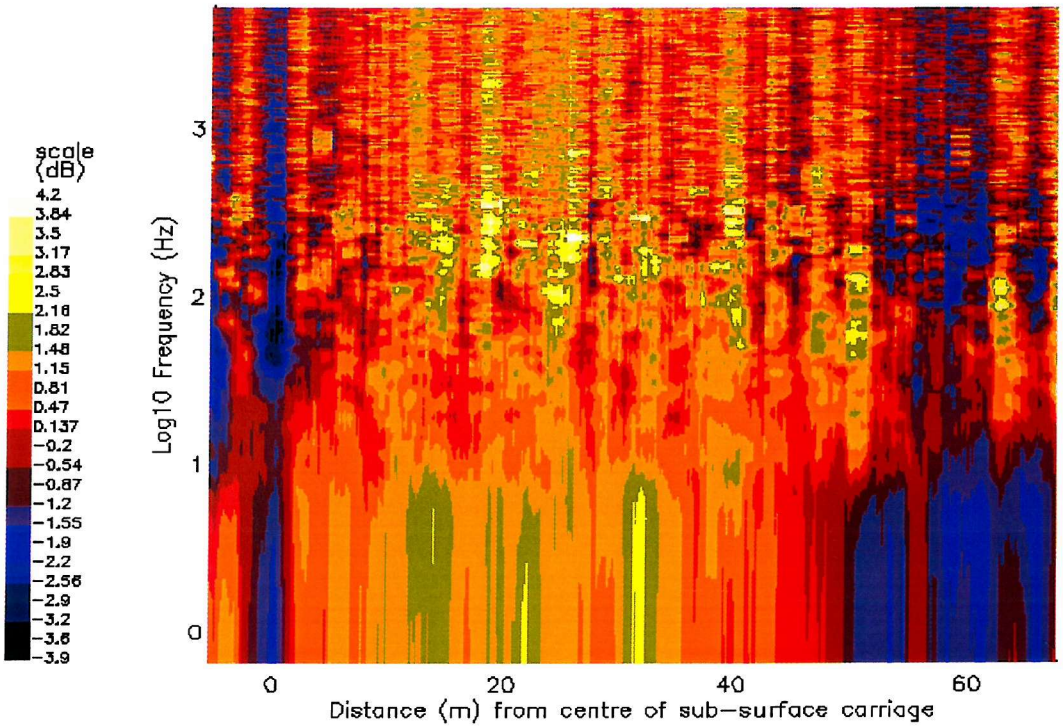

Figure 9-10b: Along tank surface slope spectrograms for wind=5m/s, sub-surface carriage speed=0.58m/s, carriage and wind anti-parallel. Peak value of current=0.092m/s

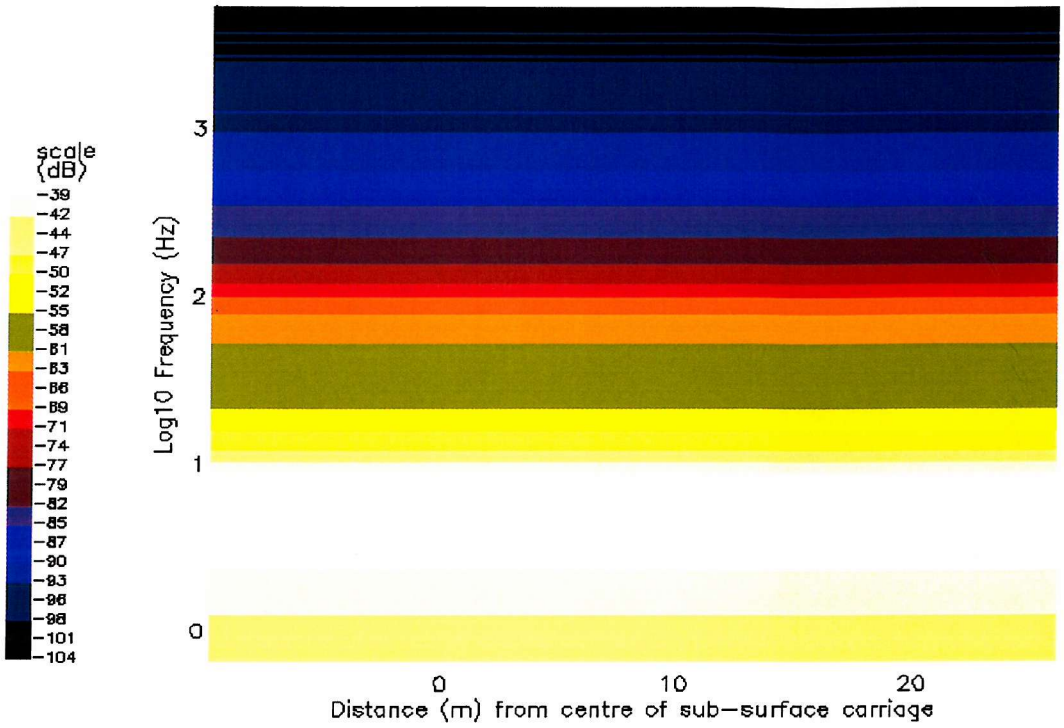

Figure 9-11a: Mean level of spectrum at each frequency for along tank surface slope spectrograms for wind=3m/s, sub-surface carriage speed=0.26m/s, carriage and wind parallel. Peak value of current=0.05m/s.

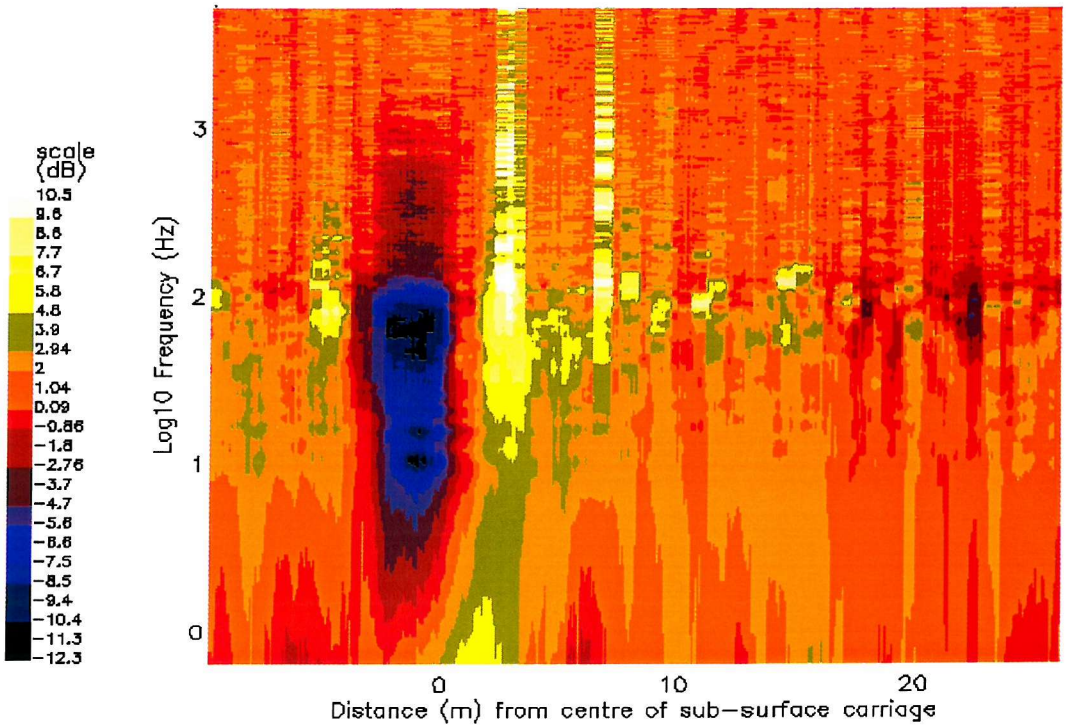

Figure 9-11b: Along tank surface slope spectrograms for wind=3m/s, sub-surface carriage speed=0.26m/s, carriage and wind parallel. Peak value of current=0.05m/s.

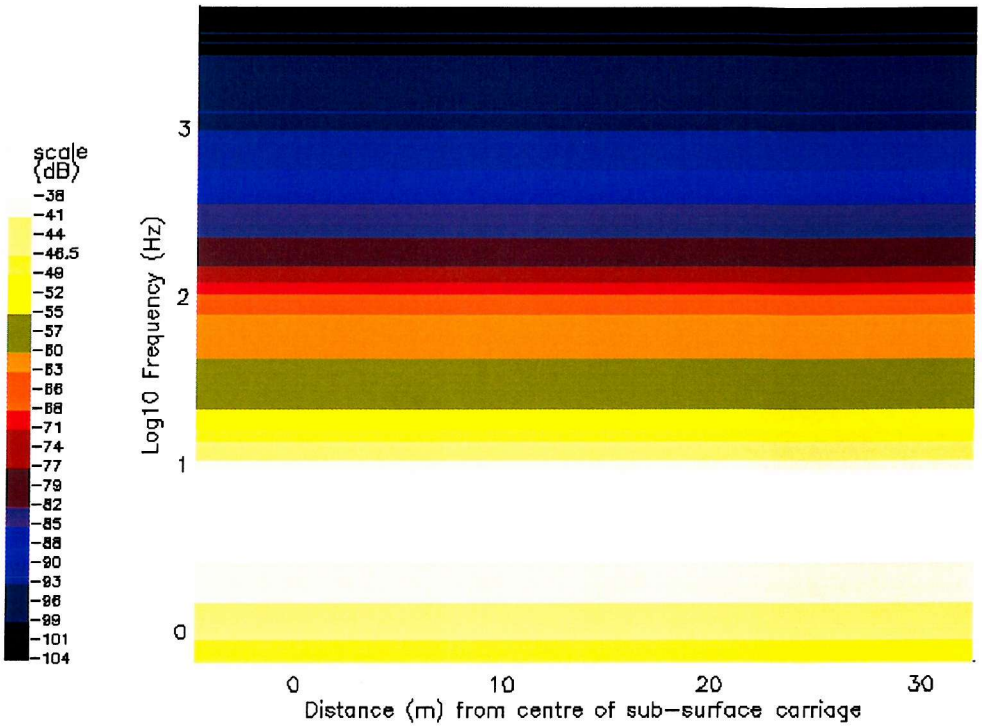

Figure 9-12a: Mean level of spectrum at each frequency for along tank surface slope spectrograms for wind=3m/s, sub-surface carriage speed=0.27m/s, carriage and wind anti-parallel. Peak value of current=0.044m/s.

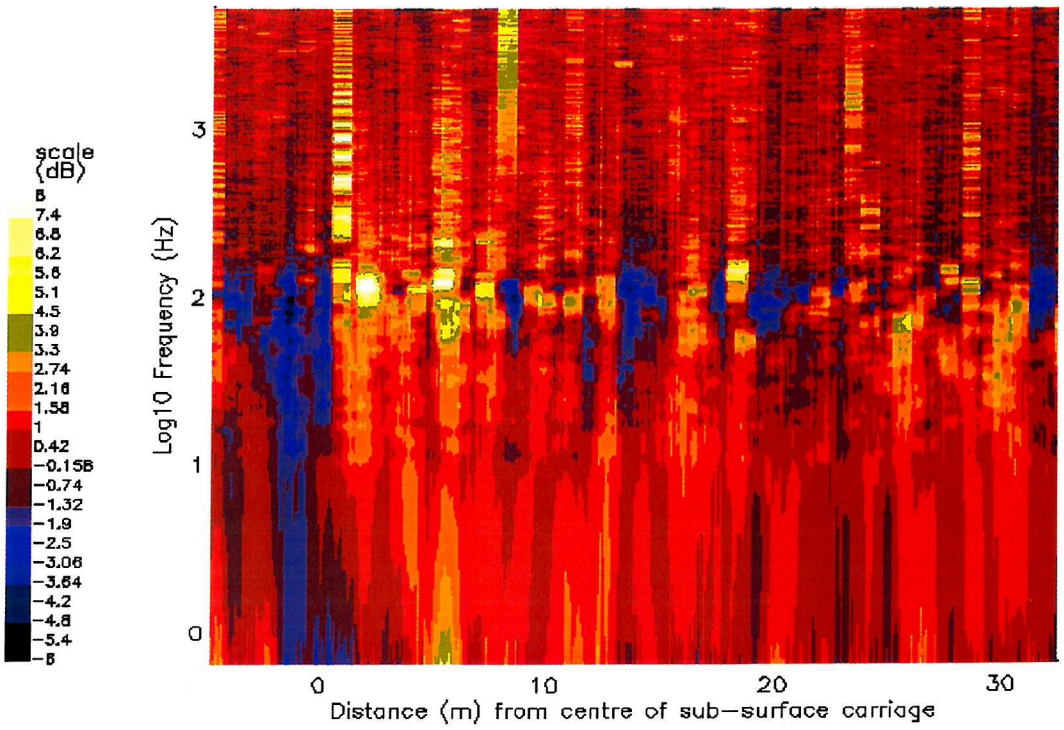

Figure 9-12b: Along tank surface slope spectrograms for wind=3m/s, sub-surface carriage speed=0.27m/s, carriage and wind anti-parallel. Peak value of current=0.044m/s.

each frequency has been subtracted from the data so that the modulations in each frequency range are enhanced, and this mean level is displayed in the 'a' figure's of 9-9 to 9-12. Each colour scale covers the full range of values plotted and so does not represent the same magnitudes in each image. The examples chosen correspond to the same data sets displayed in figures 9-5 to 9-8 for the variance modulations.

9.3.5 Spectral results

The results are summarised below for all the calculations of spectra of the along tank slope component:

- there is no clearly consistent behaviour throughout all of the data sets;
- there are no clear features at 5m/s wind with a carriage speed of 0.11m/s in either the parallel or anti-parallel runs;
- with the carriage and wind parallel, and a wind speed of 5m/s, the behaviour is similar at carriage speeds of 0.26m/s, 0.57m/s and 0.77m/s. This is a decrease in the spectral energy at the centre of the carriage at all frequencies, and particularly at the lower frequencies, followed by an increase at all frequencies, particularly from about 25Hz to 250Hz;
- similar features to the decrease at 55m in figure 9-9 are seen in several data sets and can not be explained by the expected surface current pattern;
- with the carriage and wind anti-parallel and a wind speed of 5m/s, the behaviour is also similar at 0.57m/s and 0.77m/s. There is a spectral decrease at the centre of the carriage at all frequencies with the smallest decrease at about 10 to 25 Hz;
- at a wind speed of 3m/s and with the carriage direction parallel to the wind direction, for the two carriage speeds considered, the data sets do show some similar characteristics. There is a large spectral decrease just before the centre of the carriage at all frequencies but with the largest effect at about 50 to 60Hz (this is at the mains frequency). This is followed by a general increase in the spectral level;
- with the carriage and wind anti-parallel, and with a wind speed of 3m/s, at a carriage speed of 0.27m/s, there is a spectral decrease at all frequencies just before the centre of the carriage, followed by an increase at high frequencies >100Hz. The behaviour of the data at 0.58m/s with the carriage and wind anti-parallel shows no particular correlation with the location of the carriage.

9.3.6 Discussion of experimental measurements

It is clear from the experimental results of the slope modulations that the Laser Slope meter is very capable of measuring this type of modulation. The modulations appear most strongly in the surface slope variance data and less clearly in the surface slope frequency spectra. This is likely to be due to the way in which the energy from a single variance point becomes distributed more thinly over an entire frequency spectrum. To enhance spectral modulations, an increased number of independent data runs would be required.

The experimental results can be compared with the theoretically generated surface strain rate. From the theory of the expected current pattern over the carriage, the maxima and minima in the surface strain rate occur at –1.8m and 1.8m respectively, measured from the centre of the carriage. (These peaks should be considered in reverse when they are compared with runs in which the carriage and wind direction were parallel, because of the way in which the data are displayed.) The actual current patterns generated in the tank are likely to produce a similar pattern for the surface strain rate, except that there is likely to be separation of the water flow over the trailing edge of the carriage (especially at the higher carriage speeds), which may move the location of the peak of negative strain further from the carriage centre. For the two clearest sets of results, included as the examples, with the wind and carriage parallel, the location of the minimum value of the variance is consistent with the location of the peak in the strain rate. The increase in surface variance is slightly further from the centre of the carriage than the peak in the theoretical strain rate prediction, which is consistent with separation of the water from the carriage occurring. It is not surprising that zero strain rate is not co-located with the equilibrium variance level as after the decrease caused in the surface roughness there would be a period of wave regeneration before equilibrium would be reached.

With the carriage and wind direction anti-parallel, the location of the modulations in the surface roughness measured do not correlate with the location of the peaks and troughs in the strain rate prediction. Therefore, it is clear that the direction of the carriage (and hence current variations) with respect to the direction of the wind is of great importance in these types of interaction.

Some of the anomalous behaviour, such as that at 55m in figure 9-9, may be related to reflections of the waves set up by the carriage. The wave absorbing beach at the far end of the wave tank was not designed to absorb very long wave length waves.

9.4 Theoretical calculations using numerical model

9.4.1 Introduction

In this section the numerical model developed in chapter 8 is used with the experimentally measured ambient wavenumber spectra calculated in chapter 7 and the currents measured using particle tracking. The model is used to calculate theoretically how the variance of the surface slope might be expected to alter due to the passage of the sub-surface carriage and how this is related to the spectral changes.

At this stage of the research, the emphasis is on investigating the way in which the Laser Slope meter data, recorded at a single point, can be used as an input to models such as the action balance model, and how the model output can be manipulated to provide a result which is directly comparable with the Laser Slope meter data. Once this has been established, the data can be used to test various forms of the theory. In terms of the development of the model, the emphasis was to use a numerical technique which would allow real data to be input for the ambient spectrum and surface current variations and to allow any form of growth, decay or wave-wave interaction term to be used in the solution.

9.4.2 Using the numerical program to calculate modulated slope frequency spectra

As the Laser Slope meter is stationary within the wave tank and only measures data at a single point, it can only provide temporal information. Therefore, it is possible to calculate accurately only a slope frequency spectrum. However, the numerical model presented in chapter 8 requires an action wavenumber spectrum.

In chapter 7 calculations were performed to estimate a wavenumber spectrum from the slope frequency spectra, making certain assumptions about the wave field. The action spectrum is related to the wavenumber spectrum by,

$$N(k,\phi) = \frac{\rho g}{\omega}\Psi(k,\phi) \qquad 9\text{-}1$$

Therefore, in terms of the angular distribution calculated, the action spectrum is given by,

$$N(k,\phi) = \frac{\rho g}{\omega}\psi(k)A_q \cos^{q(k)}\left(\frac{\phi}{2}\right) \qquad 9\text{-}2$$

The action spectrum calculated in this way has been used along with the corresponding information on the angular distribution, given in chapter 7, as an input into the numerical model. After stepping back in time in x,k space to the region where the wave field is unaffected by the surface current, this spectrum is used to provide the value of the ambient action spectrum at the required wavenumber and angle. The program then steps forward in time to see how this spectral value is modulated by the current.

The output from the program provides a series of values for the action density for a number of wavenumbers at different angles to the wind direction. These values can be used to calculate the frequency spectrum as modulated by the surface current. The relationship between the frequency spectrum and the program output is given by,

$$\int S(\omega')d\omega' = \int_0^{\infty}\int_{-\pi}^{\pi} \frac{\omega k^2 N(k,\phi)}{\rho g} k\,dk\,d\phi\,\delta(\pm\omega' - \omega(k) - Uk\cos\phi) \qquad 9\text{-}3$$

In this case the angle, θ, between the wavenumber, k, and the current is equal to ϕ because the wind is along the current direction. Because the dispersion relation is modified by the presence of a surface current, there is no longer a 1-1 relationship between k and ω which was used to calculate the equilibrium wavenumber spectrum. Instead, the energy in a particular frequency will come from a whole range of wavenumbers at different angles to the wind direction. As there are only a finite number of k and ϕ values from the program, the integral must be converted into a summation taking account of the range of k or ϕ represented by each value. Additionally, the frequency values must be binned into discrete bands, $\Delta\omega$, so that there is a range of values into which to put the energy from each k,ϕ pair which satisfies the delta function. The mean of the slope squared in each bin represents the

slope squared across the frequency spectrum. If the frequency bins are selected to be of a constant size, and wavenumber bins are selected to be even in wavelength, then since,

$$dk = \frac{-k^2}{2\pi} d\lambda \qquad 9\text{-}4$$

9-3 averaged over the bin can be written as,

$$S(\omega'_n) \approx \frac{\int_{\omega'_n}^{\omega'_{n+1}} S(\omega'_n) d\omega'}{\Delta\omega'_n} \approx \frac{1}{\Delta\omega'_n} \sum_n \sum_m \frac{-\omega_n k_n{}^5 N(k_n, \phi_m) \Delta\lambda_n \Delta\phi_m}{2\pi\rho g} \qquad 9\text{-}5$$

for those values of k_n and ϕ_m which satisfy,

$$\omega(k_n) + U k_n \cos\phi_m \in (\omega_n, \omega_{n+1}) \qquad 9\text{-}6$$

As a test of this method, the numerical program has been used with the estimated wavenumber spectrum at 5m/s wind speed to calculate the slope frequency spectrum using this method, where the current due to the carriage is set to zero. The original slope frequency spectrum should be reproduced if the program works correctly. Trial and error revealed that in terms of accuracy in the output spectrum, it is much more important to use many k-values rather than many ϕ-values. Ideally, a large number of each would be used but this is not possible given time constraints. The frequency bin sizes have been selected carefully to allow a reasonable number of points in each bin as this produces a smoother spectrum.

In this test example, 2000 k-values have been used spread evenly between 0.001m and 0.4m in wavelength. 15 ϕ-values have been used spread evenly between $-\pi/2$ and $\pi/2$. The resulting spectrum is displayed along with the original slope frequency spectrum for comparison in figure 9-13. It can be seen that over the most important part of the spectrum, the model has accurately reproduced the spectrum. The range of frequencies included

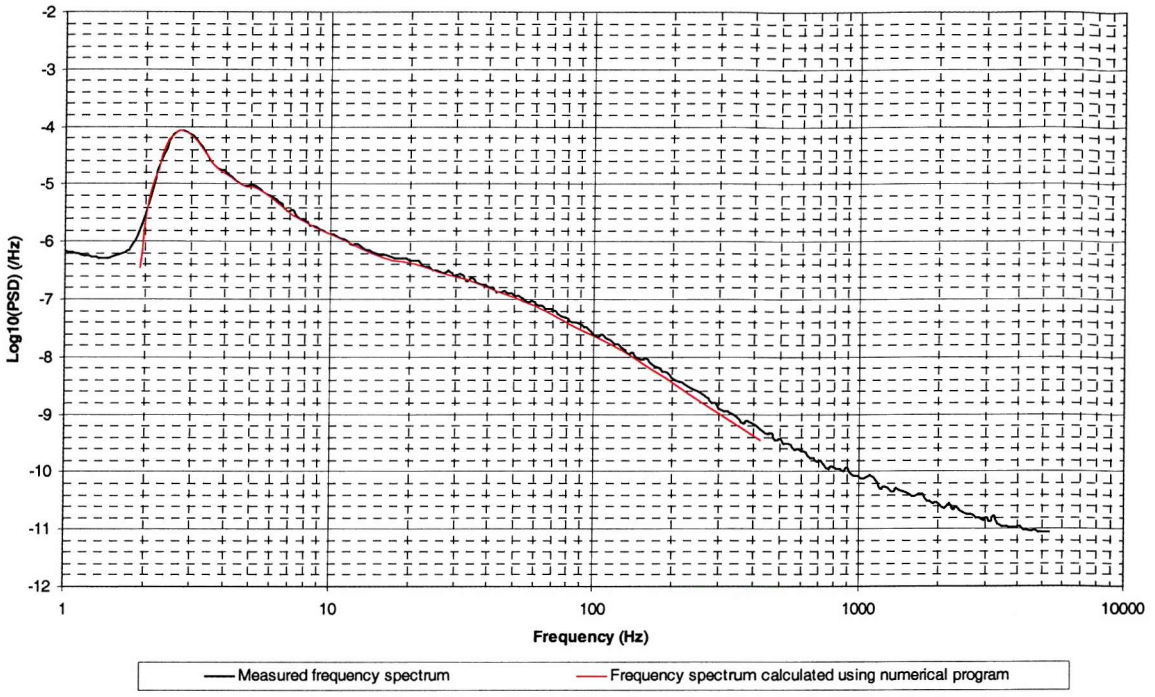

Figure 9-13: Comparison of measured frequency spectrum and spectrum calculated using numerical program

depends upon the limits in wavelength selected. The spectrum is not well reproduced at the extreme values in frequency as these regions should have contributions to the spectrum from wavelengths that have not been used in the example.

9.4.3 Numerical results

Some example graphs of the results from the numerical simulation are displayed in figure 9-14 to 9-21, corresponding to the parameter sets displayed in figure 9-5 to 9-12. These graphs have been produced using the techniques described above and include simulations of the theoretical surface slope variance changes and slope frequency spectrum variations. In each case, the ambient wavenumber spectrum estimated from the Laser Slope meter data was used. The currents measured by particle tracking were smoothed and input directly into the program. Therefore, the results are as near as possible, the theoretical estimations of modulations to the wave field present in the tank caused by the actual currents created by the carriage. A discussion on the performance of the numerical program is given in Ballard (2000).

For each data set collected by the Laser Slope meter, the program was run for each carriage speed and wind wave field combination, in both directions and with the real measured ambient spectra and surface current patterns and with the power of the decay term, p, in equation 8-2, set to 1. Some of the combinations were also run with p=2. The variance graphs have been normalised by the ambient spectral variance (or a near value taken from the calculations). The log10 of the spectral power has been calculated and then the results are displayed so that the colour represents the power change at that location relative to the mean power at each frequency.

The results will not be discussed in any detail as the objective of the exercise was to investigate the analysis techniques. Given the errors apparent in the experimental data, it would be premature to place much emphasis on the results themselves. However, the results are summarised below. In terms of comparing the numerical and experimental results, the x-axis of the experimental data is reversed where the wind and carriage directions are parallel.

The theoretical modulations to the surface slope variance were found to be very similar for both p=1 and p=2. The numerical results show that using this theory, variations created with the carriage moving parallel to the wind waves (i.e. with the current opposing the surface wind waves) are much greater than when the carriage is travelling anti-parallel to the wind direction. With the carriage and wind parallel, apart from at the lowest wind speed there is a decrease in the surface variance just before or directly over the centre of the carriage. In the majority of cases, there is a small increase in the surface roughness approximately 15 to 20m after the centre of the carriage has passed. With the wind and carriage anti-parallel, there is a decrease in the surface roughness directly over the centre of the carriage, which increases in magnitude the faster the speed of travel of the carriage.

The numerical and experimental results are now briefly compared. Overall, the theory does reproduce the reductions in the variance over the centre of the sub-surface carriage fairly well. It does not predict the sharp increase seen in many of the data sets with the carriage moving parallel to the wind waves, nor the slow decrease to the ambient level from the small region of increased variance seen in the data sets with the carriage and wind anti-parallel.

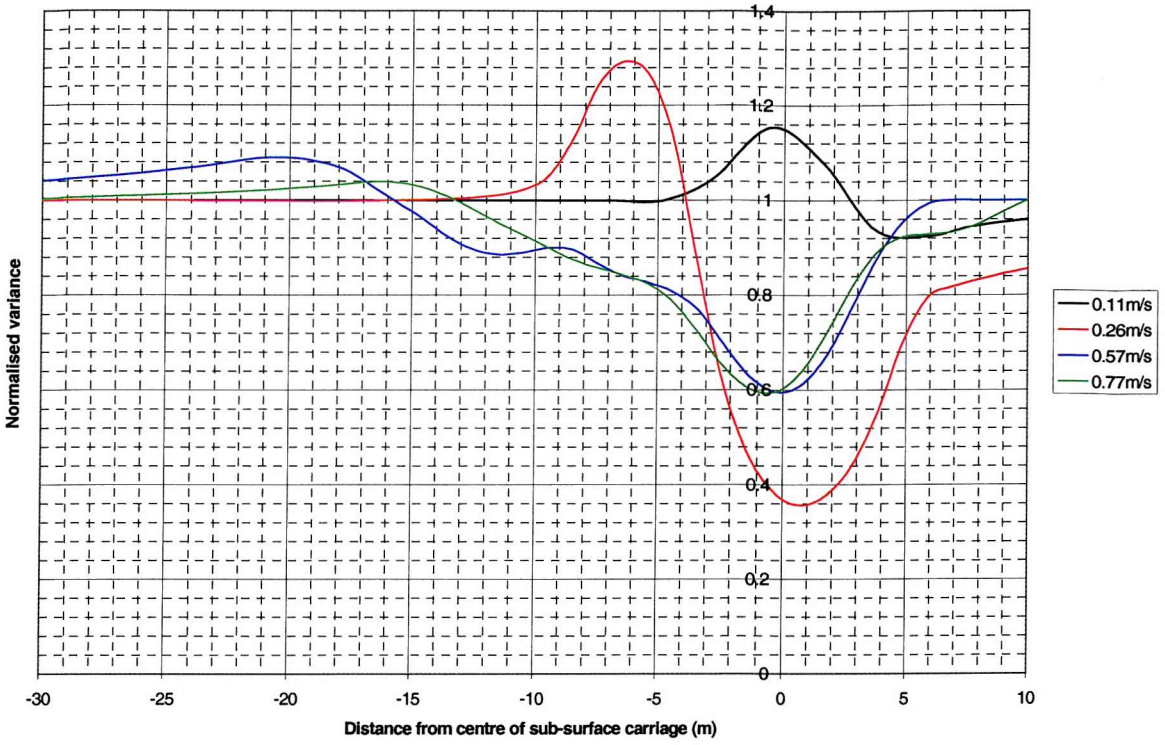

Figure 9-14: Variance variations for wind speed=5m/s, carriage and wind parallel, p=1

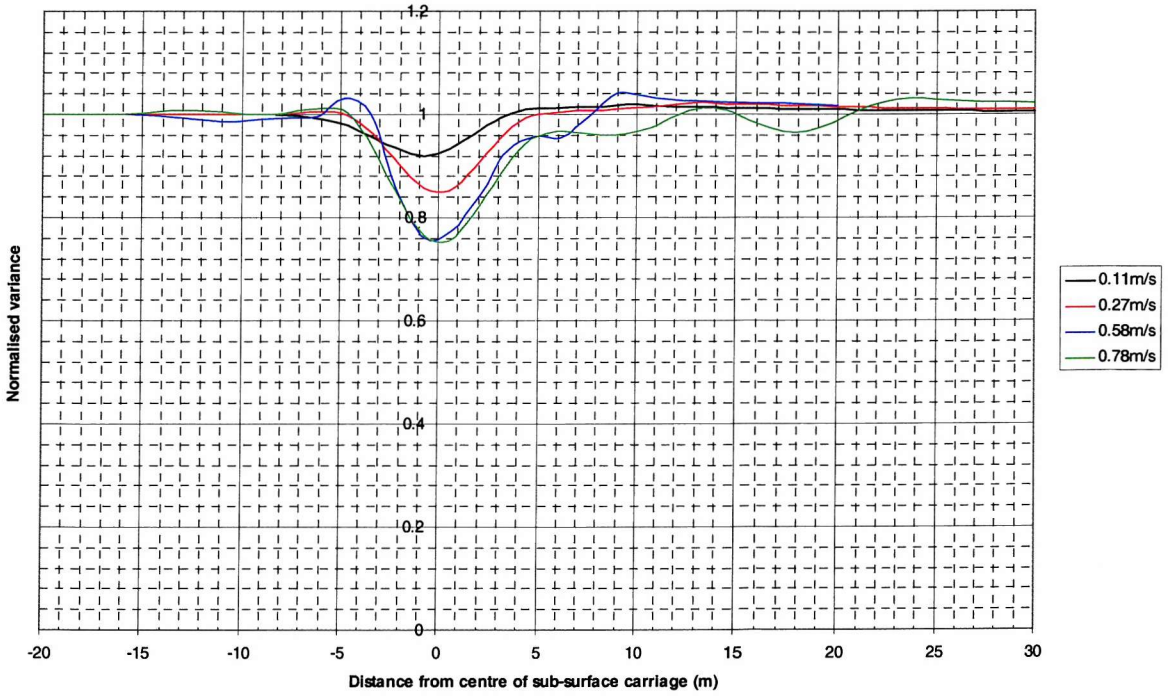

Figure 9-15: Variance variations for wind speed=5m/s, carriage and wind anti-parallel, p=1

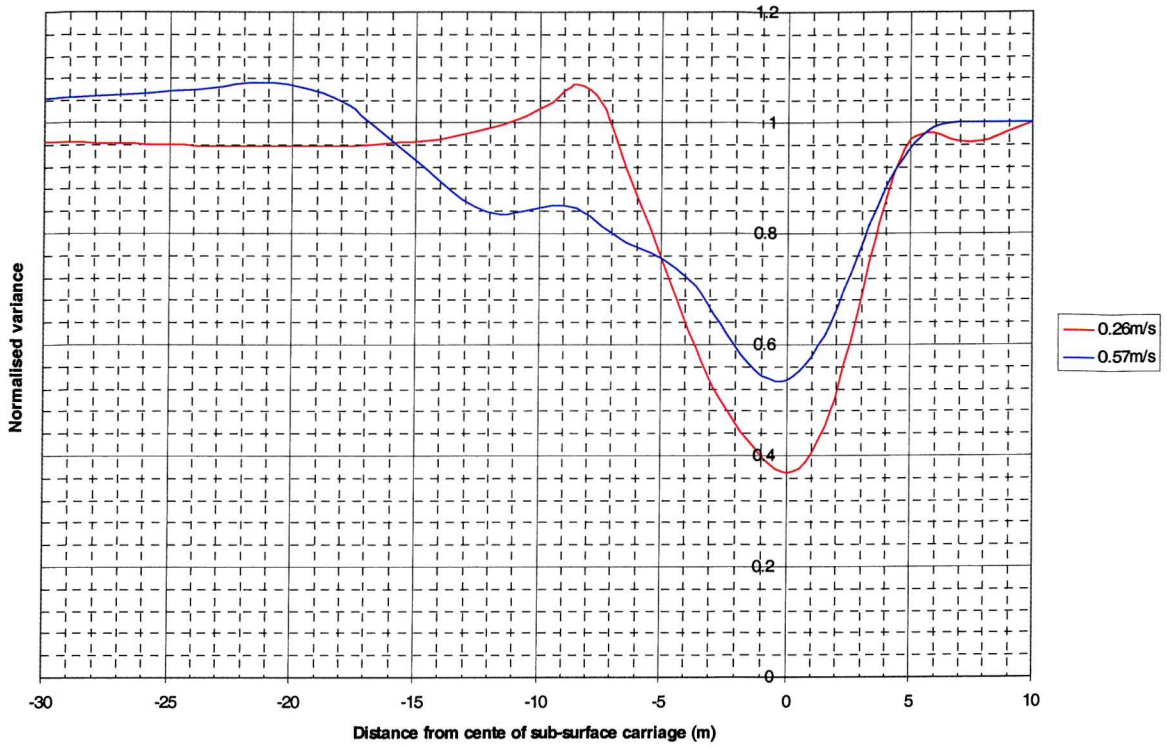

Figure 9-16: Variance variations for wind speed=3m/s, carriage and wind parallel, p=1

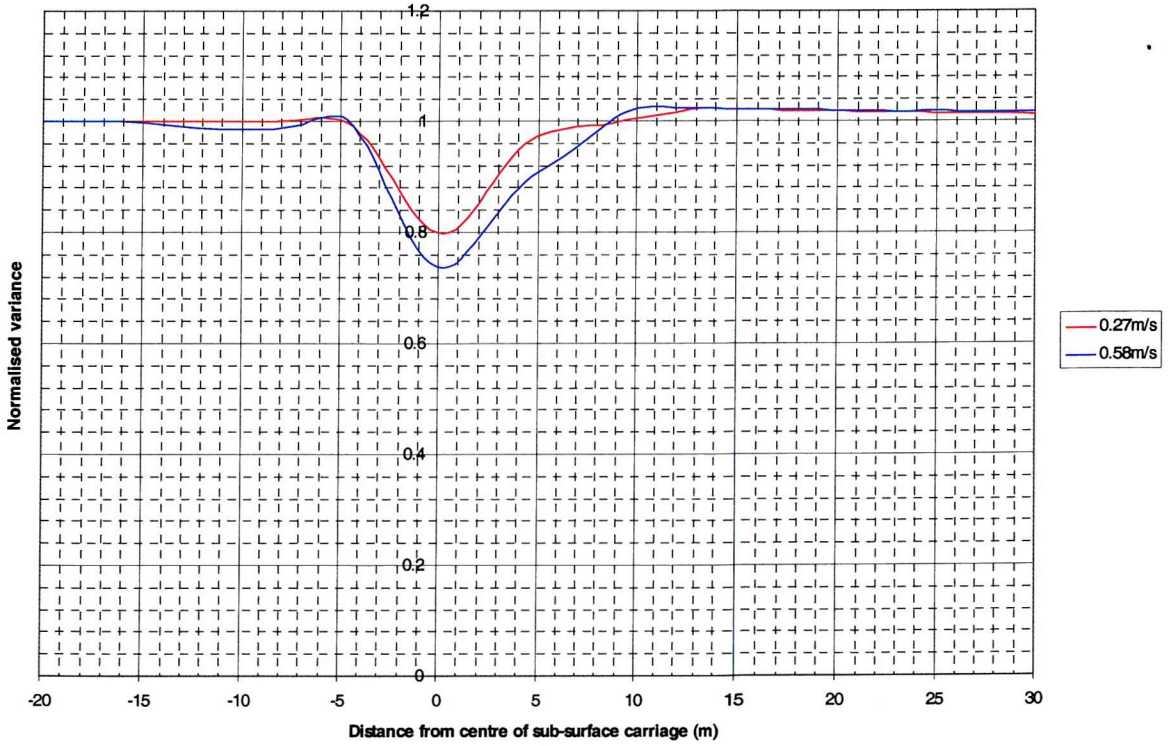

Figure 9-17: Variance variations for wind speed=3m/s, carriage and wind anti-parallel, p=1

The spectral results from the numerical model are displayed in figures 9-18 to 9-21. A detailed description of the theoretical spectral results can be found in Ballard (2000). It should be noted that at 5m/s the peak of the spectrum is at log10(frequency)=0.5 and at 3m/s it is at log10(frequency)=0.7. Each colour scale covers the full range of values plotted and so does not represent the same magnitudes in each image. It should also be noted that at the highest and lowest frequencies there is an apparently very strong effect is actually an artefact of the presentation method and is not real behaviour. This is caused by the theoretically calculated modulated spectrum extending outside the frequency range of the ambient spectrum and so the deviation of the spectrum shown is not from the ambient spectrum but from an arbitrary mean level which is used in regions outside the limits of the ambient spectrum.

Spectrally, the results were found to be qualitatively similar for p=1 and p=2, but they displayed different magnitudes of variations. Considering the variance data together with the spectral data to interpret the results, it is found that, in general, for the carriage running parallel to the wind direction, the decrease in variance over the centre of the carriage is caused by a general decrease in energy throughout the spectrum although concentrated around the spectral peak. Although the model has correctly predicted the experimentally measured variance change quite well, it has overpredicted the spectral change at the spectral peak implying that it must have underpredicted the spectral changes at other frequencies. The model does not predict well the experimentally measured increase in surface slope variance just after the carriage has passed.

For the carriage and wind direction anti-parallel, the experimentally measured variance decrease over the centre of the carriage is predicted quite well by the model. This variation is associated with a general spectral decrease, but again this is dominated by the changes around the spectral peak. For these runs, the magnitude of the changes at the spectral peak are quite similar in the experimental measurements and in the results from the numerical model.

This analysis has demonstrated the way in which the Laser Slope meter can be used to provide data which can be used to test and verify different forms of the action balance model. However, it is clear that whatever data collection and analysis techniques are

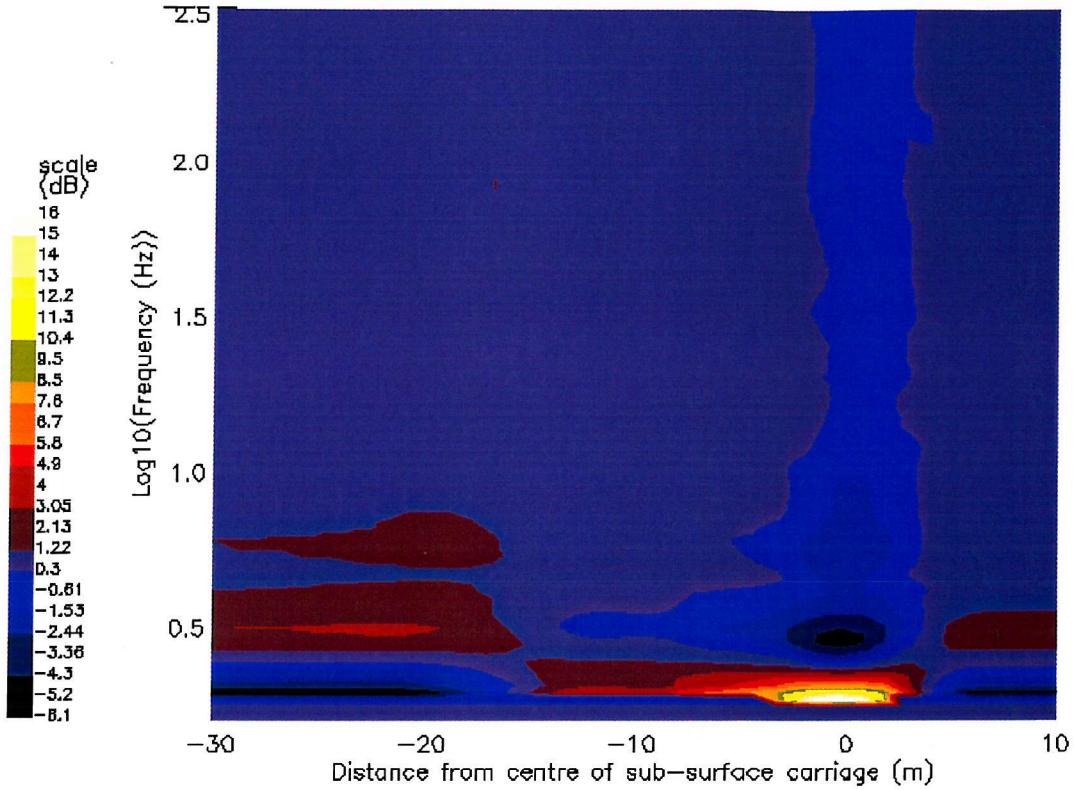

Figure 9-18: Spectral variations, wind speed=5m/s, carriage speed=0.57m/s, carriage and wind parallel, p=1

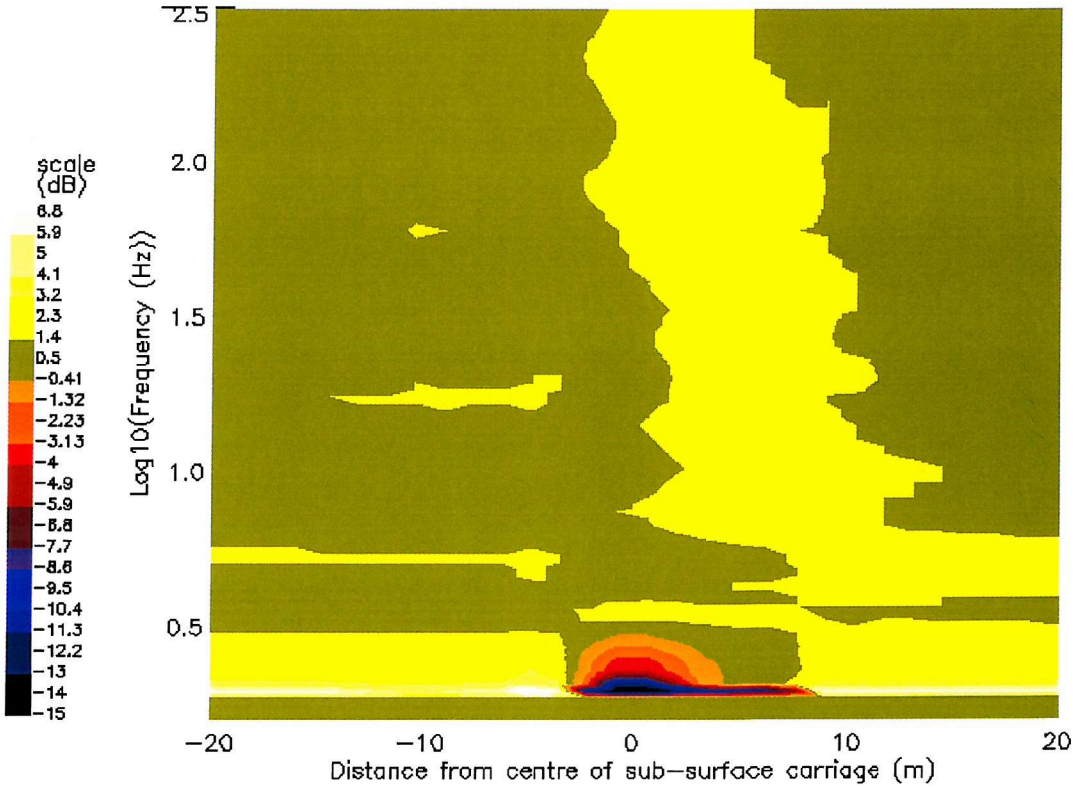

Figure 9-19: Spectral variations, wind speed=5m/s, carriage speed=0.58m/s, carriage and wind anti-parallel, p=1

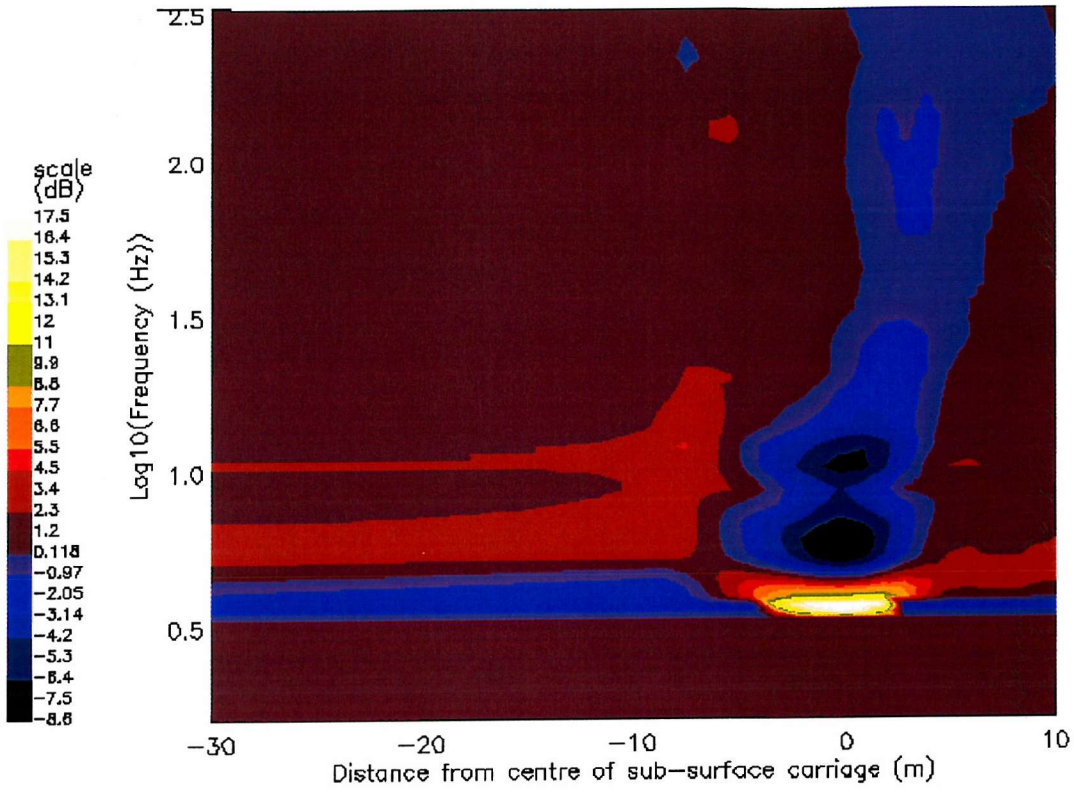

Figure 9-20: Spectral variations, wind speed=3m/s, carriage speed=0.26m/s, carriage and wind parallel, p=1

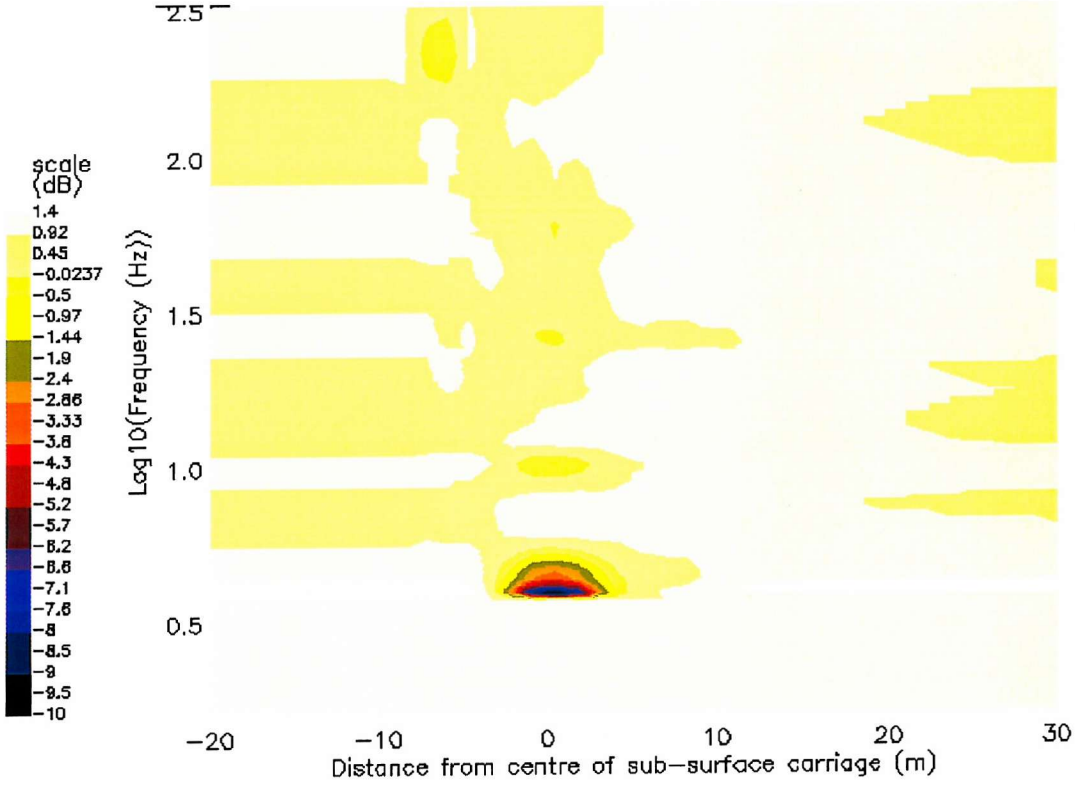

Figure 9-21: Spectral variations, wind speed=3m/s, carriage speed=0.27m/s, carriage and wind anti-parallel, p=1

employed, there will always be severe limitations for short waves and high frequencies, until more accurate knowledge about their behaviour is learnt from other sources and incorporated into the analysis presented here. Despite all the limitations, the model has predicted some of the experimentally measured variations quite well.

9.5 Discussion and conclusions

The experiment presented in this chapter has provided some useful insight into the use of the Laser Slope meter for measuring and understanding the interaction between a varying surface current and a surface wind wave field. The capabilities of the Laser Slope meter have been explored in detail for this type of research. Its strengths have been identified, as have its weaknesses and the information it cannot supply. The research has led to an improved understanding of the way in which to design such an experiment, in particular, learning that a significantly increased period of time must be left between the experimental runs for the wave field to regenerate, is an important finding. The scientific results have not been emphasised at this stage of the research as this was not the objective of this first experiment, but instead the conclusions have focused on the instrument and its limitations.

It has been shown that even with a simple single point instrument, clear modulations of the surface slope in the wave field can be measured, provided an average is taken over a sufficient number of independent measurements. These variations are clearer in the surface slope variance than in the spectra. This is likely to be due to the increased statistical errors which will be apparent in the spectra as each segment of information in the variance data is split up and spread out over the entire spectrum. It has been found to be more useful to use the variance data to determine where there are significant modulations to the wave field and then interpret these modulations spectrally using the spectrograms.

The Laser Slope meter has been used to estimate the wavenumber spectrum at each wind speed, as was described in chapter 7. The limitations of this method were discussed there but are relevant in this chapter as the spectral shape and energy will be incorrect in regions where the gravity-capillary dispersion relation is not applicable. However, given an accurate ambient spectrum, this work has shown how the output from a wavenumber based model can be used to produce theoretical estimates of the surface slope variance and slope

frequency spectra. Although there are limitations in the model used here, the exploration of how to use it and compare its output with experimental data has proved valuable. This work has demonstrated how the full action balance equation might be solved using appropriate ambient spectra and currents in order that a good comparison can be made with experimental data.

Overall, it is clear from the data analysis of both the ambient wave fields and the data presented here that the Laser Slope meter is a useful tool for the investigation of ocean phenomena. However, it has been shown that it is extremely difficult to reproduce accurately variations in the capillary wave regime and to form good scientific conclusions because of all the approximations that must be made. This is unfortunate given the capability of the instrument to measure extremely short scale waves accurately (in terms of the laser spot size and high frequencies). It is concluded that although a certain amount can be learnt about this type of interaction with this instrument, it would seem most appropriate for energy to be directed at performing similar experiments with a scanning device, which can measure the wavelength changes directly. The model presented can easily be modified to accept growth and decay terms appropriate to capillary waves and will also accept a full wavenumber spectrum from the scanning instrument due to its ability to have any reasonable spectrum as an input function.

Chapter 10

Conclusions

In this thesis an attempt has been made to determine the capability of a single point Laser Slope meter to extend and improve knowledge about the ocean surface wave field, particularly concentrating on its ability to improve understanding of radar imagery of the ocean. In order that its capability can be assessed fully, data have been studied from a number of experiments performed both in the field and in the laboratory, with the instrument stationary and with it being towed. So that conclusions can be formed about the usefulness of the instrument and the data it provides, these data have been compared with theoretical results and other experimental data, extending and manipulating the theories where necessary. The work presented demonstrates that there are a great many areas in which the Laser Slope meter has considerable potential and some of these are explored in detail. However, for certain measurements, particularly those involving spatial information, it is found that despite using sophisticated data analysis techniques, newer devices which scan the ocean surface to provide spatial information, can provide better and more accurate information. It is recommended that future effort is expended in the design of such instruments for deployment in the open ocean so that they can be used in all deployment situations to enhance the data currently available from a single-point Laser Slope meter.

The studies in this thesis have concentrated on determining the capability of the instrument in two particular areas of interest:

- the ambient ocean wave field;
- modulations to the ambient wave field caused by a varying surface current.

Each of these areas is now discussed separately, summarising the data and analysis techniques used, comparing and contrasting these data with other experimental and theoretical results, and summarising the overall potential and capability of the instrument

as explored throughout the thesis. The primary material presented within the main body of the thesis is referenced as required.

It has been shown that both in the field and in the laboratory, and with the instrument being both towed and stationary, it is capable of providing reliable slope statistics over the range of slope angles for which the instrument can measure accurately (this range was different between the field and tank experiments presented). One-dimensional histograms of these data are symmetric cross wind and skewed along wind which is in agreement with previous measurements of slope statistics using different measurement techniques (Schooley, 1954, Cox and Munk, 1944a). A Gaussian distribution has been found to fit the data reasonably, but can be improved upon by a one-dimensional Gram-Charlier distribution. However, when a full two-dimensional analysis is performed upon the data, it is found that the results are in contrast to those found by Cox and Munk. A two-dimensional Gaussian fit to the Laser Slope meter data is not good and this fit is significantly affected by the measurements of large slope components. If measurements of the largest slopes are ignored, both the Gaussian and Gram-Charlier fits are significantly improved. Cox and Munk's difficulty in measuring large slope components is a possible explanation of the difference between their results and the results presented in this thesis. Alternatively, particularly for the data collected in Loch Linnhe with the prototype Laser Slope meter, the error associated with the measurement of large slopes was increased and may have caused inaccuracies in the data. In the wave tank, however, a similar behaviour was observed, although the improved instrument did not suffer from the same high error at large angles, and was capable of measuring the majority of large wave slopes present in the wind wave fields.

From the experiments in the wave tank it was possible to study the variation of the Gram-Charlier coefficients with wind speed. It was found that these relationships differ from those calculated by Cox and Munk, with all of the coefficients remaining at a constant level except the cross wind peakedness coefficient which increased with increasing wind speed. The data collected in Loch Linnhe were not considered sufficiently reliable in terms of the cross and along wind components to be able to conduct a study of the how the coefficients vary with wind speed. However, the coefficients here were unusual as they were calculated to be particularly large. Investigations showed that this was necessary to enable a good Gram-Charlier fit from the poor Gaussian fit, which is the basis of the Gram-Charlier

distribution. If large slope components were ignored, the Gaussian fit was significantly improved and the Gram-Charlier coefficients were correspondingly smaller.

The variation of the mean square slope with wind speed has been studied. It was found that in the coastal waters of Loch Linnhe, Scotland, where there is little or no swell, the variation is very similar to data collected in wind wave tanks (including the Laser Slope meter data). A critical wind speed of approximately 1.6m/s has been determined below which no surface waves are generated. In the wave tank no waves were measured below 2m/s, whilst Wu (1971) reported no waves in his wave tank experiments before the wind speed reached 1.9m/s. Again, this is in contrast to the results of Cox and Munk (1944) who found a linear relationship right down to zero wind speed. These similarities between sheltered coastal waters and wind wave tanks and the differences from the open ocean may be explained by the presence of ocean swell. Miller *et al.* (1991) has found experimentally in a wind wave tank using mechanically generated swell that the presence of swell allows short scale surface waves to be generated at wind speeds where otherwise there would be no waves.

The wind friction velocity has been used to make further comparisons between some data sets presented in the literature, and the Laser Slope meter data collected in Loch Linnhe and in the wind wave tank. Using this parameter, rather than the wind speed, allows a comparison of the mean square slope generated by the same stress level in different environments. The Charnock relationship (Charnock, 1955) has been used to convert the wind speed measurements for the Laser Slope meter data collected in Loch Linnhe, and those of Cox and Munk (1944a), into wind friction velocity using the two different sets of coefficients suggested by Smith (1988) for coastal waters and the open ocean, respectively. It has been shown that the resulting variations of mean square slope with wind friction velocity are comparable. They are also similar to the data collected by Hughes and Grant (1978) in the Georgia Straits and with the Laser Slope meter wave tank results presented in this thesis. The greatest difference between the data sets occurs at low wind speeds, but above the critical velocity for wave generation. Greatest differences are observed between the two Laser Slope meter data sets, although the data of Hughes and Grant does not cover such low wind speeds. The Laser Slope meter tank results show slightly higher mean square slope's at the same wind stress that the Loch Linnhe Laser Slope meter data. This

could be due to inaccuracies in the measurement of the wind stress in the wave tank but is more likely to be caused by a large number of slicks on the Loch surface lowering the overall level of mean square slope. Despite all the differences in the measurement techniques and environments, the amount of similarity between these data sets gives confidence in the performance of the TLS, in the wind friction velocity conversions used and also in using wave tank data to simulate the real ocean.

In studies of the spectral characteristics of the ambient ocean surface, it has been shown theoretically that if the TLS is towed through the wave field, then in an attempt to gain spatial information, the data ambiguities associated with converting from the frequency of encounter of the waves with the TLS to the real wavenumber on the ocean surface can be reduced by towing the TLS antiparallel to the wind direction. This work illuminates the work of Hughes (1978) who found that his matrix inversion between wavenumber and frequency of encounter was only stable if the towing direction was within ±90° antiparallel to the wind direction. In this thesis, a modified version of Hughes' method of calculating a wavenumber spectrum has been used and extended with this improved understanding. In these studies, the surface wavenumber spectrum that was calculated was approximately k^{-4} with an assumed angular distribution of $\cos^2\theta$, in the gravity wave region immediately following the spectral peak. This type of spectrum has been measured experimentally (Banner *et al.,* 1989, Hughes, 1978) and also predicted theoretically (Phillips, 1958, Kitasigorodskii, 1983, Toba, 1972, 1973, Banner *et al.,* 1989), which provides confidence that this method of calculation has validity. Using this method, the TLS results from Loch Linnhe are not valid beyond the gravity wave range as only the gravity dispersion relation has been used in the conversion. For the limited data sets studied here the wavelength at the peak of the spectrum varies linearly with wind speed.

In the wave tank, the Laser Slope meter was used to make measurements of the ambient frequency spectra over a range of wind speeds between 1.6m/s and 12m/s. These spectra were analysed and found to be broadly consistent with previous experimental measurements. In detail, the total slope spectra showed approximately a f^{-1} to $f^{-1.5}$ behaviour in the region between the fall off from the spectral peak and the capillary wave region, where f is the frequency of the waves. This is roughly equivalent to a k^{-4} behaviour for the total wave height wavenumber spectrum, using the gravity dispersion relation in the

conversion. This region of the spectrum is for gravity waves, but is not quite at the spectral peak and would therefore be expected to have an equilibrium spectrum where the growth, dissipation and wave-wave interactions are balanced.

The measured spectra are in contrast to the spectrum determined by Phillips (1985) using this hypothesis of an equilibrium balance, but are consistent with Phillips earlier saturation spectrum (Phillips, 1958) where he assumed that the spectral form was governed by wave breaking. Banner *et al.* also suggested that k^{-4} spectrum may be consistent with an energy balance, depending on the particular form of the wave-wave interactions. Recently, Belcher and Vassilicos (1997) have suggested that it is possible for the wavenumber height spectrum to be k^{-4} with a frequency height spectrum of ω^{-4}, based on a wave breaking theory. This part of the measured total frequency spectrum is therefore broadly in agreement with previous measurements and theory.

Moving to the right of the spectral peak, towards higher frequencies, an increase in the spectral level over a range of frequencies has been measured. This type of behaviour has also been observed by Lange *et al.* (1982) and by Long and Huang (1976). It is difficult to know the precise details of these waves without some sort of additional information on their wavelength. Recent experiments using scanning Laser Slope meters (Hara *et al.*, 1997) have shown that capillary waves are often bound to the dominant gravity wave in a wind wave field. This may explain some of the observed spectral behaviour.

At very high frequencies, the spectrum decays. This may have a number of causes which include viscous dissipation of the shortest waves, reaching the noise level of the instrument, or the effects of the finite laser spot size. At the peak of the spectrum, the power increases approximately linearly with wind speed, as does the wavelength of the waves containing the peak energy (converted using the gravity dispersion relation). The way in which the energy at the peak of the spectrum at one wind speed is greater than the energy at that same frequency at a higher wind speed has been observed in the ocean (Komen *et al.*, 1994) and is known as the overshoot effect. This gives confidence that artificially generated wind wave spectra are similar in behaviour to the wind spectra generated in the open ocean.

The ratio of the cross to along tank frequency spectra has been used to provide information about the angular distribution of the data in the same way that Hughes used his ocean spectra (Hughes, 1978). This involves making the assumption that the angular distribution is of the form $\cos^q(\theta/2)$ and then using the cross and along tank frequency spectra to determine q. Using this method, the spectral peak is found to be quite directional with the data becoming less directional at higher frequencies. In the region of the approximately f^{-1} behaviour discussed above, the angular distribution is approximately $\cos^4(\theta/2)$. It has been found that at those wind speeds where many capillary waves were observed, the spectrum becomes more directional around the region of increased spectral level in the capillary wave regime. This is consistent with those capillary waves being parasitic.

Using the wave tank data, by allowing the angular distribution coefficient to vary at each frequency, a calculation was performed of the full wavenumber spectrum consistent with this frequency spectrum assuming the gravity-capillary dispersion relation. This spectrum should be a reasonable estimate in the gravity wave regime. It will only be correct in the capillary wave regime for those capillary waves which are generated and travel independently of the gravity waves. Given the recent findings of scanning Laser Slope meter experiments (Hara *et al.,* 1997) and the evidence presented above, it does not seem likely that the capillary wave part will be accurate. However, despite this, the spectrum shows a behaviour which is very similar to many ocean observations, summed up in empirical approach by Apel (1994). It has a spectral peak (which is not comparable with ocean data because of the limited fetch), displays an overshoot effect, shows a behaviour near k^{-4} between the spectral peak and the capillary region, a small region of slightly increased spectral value above the trend in the capillary wave regime and then decays smoothly to the noise level at high frequencies. The angular behaviour is as described above.

Finally, in the presentation of ambient wave field data in the wave tank, it has been shown how the temporal behaviour of a wind wave field varies with increasing wind speed. Once the critical wind speed is reached the range of slope values does not increase significantly. The measured peaks and troughs of the wind waves were found to be parabolic, the peaks being sharper than the troughs. This is consistent with Stokes' waves (Stokes, 1847, 1880). There is an increase in the dominant wavelength with wind speed and an increase in the

general high frequency behaviour. At approximately 4m/s, the high frequency behaviour is very ordered with clear capillary waves observed.

Some examples of these very high frequency capillary waves have been displayed. It is clear from these examples that at wind speeds of approximately 4m/s, that the noise level of the instrument is far below that which would hide such small features. The temporal resolution of the instrument and its high accuracy have allowed the measurement of the capillary waves, showing without doubt that their surfaces vary smoothly throughout the wave packet and over the gravity wave. An exercise was completed in an attempt to determine whether or not these waves are parasitic. This was not conclusive, although it was shown that they do display certain characteristics which are similar to the theory of Longuet-Higgins (1995).

Other features of surface waves revealed include group waves on the point of breaking where photographs and data have been collected simultaneously. This allows a very detailed study of the precise shape of a breaking wave. The potential of the instrument for such studies is immense, due to its high level of accuracy. By combining the data with other sources of information, such as photography, it is possible to obtain detailed profiles which may be related to spatial scales on the photographs. This type of information may be very useful in studies of radar scattering from wave features where details of the precise wave slopes are needed as well as information about the approximate shape of the waves.

Overall, in studies of the ambient wave field, the Laser Slope meter has shown that it has a great deal of potential in many areas. It is suggested that future scanning Laser Slope meters should be designed in such a way that they are capable of being deployed in the field as well as the wave tank.

In addition to the studies of the ambient wave field, the research on the modulation to the ambient surface wave field by a varying surface current has provided some interesting results and demonstrated the abilities and limitations of the Laser Slope meter in this area of research. It has been shown that a simple single point instrument can measure small modulations provided the experimental data are collected and analysed carefully. The data show that when the surface-current-generating sub-surface carriage was run in the direction

of travel of the surface waves, the surface slope variance decreased significantly and then increased above the mean level. The slope variance took some time to decrease back to the mean level. In reverse, there was a smaller decrease in the slope variance followed again by an increase which is not as great but a very long time is taken to return to the mean level. Of the 6 data sets collected, in one the current is too small for any effect to be seen and one other data set shows peculiar behaviour. The remaining four data sets all show the type of behaviour described. Spectrally, the results are harder to interpret. Taking an overview of the general behaviour of the data, it is apparent that the decrease in energy over the centre of the current pattern is caused by modulations occurring around the spectral peak. The increased energy following this can generally be attributed to spectral changes occurring at higher frequencies in the capillary wave regime. At present, given the noise in the data and the limited number of data sets, it is difficult to draw firm conclusions.

A numerical model was developed which solves the full action balance equation to determine theoretically the variations to the action density caused by the current. To allow the model to be partially valid for the full range of wavenumbers, including capillary waves, the full gravity-capillary dispersion relation has been assumed. The model was written to allow the input of any form of wave growth or decay term, which could account for terms appropriate to capillary waves as well as the well known terms for gravity waves. Thus, as new theories are developed they may be input simply and easily. In addition, the model is also capable of accepting an experimentally measured ambient wavenumber spectrum and surface current pattern. This model has been thoroughly tested and shown to be consistent with the expected output. It has also been shown that the approximations made by Phillips (1984) and Perry (1988) are invalid around resonance where the action modulation is severely underestimated. This model is an improvement over the model of Alpers (1985) or Alpers and Hennings (1984) as these models only use the dominant term in the action balance equation to calculate surface variations. It is similar to the work performed by Miller and Shemdin (1991), although in their work Hughes' method (Hughes, 1978) was used which assumes a linear approximation.

The model was used to produce a theoretical result for each the 12 experiments performed in the wave tank. A technique was successfully investigated for converting the output from the model into a form that could be directly compared with the experimental data. As a

broad generalisation, a comparison of the model output with the experimental data has shown that with the carriage and wind anti-parallel, the decrease of the surface slope variance over the centre of the carriage is modelled well, but the spectral changes creating these modulations are not modelled well around the spectral peak. The experimentally measured increase in surface slope variance just after the carriage had passed the Laser Slope meter is not modelled well. With the carriage and wind parallel, the decrease in the surface slope variance over the centre of the carriage is modelled well, as are the surface slope changes around the spectral peak resulting in this modulation. The results from the model have also shown that the power of the decay term has not significantly affected the calculation of the variance variations.

In the measurement of surface wave – surface current interactions, the Laser Slope meter has proved itself to be a useful tool for investigations. It has provided information which has been used to explore the energy variations due to the current patterns and has allowed an examination of the way in which these variations are split between the frequency bands. However, its main drawback is that it is unable to provide truly spatial information without an additional source of information. The model developed here has emphasised the need to know spatial information, particularly about the very small length scales. For this type of research, a scanning device is the best option and this should be considered for further research.

Overall, the instrument has been found to be very useful in a variety of conditions. One of its main advantages is that it can be deployed both in the ocean and the wind wave tank thus allowing a direct comparison between these types of data. Additionally, its high sampling rate, good accuracy and small laser spot size have allowed an investigation of the smallest details on the ocean surface. Its largest disadvantage is that it can only give a single point measurement and thus, to measure a wavenumber spectrum, some assumption about the directional form of the spectrum, and the dispersion relation, is always needed.

References

ALLAN,T.D., *Satellite microwave remote sensing,* Ellis Horwood Limited, 1983

ALPERS,W.R., ROSS,D.B., RUFENACH,C.L., On the detectability of ocean surface waves by real and synthetic aperture radar, *J. Geophysical Res.,* Vol. 86, No. C7, pp.6481-6498, 1981

ALPERS,W., The theory of radar imaging of internal waves, *Nature,* Vol. 314, 1985

ALPERS,W., HENNINGS,I., A theory of the imaging mechanism of underwater bottom topography by real and synthetic aperture radar, *J. Geophysical Res.,* Vol., 89, No. C6, pp.10529-10546, 1984

AMOROCHO,J., DEVRIES,J,J., A new evaluation of the wind stress coefficient over water surface, *J. Geophysical Res.,* vol. 85, no. C1, 1980

APEL,J.R., An improved model of the ocean surface wave vector spectrum and its effects on radar backscatter, *J. Geophysical Res.,* Vol. 99, No. C8, pp.16269-16291, 1994

BALLARD,V.J., *UCSB Tank Experiment, February / March 1999: Interaction between a surface wave field and a moving sub-surface carriage,* DERA/KIS/SPACE/WP00657/1.0, 2000

BANNER,M.L., JONES,I.S.F., TRINDER,J.C., Wavenumber spectra of short gravity waves, *J. Fluid Mech.,* vol. 198, pp.321-344, 1989

BARBER,B.C., Personal communication, 1999

BARNETT,S., *Matrix methods for engineers and scientists,* McGraw-Hill Book company (UK), Limited, 1979

BARTER,J.D., LEE,P.H.Y., LO,A.K., *Wind and Wave Profiles in the UCSB / OEL Wave Tank, TRW Rep. No. 63817-6001-UT-21.1,* 1998

BELCHER,S.E., VASSILICOS,J.C., Breaking waves and the equilibrium range of wind-wave spectra, *J. Fluid Mech.,* vol. 342, pp.377-401, 1997

BLACKMAN,R.B., TUKEY,J.W., *The measurement of power spectra (from the point of view of communications engineering),* Dover Publications, Inc, New York, 1958

BOAS,M.L., *Mathematical methods in the physical sciences,* Second Edition, John Wiley & Sons, Inc., 1966

BOOIJ,N., RIS,R.C., HOLTHUIJSEN,L.H., A third-generation wave model for coastal regions, 1. Model description and validation, *J. Geophysical Research,* vol. 104, no. C4, pp. 7649-7666, 1999

BOWDEN,K.F., *Physical oceanography of coastal waters,* Ellis Horwood Limited, 1983

BRETHERTON,F.P., GARRETT,C.J.R., Wavetrains in inhomogeneous moving media, *Proc. Roy. Soc.,* A, vol. 302, 1969

BROWNSWORD,C., Personal communication, 2000

CARTWRIGHT,D.E., *The use of directional spectra in studying the output of a wave recorder on moving ship,* N.A.S. Ocean wave spectra, Prentice-Hall Inc, Englewood Cliffs, N.J., pp.203-211, 1963

CHARNOCK,H., Wind stress on a water surface, *National Institute of Oceanography, Wormley, Surrey,* 1955

COOPER,T.M., Personal communication, 1998

COOPER,T.M., *An approach to finding spot positions for the new Towed Laser Slope meter,* DERA report, in preparation, 2000a

COOPER,T.M., *The theory of scanning laser slope meters,* DERA report, in preparation, 2000b

COX,C., MUNK,W., Measurement of the roughness of the sea surface from photographs of the sun's glitter, *J. Optical Society of America,* vol. 44, no. 11, 1954a

COX,C., MUNK., Statistics of the sea surface derived from sun's glitter, *J. Marine Research,* vol. 13, no. 2, 1954b

COX,C, Measurements of slopes of high-frequency wind waves, *J. Marine Res.,* Vol. 16, No. 3, 1958

DE LOOR,G.P., The observation of tidal patterns, currents, and bathymetry with SLAR imagery of the sea, *IEEE Journal of Oceanic Engineering,* 1981

DUNTLEY,S.Q., *The visibility of submerged objects. Part 1: Optical effects of water waves,* Mass. Inst. Tech. Report, 1950

EBUCHI,N., KAWAMURA,H., TOBA,Y., Fine structure of laboratory wind-wave surfaces studied using an optical method, *Boundary layer Met.* vol. 39, pp.133-151, 1987

FLATMAN,J.C., *Loch Linnhe Experiment 1997:ADCP data browse file,* DERA/CIS/CIS2/WP98022/1.0, 1998

FUCHS,J., WELCH,S., WASEDA,T., REGAS,D., TULIN,M.P., Inside the sea-spike: Low grazing angle radar imaging of laboratory waves repeatedly breaking in wave groups, presented at *IGARSS,* 1997

GARGETT,A.E., HUGHES,B.A., On the interaction of surface and internal waves, *J. Fluid Mech.,* vol. 52, part 1, pp.179-191, 1972

GARRATT,J.R., Review of drag coefficients over oceans and continents, *Monthly weather review,* 1977

GHATAURE,H.S., RAMSDEN,D., *Water Slopemeter Progress Report (Instrumentation),* Internal report to the DRA, 1992

GHATAURE ET AL., *Report on Progress of the Slopemeter (DRA Research Agreement no. 2040/509/RAE),* Internal report to DRA, 1993

GIBSON,G.E., *Loch Linnhe Experiment 1997: Trial plan,* DRA/CIS/CIS2/WP/97066/1.0, 1997

GIBSON,G.E., FLATMAN,J.C., HILL,R.D., KNIGHT,T.A.M., TAYLOR,V.J., *Initial results from the 1997 Loch Linnhe Experiment,* DERA/CIS/CIS2/CR98015/1.0, 1998

GILL,A.E., *Atmosphere-ocean dynamics,* International Geophysics series, vol. 309, Academic Press, 1982

GOMMENGINGER,C.P., ROBINSON,I.S., WILLOUGHBY,J., GREIDANUS,H., TAYLOR,V.J., Observations of bathymetry-induced ocean roughness modulation in in-situ surface slope measurements and coincident airborne SAR images, *IEEE,* 1999

GOOD,T.R., *Towed Laser Slopemeter refurbishment and improvements,* DERA contract with Aquatec Electronics, LSC/382, 1997a

GOOD,T,R., *Towed Laser Slopemeter Engineering Report,* DERA/CIS/CIS2/WP/987105/1.0, 1997b

GRIFFITHS,C.R., MACDOUGALL,N., *Data from a vertical string of interocean S4 EMCMs,* Dunstaffnage Marine Laboratory, Marine Technology Report, No. 141, 1997

HALL,J.H., MILES,S.P., *Measurement of the surface currents associated with a slow moving double-crested hump (U),* DERA/MSS/MSFC2/WP990689/1.0, 1999

HARA,T., BOCK,E.J., DONELAN,M., Frequency-wavenumber spectrum of wind generated gravity-capillary waves, *J. Geophysical Res.,* vol. 102, no. C1, pp.1061-1072, 1997

HAIMBACH,S.P., WU,J., Field trials of an optical scanner for studying sea-surface fine structures, *IEEE J. of Oceanic Engineering,* vol. OE-10, no. 4, 1985

HASSELMANN,K., On the non-linear energy transfer in a gravity-wave spectrum. Part 1: General theory, *J. Fluid Mech.,* vol. 12, pp.481-500, 1962

HASSELMANN,K., BARNETT,T.P., BOUWS,E., CARLSON,H., CARTWRIGHT,D.E., ENKE,K., EWING,J.A., GIENAPP,H., HASSELMANN,D.E., KRUSEMAN,P., MEERBURG.A., MULLER,P., OLBERS,D.J., RICHTER,K., SELL,W., WALDEN,H., Measurements of wind-wave growth and swell decay during the Joint North Sea Wave Project (JONSWAP), Dtsch. Hydrogr. Z. Suppl., A8(12), 95, 1973

HILL,R.D., LAMONT-SMITH,T., *Image directory of Loch Linnhe 1997, LGA and VLGA radar measurements,* DRA/LS2/WP97060/1.0, 1997

HMS DRYAD, *Training publication in oceanography and acoustics for underwater warfare,* The Applied Oceanography and Meteorological Centre, SMOPS, HMS Dryad, RESTRICTED

HOLLIDAY,D., ST-CYR,G., WOODS,N.E., Comparison of a new radar ocean imaging model with SARSEX internal wave image data, *Int. J. Remote Sensing,* vol. 8, no. 9, 1423-1430, 1987

HUGHES,B.A., The effect of internal waves on surface wind waves. 2:Theoretical analysis, *J. Geophysical Res.,* vol. 83, no. C1, 1978

HUGHES,B.A., GRANT,H.L., The effect of internal waves on surface wind waves. 1.Experimental measurements, *J. Geophysical Res.,* vol. 83, no. C1, 1978

HUGHES,B.A., GRANT,H.L., CHAPPELL,R.W., A fast response surface-wave slope meter and measured wind-wave moments, *Deep-Sea Res.,* vol. 24, pp.1211-1223, 1977

HWANG,P.A., SHEMDIN,O.H., Modulation of short waves by surface currents: a numerical solution, *J. Geophysical Res.,* vol. 95, No. C9, pp.16311-16318, 1990

JÄNHE,B., RIEMER,K.S., Two-dimensional wave number spectra of small-scale water surface waves, *J. Geophysical Res,* vol. 95, no. C7, pp.11531-11546, 1990

JANHE,B., SCHULTZ,H., Calibration and accuracy of optical slope measurements for short wind waves, *SPIE, Optics of the sir-sea interface,* vol. 1749, 1992

JANSSEN,J.A.M, Does wind stress depend on sea-state or not? - A statistical error analysis of HEXMAX data, *Boundary-layer Meteorology,* 83, 479-503, 1997

KAYE,G.W.C., LABY,T.H., *Tables of physical and chemical constants,* Longman, 14th Edition, 1978

KENDALL,M.G., STEWART,A., *The advanced theory of statistics, vol 1,* Charles Griffin &Company Limited, London, 1963

KINSMAN,B., *Wind waves:Their generation and propagation on the ocean surface,* Dover Publications, Inc, New York, 1984

KITAIGORODSKII,S.A., Application of the theory of similarity to the analysis of wind generated wave motion as a stochastic process, *Izv. Akad. Nauk, Ser. Geofiz,* 1, pp105-117, English Translation, 1, pp.73-80, 1962

KITAIGORODSKII,S.A., On the theory of the equilibrium range in the spectrum of wind-generated gravity waves, *J. Physical Oceanog.,* vol. 13, 1983

KLINKE,J., JANHE,B., 2D wave number spectra of short wind waves – results from wind wave facilities and extrapolation to the ocean, *Optics of the air-sea interface, SPIE,* vol. 1749, 1992

KNIGHT,T.A.M., *Loch Linnhe Experiment 1997: CTD chain data browse file,* DRA/CIS/(CIS2)/WP/97/021/1.0, 1997a

KNIGHT,T.A.M., *Loch Linnhe Experiment 1997: CTD yo-yo data browse file,* DRA/CIS/(CIS2)/WP/97/020/1.0, 1997b

KNIGHT,T.A.M., *Loch Linnhe Experiment 1997: Meteorological data browse file,* DRA/CIS(CIS2)/WP/97/022, 1997c

KOMEN,G.J., CAVALERI,L., DONELAN,M., HASSELMANN,K., JANSSEN,P.A.E.M., *Dynamics and modeling of ocean waves,* Cambridge University Press, pp.183-188, 1994

KOYUNCU,B., A laser quadrant detection technique for capillary wave measurements, *Optics and Lasers in Engineering,* vol. 22, pp.53-64, 1995

KRISTOFOROV,G.N., ZAPEVALOV,A.S., BANITY,M,V,. Statistical characteristics of sea surface slopes at different wind speeds, *Oceanology,* vol. 32, no. 3, 1992

LAMB,H., *Hydrodynamics,* Cambridge University Press, 6th Edition, 1975

LANGE,P.A., JAHNE,B., TSCHIERSCH,J., ILMBERGER,I., Comparison between an amplitude-measuring wire and a slope-measuring laser water wave gauge, *Rev. Sci. Instrum.* 53(5), 1982

LeBLOND,P.H., MYSAK,L.A., *Waves in the ocean,* Elsevier Scientific Publishing Company, 1978

LEE,C.G-Y., The design of a Towed Laser Slopemeter System for the measurement of short scale sea waves, *PhD thesis, University of Southampton,* 1995

LEE,P.H.Y, BARTER,J.D., BEACH,K.L., HINDMAN,C.L., LAKE,B.M., RUNGALDIER,H., SCHATZMAN,J.C., SHELTON,J.C., WAGNER,R.N.,

WILLIAMS,A.B., LEE,R., YUEN,H.C., Recent advances in ocean surface characterization by a scanning laser slope gauge, *SPIE, Optics of the air-sea interface,* vol. 1749, 1992

LIGHTHILL,J., *Waves in fluids,* Cambridge University Press, 1979

LOBEMEIER,P., A wire probe for measuring high frequency sea waves, *J. Phys. E: Sci. Instrum.,* vol. 14, 1981

LONG,S.R., HWANG,N.E., On the variation and growth of wave-slope spectra in the capillary-gravity wave range with increasing wind, *J. Fluid Mech.,* vol. 77, part 2, pp.209-228, 1976

LONGUET-HIGGINS,M.S., The statistical analysis of a random, moving surface, *Phil. trans. Roy. Soc. London, series A,* vol. 249, 1957

LONGUET-HIGGINS,M.S., Parasitic capillary waves: a direct calculation, *J. Fluid Mech.,* vol. 301, pp. 79-107, 1995

LONGUET-HIGGINS,M.S., STEWART,R.W., Changes in the form of short gravity waves on long wave and tidal currents, *J. Fluid Mech.,* pp.565-583, 1960

LOVE,R.I.N., Personal communication, 2000

LOVE,R.I.N., COOPER,T.M., *Outline management plan for scanning laser slopemeter,* Internal DERA memorandum, 1999

LUBARD,S.C., KRIMMEL,J.E., THEBAUD,L.R., EVANS,D.D., SHEMDIN,O.H., Optical image and laser slope meter intercomparisons of high-frequency waves, *J. Geophysical Res.,* vol. 85, no. C9, pp.4996-5002, 1980

McGOLDRICK,l.F., A sensitive linear capacitance-to-voltage converter, with applications to surface wave measurements, *The Review of Scientific Instruments,* vol. 42, no. 3, 1971

MELDRUM,D., PEPPE,O., *Loch Linnhe Experiment 1997: Vessel tracking using DGPS,* Technical report by the Marine Technology Group, Dunstaffnage Marine Laboratory under contract LSC/312. Marine Technology Report No. 142, 1997

MILES,J.W., On the generation of surface waves by shear flows, *J. Fluid Mech.,* vol. 3, pp.185-204, 1957

MILLER,S.J., SHEMDIN,O.H., Measurement of the hydrodynamic modulation of centimeter waves, *J. Geophysical Res.,* vol. 96, no. C2, pp.2749-2759, 1991

MILLER,S.J., SHEMDIN,O.H., LONGUET-HIGGINS,M.S., Laboratory measurements of modulation of short-wave slopes by long surface waves, *J. Fluid Mech.,* vol. 233, pp.389-404, 1991

NICHOLAEV,N.I., YORDANOV,O.I., Non-Gaussian effects in the two-scale model for rough surface scattering, *J. Geophysical Res.,* vol. 97, no. C10, pp. 15617-15624, 1992

PAPOULIS,A., *Signal analysis,* McGraw-Hill Book Company, 1977

PAYNE,C., *Theoretical investigation of the effects on the surface current and displacement created when moving a sub-surface carriage through a tank of water,* DERA/CIS/CIS2/TR000077/1.0, 2000

PERRY,J.R., The radar remote sensing of oceanic internal waves, *PhD thesis, Imperial College, University of London,* 1988

PHILLIPS,O.M., On the generation of waves by turbulent wind, *J. Fluid Mech.,* vol. 2, pp.417-445, 1957

PHILLIPS,O.M., The equilibrium range in the spectrum of wind-generated waves, *J. Fluid Mech.,* vol.4, pp. 426-434, 1958

PHILLIPS,O.M., *The dynamics of the upper ocean,* 2nd Edition, Cambridge University Press, 1977

PHILLIPS,O.M., On the response of short ocean wave components at a fixed wavenumber to ocean current variations, *J. Physical Oceanog.,* vol. 14, 1984

PHILLIPS,O.M., Spectral and statistical properties of the equilibrium range in wind-generated gravity waves, *J. Fluid Mech.,* vol. 156, pp.505-531, 1985

PIERSON,W.J.,Jr, MOSKOWITZ,L., A proposed spectral form for fully developed wind seas based on the similarity theory of S.A.Kitaigorodskii, *J. Geophysical Res.,* vol. 69, No. 24, 1964

PLANT,W.J., A relationship between wind stress and wave slope, *J. Geophysical Res.,* vol. 87, no. C3, pp.1961-1967, 1982

PRESS,W.H., FLANNERY,B.P., TEUKOLSKY,S.A., VETTERLING,W.T., *Numerical recipes: The art of scientific computing,* Cambridge University press, 1986

RAYLEIGH,Lord, *The theory of sound,* London: Macmillan and co. and New York, vol. 1, pp.39-42, 1894

RICE,S.O., Mathematical analysis of random noise:Part 1-shot effect, and part 2-power spectra and correlation functions, *Bell System Technical Journal,* 1944

SCHOOLEY,A.H., A simple optical method for measuring the statistical distribution of water surface slope, *J. Opt. Soc. Amer.,* vol. 44, pp.37-40, 1954

SHAW,J.A., CHURNSIDE,J.H., Ocean ripple statistics measured with a scanning-laser glint sensor, *IEEE IGARSS,* 1996

SHAW,J.A., CHURNSIDE,J.H., SMITH,S.D., Scanning-laser glint measurements of sea surface slope statistics, *Applied Optics,* vol. 36, no. 18, 1997

SMITH,S.D., Wind stress and heat flux over the ocean in gale force winds, *American Meteorological Society,* 1980

SMITH,S.D., Coefficients for sea surface wind stress, heat flux and wind profiles as a function of wind speed and temperature, *J. Geophysical Res.,* vol. 93, pp.15467-15472, 1988

SMITH,S.D., BANKE,E.G., Variation of the sea surface drag coefficient with wind speed, *Quart. J. R. Met. Soc.,* vol. 101, pp.665-673, 1975

STILWELL,D.Jr., Directional energy spectra of the sea surface from photographs, *J. Geophysical Res.,* vol. 74, no. 8, 1969

STILWELL,D.Jr., PILON,R.O., Directional spectra of the surface waves from photographs, *J. Geophysical Res.,* vol. 79, no. 9, 1974

STOKES,G.G., On the theory of oscillatory waves, Trans. Camb. Phil. Soc., 8, 441 (Also in Mathematical and Physical Papers, vol. 1, London: Cambridge University Press, 1880, pp.197-229

STOKES,G.G., Supplement to a paper on the theory of oscillatory waves, *Mathematical and Physical papers,* vol. 1, London, Cambridge University Press, pp.314-326, 1880

STURM,G.V., SORRELL,F.Y., Optical wave measurement technique and experimental comparison with conventional wave height probes, *Applied Optics,* vol. 12, no. 8, 1973

TAYLOR,V.J., *Spectral and statistical properties of sea surface slope: literature review and applicability to Towed Laser Slopemeter data,* DERA/CIS2/WP/97066/1.0, 1997

TAYLOR,V.J., *Loch Linnhe Experiment 1997: Towed Laser Slopemeter Preliminary Data Analysis Report,* DERA/CIS/CIS2/WP/97331/1.0, 1997

TAYLOR, V.J., *Study of the surface strain rate produced by long surface waves and by a moving sub-surface carriage,* DERA/CIS/CIS2/TR980290/1.0, 1998

TAYLOR,V.J., *UCSB Tank Experiment July / August 1998: Experimental procedure and preliminary results,* DERA/CIS/CIS2/WP990077/1.0, 1999

TAYLOR,V.J., COOPER,T.M., *Loch Linnhe Experiment 1997: Towed Laser Slopemeter Second Data Analysis Report,* DERA/CIS/CIS2/WP990087/1.0, 1999

THOMPSON,D.R., GASPAROVIC,R.F., Intensity modulation in SAR images of internal waves, *Nature,* Vol. 320, 1986

TOBA,Y., Local balance in the air-sea boundary processes: 1. On the growth process of wind waves, *J. Oceanog. Soc. Japan,* vol. 28, pp.109-121, 1972

TOBA,Y., Local balance in the air-sea boundary processes: 3. On the spectrum of wind waves, *J. Oceanog. Soc. Japan,* vol. 29, pp. 209-220, 1973

UNNA,P.J., Sea waves, *Nature,* Lond., vol. 159, pp.239-242, 1947

URSELL,F., Steady wave patterns on a non-uniform steady fluid flow, *J. Fluid Mech,* vol. 9, pp. 333-346, 1960

USPENSKY,J.V., *Introduction to mathematical probability,* McGraw-Hill Book Company, New York, 1937

VILENSKY,I.G., GLOUHOVSKY,B.H., KRILOV,J.M., JUSCHAK,A.A., *Some results and methods of investigation of sea wind waves,* in Annals of the International Geophysical Year, vol. XI, Symposia at the Fifth Meeting of CSAGI, New York: Permagon Press, pp.324-364

WALKER,D., *A model for low grazing angle Doppler spectra,* DERA/S&P/RAD/WP990586/1.0, 1999

WAMDI Group, The WAM model – A third generation ocean wave prediction model, *J. Phys. Oceaogr.*, 18, pp. 1775-1810, 1988

WATSON,G.N., *Theory of Bessel Functions,* Cambridge University Press, 1958

WHITHAM,G.B., *Linear and nonlinear waves,* John Wiley and Sons, New York, 1974

WILLOUGHBY,B.J., The assessment of a towed laser slopemeter for measuring short scale sea surface wave slopes, *PhD thesis, University of Southampton,* 1998

WU,J., Laboratory studies of wind wave interactions, *J. Fluid Mech.,* vol. 34, part 1, pp.91-111, 1968a

WU,J., Froude number scaling of wind stress coefficients, *J. Atmospheric Sciences,* vol.26, 1968b

WU,J., Wind stress and surface roughness at air-sea interface, *J. Geophysical Res.,* vol.74, no. 2, 1969a

WU,J., Froude number scaling of wind-stress coefficients, *J. Atmospheric Sciences*, vol. 26, 1969b

WU,J., Slope and curvature distributions of wind-disturbed water surface, *J. of the Optical Soc. Of America,* vol. 61, no. 7, 1971

WU,J., Directional slope and curvature distributions of wind waves, *J. Fluid Mech.,* vol. 79, part 3, 1976

WU,J., Wind stress coefficients over sea surface near neutral conditions-a revisit, *American Meteorological Society,* 1980

YELLAND,M.J., TAYLOR,P.K., Wind stress measurements from the Open Ocean. *J. Phys. Oceanogr.*, 26, 541 – 558, 1996

YELLAND,M.J., TAYLOR,P.K., *Does the wind stress depend on the sea state?,* Wind-Over-Wave Couplings: Perspectives and Prospects. Editors: Sajjadi, Hunt and Thomas. Oxford University Press, 107-117, 1999

ZHANG,X., Capillary-gravity and capillary waves generated in a wind wave tank: observations and theories, *J. Fluid Mech.,* vol. 289, pp. 51-82, 1995

Appendix A

Development of a 2-dimensional Gram-Charlier distribution

Consider a two-dimensional Gaussian distribution,

$$p_g(x,y)=\frac{1}{2\pi}e^{-\frac{1}{2}(x^2+y^2)} \qquad \text{A-1}$$

Derivatives of $p_g(x,y)$ up to fourth derivatives can be calculated as follows,

$$\frac{d}{dx}[p_g(x,y)]=-xp_g(x,y) \qquad \text{A-2}$$

$$\frac{d}{dy}[p_g(x,y)]=-yp_g(x,y)$$

$$\frac{d^2}{dx^2}[p_g(x,y)]=(x^2-1)p_g(x,y)$$

$$\frac{d^2}{dy^2}[p_g(x,y)]=(y^2-1)p_g(x,y)$$

$$\frac{d^2}{dxdy}[p_g(x,y)]=xyp_g(x,y)$$

$$\frac{d^3}{dx^3}[p_g(x,y)]=(3x-x^3)p_g(x,y)$$

$$\frac{d^3}{dx^2dy}[p_g(x,y)]=-(x^2-1)yp_g(x,y)$$

$$\frac{d^3}{dxdy^2}[p_g(x,y)]=-x(y^2-1)p_g(x,y)$$

$$\frac{d^3}{dy^3}[p_g(x,y)]=(3y-y^3)p_g(x,y)$$

$$\frac{d^4}{dx^4}[p_g(x,y)]=(x^4-6x^2+3)p_g(x,y)$$

$$\frac{d^4}{dx^3dy}[p_g(x,y)]=-(3x-x^3)yp_g(x,y)$$

$$\frac{d^4}{dx^2dy^2}[p(x,y)] = (x^2-1)(y^2-1)p_g(x,y)$$

$$\frac{d^4}{dxdy^3}[p_g(x,y)] = -x(3y-y^3)p_g(x,y)$$

$$\frac{d^4}{dy^4}[p_g(x,y)] = (y^4-6y^2+3)p_g(x,y)$$

The Tchebychef-Hermite polynomials are defined in terms of the derivatives of $p_g(x,y)$, where D_x and D_y represent differential operators,

$$(-D_x)^n(-D_y)^m p_g(x,y) = H_n(x)H_m(y)p_g(x,y) \qquad \text{A-3}$$

These polynomials have an important orthogonal property. If $p_{g1}(x) = \frac{1}{\sqrt{2\pi}}e^{-\frac{1}{2}x^2}$ then,

$$\int_{-\infty}^{\infty} H_n(x)H_r(x)p_{g_1}(x)dx = 0 \qquad n \neq r$$

$$= r! \qquad n = r \qquad \text{A-4}$$

If it is supposed that a two-dimensional frequency function, which is an unnormalised pdf, can be expanded formally in a series of derivatives of $p_g(x,y)$, then,

$$f(x,y) = \sum_{i,j=0}^{\infty} b_{i,j}H_i(x)H_j(y)p_g(x,y) \qquad \text{A-5}$$

Multiplying by $H_r(x)H_s(y)$ and integrating from -∞ to ∞ in both cases, by virtue of the orthogonality relationship,

$$b_{rs} = \frac{1}{r!s!}\int_{-\infty}^{\infty}\int_{-\infty}^{\infty} f(x,y)H_r(x)H_s(y)dxdy \qquad \text{A-6}$$

If the values of $H_r(x)$ and $H_s(y)$ are substituted in this equation then taking terms up to r+s=4 and writing the moments of the distribution about the origin as m′, where,

$$m'_{rs} = \int_{-\infty}^{\infty}\int_{-\infty}^{\infty} f(x,y)x^r y^s dxdy \qquad \text{A-8}$$

then,

$$\begin{aligned}
b_{00} &= 1 \qquad \text{A-9}\\
b_{10} &= m'_{10}\\
b_{01} &= m'_{01}\\
b_{20} &= \frac{1}{2}(m'_{20} - 1)\\
b_{11} &= m'_{11}\\
b_{02} &= \frac{1}{2}(m'_{02} - 1)\\
b_{30} &= \frac{1}{6}(m'_{30} - 3m'_{10})\\
b_{21} &= \frac{1}{2}(m'_{21} - m'_{01})\\
b_{12} &= \frac{1}{2}(m'_{12} - m'_{10})\\
b_{03} &= \frac{1}{6}(m'_{03} - 3m'_{01})\\
b_{40} &= \frac{1}{24}(m'_{40} - 6m'_{20} + 3)\\
b_{31} &= \frac{1}{6}(m'_{31} - 3m'_{11})\\
b_{22} &= \frac{1}{4}(m'_{22} - m'_{20} - m'_{02} + 1)\\
b_{13} &= \frac{1}{6}(m'_{13} - 3m'_{11})\\
b_{04} &= \frac{1}{24}(m'_{04} - 6m'_{02} + 3)
\end{aligned}$$

If the distribution is written in standard form then,

$$\xi = \frac{x - \bar{x}}{\sigma_c} \qquad \text{A-10}$$

$$\varsigma = \frac{y - \bar{y}}{\sigma_u}$$

The above coefficients can be written in terms of the moments about the mean, m, so that,

$$m_{10} = m_{01} = 0 \qquad \text{A-11}$$

$$m_{20} = m_{02} = 1$$

If it is assumed that the distribution is symmetrical about the y axis. Then,

$$m_{11} = m_{12} = m_{13} = m_{30} = m_{31} = 0 \qquad \text{A-12}$$

The remaining coefficients can then be written as,

$$b_{00} = 1 \qquad \text{A-13}$$

$$b_{21} = \frac{1}{2} m_{21}$$

$$b_{03} = \frac{1}{6} m_{03}$$

$$b_{40} = \frac{1}{24}(m_{40} - 3)$$

$$b_{22} = \frac{1}{4}(m_{22} - 1)$$

$$b_{04} = \frac{1}{24}(m_{04} - 3)$$

Since the Gaussian function in x and y is now normalised using the standard deviation, the full series for the frequency function is now a probability function in x,y. This can be written as,

$$p(x,y) = \frac{1}{2\pi\sigma_c\sigma_u} e^{-\frac{1}{2}(\xi^2+\varsigma^2)} \left[\begin{array}{l} b_{00} + b_{21}(\xi^2 - 1)\varsigma + b_{03}(\varsigma^3 - 3\varsigma) + b_{40}(\xi^4 - 6\xi^2 + 3) + \\ b_{22}(\xi^2 - 1)(\varsigma^2 - 1) + b_{04}(\varsigma^4 - 6\varsigma^2 + 3) \end{array} \right] \qquad \text{A-14}$$

This series is known as a Gram-Charlier series of type A.

Cox and Munk wrote their series in the following way,

$$p(x,y)=\frac{1}{2\pi\sigma_c\sigma_u}e^{-\frac{1}{2}(\xi^2+\varsigma^2)}\left[\begin{array}{l} C_{00}-\frac{C_{21}}{2}(\xi^2-1)\varsigma-\frac{C_{03}}{6}(\varsigma^3-3\varsigma)+ \\ \frac{C_{40}}{24}(\xi^4-6\xi^2+3)+\frac{C_{22}}{4}(\xi^2-1)(\varsigma^2-1)+ \\ \frac{C_{04}}{24}(\varsigma^4-6\varsigma^2+3) \end{array}\right] \qquad \text{A-15}$$

Therefore,

$$\begin{aligned} C_{00} &= 1 \\ C_{21} &= -m_{21} \\ C_{03} &= -m_{03} \\ C_{40} &= m_{40}-3 \\ C_{22} &= m_{22}-1 \\ C_{04} &= m_{04}-3 \end{aligned} \qquad \text{A-16}$$

Appendix B

Diagonalisation

A rotation of the axes can be found by applying an orthogonal transformation. (This is a special case of a linear transformation when the axes (x,y) are perpendicular.) By definitio , a transformation is orthogonal if the distance of a point from the origin in the (x,y) axes system remains the same when the point is considered in the (X,Y) axes system. Hence,

$$x^2 + y^2 = X^2 + Y^2 \qquad \text{B-1}$$

n

If,

$$\begin{pmatrix} X \\ Y \end{pmatrix} = \begin{pmatrix} O_{11} & O_{12} \\ O_{21} & O_{22} \end{pmatrix} \begin{pmatrix} x \\ y \end{pmatrix} \qquad \text{B-2}$$

Then the orthogonality condition can be written,

$$O_{11}{}^2 + O_{21}{}^2 = 1 \qquad \text{B-3}$$

$$O_{12}{}^2 + O_{22}{}^2 = 1$$

$$O_{11}O_{12} + O_{21}O_{22} = 0$$

One simple condition which an orthogonal matrix, O, satisfies is that the transpose of the matrix is equal to its inverse.

$$O^T = O^{-1} \qquad \text{B-4}$$

i.e.,

$$\begin{pmatrix} O_{11} & O_{21} \\ O_{12} & O_{22} \end{pmatrix}\begin{pmatrix} O_{11} & O_{12} \\ O_{21} & O_{22} \end{pmatrix}=\begin{pmatrix} O_{11}^{\,2}+O_{21}^{\,2} & O_{11}O_{12}+O_{21}O_{22} \\ O_{12}O_{11}+O_{22}O_{21} & O_{12}^{\,2}+O_{22}^{\,2} \end{pmatrix}=\begin{pmatrix} 1 & 0 \\ 0 & 1 \end{pmatrix} \qquad \text{B-5}$$

by equations above.

If the probability distribution of x and y is represented by p(x,y) and the probability of X and Y is given by p(X,Y), then the probability of X and Y lying in the range dXdY is given by,

$$p(X,Y)dXdY = p(x,y)\begin{vmatrix} \frac{\partial x}{\partial X} & \frac{\partial x}{\partial Y} \\ \frac{\partial y}{\partial X} & \frac{\partial y}{\partial Y} \end{vmatrix} dXdY = p(x,y)\begin{vmatrix} O_{11} & O_{12} \\ O_{21} & O_{22} \end{vmatrix} dXdY \qquad \text{B-6}$$

If the matrix is a rotation matrix then det(O)=1 and so,

$$p(X,Y) = p(x,y) \qquad \text{B-7}$$

If the matrix of variances and covariances of X and Y is considered,

$$M = \begin{pmatrix} M_{20} & M_{11} \\ M_{11} & M_{02} \end{pmatrix} = \sum p(X,Y)\begin{pmatrix} X \\ Y \end{pmatrix}\begin{pmatrix} X & Y \end{pmatrix} = \sum p(x,y)O\begin{pmatrix} x \\ y \end{pmatrix}\begin{pmatrix} x & y \end{pmatrix}O^{T} \qquad \text{B-8}$$

$$= O\sum p(x,y)\begin{pmatrix} x \\ y \end{pmatrix}\begin{pmatrix} x & y \end{pmatrix}O^{T} = O\begin{pmatrix} m_{20} & m_{11} \\ m_{11} & m_{02} \end{pmatrix}O^{T}$$

Therefore, it can be seen that the matrix, O, can be used to diagonalise m. If O is found from the unit eigenvectors of m then it will rotate m to produce a diagonal matrix M that contains the moments along the principal axes.